Optical & X-ray Studies of Ultraluminous X-ray Sources

JEANETTE CLAIRE GLADSTONE

How to cite:

GLADSTONE, JEANETTE CLAIRE (2009) Optical & X-ray Studies of Ultraluminous X-ray Sources. Doctoral thesis, Durham University.

Optical & X-ray Studies of Ultraluminous X-ray Sources

Jeanette Claire Gladstone

A Thesis presented for the degree of
Doctor of Philosophy

X-Ray Sub-Group
Extragalactic Astronomy and Cosmology
Department of Physics
University of Durham
United Kingdom

September 2009

Dedicated to

Stuart, without you I would not be here now.

Thank you for everything.

Abstract

Ultraluminous X-ray Sources (ULXs) are point like X-ray sources situated external to the nucleus of their host galaxy, with inferred X-ray luminosities in excess of 10^{39} erg s^{-1}. Although first observed $\sim$ 30 years ago, these sources are yet to be fully understood. Some have suggested that these fascinating objects may contain intermediate mass black holes, whilst others have proposed they are stellar mass black holes residing in a new extreme accretion state. This thesis works towards the conclusion of this debate, by developing our understanding of these systems and their environments.

This work begins with a photometric survey of the optical counterparts of ULXs. The main aim of this survey is to find plausible candidates to gain radial velocity measurements and therefore mass functions of these systems. However, the collation of this sample also provides the opportunity to classify the stellar objects held within these systems. From this work, we find seven good candidates for optical spectroscopic follow-up. Our results also show that many of our sample are consistent with OB type stars, while some contain later type bright giants/supergiants.

Possibly our best chance to gain precise measurements of $M_{\rm BH}$, and settling the debate over the nature of these systems, is by using radial velocity curves of their optical counterparts to calculate a mass function of ULXs. We are currently undertaking a programme to pursue mass function measurements for these systems. To date, we have received the pilot spectra of three optical counterparts.

We discuss the progress of this programme to date and perform analysis on both the absorption/emission features and the continuum of these spectra. Initial analysis reveals the presence of the He II 4686 Å line in two of our pilot spectra. This line may be associated with the accretion disc of these systems, and could therefore be used in our pursuit of the mass function. We also find the presence of both low and high ionization lines, with some evidence for shock ionisation, and electron temperature of 7,000 – 10,000 K. This Balmer decrement also indicates that the extinction can be highly variable across ULX field. This combination may suggest a 'patchy' environment with separate shock and photoionisation emission regions. While the continuum emission of one of our sample can be explained by either the spectra of an OB star or of a standard accretion disc, the steep slopes of two of our sample indicates non-stellar origins that could represent the optical spectrum of a super-Eddington accretion disc. Finally, this work highlights the need for further observations of these sources in order to unlock their nature.

We present results of X-ray spectral variability studies of the ULX population contained within NGC 4485 & 4490. We collate *Chandra* and *XMM-Newton* observations of the interacting galaxy pair, to analyse the emission from the six ULXs previously identified, and one additional source observed in the a recent exposure. This provides us with an opportunity to study variability on both short and longer time scales. The spectral variability is generally characterised by a hardening of the source spectra as their luminosities increase. The sources show a variety of long-term light curves; however, short-term (intra-observational) temporal variability is conspicuous by its absence. This survey also reveals the detection of a possible change in accretion state that could be used to gain crude mass estimates of the compact objects. Finally, we explore further the variability of these systems with the aid of two new proprietary observations.

Finally, analysis of some of the best quality X-ray spectral data publicly available on these sources has provided the opportunity to explore the nature of these systems. We apply phenomenological models to characterise the spectra of these objects and more physically motivated models in order to explore the physical processes underlying these characteristics. Results show that the spectra of these sources are fundamentally different to that of Galactic X-ray binaries, whilst the application of physical models indicates a more extreme version of the highest known luminosity state, the very high state. We therefore speculate that in observing ULXs we are observing stellar mass black holes residing in a new '*ultraluminous*' state.

Contents

Declaration

The work described in this thesis was undertaken between 2006 and 2009 while the author was a research student under the supervision of Dr Timothy Roberts and Professor Christine Done in the Department of Physics at the University of Durham. This work has not been submitted for any other degree at the University of Durham or any other University.

Portions of this work have appeared in the following papers:

- Gladstone J. C., Roberts T. P., 2009, MNRAS, 397, 124
- Gladstone J. C., Roberts T. P., Done C., 2009, MNRAS, 397, 1836

Acknowledgements

I would like to begin by thanking my supervisors Dr Timothy Roberts and Prof Christine Done, for providing help, guidance and and a great deal of patience during the course of my PhD. Thank you for inviting me to work with you as I have developed my knowledge and skills.

I appreciate the useful discussions with friends and colleagues for making this period of study so enjoyable. This includes Dr Marek Gierliński & Matthew Middleton, for their discussions and guidance in understanding X-ray astronomy. I would also like to thanks Dr Mark Swinbank, Dr Mike Goad and Sarah Hutton for helping me get to grips with optical astronomy. I thank Andrew Goulding & Julie Wardlow for all their help during my struggles with IDL. I would also like to mention Dr Richard Bielby, Dr Jonathan Gelbord, Floyd Jackson, Jennifer Gray, Lisa Davies and finally Dr Nick Schurch for the thought provoking discussions (and distractions!) they have been a part of during my time at Durham.

Thanks must also be given to the Science and Technology Facilities Council for funding this work (PPA/S/S/2006/04340).

Last, but by no means least, I am very grateful to my family for giving me so much encouragement and support. You've been fantastic.

Thank you all!

Chapter 1

Introduction

1.1 The optical sky

For thousands of years people have looked at the sky above us and tried to understand what they saw. It has inspired generations to look for its meaning, leading to the development of a range of subjects and applications in both theology and science. In ancient times, many structures were built in conjunction with astronomical events. These structures also had close links to their cultural heritage and belief systems. For example, Stonehenge is a stone circle, near Salisbury in the UK, that marks the rise and set of both the Sun and the Moon on the solstice (the longest and briefest days of the year). The Mayans chose to mark only the winter solstice, or as they termed it the annual 'death' of the Sun, by building the Chichén Itzá in Yucatan. Alternatively the Great Kiva (a ceremonial underground chamber) in Chaco Canyon, New Mexico, was built by the Anasazi, and its entrance marks sunrise on summer solstice (Ruggles & Hoskin 1997).

It is understandable that the cycles of the Sun and Moon would have a huge impact on the lives of these cultures and that structures and belief systems could be build around these. Some nations, however, kept records of precise measurements in order to track, and in some cases predict, the occurrence of such events taking place in the sky. A tower was built in Yan-chhêng (considered the centre of the world by the Chinese in the Han era), and used as a gnomon to take solar measurements, from which they were able to construct 365 day calendar with considerable precision. The Egyptians also constructed a calendar based on accurate observations of the star Sirius, or Sothis as it was known to the Egyptians. This marked the time of the annual flooding of the Nile, and so was an extremely important measurement. Using this method they were able to calculate the length of year to be 365.25 days (Wells 1996).

The Babylonians, from Southern Mesopotamia, were the most thorough of record keepers though, and it is their writings that contain the earliest known observational records. They were actively studying the sky as early as 3000 B.C. and identified constellations, developing a calendar tied to the recurrence of certain astronomical events and in later times used this to predict events with impeccable accuracy (for more information see Britton & Walker 1996).

As time advanced, so did the observations of the sky and the knowledge that could be derived from it. In Greece, Anaxagoras was able to describe for the first time the process of an eclipse without the need for supernatural creatures or mythology. Aristarchus proposed that the Sun might be at the centre of our system, and that we may be orbiting it. Little was thought of this theory at the time and it disappeared into obscurity. It was Ptolomy's development of Aristotle's geocentric system that became the recognised theory of the time. This complex explanation used a system of deferents and epicycles to explain the motions of the planets in order to keep the Earth at the centre of our system (Toomer 1996).

Also in Greece, Hipparcus created the first system for classifying stars. This was a six-degree scale, ranging for 1 for the brightest stars to 6 for the faintest, with magnitudes determined by the sensitivity of the eye. This is a system that has persisted to this day, although it has been quantitatively refined and extended to fall in line with an increase in our observing power.

During the dark ages, Greek texts were transported to Arabia and translated. It was during this time that stellar catalogues were developed, along with the refinements of many calculations, including the prediction of eclipses, the position of the ecliptic and the length of a year (for more information, we direct the interested reader to King 1996 or Hoskin & Gingerich 1997).

When Arabian and Greek texts returned to Europe, during the resurgence of science, Copernicus began to question the work of Ptolomy, and the idea that the Earth was at the centre of the Universe. Using this wealth of information, he re-discovered the writings of Aristarchus, and developed his theories of the heliocentric system stating that this was "more pleasing to the mind". Although his theories were circulated privately from 1514, there were not published until much later (Copernicus 1543).

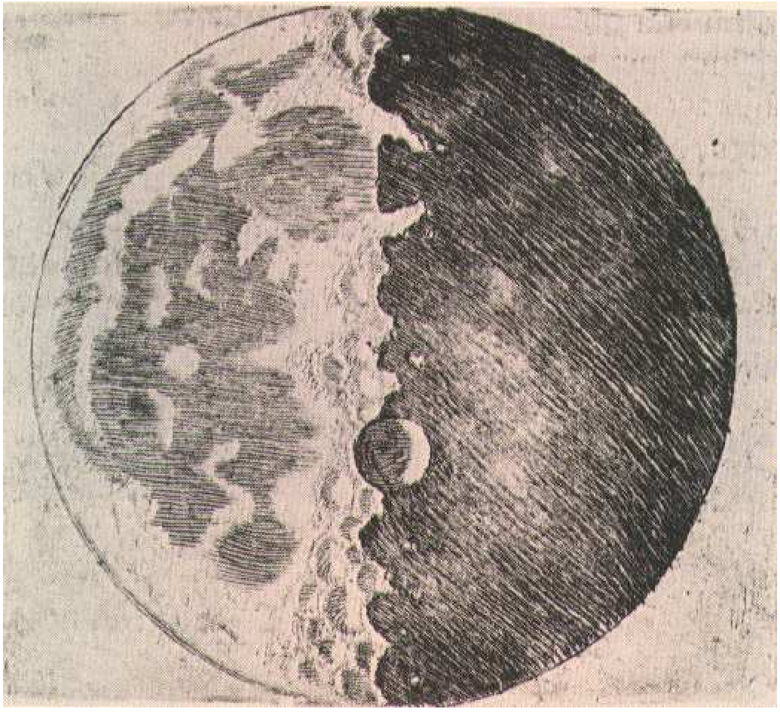

Figure 1.1: Drawing of the Moon as seen through Galileo's telescope, which he first observed on November 30th 1609 (image taken from `http://www.astro.umontreal.ca/∼paulchar/sp/images/galileo.2.html`).

It was only sixty-six years later that Johannes Kepler published his first two laws of planetary motion (Kepler 1609). Eight years earlier Kepler had set to work trying to harmonise the heliocentric system. He did this using the vast array of precise observations left to him following the death of his mentor, Tycho Brahe. It took a further ten years for him to publish his third law (Kepler, Ptolemaeus & Fludd 1619).

It was around the same time that Galileo turned the first astronomical telescope skywards. He saw seas (craters) on the Moon (see Figure 1.1) and blemishes on the Sun, now known as Sun spots. Galileo made multiple observations of these spots, which led him to the idea that the Sun was in fact rotating on its axis. One of the other major observations of this time was of the moons of Jupiter. Galileo was able to observe four of the moons of this planet as they orbited, providing evidence that not all things the sky orbited the Earth.

One of the next leaps in our understanding came with Isaac Newton and his book, Principia (1687). It was here that Newton presented his theories on gravity (among many others). This was a force that could explain not only occurrences here on the Earth, but also applied to everything in the Universe. It was this idea that ultimately lead to the search and discovery of the three outermost planets (Uranus, Neptune & Pluto).

Over the years more detailed observations were made of the night sky, leading to a re-evaluation of the classification of stars. For example, in 1953 Johnson & Morgan, constructed one of the more recent revisions of the magnitude scale, a scale that is used as one of the current standards for optical observations. In this system the magnitude of the star Vega, in the constellation Lyrae, is defined to have a magnitude of zero. Therefore the brightness, or luminosity, of each star can be compared to this zero point in order to provide a derived value for the magnitude of a given star (in a logarithmic scale). These magnitudes are a helpful measure of the brightness of a source, but they do not tell us anything about the intrinsic luminosity for the star. For this astronomers created the absolute magnitude scale, the magnitude we would observe if the source was positioned at a distance of 10 parsecs.

To quantify the magnitudes of a large numbers of stars, many measurements were made using photographic plates, that were mainly sensitive in the blue. However, stars display many different colours, as can be observed just by looking up at the night sky. In order to standardise the measurement of these colours, astronomers measured the apparent (observed) magnitudes at three specified wavelengths; one in the ultraviolet (U, $\sim$ 3600 Å), one in the blue (B, $\sim$ 4300 Å) and one in the visual (V, $\sim$ 5500 Å). This UBV system uses the difference in these values (U – B & B – V) to define the colour of a star. In this system, each value is known as a colour (e.g. B – V colour)[1].

Another method used to characterise stars is their optical spectrum. The first stellar lines were observed in the Sun's spectrum by Fraunhöfer (now known as Fraunhöfer lines). When astronomers turned to other stars, a range of spectra were observed (see Figure 1.2). Originally astronomers did not fully understand the meaning of the array of lines in various stars, but noted that a number of strong lines were common in almost all cases.

---

[1] The interested reader is directed to Böhm-Vitense (1989) for more information on a wide range of information relating to stellar astrophysics

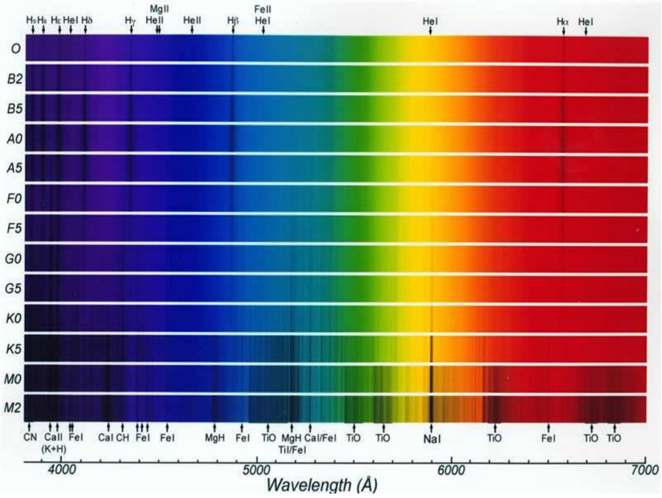

Figure 1.2: Spectral for a range of stellar types, demonstrating a range of lines and line strengths (image taken from `http://academics.smcvt.edu/abrizard/Astronomy/astronomy.htm`).

The strength of these lines were used for an initial classification scheme. The spectra with the strongest Hydrogen line was denoted as type A. Stars were then listed alphabetically as this line strength weakened, through types B, F, G, K, M, N, O, R and S. However, throughout this scale, other lines varied in an irregular manner, as did the colours. The stellar sequence was finally established by Morgan, Keenan & Kellman (1943), in which star are placed in the sequence O, B, A, F, G, K, M, N & S. Over time sub-classes have also been applied, for example B0, B1, ... B9, which is then followed by A0.

Although vast amounts had been learned about the Universe in many millennia of stargazing, it was not until 1945 that our eyes were opened up to new views of the sky. In the 1940's other wavelengths first became observable to astronomers. New disciplines and discoveries became available with the advent of radio astronomy, rapidly followed by millimetre, infrared, ultraviolet, X-rays and γ-rays. This allowed for the development of new areas of astrophysics, one area of which will be explored in the next section.

1.2 The X-ray sky

In 1895, Professor Wilhelm Röntgen conducted experiments into the external effects from the various types of vacuum tube equipment as electrical discharge passed though them. On the 8th of November of that year, he announced the discovery of a new form a 'light' that was able to penetrate a range of materials (Stanton 1896). Although Röntgen declined to comment on the nature of this new light, he termed it "a new mode of motion" (Dam 1896). This discovery of Röntgen rays, or X-rays as they became known (as a result of there unknown nature), subsequently earned him the Nobel prize for Physics in 1901 (the first Nobel prize ever awarded for Physics[2]). This discovery opened up many further areas of research, although the discovery of the wave nature of X-rays was not made until much later, with the realisation that they could be diffracted by the use of a crystal lattice (Laüe 1912; Bragg 1913).

The obvious medical applications of such a penetrating form of light provoked much interest, and the inception of many significant applications. One of the most obvious examples of such would be the birth of radiography, although many other uses were also spawned, including the X-ray diffraction techniques that allowed for analysis of the structure of DNA molecules (Watson & Crick 1953). X-rays and their applications also lead to advancements in the areas of atomic, nuclear and solid state physics, all of which aided in the development of sophisticated techniques for the detection and analysis of these rays.

Although these penetrating rays allowed for great advancements in our understanding of other sciences, X-rays are easily absorbed by our atmosphere, as can be seen in Figure 1.3. This clearly shows that a detector would need to be placed 100 km above the Earth's surface in order to obtain X-ray information from outside our atmosphere. Hence, it was not till the advent of scientific rocketry, that we were able to begin to glimpse the extra-terrestrial X-ray sky. It was in 1948, when the US Navel Research Laboratory launched such a rocket, that scientists received their first view of that sky with the first X-ray observations of our Sun. These were taken using photographic plates with Beryllium filters, an observation that marked the beginning of X-ray astronomy.

Early X-ray astronomy focused solely on the Sun, allowing us to observe different

---

[2] `http://nobelprize.org/nobel_prizes/physics/`

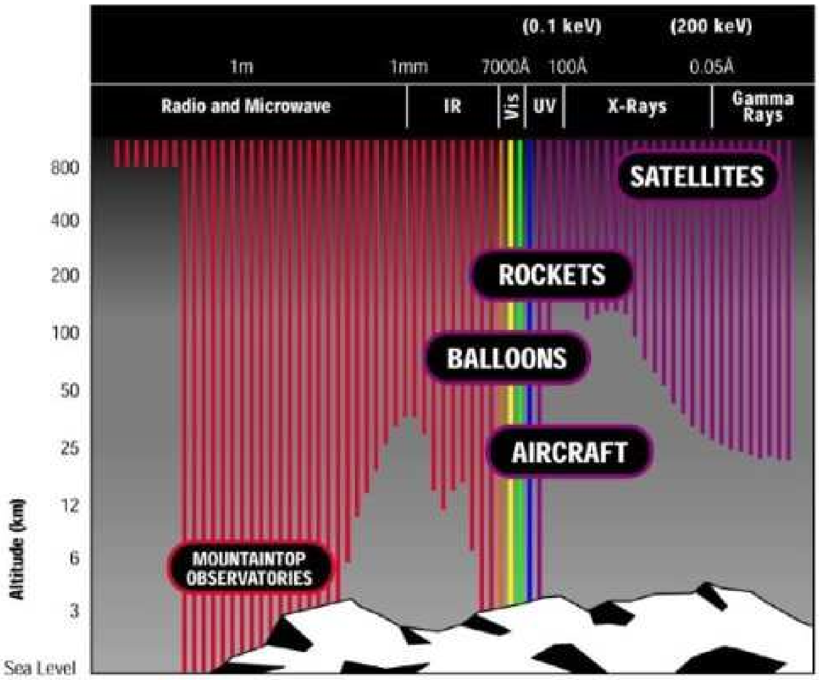

Figure 1.3: A demonstration of the penetration into the atmosphere of photons from across the electromagnetic spectrum, assuming vertical incidence. It is clear from this figure that a proportion of the X-ray spectrum is inaccessable below 100 km (`http://snap.lbl.gov/science/space.php`).

aspects of our nearest star. Although the Sun is an incredibly intense source of X-rays, this is due to its proximity. If we were to move the Sun to a distance similar to that of our second closest star, Proxima Centauri, we would only receive ~ 4 photons s^{-1} cm^{-2}. As a result, many astronomers were pessimistic in their expectations of this new bandwidth. In fact the first detection of non-solar X-rays were noted at a meeting of the IAU in 1958, by Herbert Friedman, although at the time it was proposed to be due to localised productions within the atmosphere. This did not discourage all, and a number of X-ray detectors were placed as payloads within scientific rocketry flights. In 1962 a team led by Riccardo Giacconi discovered an intense source of X-rays in the direction of the constellation Scorpius (Giacconi et al. 1962). In 1963, the group launched two further rocket experiments that revealed the presence of a second source in the vicinity of the Crab nebula, and a third in the constellation of Cygnus (Gursky et al. 1963). With the distance to this last source known from optical observations, it was possible to determine the luminosity of this source. This revealed an X-ray luminosity, $L_{\mathrm{X}} \sim 1000$ times brighter than the Sun (Culhane & Sanford 1981).

As X-ray observations of the sky continued to be launched in sounding rockets, greater accuracy was achieved for Sco X-1, finding it to be a point source. Ground-based follow-up revealed a faint blue optical counterpart (Sandage et al. 1966), with later observations revealing its binary nature. This discovery prompted the suggestion that the X-ray source was fuelled by matter transfer from the star to a smaller more massive object, such as a white dwarf, neutron star or black hole (see Section 1.5). This opened up a new area of astrophysics, the study of accretion (see Section 1.6).

X-ray astronomy had been successful during the era of sounding rockets, but in order to explore further the nature of these systems an orbital X-ray programme was required. The first orbiting observatory was the *UHURU* satellite (Giacconi et al. 1971), launched in 1970 with the aim of providing the first all-sky survey in the 2 – 20 keV energy range. It provided a comprehensive view of the X-ray sky, identifying more the 150 X-ray emitting sources within its first two years. The final catalogue, produced in 1978, contained 339 objects (Forman et al 1978). It found that the majority of the brightest sources are associated with binary systems and supernova remnants. This survey also demonstrated a clustering of sources along the Galactic plane, with an isotropy of the extra-galactic source population. The results of this survey laid the foundations and opened up possibilities for further X-ray missions.

In August of 1972, the *Copernicus* satellite was launched as part of the National Aeronautics and Space Administrations (NASAs) *Orbiting Astronomical Observatories* (OAO) programme. This mission was a collaborative effort between the UK's Science and Engineering Research council and NASA, with the on-board instruments comprising of a UV telescope built at Princeton University and an X-ray astronomy experiment developed at University College London/Mullard Space Science Laboratory. The two instruments were co-aligned, allowing scientists working on the project to begin to identify some of the X-ray sources residing outside our solar system. Among the many highlights of this mission was the discovery of several long period pulsars[3] (e.g. X Per), and the rapid

---

[3] Pulsars are highly magnetised, rotating neutron stars emitting a beam of high energy photons along

intensity variability from a source designated as Cen A. The 8 year life span of this project also allowed for the long-term monitoring of pulsars and other bright X-ray binaries.

This mission was followed, in 1974, by the launch of *ARIEL V* satellite (Smith & Courtier 1976). This joint UK & USA mission was designed to monitor the entire sky. It was able to provide long-term monitoring of numerous X-ray sources, discovering several long-period (minutes) X-ray pulsars and several bright transients[4]. The final catalogue release was published in two parts and contained more than 350 sources (Warwick et al. 1981; McHardy et al. 1981). Around the same time, the third *Small Astronomy Satellite* (SAS-3) was launched (Mayer 1975). This mission provided a complimentary facility in the form of pointed exposures of the range 0.1 – 55 keV. This mission was launched with three major aims: to determine bright X-ray source locations to an accuracy of 15 arcseconds, to study selected sources over the energy range 0.1 – 55 keV, and to continuously search the sky for X-ray transient phenomena. It was successful in many ways, with highlights such as the discovery of many X-ray burst sources[5] including the Rapid Burster (Lewin et al. 1976) and a survey of the soft (0.1 – 0.28 keV) X-ray background (Marshall & Clark 1984).

The late 1970's saw the launch of the *High Energy Astronomy Observatory* (*HEAO*) resulting in an all-sky survey catalogue containing 842 sources (Wood et al. 1984), using the Large Area Sky Survey experiment (LASS) which covered the 0.25 – 25 keV range. An image of which can be seen in Figure 1.4. This mission provided the first comprehensive measurement of X-ray background spectrum and performed timing studies on millisecond time-scales. The successful mission was followed by *HEAO-2* (Giacconi et al. 1979), better known as the *Einstein* telescope, which went into orbit in November of 1978. This mission carried the first imaging X-ray detectors, along with spectroscopic instruments with unprecedented sensitivity and resolution (observing objects 10^4 × fainter than *UHURU*). The quality of data received from this mission opened up new doors within X-ray astronomy including for the first time, studies of the hot interstellar medium of galaxies (Forman

---

their polar axis. If this axis is inclined to the rotational axis, it is possible to observe flashes as the beam sweeps through our line of sight.

[4] Transient sources are X-ray systems that emit for short periods of time and then disappear.

[5] X-ray burst sources are X-ray binary systems (see Section 1.7 for more information) that periodically exhibit rapid increases in their luminosity, typically by a factor of 10 or more.

et al. 1979) and the detection of discrete X-ray sources in the Magellanic clouds and in M31 (Long, Helfand & Grabelsky 1981).

Next came the *European X-ray Observatory Satellite* (*EXOSAT*, White & Peacock 1988), which was operational from May 1983 to April 1986. This mission was placed in an eccentric orbit of $\sim$ 90 days to allow for the continuous study of sources, providing 1780 such observations of a wide range of X-ray sources over its life-span. Around the same time the Japanese launched *Tenma* (Japanese for Pegasus), with instruments able to measure the 0.1 – 60 keV band of the X-ray sky. The spectral resolution of its instruments allowed for the discovery of helium-like iron emission lines in a number of sources. The success of Terma preceded the launch of the next Japanese satellite *GINGA* (Turner et al. 1989). It carried three instruments, which were a large area proportional counter, an all-sky monitor and a γ-ray burst detector. Highlights of this mission included the discovery of the first transient black hole candidates (e.g. Tsunemi et al. 1989) and the discovery of intense 6 – 7 keV iron line emission from the Galactic centre region.

In 1990 *Röntgensatellit* (or *ROSAT*; Trümper 1982) was launched, a co-operative satellite by Germany, the UK and the USA. It carried three imaging instruments onboard, operating in soft X-rays (0.1 – 2.4 keV) range and the extreme ultraviolet (EUV, 0.06–0.2 keV). The first six months of the mission were dedicated to an all-sky survey, which was then followed by a pointed phase, with the telescope remaining operational for a total of 9 years. This mission mapped $\sim$ 98 per cent of the sky in the 0.25, 0.75 and 1.5 bands (e.g. Snowden et. al 1995). Images of these bands can be seen in Figure 1.4. These surveys also resulted in the cataloguing of more than 150,000 objects in the X-ray and 479 in the EUV. In addition to this, considerable diffuse galactic emission was mapped to an unprecedented resolution (see Figure 1.4). The improvement in resolution is clearly visible in comparison to the the previous *HEAO-1* survey. Further to this, deep surveys carried out later in the mission also resolved 70 – 80% of 0.2 – 2.0 keV background into discrete point sources (Hasinger et al. 1998).

The next major X-ray observatory to be launched in the 1990's was the *Advance Satellite for Cosmology and Astrophysics* (*ASCA*; Tanaka, Inoue & Holt 1994). This was the first mission to use CCD detectors for X-ray astronomy, providing imaging capabilities above 4 keV, with moderate spatial resolution ($\gtrsim$ 1 arcminutes on axis). This was com-

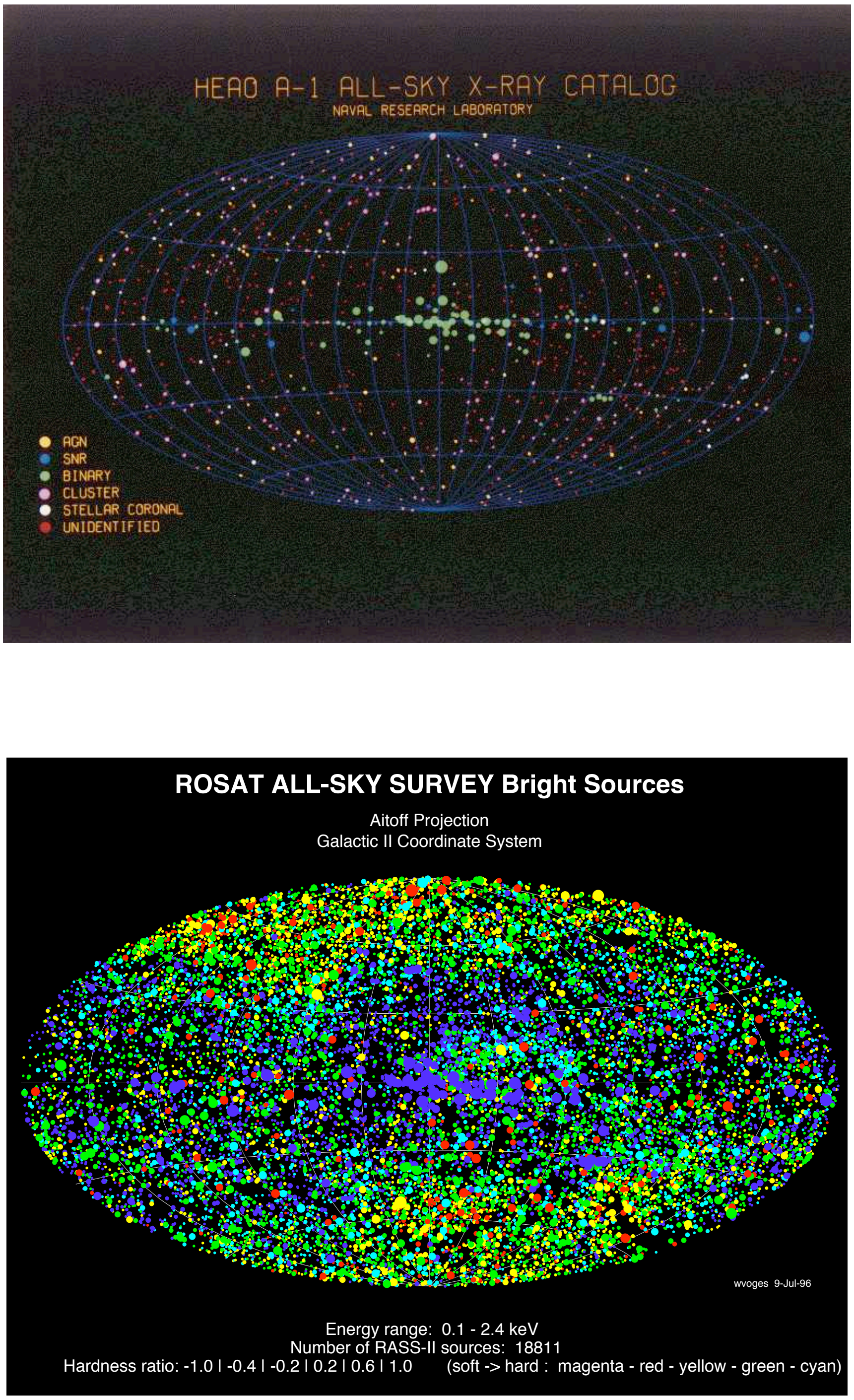

Figure 1.4: All-sky survey results from *HEAO-1* (from `http://heasarc.gsfc.nasa.gov/Images/heao1/heao1.gif`) and *ROSAT* (from `http://www.mpe.mpg.de/xray/wave/rosat/gallery/calendar/1997/jun.php`) indicating the number of sources present, and their locations, in the respective catalogues.

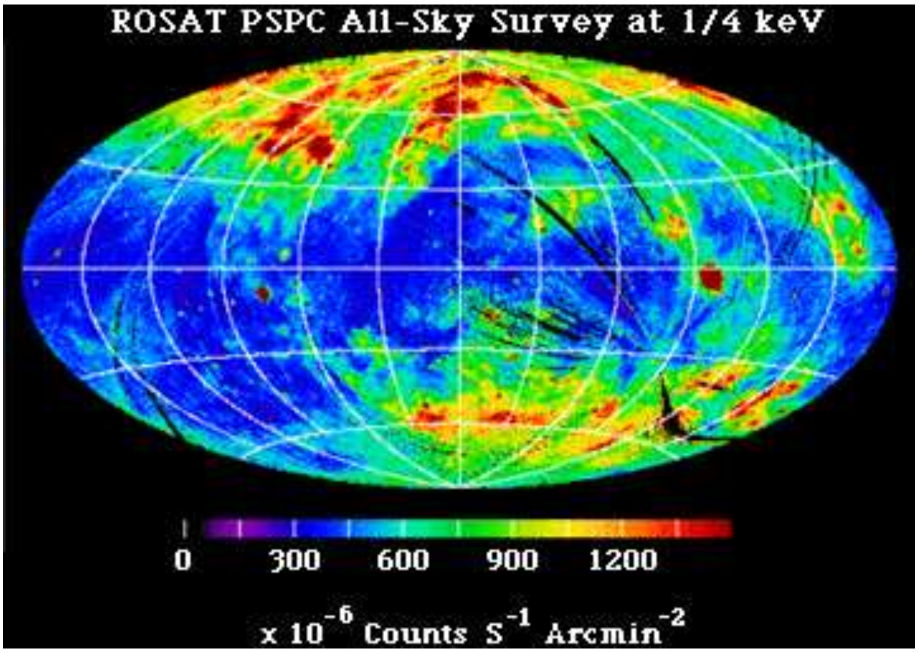

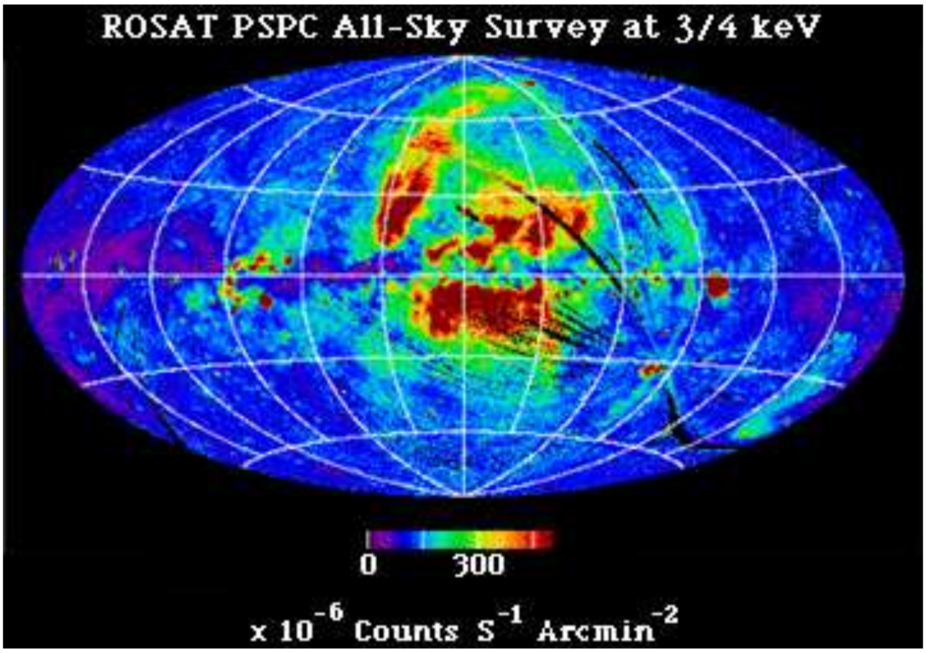

Figure 1.4: (*continued*) *ROSAT* All Sky Survey (RASS) maps for three energy bands (0.25, 0.75 & 1.5 keV respectively). Images available at `http://www.mpe.mpg.de/xray/wave/rosat/gallery/images/survey.php`

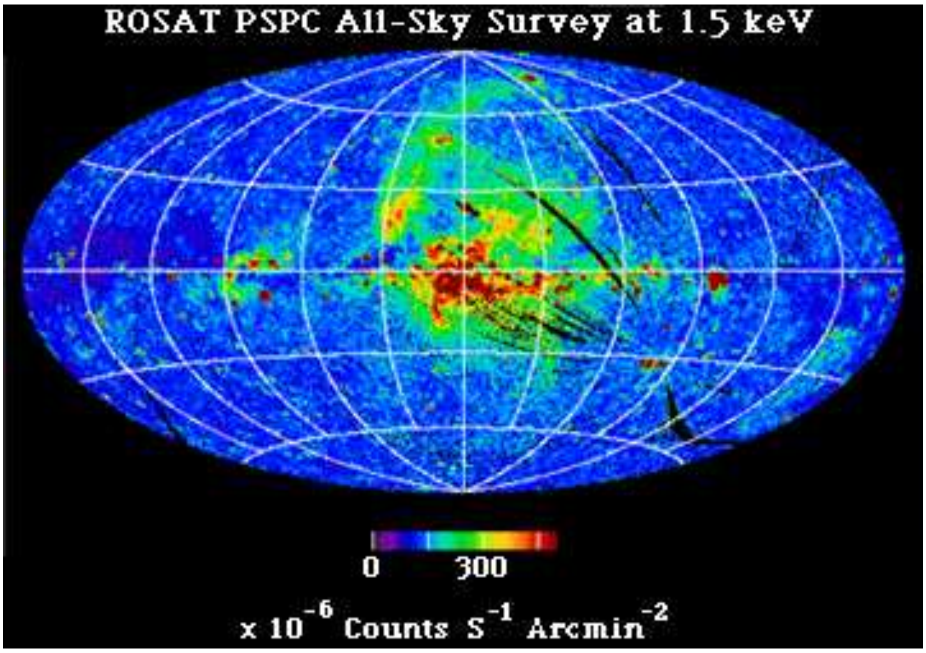

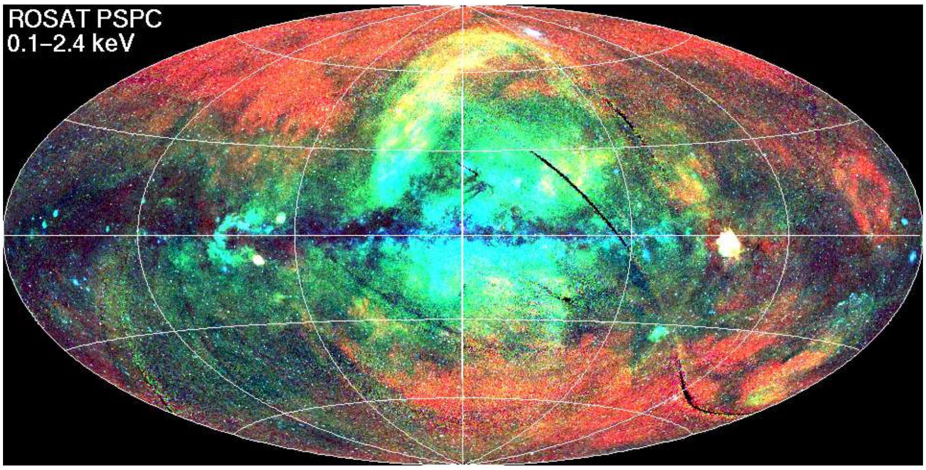

Figure 1.4: (*continued*) *ROSAT* All Sky Survey (RASS) map for 1.5 keV, with the final image showing the distribution of diffuse X-ray emission across the sky in three colours (red - 0.1 – 0.4 keV, green - 0.5 – 0.9 keV & blue - 0.9 – 2.0 keV).

bined with medium spectral resolution over the 0.5 – 10.0 keV energy range. High quality broad band spectral observations were carried out for many astrophysical objects, showing resolved X-ray emission and absorption features (e.g. NGC 6552, Fukazawa et al, 1994; CAS A, Holt et al. 1994), whilst a survey performed using 2 – 10 keV images revealed that roughly 30 per cent of the cosmic X-ray background could be directly resolved into discrete sources (Ueda et al. 1998).

The *Rossi X-ray Timing Explorer* (*RXTE*) was launched in the December of 1995 from the Kennedy Space Flight Centre to observe the 2 – 250 keV energy range. This outstanding satellite is still in use today, stationed in a low-earth, 90 minute circular orbit. It is still making major contributions to the scientific understanding of collapsed stars and compact objects. The launch of this satellite provided an excellent opportunity for the study of timing variability, tagging events with an unprecedented timing resolution of microseconds. It has played a vital role in the analysis and understanding of Galactic sources.

BeppoSAX was launched only four months after the *RXTE* mission, by the Italian Space Agency, in collaboration with the Netherlands Agency for Aerospace. This mission operated over a span of 6 years, and was the first mission to cover three decades of energy (0.1 – 300 keV). This telescope had a relatively large effective area, with moderate spectral resolution, and imaging capabilities in the 0.1 – 10.0 keV range. It was designed primarily for spectral and variability studies. The main highlights of this mission came from the observations of γ-ray bursts (GRBs), bursts of intense γ-ray radiation occurring about once per day, at random locations across the sky. This mission provided the first accurate positions for GRBs, via their X-ray afterglows, demonstrating that they were located in different galaxies (e.g. Feroci 1999)

In 1999, the current generation of X-ray telescopes were launched, providing astronomers with a combination of unprecedented spatial and spectral resolution. This was the launch of NASA's *Chandra* satellite (formerly the *Advanced X-ray Astrophysics Facility*, *AXAF*; Holt 1993, Weisskopf 1999), and the European Space Agency's *X-ray Multi-mirror Mission*, known as *XMM-Newton* (Mason et al. 1995). The first to launch was *Chandra* in the July of that year, being deployed by the Space Shuttle. *XMM-Newton* was launched by Ariane 504 approximately five months later. The large collecting area

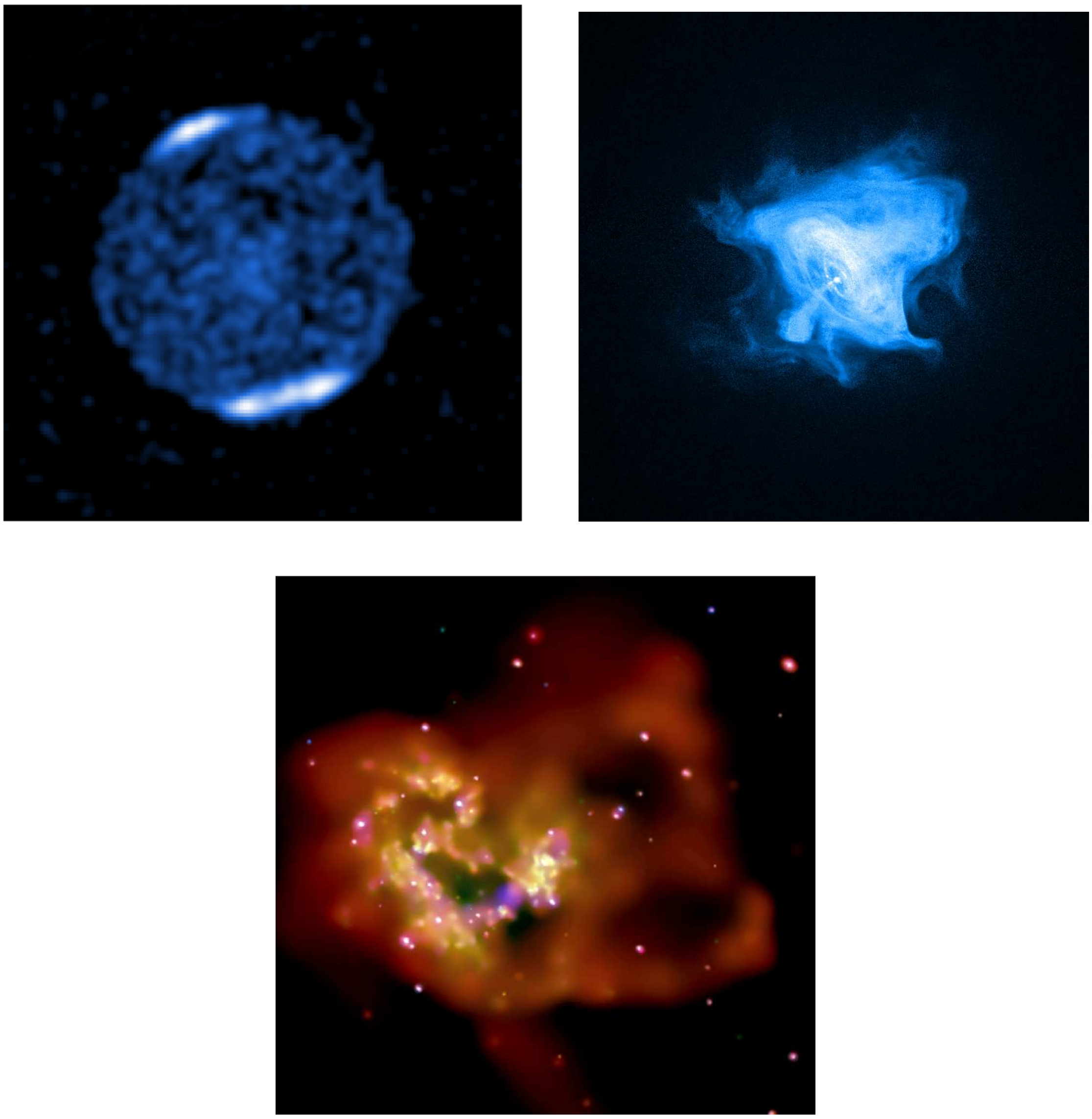

Figure 1.5: Images from the current generation of X-ray telescopes. From *Chandra*; Jupiter showing intense X-ray emission associated with auroras in its polar regions (Credit: X-ray: NASA/CXC/MSFC/R. Elsner et al.), the Crab nebula (Credit: NASA/CXC/SAO/F.Seward et al) and the Antennae galaxy (Credit: NASA/CXC/SAO/ G.Fabbiano et al.

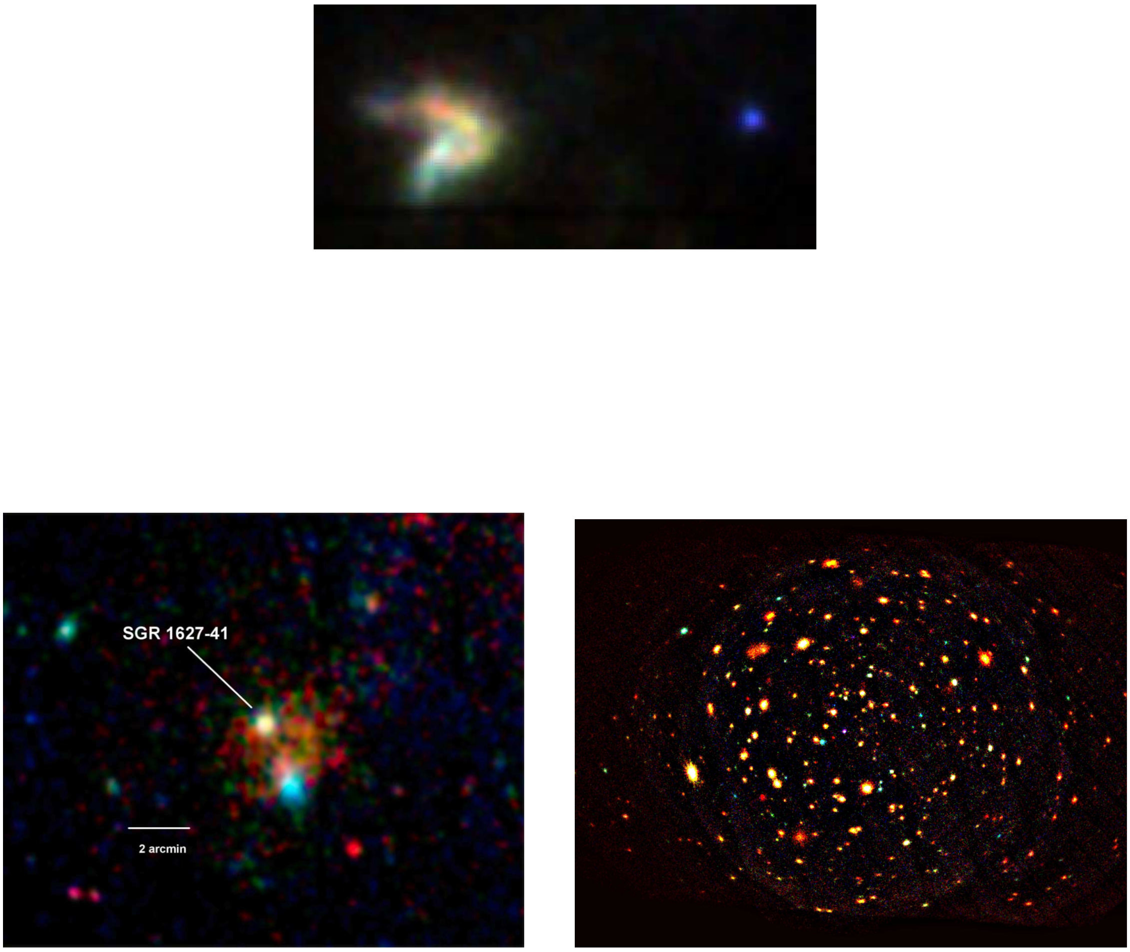

Figure 1.5: (*continued*) Images from the current generation of X-ray telescopes. Images for *XMM-Newton* include the young, luminous supernova remnant G350.1-0.3 (left of figure) and its neutron star companion (to the right) (Credits: ESA/ XMM-Newton/ EPIC, Gaensler et al.), SGR 1627-41 (P. Esposito and ESA and three colour image of the Lockman Hole (image courtesy of G. Hasinger, MPE Garching, Germany and ESA).

and outstanding spectral resolution of *XMM-Newton* was complimented by the superb sub-arcsecond imaging capabilities of *Chandra*. The combination of these two telescopes have revolutionised the study of the X-ray sky, providing the first high resolution X-ray spectra of a variety of astrophysical objects, and significantly advancing our knowledge of both discrete and diffuse sources across a range of size scales.

The interested reader is referred to the *XMM-Newton* Users Handbook[6] and the *Chandra* Proposes' Observatory Guide[7] for detailed information on the respective missions and instrumentation housed on-board. The reader is also referred to the mission websites for details of their numerous respective science highlights, with Figure 1.5 providing some examples of the outstanding images provided by these missions.

1.3 Black holes and other compact objects

The concept of an object so massive that even light could not escape its grasp has been around for more than 200 years. The English Geologist John Mitchel first noted in a letter to the Royal Society that "*if the semi-diameter of a sphere of the same density as the Sun were to exceed that of the Sun in the proportion of 500 to 1, a body falling from an infinite height towards it would have acquired at its surface greater velocity than that of light and consequently supposing light to be attracted by the same force in proportion to its vis inertiae* (inertial mass)*, with other bodies, all light emitted from such a body would be made to return towards it by its own proper gravity*". However, he thought such a scenario would be unlikely.

By 1916, Albert Einstein had developed and published his theories of gravity and general relativity. Soon after, Karl Schwarzschild, using Einstein's theories, gave a solution for the gravitational field of a point mass showing that such compact objects could *theoretically* exist. The equation predicted a true singularity, a point mass with infinite curvature of space time. However, this is shielded from the observer by an 'event horizon', the surface at which the escape velocity is equal to the speed of light. This is at the Schwarzschild

---

[6] The *XMM-Newton* Users Handbook can be found online at `http://xmm.esac.esa.int/external/xmm_user_support/documentation/uhb/index.html`.

[7] The *Chandra* Proposes' Observatory Guide is available at `http://asc.harvard.edu/proposer/POG/html/index.html`.

radius, $R_S = 2GM/c^2 \simeq 3 \times 10^3 \ M/M_\odot$, where G is the gravitational constant, M is the mass of the black hole and c is the speed of light. Slightly further out, at $3R_S$, is the last stable orbit, the smallest distance from the singularity at which material can orbit the compact object.

Following on from this in the 1920's, Chandrasekhar argued that special relativity demonstrated that a non-radiating body that was above a certain mass (the Chandrasekhar limit) would collapse into an object known at that time as a 'frozen star'. At that time, this name was given to compact objects because the collapse would be observed to rapidly slow and become heavily red shifted as it approached the Schwarzschild radius.

Although predicted, little thought was given to these hypothetical objects until 1967. In this year Roger Penrose and Steven Hawking were able to show that compact objects (particularly BHs) were not only predicted by Einstein's theory of general relativity, but that they would exist wherever sufficient mass was packed into a given region of space. Interest in these objects was renewed and shortly after this the physicist John Wheeler coined the expression 'black hole' to describe them.

As theoretical knowledge of these systems grew, so did the concept of their formation. Such objects can be created only by the collapse of stars. Stellar mass stars will collapse until they reach a state where electron degeneracy is enough to halt the compression due to gravity (according the Pauli exclusion principle). This type of compact object is known as a 'white dwarf'. For stars larger than about $6M_\odot$ the degenerate core mass is greater than the Chandrasekhar limit of $\sim 1.4M_\odot$, triggering a supernova explosion. This blows off much of the mass surrounding the core as it crosses beyond the maximum mass which can be supported by electron degeneracy, instead it is neutron degeneracy that ultimately stops the collapse. Electrons combine with protons to form neutrons and neutrinos such that the only material left is highly compacted neutrons, hence the name of the compact object formed, a 'neutron star'. If neutron degeneracy is still not enough to resist the core's collapse then it will continue until the matter is compressed into an infinitely small, infinitely dense singularity at the centre of a 'black hole'. This third and final form of compact object will be considered throughout this thesis, we will therefore look at these objects in more detail before continuing.

1.3.1 Observing black holes

Black holes, occupy the highest position on the density scale, with gravity so extreme that not even light can escape it (from within the event horizon). So, as stated on a popular 1980's TV show, "*the thing about a Black Hole – its main distinguishing feature – is it's black. And the thing about space, your basic space colour is black. So how are you supposed to see them?*" (Red Dwarf, Series 3, Episode 2). The answer to this question is that we cannot observe these sources directly, so we must observe them via their impact on their surroundings. In the majority of cases this will be in the form of accretion, hence the observations of in-falling material (see Section 1.6 for more information), although there are other methods. To explore some of these, we will now focus on one of the earliest observationally confirmed black holes, Cygnus X-1 (or Cyg X-1), so named as it is the brightest X-ray source in the direction of the constellation Cygnus.

Observations made using sounding rockets noted the presence of a source of X-ray emission in the region of Cygnus (Gursky et al. 1963), while rocket flights in 1964 revealed two X-ray sources in the same region of space (Bowyer et al. 1965). Subsequent rocket and balloon flight experiments confirmed the presence of these two distinct objects, but the angular resolution of these experiments was too coarse to allow for optical and radio follow-up (Giacconi et al 1967a). Giacconi et al (1967) reported on a survey of the Cygnus region, making reference to a total of four X-ray sources in the region, with a positional accuracy of 10 arcmins. The authors also noted the variability in the X-ray emission of Cyg X-1. In 1971, counterparts to this source were identified in both the radio (Braes & Miley 1971) and subsequently the optical (Murdin & Webster 1971). The association with HD 226868, a B0 Ib type star, lead to further observations of this source, and in 1972 it was suggested this source was a binary system. Webster & Murdin (1972) reported on the spectrum, colours and interstellar features of HD 226868, making measurements of the radial velocity of this source (see also Bolton 1972). The results (seen in Figure 1.6) revealed an orbital period for the star of 5.6 days around its unseen companion. This information, when combined with a periodic dip in the X-ray emission of this source (Dolan 1970; 1971), supported the interpretation of a binary system. A mass function was independently calculated by each author, which when combined with the classification of

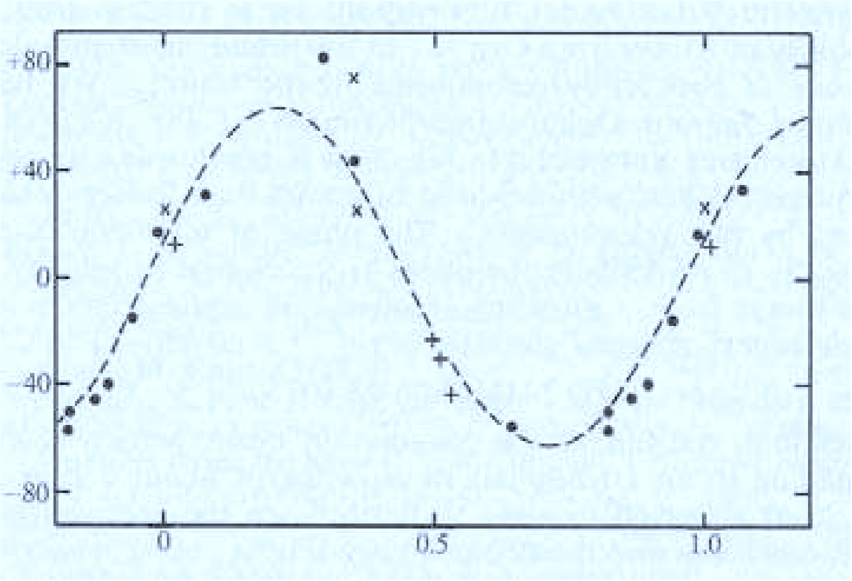

Figure 1.6: Radial velocity curve of HD 226868, the optical counterpart of Cyg X-1, folded on the 5.6 day orbital period. (Webster & Murdin 1972).

the bright star revealed a mass of the 'dark' object to be in the range $\gtrsim 2\ M_\odot$ and $\gtrsim 3\ M_\odot$ respectively. Based on these results, and the lack of optical emission, Webster & Murdin wrote "*it is inevitable that we should also speculate this this might be a black hole*" whilst Bolton wrote "*this raises the distinct possibility that the secondary is a black hole*". Later work placed the mass even higher, at $\gtrsim 9\ M_\odot$ (Paczynski 1974).

Continued multi-wavelength observations of this source highlighted the presence of a He II 4686 Å line, which was 120° out of phase with respect to the absorption spectrum, with about 1.8 times the velocity amplitude (Hutchings et al. 1973). This lead to the idea that the He II line emission did not come from the companion star, but instead from a stream of material being passed from the star to the compact object (Bisiacchi et al. 1974). This stream of material would be carrying a certain amount of angular momentum though, and so as it falls towards the compact object it would form a disc, known as an accretion disc.

1.3.2 Black hole masses

The black holes discussed above are formed as the end point in the lifetime of a single massive star that resided in our own Galaxy. As such, these objects cover the mass range $3 \lesssim M_{\rm BH} \lesssim 20\ M_{\odot}$, where $M_{\rm BH}$ is the mass of a black hole. When considering other galaxies, we find that some have sub-solar abundances (low metallicity; e.g. Lee et al. 2006). The lower opacity of these sub-solar environments means that massive stars born in these regions lose less mass through winds during their evolution. As a result, they can potentially collapse to form a relatively high mass black hole at the end of their stellar lifetime, with $\rm M_{BH} \lesssim 100\ M_{\odot}$ (Fryer & Kalogera 2001; Heger et al. 2003; Belczynski, Sadowski & Rasio 2004). Here we consider the definition of a stellar mass black hole as the end point of a single star. As a result we define stellar mass black holes to be a compact object over the mass range $3 \lesssim M_{\rm BH} \lesssim 100 M_{\odot}$.

Black holes are also thought to reside at the centre of most galaxies. These objects are of considerably higher mass, where $M_{\rm BH} \sim 10^5 - 10^{10} M_{\odot}$. These objects are known as supermassive black holes, and are thought to power active galactic nuclei (AGN) via an accretion disc. There is no AGN at the centre of our Galaxy, although there is compelling evidence for the existence of supermassive black holes. By mapping the paths of stars around the Galactic centre we are able to see that stars paths are altered due to this gravitational attraction (as seen in Figure 1.7). This pattern could only occur if there is an object of supermassive proportions, that is not optically visible to us, at the centre of the region of space observed.

If we consider the mass scale of black holes we see that the those confirmed to date cluster around either the lowest (stellar mass) or the highest (supermassive) ends of the mass spectrum. Intermediate mass black holes (IMBHs) are an interesting concept, and would provide a ‘missing link’ in the mass scale of black holes. Such objects would also have significant implications on our understanding of the formation and evolution of both supermassive black holes and galaxies (e.g. Madau and Rees 2001; Ebisuzaki et al. 2001). Various pathways for the formation of such IMBHs have been suggested, from both primordial (from the collapse of Population III stars; Madau & Rees 2001), and ongoing (runaway mergers of massive stars, and their subsequent collapse to a massive black hole,

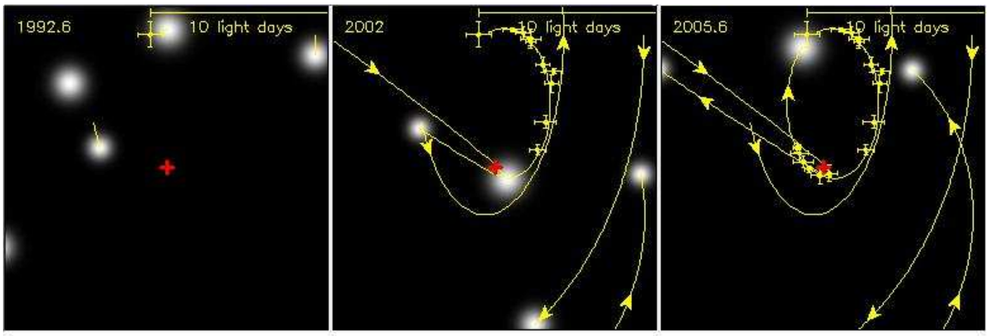

Figure 1.7: Three images taken the Max Plank Institutes Galactic Centre Research pages. They illustrate the affect of a supermassive black hole has on the region of space surrounding it. The stars motions can be used as an indirect method of observing this class of object (from `http://www.mpe.mpg.de/ir/GC/index.php`).

in the densest star-formation regions e.g. Portegies-Zwart et al. 2004) stellar populations, but to date conclusive proof of their existence is still elusive. For more information on IMBHs, we refer the reader to Miller & Colbert (2004).

1.4 Radiation processes

There are a number of fundamental processes that are required to explain the radiation observed form X-ray binary systems, some of these processes are outlined below. Further information on any of these processes can be found in many undergraduate textbooks (e.g. Serway 1996; Tipler 1999)

1.4.1 Blackbody radiation

An object at any temperature emits radiation, known as thermal radiation. The characteristics of the emission are dependent on the temperature and the properties of the object. At low temperatures astronomical objects will emit in the radio and microwaves (for example the cosmic microwave background), as the temperature increases the wavelength of the emitted light will decrease within emission found in the infrared, visual, ultraviolet and beyond into the X-ray band of the electromagnetic spectrum.

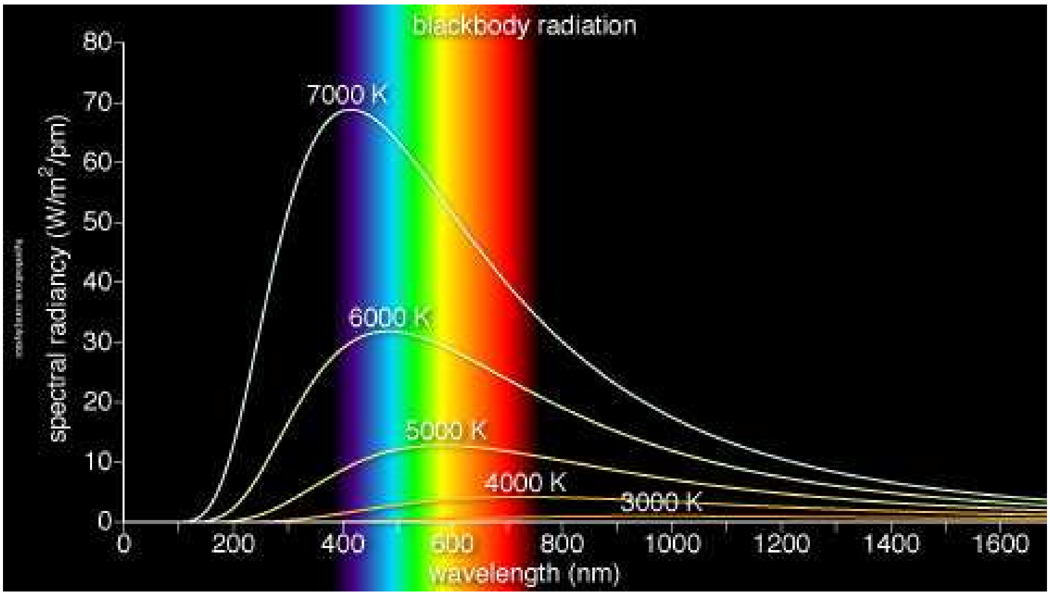

Figure 1.8: Spectra of a blackbody observed at a range of temperatures (image taken from `http://hypertextbook.com/physics/modern/planck/`).

The properties of the material will determine bands of the spectrum which will be absorbed and/or emitted from the object, for example the colour of a red door, or the shades of brown observed in wood (where the colours that are emitted are not dependant on the temperature of the object). There is a one type of object however, that allows us to consider only the thermal aspects of radiation, this is known as a blackbody. A blackbody is an object that absorbs all radiation incident upon it, and re-emits that radiation at all wavelengths. The spectrum of this source varies with temperature. As the temperature of the blackbody increases, the amount of energy emitted increases, and the peak wavelength shifts to shorter wavelengths. This can be clearly seen in Figure 1.8. The observed shift in the peak of the emission obeys Wien's displacement law, which states $\lambda_{\max}T = 0.2898 \times 10^{-2} m \cdot K$.

1.4.2 Comptonisation

Compton scattering, or the Compton effect, explains how energy is exchanged between photons and electrons. This effect was observed in 1923 by Arthur Compton, for which he

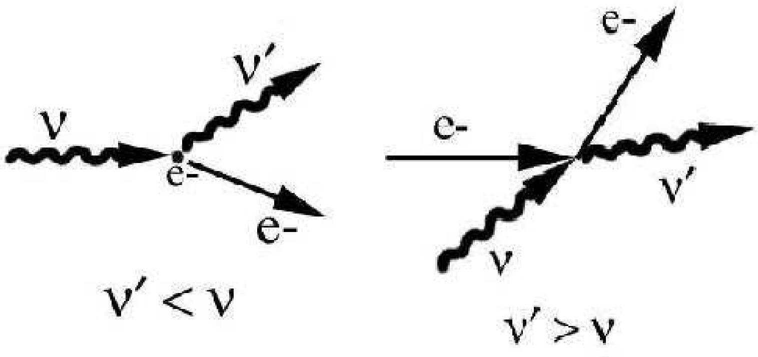

Figure 1.9: This image shows the processes and particles involved in (a) Compton and (b) Inverse Compton scattering (taken from `http://venables.asu.edu/quant/proj/compton.html`).

was awarded the Nobel Prize for Physics in 1927. It is the collision of a particle of light (or photon) with an electron that results in the electron gaining energy as it recoils, so the photon loses energy. This process is shown in 1.9(a) in the rest frame of the electron. Here energy is passed to the electron sending it off in one direction as the photon moves off in another.

However, if the electrons are relativistic, with more energy than the surrounding photons, the collisions result in the photon gaining energy, or being ‘up-scattered’ by the electron (inverse Compton scattering). Figure 1.9(b) shows this interaction between a photon and a high energy electron (again in the rest frame of the electron). The more collisions that occur, the more energy is given to the photons, increasing the hard component of the spectrum. There is a limit to this ‘up-scattering’ though, occurring when the electron and photons reach a stage of energetic equilibrium . The rate (and opportunity) to reach this stage of equilibrium is also related to the destiny of the material, so at lower densities equilibrium may not be achieved.

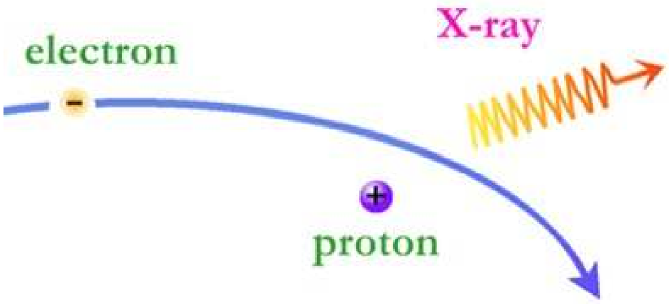

Figure 1.10: Bremsstrahlung radiation produced by a high-energy electron deflected in the electric field of a charged particle (from `http://www.astro.wisc.edu/∼bank/index.html`)

1.4.3 Bremsstrahlung

‘Bremsstrahlung’, from the German bremsen “to brake” and strahlung “radiation”, is radiation that is emitted (primarily in the X-rays) as a result of electron and ion interactions within a plasma. This form of radiation occurs when a fast moving electron passes a charged particle and is deflected by the strong electromagnetic attraction, altering the trajectory of the charged particle. This usually occurs in the field of a positively charge nucleus. This can be seen in Figure 1.10.

Bremsstrahlung can also be termed as free-free radiation. This refers to the radiation that arises as a result of a charged particle that is free both before and after the deflection of the electron which results in the emission of radiation.

So called thermal Bremsstrahlung occurs within a plasma, where the rapid and continuous motions of particles in the hot gas result in free electrons that are constantly producing Bremsstrahlung as they interact with the free ions within the field. Such emission produces a continuous and characteristic spectrum.

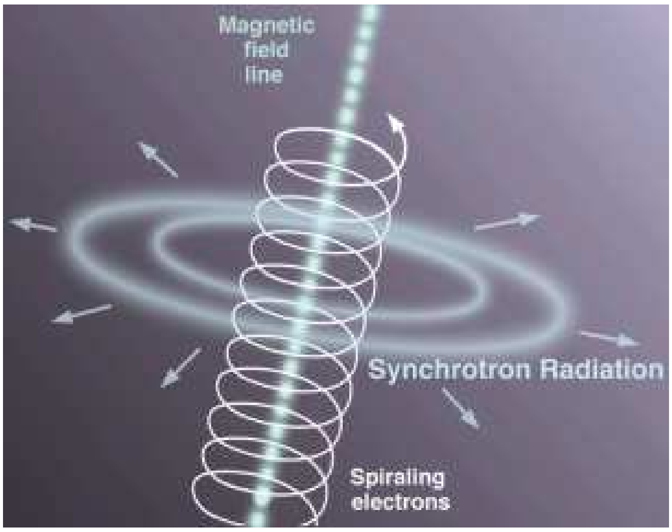

Figure 1.11: Schematic of synchrotron radiation, generated as reletivistic particles travel through magnetic fields (image from `http://www.astroearth.org/astrophysics.html`).

1.4.4 Synchrotron

A relativistic electron that is travelling along a curved path in a magnetic field will produce electromagnetic radiation. This form of radiation is known as synchrotron radiation and is non-thermal, concentrated in the direction of the electron's motion and strongly plane polarised. This form of radiation is shown in Figure 1.11.

1.4.5 Discrete line emission

Spectral lines are the result of interaction between atoms, or atomic nuclei and a single photon. The energy from the photon can allow a change in the energy state of the system, such that the orbiting electron can transit between energy states, or if enough energy is provided (for example from ultraviolet / X-ray photon) they can escape completely leaving behind a positively charged atom/particle (in which case it is known as the photoelectric effect, see next section). In the former case the photon is absorbed and the system is considered to be excited. This energy will be re-emitted as the system relaxes, resulting in the emission of either a single photon of the same frequency as the original or in a cascade of photons, where the sum of the energies will be equal to the energy of that

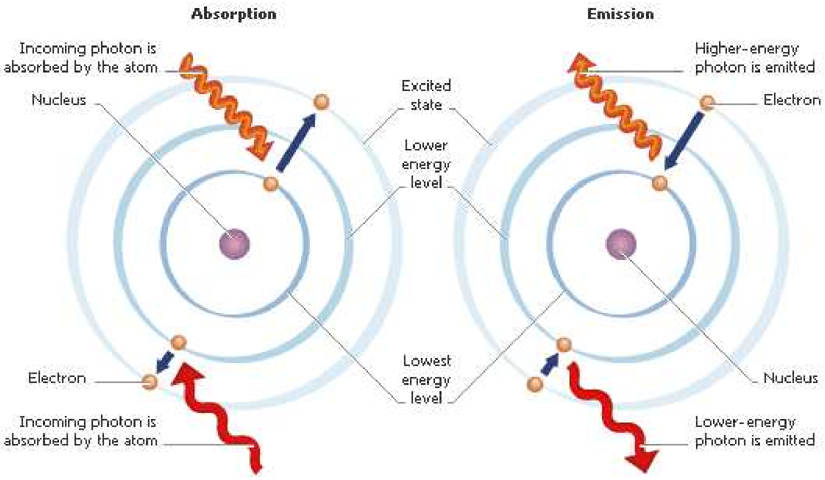

Figure 1.12: Figure shows the mechanics of discrete line emission (`http://images.encarta.msn.com/xrefmedia/aencmed/targets/illus/ilt/T028540A.gif`)

absorbed (assuming the system returns to its original state). An example of this can be seen in Figure 1.12. The direction of the new photons will be unrelated to that of the original and will carry the characteristic energy difference of the states between which the electron transited as it was emitted. This will be observed as a discrete line feature within the emission spectrum. Depending on the type of gas/material being observed, and its position in relation to the photon source, it will create either an emission or absorption line. This characteristic difference is unique to each type of atom, so observations of these line features can unlock information relating to the constituents and abundances of these elements within the material being observed, its density and its temperature.

Emission and absorption features are observed in a range of astronomical objects, including some discussed previously (e.g. the observed spectra of stars used for typing, He II emission from Cyg X-1). They can also be observed across a broad range of wavelengths, including in X-rays (e.g. Fe-Kα emission from active galactic nuclei; see Pounds et al. 1989).

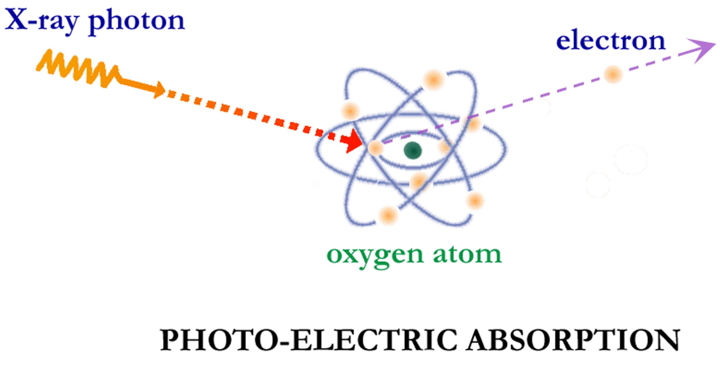

Figure 1.13: Photo-electric absorption process (image taken from `http://chandra.harvard.edu/xray_astro/absorption.html`).

1.4.6 Photoelectric effect

This effect was briefly mentioned in the previous section, and occurs when high energy photons interact with matter. The incoming energy is used to remove a bound electron from an atom. This ionises the atom and removes the photon from the spectrum of the high energy source. The mechanics of this can be seen in Figure 1.13.

Here we see that the X-ray photon, carrying an energy $E = h\nu$ (where h is Planck's constant and ν is the frequency of the photon), is completely absorbed during the collision. Some of the photon's energy is used to overcome the binding energy of an electron, where the binding energy $E_{\rm B} \lesssim h\nu$, whilst the remaining energy provides a velocity to the electron. Photons carrying less than the binding energy of an electron may be absorbed and re-emitted at similar or lower energies, by the process outlined in the previous section.

This is a commonly observed effect in astrophysical sources, and is prevalent with lower energy X-ray photons. It is this effect that causes the deficit at low energies in the spectrum of various sources, it is therefore also known as X-ray absorption.

1.5 Matter Transfer

As mentioned in Section 1.3.1, it was proposed that emission from the systems containing a compact object may be the result of matter transfer from the star onto the compact object, but by what process is matter transferred? To answer this we now consider the work of a French astronomer named Édouard Roche, who developed the concept of the Roche lobe. This is a region of space around a star, contained within a binary system, within which any orbiting material is gravitationally bound. The shape of this region is built up by plotting surfaces of equal potential (including terms for the centrifugal force as well as gravity). Close to each star (or object) these boundaries can be approximated to concentric spheres. Moving further from each object the shape of the surface is distorted due to its companion until a point is reached where these surfaces intersect. This gives an approximate tear-drop shaped region around each object, joining at the Lagrange point, the position where the gravity of both objects effectively cancel out. This surface is labelled as the Roche Lobe in Figures 1.14 and 1.16.

Figure 1.14 shows a star that has not filled its Roche lobe. In this case matter cannot be transferred to the companion directly as it is gravitationally bound to the star. However, high mass stars have strong winds, and so if the star is of this type some fraction of its wind can be captured by the compact object. This low angular momentum wind may then feed the accretion process. Due to the process of transfer this is known as wind-fed accretion.

This type of matter transfer has been discussed and explored in a three main formats, depending on the type of companion star and the details of the wind/flow. The first of these was outlined above in the broad description of wind-based matter transfer. In this case the wind is considered to be homogenous (Negueruela 2009). The wind particles are deflected by the gravitational field of the compact object and this causes the particles to lose kinetic energy, allowing them to begin to fall towards the compact object (Ducci et al. 2009).

The second form of wind-fed system is observed when the out-flowing wind from the star is inhomogeneous in nature and appears ‘clumpy’ (Ducci et al. 2009). When a clump of material passes within the sphere of gravitational influence of the compact object it is

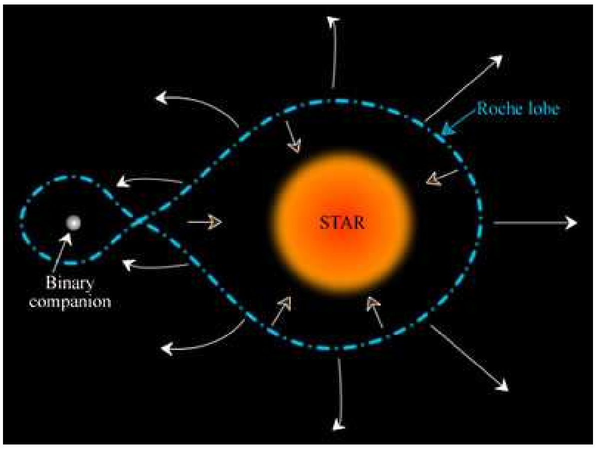

Figure 1.14: Diagram to show mass transfer via stellar winds accreting onto a compact object, known as wind fed matter systems (image from `http://cosmos.swin.edu.au/lookup.html?e=roche-lobe`).

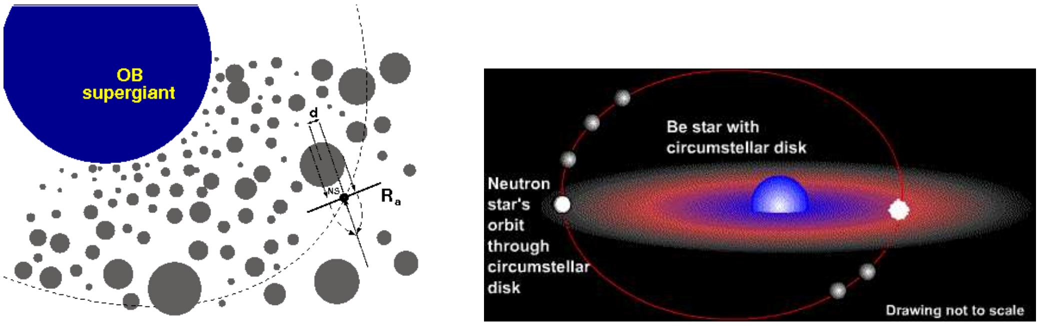

Figure 1.15: Further views of wind-fed accretion systems. (a) Mass transfer via in inhomogeneous 'clumpy' wind. The schematic demonstrates this where d is the distance between the centre of the clump and the centre of the accreting compact object and $R_{\rm a}$ is the accretion radius (image from Ducci et al. 2009). (b) A disc of gas forms around the Be star and orbits at the equator. as the compact object's orbit is inclined to the equator, mass will be able to transfer only when it encounters the disc. It will therefore occur at regular intervals (image from `http://science.nasa.gov/newhome/headlines/ast25mar98_1.htm`). In each case the compact object identified within these figures is a neutron star, but it is also possible for this object to be a black hole.

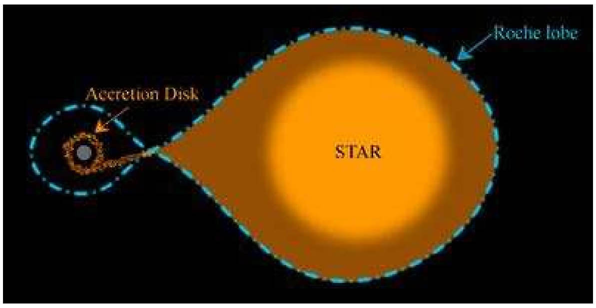

Figure 1.16: Roche lobe overflow, which can feed the accretion process in X-ray binary systems (image from `http://cosmos.swin.edu.au/lookup.html?e=roche-lobe`).

attracted by the same process as outlined above. This is demonstrated in Figure 1.15(a).

The third main type occurs in systems known as Be X-ray binaries. In this case the stellar wind from the giant Be companion collapses to form a disc around the star. This disc is confined to a plane that is often different to that of the orbital plane of the compact object (see Figure 1.15(b)). As the compact object passes through the disc of wind material, this leads to a short period of mass transfer, and a burst of accretion (Belczynski & Ziolkowski 2009). The majority of these systems have been identified as containing neutron stars, although it is predicted that a small number will contain black holes.

If the companion star is more tightly bound to the compact object then it is possible for the star to fill its Roche lobe (as shown in Figure 1.16). In this case material at the Lagrange point will feel an equal pull from both the star and the compact object. This allows material to flow across and feed the accretion process whilst slowly tearing away the stellar surface by a process called Roche lobe overflow. Material crossing the boundary carries with it considerable angular momentum, which prevents free fall onto the compact object. Instead the matter begins to rotate in circular orbits, forming an accretion disc. This material is only able to accrete if it is able to find an effective means by which to transport the angular momentum outwards. We shall discuss this in the following section.

1.6 Accretion onto Compact Objects

As stated above, material falling towards the compact object will carry some angular momentum from the companion star. Conservation of angular momentum means that this material will collapse into a disc of material around the black hole, known as an accretion disc. The form taken by the disc, and so the accretion flow system observed, depends on whether the material collapsed into an optically thick accretion flow, or whether it remains optically thin (it is possible to observe a combination of these flows, but this will be discussed later).

1.6.1 Optically Thick Accretion

The standard view of this disc is that published by Shakura & Sunyaev in 1973. The authors general description of accretion portrays a system in which matter is transferred from the companion star, by some form of matter transfer (as outlined above), carrying considerable angular momentum. This would prevent free fall onto the compact object, but at some distance centrifugal forces would be comparable to those of gravitational attraction. Here, the material would begin to form a disc around the compact object, in roughly circular orbits. In order for this matter to accrete toward the black hole or neutron star (or even in some cases a white dwarf), the angular momentum must be transported outwards by some method. The authors make suggestions for possible methods of angular momentum transport that include friction, turbulent motion caused by magnetic fields and viscous stresses, although the actual method was not fully determined. In fact it is only in the last ten years that the origin of the viscous stresses has been identified as the magnetic rotational instability (e.g. Balbus 2005).

The outward movement of angular momentum allows for the release of gravitational energy as material spirals inwards. Some of the energy released is used to increase the kinetic energy of rotation, whilst the rest is radiated away. This radiation is emitted from a disc that is optically thick and geometrically thin, and so emits a blackbody. The emission spectrum from such a source is thermal and can be summarised as follows, by making the following assumptions: energy radiated locally is emitted locally and the accretion rate is constant with radius. The resulting radiation at a given radius ($r =$

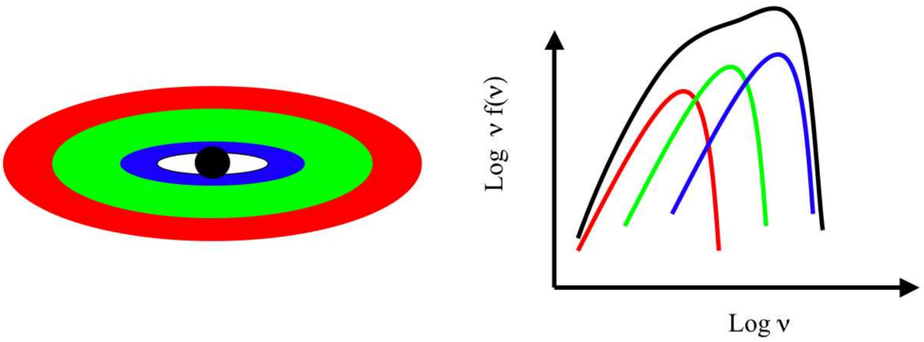

Figure 1.17: Multicoloured disc blackbody spectrum. Thermal radiation is emitted at each radius, with the temperature increasing as we move in towards the centre of the accretion disc. As a result the predicted spectrum can be constructed by superimposing a number of blackbody spectra.

$R/R_{\rm G}$ where $R_{\rm G}$ is the gravitational radius, GM/c^2) is given by a (quasi) blackbody spectrum of temperature $T(r) \propto r^{-3/4}$. As material moves in through the accretion disc, more luminosity is generated over a smaller region that results in emission at a higher temperature. This can be seen in Figure 1.17, where we show this type of a spectrum, generally known as a multicoloured disc blackbody spectrum.

The amount of gravitational energy that can be tapped in this way is $GM\dot{m}/2r$ (using Virial theorem). This shows that the emission from the system is also dependent on the mass if the compact object (M) and the rate at which material is accreted through the disc ($\dot{m}$). This tells us that with increased mass accretion rates, come increased luminosities. However, there is a point at which the outward pressure of the accretion luminosity (radiation pressure) is greater than the inward force of gravity, that is known as the Eddington limit. The resulting limit is shown to be:

$$L_{Edd} = \frac{4\pi GMm_pc}{\sigma_T} \simeq 1.3 \times 10^{38} \left(\frac{M}{M_\odot}\right) \mathrm{ergs}^{-1}$$

where G is the gravitational constant, M is the mass of the central object, m_p is the mass of a proton, c is the speed of light and σ_T is the Thomson cross-section for the electron.

1.6.2 Optically Thin Accretion

In the optically thick regime discussed above, we find that all the energy emitted from the system has been thermalised as a result of numerous collisions within the disc. If the accretion rate is much lower, then the density of the accretion flow will also be lower, and at the lowest rates may become optically thin to electron-proton collisions. This is an important point to consider as it is the protons in this flow that carry the majority of the mass, and as such tap the majority of the available gravitation energy. However, it is the electrons that are more efficient at radiating this energy. In the optically thick regime, collisions between these two particles will result in thermal equilibrium and the emission of a blackbody spectrum. In this case though, we find that incomplete thermalisation leads to a two temperature plasma in which the protons gain most of the gravitational energy and transfer only a little of this to the electrons via Comptonisation, Bremsstrahlung and synchrotron radiation, whilst the rest is advected in through the accretion disc and lost beyond the event horizon of the black hole. This is known as an advection dominated accretion flow (ADAF; Shariro, Lightman & Eardley 1976; Narayan & Yi 1995).

1.6.3 Accretion instabilities

Variations in the mass accretion rate can change the amount of energy emitted from these systems, but more dramatic changes occur due to instabilities in the accretion disc. This occurs in two major forms; the hydrogen ionisation and radiation pressure instabilities. The first of these occurs at fairly low luminosities, and is linked to the long term outbursting behaviour of X-ray binary systems (for more details of X-ray binaries see Section 1.7), whilst the second should occur at higher luminosities.

The hydrogen ionisation instability can occur when the accretion disc surrounding the compact object is quite large, meaning that material towards the outer edge of the disc is cool. At low mass accretion rates the hydrogen in a cool region of the disc can be mostly neutral. Fluctuations in the accretion disc can increase the temperature in a region to a point at which hydrogen ionises. The energy in that particular region can no longer escape, which causes further heating in the disc, and then causes more hydrogen to ionise so that more energy is trapped. This runaway effect only stops when the disc becomes mostly ionised. In this way, the whole disc becomes unstable causing an outburst of energy to occur. This thermal instability causes a viscous instability, such that an increase in temperature will also increase the mass accretion rate through each annulus. As material moves in through the disc, this causes a drop in pressure, which results in a drop in temperature, allowing hydrogen to recombine. This once again triggers an instability causing a run-away cooling of the disc. This causes the mass accretion rate to be reduced and the cycle to start again. This cyclical behaviour, resulting from the hydrogen instability, has been linked with hysteresis.

Instabilities can also occur at higher mass accretion rates/luminosities. At these higher rates we find that the standard Shakura-Sunyaev disc becomes unstable at small radii due to the rapid increase in the heating of the disc as radiation pressure becomes dominant. As a result a small increase in temperature will lead to a large increase in pressure, which will in turn lead to a further increase in temperature creating another runaway effect. It is at this stage that the Shakura-Sunyaev equations become unstable and we must consider other options (see discussions of super-Eddington accretion below).

For further information and discussion on either of these instabilities, the interested reader is directed to Done, Gierliński & Kubota (2007).

1.6.4 Accretion States

Early X-ray observations of the source ‘Cyg X-1’ revealed the presence of two different (apparently stable) accretion states. One of these appeared thermal in nature, while the other appeared non-thermal in its origins. Each of these could naturally be explained by one of the above accretion flow systems, but it became apparent that these states may be equally or better explained using a combination of the two when using data of higher quality.

The two accretion flows can be combined by considering a truncated optically thick, geometrically thin Shakura-Sunyaev disc in combination with an optically thin hot inner flow. In order to explain the changing shape of the spectra, we can vary the emission of the components in line with the mass accretion rate. As the mass accretion rate increases, the disc moves in towards its inner-most stable orbit, collapsing the hot inner flow, with the disc emission becoming dominant (thermal spectrum; Esin, McClintock, & Narayan 1997;

Table 1.1: Summary of accretion state characteristics.

Accretion state	Spectral shape	Simple spectral fit	Other details
Quiescent	Non-thermal & hard	$\Gamma = 1.5 - 2.1$	
Low / Hard	Non-thermal (80 %) with possible cool faint thermal contribution	$\Gamma = 1.5 - 2.1$ (~ 1.7) ($kT_{\mathrm{in}} = 0.1 - 0.2$ keV)	Radio jet present Strong power continuum
Intermediate	Characteristics of both hard and soft states		
High / Soft	Thermal (75 %) with steep faint non-thermal tail	$kT_{\mathrm{in}} = 0.7 - 1.5$ keV ($\Gamma = 2.1 - 4.8$)	No QPOs present Weak power continuum
Very High	40 – 90 % non-thermal with warm thermal component	$\Gamma \gtrsim 2.4$ $kT_{\mathrm{in}} \sim 1$ keV	Range of QPOs present Jet emission occasionally present

Notes: Information included in table was collated from McClintock & Remillard (2006).

Poutanen, Krolik, & Ryde 1997). Conversely as the accretion rate drops, the optically thick disc becomes truncated once again (possibly by evaporation) and is replaced by an optically thin hot inner flow (e.g. Meyer & Meyer-Hofmeister 1994; Mayer & Pringle 2007). In this case the emission from the optically thin inner regions can become dominant, producing a non-thermal spectrum.

The increase in data quality also showed the presence of further spectral shapes, covering a range of accretion rates. This lead to the identification of five accretion states in Galactic X-ray binary systems; the quiescent, the low/hard, intermediate, high/soft and the very high state (or steep power-law state). Each of these can be described by a slightly different accretion geometry, accretion rate and spectral shape, all of which are summarised in Figure 1.18. Details of these states are also summarised in Table 1.1 and discussed below[8].

---

[8] The interested reader is also referred to Frank, King & Raine (2002), McClintock & Remillard (2006) and Done, Gierliński & Kubota (2007) for a more detailed look at accretion and accretion states.

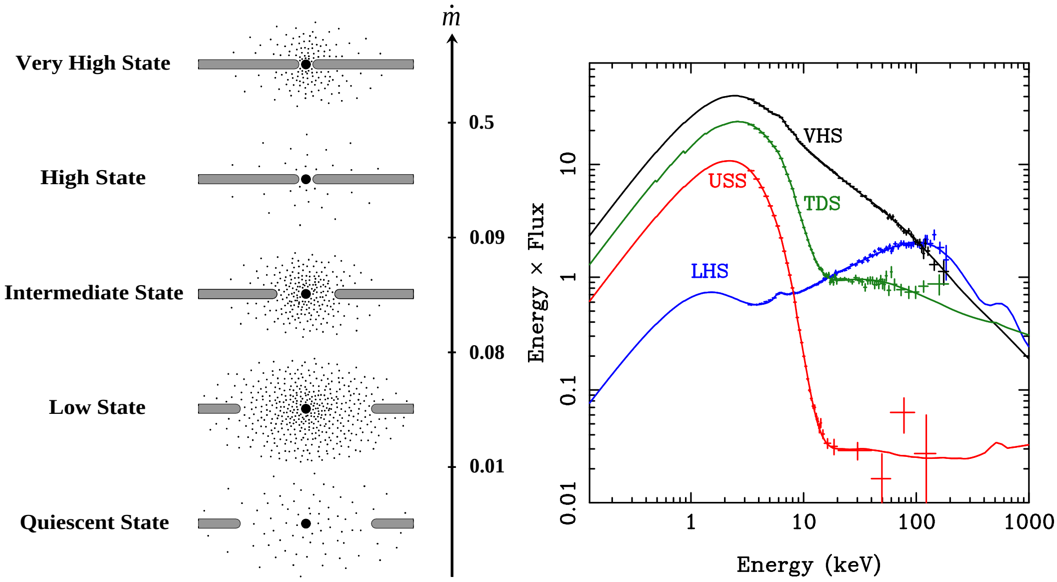

Figure 1.18: Accretion state geometry. (a) Schematic of accretion flow geometry in a range of spectral states, and how they change with mass accretion rate. This is taken from McClintock & Remillard (2006). (b) Range of observed spectra in different accretion states. These are from the outburst of GRO J1655-40, published in Done, Gierliński & Kubota (2007). The states are labelled as follows; LHS - low hard state, TDS - Thermal dominant or high state, USS - ultra soft state (also part of the disc dominated high state), and VHS - very high state or steep power-law state.

Quiescent State

This state, as its name suggests, is the faintest of the accretion states, with an X-ray luminosity of $10^{30.5} - 10^{33.5}$ erg s^{-1}. An accreting black hole binary system may spend most of its life in this quiescent state (McClintock & Remillard 2006), with an X-ray luminosity that can be difficult to observe without the most sensitive X-ray telescopes currently available. This can however be an excellent time to observe these systems in the optical, as it is at this time that the stellar component of this emission could become dominant in some systems (see the Section 1.7 for more information). The X-ray spectrum of this state is best represented by an absorbed power-law with a hard photon index ($\Gamma \sim 2$), which implies that the geometry of this system is primarily an optically thin ADAF.

Low-Hard State

The low hard state was so named as a result of its hard, non-thermal spectrum ($\Gamma \sim 1.7$; McClintock & Remillard 2006) which was present at lower luminosities. As further observations have been made of a range of sources, it has become evident that a luminosity criterion may not be the best way to differentiate between states. This led some authors to drop the term ‘low’, referring to this state as just the ‘hard’ state.

The spectrum of this state is well fitted by a strong (~ 80 per cent of the X-ray emission in the $2 - 20$ keV band) non-thermal component ($\Gamma = 1.5 - 2.1$), with the addition of a faint cool thermal component ($kT_{\rm in} = 0.1 - 0.2$ keV, when modelled by a multicoloured disc blackbody). The physical interpretation of this spectrum is that we are observing a truncated accretion disc observed in combination with an optically thin hot inner flow that is coupled to the disc corona (Done, Gierliński & Kubota 2007). Another suggestion is that the hard spectrum is due to the release of gravitational energy, dissipated through an optically thin disc corona via magnetic flares above the surface of the disc. Such flares would be generated by magneto-hydro-dynamical interactions responsible for the disc viscosity (Balbus & Hawley 1991; Done 2002).

Recent observations of systems inhabiting this accretion state have revealed an association with quasi-steady radio jets (for more information see Fender 2006). Timing studies have also developed over recent years (since the advent of *RXTE*) to reveal the presence of a strong power continuum (McClintock & Remillard 2006) and a range of quasi periodic oscillations (QPOs) found in the power spectra of these sources (with a greater number observed in the power spectra of neutron star systems; Belloni, Psaltis & van der Klis 2002).

High-Soft State

Emission from this state is dominated by a thermal component that can easily be explained by the standard optically thick accretion disc (Shakura & Sunyaev 1973). As a result this is sometimes referred to as the thermal dominant state. In this case we would expect the disc to continue down to the last stable orbit, where the temperature of the accretion disc will be at its peak. In black hole binary systems we tend to observe an inner radius temperature ($kT_{\rm in}$) of 0.7 – 1.5 keV in this state.

The name of this state is derived once again from early observations, where the terms refer to a spectra dominated by soft photons, while appearing to radiate at a higher luminosities. The thermal component of this spectrum may be dominant (~ 75 % of the X-ray emission in the 2 – 20 keV band) but a faint steep power-law tail ($\Gamma = 2.1$–4.8) is usually present. The physical explanation of this power-law component is an optically thin disc corona sitting above the accretion disc, with emission resulting from magnetic reconnection in this region (Done 2002). This is demonstrated in Figure 1.18.

Another feature has become evident whilst studying the temporal variability of this state. Authors have highlighted a lack of QPOs, along with the presence of a weak power continuum (McClintock & Remillard 2006).

Very High State

The very high state or steep power-law state displays both strong thermal and non thermal emission, with the non-thermal contribution ranging from 40 – 90 per cent of the total flux (2 – 20 keV band) and a photon index of $\gtrsim 2.4$. The geometry of this system requires a Comptonising corona that has become marginally optically thick covering a large fraction of the inner accretion disc. A corona such as this would distort our view of the inner accretion disc, and draw material and energy from it, leaving it slightly depleted (Done & Kubota 2006).

Temporal studies of this state have revealed the presence of a wide range of both low frequency (0.1 – 30.0 Hz) and high frequency (40 – 450Hz) QPOs (McClintock & Remillard 2006) or if the disc component contributes less than 50 per cent of the flux (unabsorbed 2 – 20 keV band pass) no QPOs are present (Remillard & McClintock 2006).

Intermediate State

The four states outlined above explain the majority of observations made of Galactic X-ray binary systems. However, they cannot explain all of them. There are some spectra that show characteristics of both the hard and soft states in combination, whilst lying within the boundaries defined for the hard state (e.g. Mendez & van der Klis 1997). It has therefore been suggested that this could be an intermediate state between the two. Other observations have also indicated that this may be an alternative route between the low state and the very high state (McClintock & Remillard 2006). The only conclusion to date is that the nature of this state is not well understood. Although it has been suggested that it could be used as a description for transitory observations, if the states it is transiting between are quoted.

Super-Eddington Accretion

When discussing optically thick accretion, it was noted that the Shakura – Sunyaev disc makes the assumption that the mass accretion rate is constant with radius, resulting in a ‘stable’ accretion disc. Two forms of disc instability were mentioned though, one of which is at low mass accretion rates: the hydrogen instability (discussed in Section 1.6.3) that is thought to be linked to the well known black hole hysteresis effect. At higher mass accretion rates, the radiation pressure instability can become an issue. In the Shakura – Sunyaev disc model, there is no high temperature stable solution, so this instability could lead to complete disruption of the accretion disc. This would imply that accretion beyond this rate (i.e. Eddington and super-Eddington accretion rates) would not be possible. However, there have been suggestions made over the years to circumvent this issue, some of which are discussed briefly below.

One suggestion is that of a 'slim disc'. In this scenario, the increase in mass accretion rate causes the disc to become so optically thick that the energy released in the mid-plane of the disc does not have time to diffuse to the photosphere before material is lost over the event horizon. Instead, the photons are carried along with the inflowing material, being advected radially rather than radiated vertically (Abramowicz et al. 1988). Such radiatively inefficient, optically thick, advection dominated disc solutions are physically very different to the optically thin, advection dominated flows (ADAFs) of Narayan & Yi (1995) discussed previously, as the energy is advected in photons rather than in protons. The additional cooling from advected photons is most important in the inner regions of the disc, so the expected luminosity from each disc radius of the slim disc is progressively lower than that of a standard accretion disc at the same mass accretion rate (Abramowicz et al. 1988). Thus these models predict that the slim disc spectra are less sharply curved than that of a standard disc. Additionally, the slim discs may extend down to smaller radii than the classic last stable orbit due to non-negligible pressure support, so their spectra can include higher temperature components than expected from a standard disc (Abramowicz et al. 1988, Watarai et al. 2000, but see also Beloborodov 1998).

Another suggestion relating to the radiation instability is that of geometrical beaming (King et al. 2001; King 2008; 2009). At high mass accretion rates, material moving through the accretion disc will reach a point at which the radiation pressure will become important and the material will enter a region of instability. The inflowing material being fed through the accretion disc at this radius reaches the Eddington limit (locally). This is known as the spherization, or trapping radius. In order to keep the local radiation energy release close to Eddington, the excess energy and matter is carried away in a strong accretion disc outflow. This in-turn causes the accretion rate within the disc to drop to $\sim$ Eddington rates. The wind formed by this process travels at the escape velocity of the orbit from which it escaped. It is dense in the outer regions (close to the spherization radius), while appearing more tenuous towards the inner regions of the disc (at this stage the majority of the excess material has already been fed into the wind). This results in the formation of a vacuum funnel at the centre, a funnel by which radiation can escape. This collimation causes a beaming effect that boosts the apparent emission from the source for an observer in the line of sight of the cone of emission.

The idea of geometric beaming was developed further by Poutanen et al. in 2007. Here the authors commented on the development of outflows within the spherization radius, but combined this with the advective transport of heat through the remaining accretion disc. This diminishes the amount of mass lost via the outflow by a factor of 2. The authors also consider the emission that would be viewed from a range of inclination angles. The emission from the accretion disc would be sub-critical (sub-Eddington and therefore a standard optically thick accretion disc) outside the spherization radius, and beamed by a factor of 2 – 7 inside this radius when observed face-on. However, at higher inclination angles the observer will see emission from a cool accretion disc and a photosphere which can exceed the spherization radius by orders of magnitude. This photosphere would emit a blackbody-like spectrum and would peak in the soft X-ray band.

There is another form of anisotropic beaming which is often discussed with the above, and that is relativistic beaming (Körding, Falckeet & Markoff 2002). In this case we find that the Eddington limit is not actually reached (or broken): it is a consequence of the observer looking down the cone of a jet, resulting in apparently super-Eddington emission. As a result the emission is Doppler boosted, if the jet is relativistic. This could occur in either the hard or (occasionally) very high state, when jet emission is present. As this is not truly super-Eddington accretion, we do not discuss this type further here.

1.7 X-ray binary systems

X-ray binary systems contain a compact object and a companion star in orbit around their combined centre of mass, with the majority of these sources falling into one of three distinct categories. The first of these are systems that contain a white dwarf, and in this case the system is known as a Cataclysmic Variable, or CV. The other two forms of X-ray binary systems (seen in Figure 1.19) contain either a neutron star or a black hole. These systems are known as low mass X-ray binaries (LMXBs) and high mass X-ray binaries (HMXBs), although in each case the name is not dependent on the nature of the compact object, but on the mass of the companion star. This divide is based on optical observations of these systems, which reveal that the majority of these systems have companions with masses $\gtrsim 10$ or $\lesssim 1$ $M_\odot$ (van Paradijs & McClintock 1995), although in recent years a

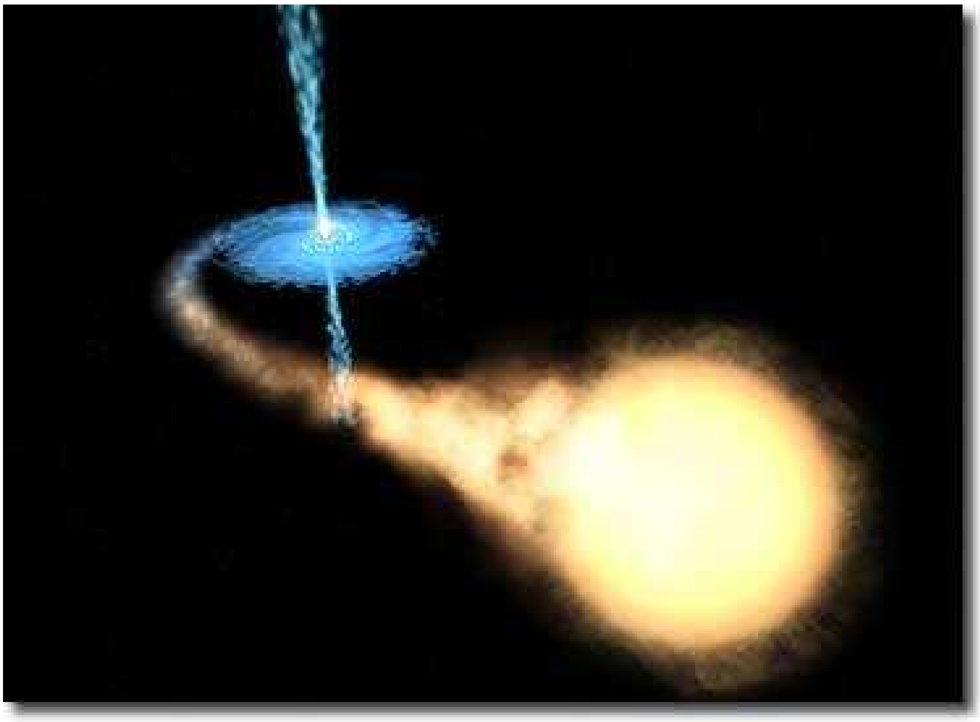

Figure 1.19: Artist impression of an accreting X-ray binary system (from `en.wikipedia.org`).

number of intermediate mass counterparts have been identified (Charles & Coe 2006). Identification of this counterpart can help to reveal information on the geometry of these systems, along with possible determinations of the mass of the compact object (see earlier discussion on the first optical observations of the black hole candidate Cyg X-1, Section 1.3.1).

The main factors that determine the X-ray emission properties of these systems are the mass of the compact object, the strength and geometry of any visible magnetic fields (for neutron star sources) and the geometry of the accretion flow. The emission from these systems can also be strongly affected by the type of companion, as can be seen in the varying size scales of these systems (Figure 1.20). As a result we will now briefly consider each of these systems to explore the implications of this on the observed behaviours of these systems.

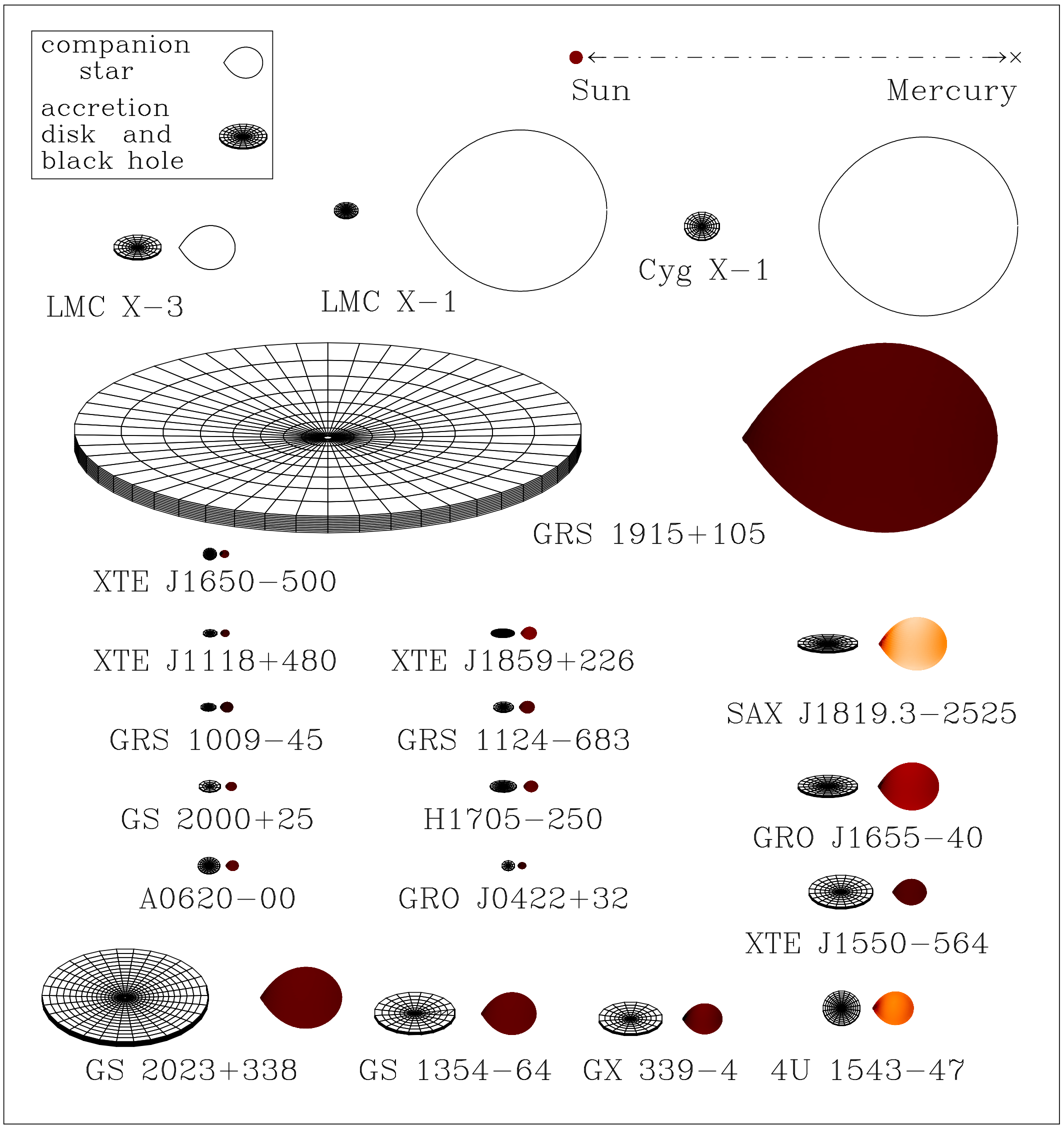

Figure 1.20: Schematic diagram of 20 X-ray binary systems. Image, by Jerome Orosz, can be found at `http://mintaka.sdsu.edu/faculty/orosz/web/`.

1.7.1 Low Mass X-ray Binaries (LMXB)

When the companion star is of comparable or lower mass than that of our Sun, the system is a low mass X-ray binary (Charles & Coe 2006). The stars contained within these systems are typically older and do not have strong stellar winds, so accretion can only take place through Roche lobe overflow. Such flows can occur as a result of a compact orbit, or as the companion expands during the later stages of its life cycle to fill its Roche lobe. As a result of this we find a wide range in orbital periods (0.19 – 398 hrs; van Paradijs & McClintock 1995).

The life times of these systems are usually quite long ($\sim 10^7 - 10^9$ yrs; Tauris & van den Heuvel 2006), and they are observed both in the Galactic centre and around the plane of our Galaxy. Companions tend to be A type or later (White, Nagase & Parmer 1995), although it can be difficult to type the stars in these systems accurately, as the optical emission can be dominated by the accretion disc. This results in the observation of mainly blue counterparts with a large amount of variation in their optical emission (usually tied to that of the X-ray variability; van Paradijs & McClintock 1995).

1.7.2 High Mass X-ray Binaries (HMXB)

If the companion has a relatively high mass, usually a Be or type O star for example, the system is known as a high mass X-ray binary. High mass stars of these types often expel strong winds that can be captured by the compact object. The resulting accretion flows are therefore usually wind-fed systems (van Paradijs & McClintock 1995). These systems are usually young due to the comparatively short lifetimes of their companion stars ($\sim 10^5 - 10^7$ yrs; Tauris & van den Heuvel 2006), which can result in wider orbital separations and typically longer orbital periods ($\lesssim 187$ days; van Paradijs & McClintock 1995).

Massive stars are very luminous and therefore easily detected, aiding the search for the optical counterparts of these sources. Astronomers have also found that the optical emission from these systems is dominated by the stellar counterparts, unlike their low mass cousins, due to their size and the scale of their emission (van Paradijs & McClintock 1995). This also impacts the variability of the optical spectrum, resulting in only roughly $\lesssim 10$

per cent variation in the optical light curves of these systems, which is due to observations of the the irradiated face of the companion (van Paradijs & McClintock 1995).

These systems are usually found in regions of younger stellar populations. As a result of this, we mainly tend to observe this type of system along the Galactic plane, or in the Magellanic clouds.

1.8 Ultraluminous X-ray Sources

Ultraluminous X-ray Sources (ULXs) are extragalactic, non-nuclear X-ray point sources that display X-ray luminosities in excess of 10^{39} erg s^{-1}. Although first observed $\sim$30 years ago by *Einstein* (Fabbiano 1989), these sources are yet to be fully understood, with the only certainty being that they cannot all be explained by stellar mass black holes (with masses 3 – 20 $M_{\odot}$) radiating isotropically below their Eddington limit. These intriguing systems will be the main focus of this thesis, we therefore review some of the major developments in our understanding of these sources in the following subsections.

1.8.1 X-ray observations

When early galaxy studies were performed with the *Einstein* telescope, the number of higher luminosity ($\gtrsim 10^{38}$ erg s^{-1}) discrete X-ray sources was considered surprising (Fabbiano 1995). A number of names were given to these sources including 'anomalously bright' and 'super-Eddington' sources (as they were emitting above the Eddington limit for a neutron star). It was thought that these sources could represent the upper end of the luminosity expected from 'normal' X-ray binary systems, but others suggested that their presence may mean that unusually massive compact objects were common. The capabilities of the *Einstein* mission limited observations of these sources to only the nearest galaxies, although several bright source were identified in M81. Nine extra-nuclear source were identified in total with *Einstein*, each emitting in the range 1.8×10^{38} – 1.4×10^{39} erg s^{-1} (Fabbiano 1995). This demonstrated a much higher incidence of these sources in M81 than when compared to the Milky Way, or our closest neighbour (M31), although a period of recent star formation was also noted in M81. It was thought therefore that the two may be linked, and that this increased number of bright X-ray sources may be related to an increased number of HMXBs.

The brightness of these sources also led to other suggestions on their nature. The spatial resolution of *Einstein* may have been considered excellent at the time of its launch, but when considering objects in other galaxies, astronomers were unable to determine if these bright sources were single or multiple objects (e.g. Fabbiano & Trinchieri 1987), or whether in some cases they were actually coincident with the nuclei of their host galaxy. It could also be that these objects were young X-ray supernovae (see Schlegel 1995). Unfortunately the spectral and imaging capabilities of this telescope were not sufficient to distinguish between these options. An example of this can be seen in Figure 1.21(a).

Later observations with *ROSAT* were able to look deeper into the fields of galaxies. The improved resolution of this instrument allowed for the observation of many more sources, and a clearer view of the emission from these systems (see Figure 1.21(b)). This telescope was also instrumental in constructing the first catalogues of these bright objects (e.g. Colbert & Mushotzky 1999; Roberts & Warwick 2000; Colbert & Ptak 2002). These surveys showed that non-nuclear luminous X-ray sources were quite common, appearing in up to ~ 20 per cent the galaxies sampled (Miller & Colbert 2004). It was at this stage that suggestion of intermediate mass black holes were introduced (Colbert & Mushotzky 1999). As the emission from these sources was intermediate between the luminosity of these two black hole populations, it seemed like a simple and sensible suggestion that they may also be intermediate in mass.

The improved spectral resolution of *ASCA* allowed researchers to begin to apply simple phenomenological models to the X-ray spectra of ULXs. The results of these fits for some ULXs indicated the presence of a thermal spectrum that could be well fit by an accretion disc. This suggested that the emission came from a single disc accreting system, most likely an X-ray binary. The temperature at the inner radius of the accretion disc was typically found to be $kT_{\rm in} \simeq 1.1 - 1.8$ keV (Makishima et al. 2000), which is at this higher end of the temperature scale in Galactic X-ray binaries. The high temperatures of these systems led to the introduction of further theories to explain the nature of these systems. These included beamed emission from a system containing a stellar mass black hole (e.g. King et al. 2001; see Section 1.6.4). Another suggestion was that we are observing rapidly spinning (Kerr) black holes. In this case, the resulting frame dragging would cause the

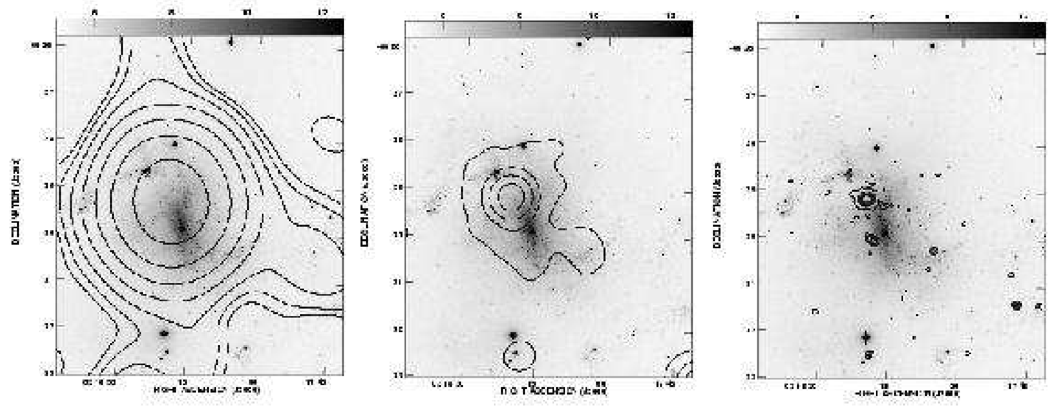

Figure 1.21: Comparison of X-ray telescopes on-board three separate missions. In each case the grayscale image is an optical I band image of NGC 1313. From left the right, the image is overplotted with the X-ray contours from (a) the *Einstein* telescope, (b) *ROSAT* – HRI and (c) *Chandra* –ACIS. All three images are taken from Miller & Colbert (2004).

inner radius to shrink by up to six times (e.g. Makishima et al. 2000; Mizuno et al. 2001; Ebisawa et al. 2003) leading to the increase in temperature. An alternative idea was that the we are observing a slim disc. In this case the increased mass accretion rate would cause a swelling in the accretion disc, resulting in an optically thick, geometrically 'slim' disc which advects photons in through the flow (Abramowicz et al 1988; see Section 1.6.4 for more information).

The data quality of some observations also allowed for the application of some two component models (e.g. Takano et al. 1994), with results showing consistency with a standard accretion flow (multicoloured disc + power-law), although they indicated that the observed disc appeared to be cool. Colbert & Mushotzky (1999) observed the presence of a soft excess or cooler accretion disc component in this way, but the statistical significance of these claims were not very high.

ASCA observations also gave evidence of state transitions, giving further support to the idea of emission from an X-ray binary. Transitions from a high/soft type spectrum to a low/hard like spectrum were observed in the the ULXs in IC 342 (Kubota et al. 2001).

These were similar transitions to those observed in Galactic sources (see Section 1.6 for more information).

With the advent of *Chandra* and *XMM-Newton*, came a new era in the observation and analysis of these sources. The dramatically improved spatial and spectral resolution for these instruments lead to new developments in many fields, including ultraluminous X-ray sources (see Figure 1.21(c)). Spectral results from some ULXs appeared to show the opposite trend to that which had been previously observed by *ASCA*, with spectra transiting between a high/hard and low/soft state (e.g M51 X-7, Liu et al. 2002; Antennae sources , Fabbiano et al. 2003), this did not fit with the general trend of state transition observed in the Galactic population, but was not unheard of (e.g. Cyg X-1). Surveys with these telescopes also reveals an over-density in some galaxies, for example NGC 4038 & 4039 (also known as the Antennae) was found to have $\gtrsim$ 10 sources emitting in the ultraluminous regime ($\gtrsim 10^{39}$ erg s^{-1}). The mass of these objects was initially estimated by assuming they were X-ray binary systems containing a black hole emitting at the Eddington limit. The luminosity of these sources suggested that we were observing black holes of mass $M_{\rm BH} \gtrsim 10 -$ (few $\times$) 100 $M_{\odot}$ (assuming no beaming; Miller & Colbert 2004). Some of the highlights will be discussed in the next section.

Modern Spectral analysis

As a first stage of spectral analysis, simple phenomenological models were once again applied to observations of these sources. Simple power-law fits resulted $\Gamma \simeq 2$ in many cases (e.g. ULXs contained in NGC 3628, Strickland et al. 2001; ULXs in Circinus, Smith & Wilson 2001; NGC 5204, Roberts et al. 2001). Power-law fits were also compared to multicoloured disc fits in many systems, with Foschini et al. (2002) indicating that the eight ULXs contained within their nearby galaxy survey were never described best by a multicoloured disc. Conversely, Roberts et al. (2002) found that the five brightest sources in NGC 4485/4490 were better or equally well fitted by a multicoloured disc.

With the improved statistics of these instruments, it became possible to fit the spectra of more sources with two component models, combining both a disc and power-law component which had been used with great success in Galactic systems. By doing so it is possible to use the temperature of the accretion disc emission, together with its luminosity to determine the mass, as Shakura – Sunyaev models predict the disc temperature $kT \sim (M/10M_{\odot})^{-1/4}(L/L_{\rm Edd})^{1/4}$ keV (Shakura & Sunyaev 1973). The higher signal-to-noise spectra of ULXs can often be well fitted by composite models of a disc together with a hard ($\Gamma < 2$) tail, with the low measured disc temperature of ~ 0.2 keV. If we assume that the disc is accreting to its last stable orbit, this would imply a high black hole mass of $\sim 10^2\ M_{\odot}$ (e.g. Miller et al. 2003; Kaaret et al. 2003; Miller, Fabian & Miller 2004). There is however a problem with this; this calculation can only give reliable results when the X-ray spectrum is dominated by the disc component (the high/soft or thermal dominant state) (Done & Kubota 2006). The derived disc temperature is increasingly distorted as the tail increases in importance. Such low temperature, high luminosity discs are also seen in the very high or steep power law state, in conjuction with a strong tail (Kubota & Done 2004, Done & Kubota 2006). The ULX spectral decompositions of Miller et al. (2004) all have strong tails ($\gtrsim 80\%$ of the 0.3 – 10 keV flux; Stobbart, Roberts & Wilms 2006), so a straightforward interpretation of the derived disc parameters is unlikely to give a robust mass estimator[9].

It was noted by Miller & Colbert (2004) that this cool disc component does not prove that the inner disc temperature was cool, it only demonstrates that the previous identification of high temperature discs my be unwarranted. However, further arguments were provided in Miller et al.'s (2003; 2004) results. The resultant fit parameters were similar to that of the low/hard state in black hole binaries, suggesting very sub-Eddington accretion rates ($< 0.1\ L_{\rm Edd}$). At these luminosities, it would also imply the need for IMBHs. Further mass estimates were achieved using the Eddington argument highlighted above. The brightest detected in these galaxy surveys was, by far, M82 X-1, emitting with a peak luminosity (as of 2004; Miller & Colbert 2004) of 9×10^{40} erg s^{-1}. Applying Eddington arguments to this source, it would imply a mass of $> 700\ M_{\odot}$ (Matsumoto et al. 2001).

---

[9] It should also be noted that band pass is a potential problem in comparing ULX results with those of black hole binaries. Given their high fluxes, Galactic sources have been most commonly studied in detail using telescopes such as *RXTE*, so are generally characterised by their behaviour in the 3 – 20 keV regime. The more distant (and hence fainter) ULXs instead require the more sensitive, high spatial resolution telescopes of *Chandra* and *XMM-Newton* for detailed studies, whose CCD detectors cover the 0.3 – 10 keV band. This difference in typical energy range between the ULX and black hole binary data mean that any comparison between the two must be made with care.

However, the best data also shows the limitations of this simple spectral fitting. There is clear evidence for curvature of the power-law tail at the highest energies, with a deficit of photons above 5 keV (Roberts et al. 2005; Stobbart, Roberts, & Wilms 2006; Miyawaki et al. 2009). Such curvature is never seen in the low/hard state at these low energies, and so should not be present if we were observing IMBHs in the that state. Only the very high state shows curvature at such low energies, but these generally have spectra which are steep.

As higher quality data became more widely available, more physical models started to be applied. Some Japanese X-ray astronomers turned to the slim disc model to explain the spectral shape and accretion flow of these objects. As less energy is radiated away (within this model), this affects the temperature of the disc, and to track this they use the exponent of the radial dependance, p, where $T(r) \propto r^{-p}$. For a standard optically thick geometrically thin accretion disc, $p = 0.75$, but for a slim disc it drops to $p \simeq 0.5$. To test this, Okajima et al (2006) and Vierdayanti et al. (2006) among others, have been fitting ULX spectra with p as a free parameter. Their results have given values ~ 0.6, which they state must imply advective flow and therefore the presence of a slim disc.

Others, such as Stobbart, Roberts, & Wilms (2006) applied a combination of accretion disc and Comptonisation models to a sample of 13 bright ULXs, finding a preference for a cool disc with an optically thick corona ($\tau > 8$). These results described a new accretion geometry, that took a more extreme form than the very high state. Each of these suggestions indicates that we may be looking at a form of extreme accretion onto stellar mass black holes.

Spectral variability

Spectral variability studies of Galactic sources have proved invaluable to our understanding of these systems (see review in earlier sections with further details in McClintock & Remillard 2006 or Done Gierliński & Kubota 2006), yet it is avenue that remains under-explored in ULXs. This is due, in part, to ULXs being too faint to be picked up by monitoring missions such as *RXTE* (with the exception of M82 X-1, Kaaret, Simet & Lang 2006). Some studies have been performed, such as the investigation into the X-ray source population of the Antennae performed by Fabbiano et al (2003). This, along with other studies, show that the majority of ULXs display a general hardening as the luminosity of the system increases (e.g. Homberg II X-1, Dewangan et al. in 2004; NGC 5204 X-1, Roberts et al. 2006). The results also show that this behaviour can be modelled by changes in the temperature of an optically thick disc coupled with an optically thick corona (Roberts et al 2006).

Temporal variability

Temporal variations of X-ray sources have been highlighted on a number of occasions throughout this introduction, but it has mainly been considered on longer time-scales (e.g. orbital period of Cyg X-1, state transitions). When considering ULXs on these time-scales we find that few sources have been regularly observed. Unlike their Galactic stellar mass counterparts or the brighter quasars, which can be monitored daily by instruments such as the All Sky Monitor on board the *RXTE*, analysis can only be carried out using pointed observations. This leads to large gaps in the light curves, making it difficult to track the trends of these systems. Some authors have managed to find evidence for variation of time-scales of months to years with the use of multi-mission data. Examples include the ULXs in M81 (La Parola et al. 2001), Ho II (Miyaji et al 2001), IC 342 (Kubota et al 2001) NGC 4485 & 4490 (Roberts et al. 2002) and M51 (Terashima & Wilson 2003)

If we consider slightly shorter time-scales, with periods of days to weeks, we find that fewer studies have been reported. In 2006, one such study was reported by Roberts et al., observing NGC 5204 X-1. The authors had been awarded time on the *Chandra* telescope to observe this source over a period of 2 month. Over time-scales of days they observed a factor 5 variation in the flux of the source. This observing campaign also allowed them to explore variation over a period of hours (and less), but no variations were observed on these time-scales.

Little evidence has been observed of timing features, in fact intra-observational studies have revealed that only $\lesssim$15% of ULXs exhibit measurable short-term variability (Swartz et al 2004; Feng & Kaaret 2005).

Intra-observational analysis for both stellar and supermassive black holes is explored using power spectral densities (PSD). It has been shown that many features are common to both stellar and supermassive black holes (McHardy et al. 2006; McClintock & Remillard 2006; van der Klis 2006). For example a scaling in the PSD break time-scales (e.g. McHardy et al 2006) has also been observed, relating to mass and accretion rate. If any of these features were to be observed in the spectrum of a ULX, they would allow for mass estimates of the source. Unfortunately very few ULXs show much variability power, but some measurements have been made, for example Soria et al (2004) detected a break at 2.5 mHz in the PSD of NGC 5408 X-1 indicating a mass of $\sim$100 $M_{\odot}$, while Cropper et al. (2004; 2004a) detected a 28 mHz break in the PSD of NGC 4559 that provides a mass estimate of 38 $M_{\odot}$ or 1300 $_{\odot}$ depending on the calibration used. Quasi-periodic oscillations (QPOs) have also been detected, showing that these systems may have similar variability properties as Galactic sources. To date only two sources have displayed these features (M82 X-1, Strohmayer & Mushotzky 2003; NGC 5408 X-1, Strohmayer et al. 2007). These features have also been given as evidence against beaming, *potentially* lending support toward IMBHs.

1.8.2 Optical/UV studies

Since these objects first came to light, astronomers have been searching for more information on their nature from multiple wavelengths. This task was difficult before the advent of *Chandra*, due to the large number of sources available within the positional error circle of *ROSAT*. However, in the decade since its launch, much progress has been made. Starting from the largest size scale and moving inwards, we find that ULXs have been found preferentially in actively star-forming galaxies (Kaaret 2005), along with starburst, interacting/merging and dwarf galaxies (Swartz et al. 2008) preferably with low metallicities (Mapelli, Colpi & Zampieri 2009). In the case of dwarf galaxies there does appear to be a preference for low metalicities (Pakull & Mirioni 2002).

An observed correlation between the number of ULXs and the global star-formation rate in spirals has also been noted (Swartz et al. 2004; Liu, Bregman, & Irwin 2006). The sheer number of sources observed in starburst galaxies together with their short lifetimes (implied by their location in regions of active star formation) mean that, if these systems were all to contain IMBHs, an unrealistically large underlying population must be present (see Figure 1.22; King 2004). Instead it is much more likely that the bulk of the population are the most extreme examples of High Mass X-ray Binaries (HMXBs) that somehow

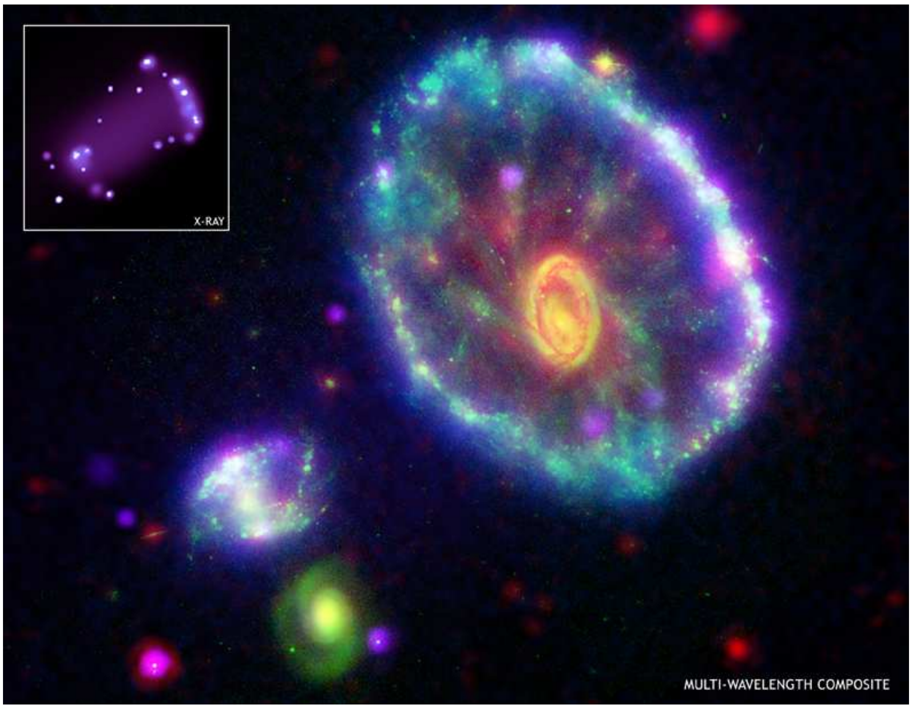

Figure 1.22: Cartwheel galaxy: this image combines data from four different observatories: the Chandra X-ray Observatory (purple); the Galaxy Evolution Explorer satellite (ultraviolet/blue); the Hubble Space Telescope (visible/green); the Spitzer Space Telescope (infrared/red). The insert highlights the large X-ray population contained within this galaxy (Image composite: NASA/JPL/Caltech/P.Appleton et al. X-ray: NASA/CXC/A.Wolter & G.Trinchieri et al.).

exceed the Eddington limit. These high mass companions provide a natural origin for the high mass transfer rates required to power the observed luminosities (Rappaport, Podsiadlowski & Pfahl 2005).

An association with star-forming regions (Fabbiano, Zezas & Murray 2001; Lira et al. 2002; Gao et al 2003) and the unbroken luminosity function connecting ULXs to the standard X-ray binary population (Grimm, Gilfanov & Sunyaev 2003) also indicates that we may be observing HMXB systems. A recent survey by Swartz, Tennant, & Soria (2009) sought to investigate the nature of the regions surrounding ULXs (100 by 100 pc^2 regions). They found a significant correlation between young star forming regions (OB type stars) and ULXs. This result links in to the array of recent studies that have sought to identify potential counterparts of these sources and look at their immediate environments (see below).

Stellar counterparts

The search for optical counterparts has mainly focused on nearby systems ($\lesssim$ 10 Mpc), with individual counterparts observed over the range $m_{\rm V} \sim$ 22-26 (Roberts et al. 2008). Many of these are observed to be blue, suggesting an OB star and so the presence of HMXB, or that we are observing reprocessed emission from the accretion disc (e.g. Copperwheat et al 2005). Much of this work is discussed further in Chapter 2.

Of course one of the main reasons to identify these counterparts is to perform spectroscopic studies of these systems. This will provide a means of answering the question of their nature conclusively by a direct mass measurement based on constraints placed by the binary orbit. To date this has not been achieved, but similar methods have been applied to numerous Galactic stellar mass black hole systems (van Paradijs & McClintock 1995; Charles & Coe 2006), and to an extra-galactic stellar mass black hole in IC 10 X-1, a Wolf-Rayet black hole binary. A radial velocity curve of this source was constructed from repeated optical observations, which provided a mass estimate of $23 - 34\ M_{\odot}$ (Prestwich et al. 2007; Silverman & Filippenko 2008). Although the line features used here are emitted from the star, it proves that the concept of radial velocity curves for extra-galactic sources, using a method that was instrumental in proving the first observational evidence of the existence of black holes (see Section 1.3.1), can work well for extra-galactic sources.

Only a small number of pilot optical spectra of ULX counterparts have been taken and published to date. Roberts et al. (2001) studied the counterpart of NGC 5204 X-1, finding a blue, featureless spectrum. Similar results were also found in the spectrum of NGC 1313 X-2, possibly the most explored counterpart to date (Zampieri et al. 2004; Pakull, Grisé & Motch 2006; Liu et al. 2007; Grisé et al. 2009). A He II 4686 Å line was identified in its spectum, and an observed velocity shift in the line was reported in VLT observations of this source. The shift was of $\sim$ 300 km s^{-1} over approximately a 3 week period (Pakull, Grisé & Motch 2006).

ULX nebulae

Pakull & Mirioni presented a study of a small number of ULX environments in 2002. They showed that each of the ULXs in the sample resided in emission nebulae that were up to a few hundred parsecs in diameter. They also reported that may of the nebulae showed evidence of both low and high ionisation emission lines within their spectra. This indicated that the nebula could be either shock ionised or photoionised. Such photoionisation could easily be caused by emission from the ULX. It can also be used to place limits on the X-ray emission powering the photoionisation of the nebula (if we assume this is the source of the energy). By comparing this to the observed X-ray luminosity of the source, Pakull & Mirioni (2002) were able to conclude that the optical emission was consistent with emission from an isotropic X-ray emitter. This appears to rule out beamed emission, suggesting that we are observing either IMBHs or some form of super-Eddington accretion state. Later results also showed evidence of the presence of cavities in the nebulae of these systems, possibly cleared by shocks (Roberts et al. 2002a). Further explorations of the spectra of ULX nebulae also showed evidence of both photoionisation and shocks (e.g. Pakull & Mirioni 2003), and in some cases the ULX must power strong winds and/or jets in order to power the nebulae (Abolmasov et al. 2007). From these results, it would suggest that we may be looking at a heterogeneous sample of sources.

1.8.3 Radio studies

It has been suggested that the X-ray emission from ultraluminous X-ray sources can be explained by an IMBH residing in the hard state, or by relativistically boosted emission from a stellar mass black hole (among others). If we are observing IMBHs, we would expect to observe steady state emission in the hard state, with correlated Radio and X-ray emission. This would be observed as $L_{\rm X} \propto L_{\rm R}^{1.38} M^{0.81}$ (Falcke et al. 2004). Such steady state emission has been observed in two of the ULXs within M82, and in one of those located in NGC 4736 (Körding et al. 2005). If we assume that these systems are in the hard state, this implies an $M_{\rm BH} \simeq 10^2 - 10^5 M_{\odot}$. The second suggestion is also known as the microblazar model (Mirabel & Rodríguez 1999; Körding et al. 2002). In this case the compact object would be of stellar mass, and the jet emission would be Doppler boosted along the jet. Such emission would be observed if the jet were to point in the direction of the observer. This emission would most likely be observed as flaring (often seen in both the hard and very high states), but a study by Körding et al. (2005) found no significant detections in their sample of nine sources, over a five month observing period. However, the authors argue that this could be due to an under sampling of the ULX light curves.

A study by Miller, Mushotzky & Neff (2005) identified region of diffuse resolved radio emission in the area surrounding Ho II X-1. An extended H II region is also coincident with this location, and these regions are known to emit in the radio via thermal Bremsstrahlung. The authors found though that only ~ 5 per cent of the observed radio emission could be explained by these processes. Their analysis noted that the radio emission could arise from the ULX, but that this resolved emission ruled out the possibility of relativistic beaming as its source. It would therefore need to be powered by either some form of super-Eddington accretion or by an IMBH.

The nebula surrounding NGC 5408 X-1 also shows evidence of radio emission (Kaaret et al. 2003), although the authors note that this emission could be the result of relativistic beaming from a jet. Later work, however, revealed this emission to be slightly extended, with a diameter of 35 – 46 pc (Lang et al. 2007). Their results could not rule out relativistically beamed emission, but highlighted the fact that that the nature of the emission appeared to be comparable with SS 433. This would indicate that we are observing radio emission powered by outflows from a super-Eddington system, similar to the W50 nebula around SS 433 (Dubner et al. 1998).

1.8.4 Intermediate mass verses stellar mass black holes

Despite large developments in the ULX field, we are still unable to answer the basic question: 'what is the nature of ULXs?'. As stated above, the only certainty is that they cannot all be explained by stellar mass black holes (with masses 3 – 20 $M_{\odot}$) radiating isotropically below their Eddington limit. The simplest explanation is to assume that larger compact objects resides within these systems. This approach would indicate that we are observing a compact object that is intermediate in mass (IMBH, of mass $\sim$100 – 10,000 $M_{\odot}$; Colbert & Mushotsky 1999), as well as luminosity, between that of its stellar mass and supermassive black hole cousins. Early *XMM-Newton* observations appeared to support this idea, as does the presence of a QPOs in M82 X-1 and NGC 5408 X-1. The observation of steady state radio emission has also added weight to this idea.

However, more recent multi-wavelength observations appear to favour higher rates of mass transfer onto a stellar mass black hole. Such evidence includes an apparent association with young star-forming regions, and more specifically high mass OB stars. The number observed in starburst galaxies also raise questions over the possibility of such large IMBH populations. High quality X-ray spectra have also started to show the presence of a possible break at higher energies (e.g. Stobbart, Roberts, & Wilms 2006). If such a break is common to these sources, it would argue against the possibility that we are observing an IMBH in the low hard state. Stellar mass black holes would also explain the unbroken X-ray luminosity function connecting ULXs to the standard X-ray binary population (Grimm, Gilfanov & Sunyaev 2003).

A majority of evidence appears to be mounting in favour of stellar mass objects, but there is no conclusive evidence and there are still some sources which show evidence to the contrary. It is against this backdrop that we start to explore both the optical and X-ray emission of these sources to try and unlock their nature.

1.9 Aims of this work

Ultraluminous X-ray sources are an intriguing class of object, with controversy over their nature still present after ~ 30 years of study. We will attempt to answer some of the remaining fundamental questions in order to constrain the nature of these systems. These questions include:

what are the stellar counterparts to ULXs?
how do these sources vary over time?
what is the accretion geometry of these systems?
do these systems contain intermediate mass black holes?
are there multiple classes of ULX?

This thesis intends to investigate the underlying nature of ultraluminous X-ray sources and explore the questions outlined above. Chapter 2 provides details of a photometric study of the optical counterparts of ULXs. Chapter 3 outlines the initial stages of our optical spectroscopic programme currently underway with the *Gemini* telescope. Chapter 4 discusses the X-ray variability of the ULXs residing in NGC 4485 & 4490, with data from both the *Chandra* and *XMM-Newton* public archives. Chapter 5 investigates the nature of ULXs by performing X-ray spectral studies with some of the highest quality data currently available in the *XMM-Newton* public archive. The major results of this work are summarised in Chapter 6, and possible directions for future study are highlighted.

Chapter 2

Optical Counterparts Survey

2.1 Introduction

In the late 1970's and early 1980's the *Einstein* telescope was used to perform studies of normal galaxies, in which researchers noted the presence of X-ray luminous non-nuclear objects, brighter than those in our own galaxy ($10^{39} \lesssim L_X \lesssim 10^{40}$ erg s^{-1}; Fabbiano 1989), objects that were later termed ultraluminous X-ray sources (ULXs). Since their initial discovery, much analysis has been performed in the X-ray bands, but as with Galactic X-ray sources (e.g. van Paradijs & McClintock 1995; Charles & Coe 2006), astronomers now turn to a wider range of wavelengths to unlock the nature of these systems. To date much of this work has focused on individual source and/or their host galaxies (e.g. Ho II X-1, Kaaret, Ward & Zezas 2004; NGC 1313 X-2 Mucciarelli et al. 2005; NGC 5408, Lang et al. 2007; M51 population, Terashima, Inoue &Wilson 2006; Antennae galaxy, Zezas et al. 2002; Cartwheel galaxy, Gao et al. 2003), whilst only a small number of larger surveys have taken place (e.g. Ptak et al 2006, Swarz, Tennant & Soria 2009). A summary of these findings can be found in the Introduction chapter to this thesis.

Here we turn to optical wavebands to search for potential optical counterparts to these sources, to primarily search for candidates for optical follow-up studies (see Chapter 3). However, the identification of counterparts is not trivial, as many of these objects reside in crowded stellar fields (Liu et al. 2009). Zampieri et el. (2004) highlighted this issue during their search for a counterpart to NGC 1313 X-2. Figure 2.1 shows an ESO 3.6 m R-band image of the field around this source, revealing the presence of a number of possible counterparts. Over-plotted are the positional 90 per cent confidence regions for

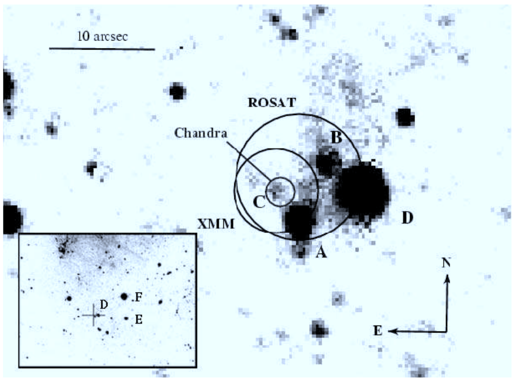

Figure 2.1: ESO 3.6m R-band image of the field of NGC 1313 X-2 (from Zampieri et al. 2004). The estimated 90% confidence circles for the *ROSAT* HRI, *XMM-Newton* EPIC MOS, and *Chandra* ACIS-S, centred on respective source positions. Labels A, B, C, and D mark the 4 field objects inside or close to the X-ray error circles. The insert at the bottom left shows a larger portion of the image with the position of the X-ray source (cross).

ROSAT HRI, *XMM-Newton* EPIC MOS, and *Chandra* ACIS-S detectors. In fact previous observations by Stocke et al. (1995) had identified star A as the possible counterpart using the *ROSAT* position. This highlights the need for good spatial resolution and positional accuracy in the X-ray regime, demonstrating the need for the subarcsec resolution of *Chandra*. The findings of Zampieri el al (2004) also highlight the need for very high spatial resolution and sensitivity in the optical and ultraviolet bands, with the nature of this source C unknown at that time, and with various options being discussed within the text[1]. Such high spatial resolution and sensitivity is available with the *Hubble Space Telescope*, and work that has combined the imaging capabilities of these two telescopes has been met with great success, for example observations of the Antennae starburst galaxy found that 10 of the 14 ULXs contained within this galaxy are associated with stellar clusters (Zezas et al. 2002), whilst data from NGC 5204 was able to identify a unique O/B stellar counterpart to the ULX X-1 (Liu et al. 2004). We now follow the example

---

[1] Subsequent work, using data from *HST* revealed that source C was not the counterpart of this source (Ramsey et al. 2006).This highlights the need for high quality optical data.

of these and other studies to combine the sub-arcsecond X-ray astrometry provided by *Chandra* with the imaging capabilities of the *HST*, and reveal 38 potential counterparts within 5 Mpc.

2.2 Sample selection

We compiled a catalogue of the known ultraluminous X-ray sources as a starting point for a study of the spectra of the ULX optical counterparts population. To do this we draw on a number of ULX catalogues available in the public domain; including Roberts & Warwick (2000), Swartz et al. (2004), Liu & Mirabel (2005), Liu & Bregman (2005), Ptak et al (2006) and Winter, Mushotzky, & Reynolds (2006). A concise primary list was formed by merging duplicate identifications and removing any sources for which subsequent research has indicated that a ULX is not present (based on luminosity criteria or miss-identification of object, e.g. foreground star, background quasar).

Many of the optical counterparts identified to date are faint ($\gtrsim$ 24 mag; Roberts, Levan & Goad 2008). At this magnitude follow-up spectral observations with ground based telescope are impractical in reasonable periods of time (observations of a 23$^{\rm rd}$ magnitude B0 V star would require $\sim$ 3 hours per observation[2], with a minimum of 10 observations required for radial velocity curve measurements). As one of the aims of this project is to identify candidates for follow-up studies, we place an additional distance constraint on our sample selection criteria of 5 Mpc (where distances have been collated via literature search) to allow the greatest opportunity to identify counterparts for potential follow-up. At this distance, a B0 V star would have an apparent magnitude of 24.4 (M_V = -4.1, Zombeck 1990), so more distant objects would be likely to be impractical for follow-up. It should be noted that we retain the ULXs residing within NGC 3034 as some distance estimates have indicated that this galaxy may by located within 5 Mpc (e.g. Freedman et al. 1994). This provides a sample of 45 nearby ULXs that we list in Table 2.1, along with their published luminosities, distances and Galactic absorption and extinction columns for both the optical and X-ray bands.

---

[2] The time required to observe a B0 V star of this magnitude was found using the Gemini ITC. This can be found at `http://www.gemini.edu/sciops/instruments/itc/itcHelp/ITChelp.html`.

Table 2.1: The ULX sample listed by distance.

Source	Alternative names	RA (J2000)	Dec. (J2000)	d ^{a} (Mpc)	N_{H} ^{b} (10^{20} cm^{-2})	E(B-V)^c	L_{X} ^{d} (10^{39} erg s^{-1})
NGC 598 ULX1(1)	Source 3(7) Source 7(9) M33-X-8(10) CXOUJ013351.0+303937(11)	01 33 50.9	+30 39 37	0.9(7)	5.58	0.042	2.5 αXI(7)
NGC 55 ULX1(2)	Source 7(7) NGC 55 6(12) XMMU J001528.9-391319(13)	00 15 28.9	-39 13 19	1.74(2)	1.72	0.014	1.3 αX(2)
NGC 4190 X1(3)		12 13 45.4	+36 37 55	2.8(3)	1.6	0.030	2.31βRP(3)
NGC 253 ULX1(1)	NGC 253 PSX-1(1) CXOUJ004734.0-251637(16)	00 47 34.0	-25 16 37	3.0(3)	1.42	0.019	1.2 ϵC(16)
NGC 253 ULX2(1)	NGC 253 PSX-2(1) NGC 253 X2(3) NGC 253 XMM1(4) CXOUJ004733.0-251749(16)	00 47 33.0	-25 17 49	3.0(3)	1.42	0.019	5.7 αXI(4)
NGC 253 ULX3(1)	NGC 253 PSX-3(1) NGC 253 X1(3) CXOUJ004733.4-251722(16)	00 47 33.4	-25 17 22	3.0(3)	1.42	0.019	1.74 βRP(3)
NGC 253 X20(3)*	NGC 253 ULX1(3)	00 48 20.0	-25 10 10	3.0(3)	1.42	0.019	2.37 βRP(3)
NGC 253 XMM2(4)*	NGC 253 X9(3)	00 47 22.4	-25 20 55	3.0(3)	1.42	0.019	2.7 αXI(4)
NGC 253 XMM4(4)*		00 47 23.3	-25 19 07	3.0(3)	1.42	0.019	2.2 αXI(4)

Source	Alternative names	RA (J2000)	Dec. (J2000)	d [a] (Mpc)	N_{H} [b] (10^{20} cm^{-2})	E(B-V)[c]	L_{X} [d] (10^{39} erg s^{-1})
NGC 253 XMM5(4)*	NGC 253 X7(3)	00 47 17.6	-25 18 12	3.0(3)	1.42	0.019	2.2 αXI(4)
NGC 253 XMM6(4)	NGC 253 X6(3) RX J004742.5-251501(17)	00 47 42.8	-25 15 06	3.0(3)	1.42	0.019	3.1 αXI(4)
NGC 253 XMM7(4)*	NGC 253 X13(3)	00 47 09.2	-25 21 22	3.0(3)	1.42	0.019	1.8 αXI(4)
M81-X-6(1)	NGC 3031 X9(3) NGC 3031 ULX1(3) M81 XMM1(4) Source 7(7) CXOUJ095532.98+690033.4(8)	09 55 33.0	+69 00 33	3.4(3)	4.16	0.080	3.84 δC(8)
Hol IX X-1(2)	NGC 3031 ULX 2(1) M81-X-9(2) Hol IX XMM1(4) Source 17(7) NGC 3031 10(18) H 44(19) IXO 34(20)	09 57 54.1	+69 03 47	3.42(3)	4.07	0.079	13.4 γRP(3)
NGC 4395 ULX1(1)	NGC 4395 X-1(3) NGC 4395 XMM1(4) Source 12(7) NGC 4395 X2(17) IXO 53(20)	12 26 01.9	+33 31 31	3.6(3)	1.35	0.017	1.73 γRP(3)
NGC 1313 X-1(1)	NGC 1313 X2(3) NGC 1313 ULX1(3) NGC 1313 XMM1(4) Source 4(7) IXO 7(20)	03 18 20.0	-66 29 11	3.7(3)	3.98	0.110	1.3 αXI(4)

Source	Alternative names	RA (J2000)	Dec. (J2000)	d [a] (Mpc)	N_{H} [b] (10^{20} cm^{-2})	E(B-V)[c]	L_{X} [d] (10^{39} erg s^{-1})
NGC 1313 X-2(1)	NGC 1313 ULX2(1) NGC 1313 X7(3) NGC 1313 ULX3(3) NGC 1313 XMM3(4) Source 5(7) IXO 8(20)	03 18 22.3	-66 36 04	3.7(3)	3.98	0.085	4.2 αXI(4)
XMM J031747.6-663010(5)*		03 17 47.6	-66 30 10	3.7(3)	3.98	0.109	1.6 ϵX(5)
IC 342 X-1(6)	PGC13826-X6(3) PGC 13826 ULX3(3) IC 342 XMM1(4) Source 2(7) CXOUJ034555.7+680455(14) IXO 22(20)	03 45 55.17	+68 04 58.6	3.9(3)	30.2	0.565	12.77 γRP(3)
IC 342 X-2(2)	PGC13826-X7(3) IC 342 XMM2(4) IC 342 X-3(6) IC 342 X-13(15)	03 46 15.0	+68 11 11.2	3.9(3)	30.2	0.559	8.43 αXI(4)
IC 342 ULX2(1)	PGC 13826 X1(3) IC 342 XMM3(4)	03 46 48.6	+68 05 51.0	3.9(3)	30.2	0.558	2.57 γRP(3)
IC 342 X-4(6)*	PGC13826-X3(3) PGC 13826 ULX2(3)	03 46 45.54	+68 09 51.7	3.9(3)	30.2	0.557	1.49 γRP(3)
IC 342 X-6(6)	PGC13826-X2(3) PGC 13826 ULX1(3) IC 342 XMM4(4)	03 46 57.17	+68 06 22.4	3.9(3)	30.2	0.558	1.21 γRP(3)

Source	Alternative names	RA (J2000)	Dec. (J2000)	d ^{a} (Mpc)	$N_{\rm H}$ ^{b} (10^{20} cm^{-2})	E(B-V)^{c}	$L_{\rm X}$ ^{d} (10^{39} erg s^{-1})
Circinus l ULX1$^{(1)}$	CG-X-1$^{(1)}$ ULX 42$^{(21)}$ CXOUJ141312.3-652013$^{(22)}$	14 13 12.3	-65 20 13.0	4$^{(5)}$	55.6	1.488	3.72 δC$^{(8)}$
Circinus ULX3$^{(1)}$	CXOUJ141310.3-652017$^{(22)}$	14 13 10.3	-65 20 17.0	4$^{(5)}$	55.6	1.468	1.4 βCI$^{(22)}$
Circinus ULX4$^{(1)}$	CXOUJ141310.4-652022$^{(22)}$	14 13 10.4	-65 20 22.0	4$^{(5)}$	55.6	1.464	2.09 βC$^{(22)}$
Circinus XMM1$^{(4)*}$	Source 1$^{(7)}$	14 12 54.2	-65 22 55.3	4$^{(5)}$	55.6	1.028	23 αXI$^{(4)}$
Circinus XMM2$^{(4)*}$		14 12 39.2	-65 23 34.3	4$^{(5)}$	55.6	0.891	10.7 αXI$^{(4)}$
Circinus XMM3$^{(4)*}$		14 13 28.3	-65 18 08.3	4$^{(5)}$	55.6	1.363	14.5 αXI$^{(4)}$
NGC 2403 X-1$^{(1)}$	NGC 2403 X2$^{(3)}$ NGC 2403 ULX1$^{(3)}$ NGC 2403 XMM1$^{(4)}$ CXOUJ073625.5+653540$^{(8)}$ Source 21$^{(23)}$ Source 6$^{(7)}$	07 36 25.55	+65 35 40.0	4.2$^{(2)}$	4.17	0.040	1.73 δC$^{(8)}$
NGC 2403 XMM2$^{(4)*}$	CXOUJ073650.0+653603$^{(24)}$	07 36 50.2	+65 36 02.1	4.2$^{(2)}$	4.17	0.040	1.6 αXI$^{(4)}$
NGC 2403 X3 $^{(3)*}$	NGC 2403 X-4$^{(6)}$ NGC2403 XMM4$^{(4)}$	07 37 02.1	+65 39 35.0	4.2$^{(3)}$	4.17	0.040	2.2 β?$^{(1)}$
NGC 5128 ULX1$^{(3)}$	NGC 5128 X4$^{(3)}$ IXO-76$^{(20)}$ ULX 40$^{(21)}$ CXOUJ132519.9-430317$^{(25)}$	13 25 19.9	-43 03 17.0	4.21$^{(3)}$	8.41	0.115	9.27 γRP$^{(6)}$

Source	Alternative names	RA (J2000)	Dec. (J2000)	d [a] (Mpc)	$N_{\rm H}$ [b] (10^{20} cm^{-2})	E(B-V)[c]	$L_{\rm X}$ [d] (10^{39} erg s^{-1})
NGC 5128 X37(3)*		13 26 26.16	-43 17 15.6	4.21(3)	8.41	0.109	1.96 γRP(3)
NGC 5128 X38(3)*		13 26 56.81	-42 49 53.6	4.21(6)	8.41	0.095	1.97 γRP(3)
NGC 4736 XMM1(4)	NGC 4736 X-1(6) NGC 4736 X-4(26) CXOUJ125050.3+410712(27)	12 50 50.2	+41 07 12.0	4.3(4)	1.44	0.018	17.9 γXI(4)
Holmberg II X-1(1,2)	PGC 23324 ULX1(3) Hol II XMM1(4) Source 28(7) CXOUJ081928.99+704219.4(8) IXO-31(20)	08 19 30.2	+70 42 18.0	4.5(2)	3.41	0.032	17 αX(2)
M83 XMM1(4)	NGC 5236 X11(3) NGC 5236 ULX1(3) Source 24(7) IXO-82(20) CXOUJ133719.8-295349(27)	13 37 19.8	-29 53 49.8	4.7(3)	3.70	0.066	2.8 αXI(4)
M83 XMM2(4)	NGC 5236 X6(3) CXOUJ133659.5-294959(27)	13 36 59.4	-29 49 57.2	4.7(3)	3.70	0.066	3.4 αXI(5)
NGC 5204 X-1(6)	Source 23(7) CXOUJ132938.61+582505.6(8) IXO 77(20)	13 29 38.6	+58 25 06.0	4.8(2)	1.38	0.013	4.4 αX(2)
NGC 5408 X-1(2)	NGC 5408 ULX1(1) NGC 5408 XMM1(4) Source 25(7) J140319.606-412259.572(28)	14 03 19.61	-41 22 59.6	4.8(4)	5.93	0.069	10.9 αXI(4)

Source	Alternative names	RA (J2000)	Dec. (J2000)	d [a] (Mpc)	N_{H} [b] (10^{20} cm^{-2})	E(B-V)[c]	L_{X} [d] (10^{39} erg s^{-1})
NGC 3034 ULX3(1)	CXOUJ095551.2+694044(29)	09 55 51.4	+69 40 44.0	5.2(3)	5.04	0.159	1.34 β?(1)
NGC 3034 ULX4(1)	ULX 14(21) CXOUJ095551.07+694045(29)	09 55 51.1	+69 40 45.0	5.2(3)	5.04	0.159	3.50 β?(1)
NGC 3034 ULX5(1)	ULX 13(21) CXOUJ095550.2+694047(29) M82 X-1(30)	09 55 50.2	+69 40 47.0	5.2(3)	5.04	0.159	40-50 ζX(30)
NGC 3034 ULX6(1)	NGC 3034 X1(3) CXOUJ095546.6+694037(27) CXOM82 J095547.5+694036(31)	09 55 47.5	+69 40 36.0	5.2(3)	5.04	0.160	4.14 β?(1)

Notes: [a]Distance to host galaxy collated via literature search. [b]Absorption column values taken from Dickey & Lockman (1990) using the NASA HEASARC tool WEBPIMMS, and the positions of ULX. [c]Extinction values found using Schlegel, Finkbeiner, & Davis (1998) via NED extinction calculator at ULX positions. [d]Luminosity of ULX, energy band, telescope and comments relating to calculation of luminosity, all of which are discussed in Section 2.2. Energy bands are noted as follows; $\alpha = 0.3 - 10.0$ keV, $\beta = 0.5 - 10.0$ keV, $\gamma = 0.3 - 8.0$ keV, $\delta = 0.5 - 8.0$ keV, $\epsilon = 0.3 - 7.0$ keV & $\zeta =$ bolometric luminosity. Telescope notation is as follows; C - *Chandra*, R - *ROSAT*, X - *XMM-Newton*. *Removed from sample due to lack of *Chandra* and/or *HST* data, see Section 2.3 for further details. Numbers shown in superscript relate to the following references: (1)Liu & Mirabel (2005), (2)Stobbart et a. (2006), (3)Liu & Bregman (2005), (4)Winter et al. (2006), (5)Trudolyubov (2008), (6)Roberts & Warwick (2000), (7)Feng & Kaaret (2005), (8)Swartz et al. (2004), (9)Schlegel et al. (1998), (10)Trinchieri et al. (1988), (11)Grimm et al. (2005), (12)Read et al. (1997), (13)Stobbart et al. (2004), (14)Roberts et al. (2004), (15)Kong (2003), (16)Humphrey et al. (2003), (17)Vogler & Pietsch(1999), (18)Radecke (1997), (19)Immler & Wang (2001), (20)Colbert & Ptak (2002), (21)Ptak et al. (2006), (22)Bauer et al. (2001), (23)Schlegel & Pannuti (2003), (24)Yukita et al. (2007), (25)Kraft et al. (2001), (26)Eracleous et al. (2002), (27)Colbert et al. (2004), (28)Kaaret et al. (2003), (29)Kong et al. (2007), (30)Stronmayer & Mushotzky (2003), (31)Griffiths et al. (2000).

We find that our sample of ultraluminous X-ray sources vary in foreground Galactic absorption in the X-ray and extinction in the optical over the range 1.4 – 55.6 $\times 10^{20}$ cm^{-2} and 0.01 – 1.50 ($E(B-V)$) respectively. This covers a vast range as some of these objects reside behind the Galactic plane (e.g. Circinus galaxy). Table 2.1 also indicates that the ULXs residing within 5 Mpc cover the majority of the ULX X-ray luminosity range ($L_{\rm X} \sim 1 \times 10^{39}$ – a few $\times 10^{40}$ erg s^{-1}).

The X-ray luminosities listed within this table are taken from the references denoted in superscript. As the data is collated from published results we highlight inconsistencies in their calculation. Many of the luminosities listed are observed, although some are intrinsic/de-absorbed (identified by 'I'). The luminosities presented above include values derived from observations using three separate X-ray telescopes (*ROSAT* – R, *Chandra* – C and *XMM-Newton* – X), with detectors that are sensitive to differing energy ranges within the X-ray spectrum.

Liu & Bregman (2005) use the *ROSAT* archive in combination with the online tool WEBPIMMS[3] to extrapolate a luminosity over the 0.3 – 8.0 keV energy range. In each case they use a photon index of 1.7 and Galactic N_H. Luminosities calculated using WEBPIMMS are marked with a 'P'. The authors Swartz et al. (2004), Humphrey et al. (2003) and Bauer et al. (2001) each use data from the *Chandra* X-ray space telescope to provide luminosities over the ranges 0.5 – 8.0, 0.3 – 7.0 and 0.5 – 10.0 keV ranges respectively. Some authors provide luminosities calculated using observations from the *XMM-Newton* telescope including Winter et al. (2006), Stobbart et al. (2006) and Feng & Kaaret (2005), who each calculate luminosities over the 0.3 – 10.0 keV. Truolyubov (2008) also uses *XMM-Newton*, but considers only the 0.3 – 7.0 keV band pass, whilst Strohmayer & Mushotzky (2003) calculate the bolometric luminosity for each source. Finally, Liu & Mirabel (2005) collated information from published works and so provide details of the observed peak luminosity over an identified range individual to each source (all luminosity taken from this work were calculated over the 0.5 – 10.0 keV energy range).

We searched the *Chandra* archive and *Hubble Legacy Archive* (HLA) for publicly available observations of each source (data retrieved in August/September 2008). This reveals an absence of data in either one or both archives for 14 of our sample. Each of these

---

[3] `http://heasarc.gsfc.nasa.gov/Tools/w3pimms.html`

objects are marked with a '*' in Table 2.1, and we do not discuss them further within this chapter.

2.3 Data reduction

We collated and downloaded *Chandra* observations for each of our ULX sample. Wherever more than one observation was available in the public archive, we chose the most recent containing that source. In the case of transient ULXs this was not always the most recent observation of the field. Data was reduced using CIAO version 3.4.1.1, and the standard *Chandra* threads[4]. Each observation was checked to correct for any known aspect offset (which are applied wherever they arise[5]), and accurate source positions are found using the tool *WAVDETECT*. The *Chandra* observation IDs of the downloaded data are listed in Table 2.2, along with the positions (and associated 3 σ errors) for each source. At this point we also note the presence of the small intrinsic astrometric uncertainty in most *Chandra* observations, an error of 0.5 arcsec, with an error of 0.6 arcsec in ACIS-I fields (90 % confidence region for absolute positional accuracy[6]). This is incorporated into all positional error calculations, but is not included in Table 2.2.

With the inception of the HLA[7], designed to optimise the science from the *Hubble Space Telescope*, we are able to collate pre-processed data. These data sets are produced using the standard HST pipeline products, and are combined using the IRAF task *MULTIDRIZZLE* [8]. Each field has been astrometrically corrected (whenever possible), by matching sources in the field to one or more of three catalogues; Sloan Digital Sky Survey (SDSS), Guide Star Catalogue 2 (GSC2) and 2MASS in order of preference (with 2MASS used to mainly to assess the quality of the solution). Finally all observations are aligned such that North is up.

Information provided on the HLA pages states that this approach is only possible in ~ 80 per cent of ACS - WFC fields, due to crowding, lack of matching sources or sources

---

[4] Standard *Chandra* threads can be found at `http://asc.harvard.edu/ciao`.

[5] Aspect correction can be found using `http://cxc.harvard.edu/cal/ASPECT/fix_offset/fix_offset.cgi`

[6] Details of *Chandra* absolute astrometric accuracy can be found at `http://cxc.harvard.edu/cal/ASPECT/celmon/index.html`

[7] details of the HLA archive can be found at `http://hla.stsci.edu`.

[8] see *MULTIDRIZZLE* website, `http://www.stsci.edu/~koekemoe/multidrizzle`, for more details

Table 2.2: *Chandra* observations details and detected source positions

Source	Observation	Source position^b	
	ID^a	RA	DEC
NGC 598 ULX1	6376	01 33 50.8957 ± 0.0005	+30 39 36.763 ± 0.006
NGC 55 ULX1	2255	00 15 28.8912 ± 0.0007	–39 13 18.772 ± 0.007
NGC 4190 X1	8212	12 13 45.273 ± 0.004	+36 37 54.656 ± 0.005
NGC 253 ULX1	969	00 47 33.997 ± 0.001	–25 16 36.35 ± 0.02
NGC 253 ULX2	3931	00 47 32.9659 ± 0.0004	–25 17 48.917 ± 0.006
NGC 253 ULX3	3931	00 47 33.437 ± 0.001	–25 17 21.99 ± 0.02
NGC 253 XMM6	3931	00 47 42.7655 ± 0.0008	–25 15 02.153 ± 0.008
M81-X-6	735	09 55 32.9500 ± 0.0009	+69 00 32.729 ± 0.005
Hol IX	4752	09 57 53.292 ± 0.003	+69 03 48.07 ± 0.04
NGC 4395 ULX1	402	12 26 01.439 ± 0.006	+33 31 30.99 ± 0.08
NGC 1313 X-1	2950	03 18 20.03 ± 0.09	–66 29 11.095 ± 0.009
NGC 1313 X-2	3550	03 18 22.241 ± 0.001	–66 36 03.40 ± 0.01
IC 342 X-1	7069	03 45 55.6165 ± 0.0009	+68 04 55.413 ± 0.005
IC 342 X-2	2936	03 46 15.734 ± 0.007	+68 11 12.65 ± 0.06
IC 342 ULX2	7069	03 46 48.523 ± 0.008	+68 05 46.83 ± 0.04
IC 342 X-6	7069	03 46 57.36 ± 0.01	+68 06 18.80 ± 0.07
Circinus ULX1	356	14 13 12.218 ± 0.001	–65 20 13.854 ± 0.008
Circinus ULX3	356	14 13 10.255 ± 0.003	–65 20 17.97 ± 0.02
Circinus ULX4	356	14 13 10.3299 ± 0.0009	–65 20 22.445 ± 0.001
NGC 2403 X-1	2014	07 36 25.568 ± 0.002	+65 35 39.875 ± 0.006
NGC 5128 ULX1	316	13 25 19.834 ± 0.002	–43 03 17.20 ± 0.03
NGC 4736 XMM1	808	12 50 50.3261 ± 0.0009	+41 07 12.19 ± 0.01
Holmberg II X-1	1564	08 19 29.004 ± 0.002	+70 42 19.081 ± 0.009
M83 XMM1	793	13 37 19.8037 ± 0.0009	–29 53 48.80 ± 0.01
M83 XMM2	793	13 36 59.452 ± 0.002	–29 49 59.21 ± 0.02
NGC 5204 X-1	3943	13 29 38.612 ± 0.003	+58 25 05.55 ± 0.02
NGC 5408 X-1	4557	14 03 19.611 ± 0.001	–41 22 58.65 ± 0.01
NGC 3034 ULX3	8505	09 55 51.326 ± 0.003	+69 40 43.65 ± 0.02
GC 3034 ULX4	2933	09 55 51.016 ± 0.002	+69 40 45.02 ± 0.01
NGC 3034 ULX5	8505	09 55 50.1660 ± 0.0008	+69 40 46.472 ± 0.004
NGC 3034 ULX6	379	09 55 47.460 ± 0.006	+69 40 36.28 ± 0.03

Notes:^{a} *Chandra* observational IDs of the data used in finding accurate positions of each source. ^{b}Position of source obtained using the CIAO tool *WAVDETECT*.

that are unresolved from the ground (and therefore not present in the catalogues), with no mention of the provision for other detectors. To gain a good astrometric corrections of these fields using this method, it is important to have a number of sources in the field. We therefore opt to use observations with large fields of view wherever possible, and so select the *HST* instrument and detector based on these criteria and select observations in available bands from the Advanced Camera for Surveys (ACS) - Wide Field Camera (WFC), the Wide Field Planetary Camera 2 (WFPC2) and ACS - High Resolution Camera (HRC) in order of preference, to maximise the possibility of good astrometry.

Another consideration that impacts on our sample is the variability which may occur within these systems, variability would affect the emission observed in the optical and UV bands. From the X-ray spectra of these systems, we see variability on both short, intra-observational time scales (e.g. Heil et al. 2009), to longer inter-observational time scales of hours to years (e.g. Fabbiano 2004). Such variability is likely to affect the optical and UV emission, as seen in Galactic X-ray binary systems (e.g. Charles & Coe 2006).

Roberts et al. (2008) reported on near simultaneous (within 8 days) tri-band observations of NGC 5055 X-2, in the F300W, F450W and F606W bands. Photometric analysis revealed that $U-B$ colours were too blue for and OB type star, whilst the $B-V$ colours were too red. This combination, along with the 8 day offset led to the suggestion that the cause may be rooted in variable non-stellar processes. The authors postulate that the unusual colours may be attributed to the variability in the accretion disc of the system. Conversely, when the authors compared their observations and analysis of the optical counterpart of IC 342 X-1 to that performed by Feng & Kaaret (2008) on observations taken three months earlier, they found this object to be remarkably stable.

We fold these considerations into our observation selection criteria, awarding observations of multiple bands over short time scales higher priority. When this was not possible, bands were selected from multiple observations IDs, in order to give a fuller view of the source. In these cases we must seriously consider the potential impact of optical variability (see Section 2.5.5). The observation IDs and filter band information for selected observations throughout our analysis of these systems are listed in Table 2.3.

In addition to those observations retrieved from the HLA, an observation of NGC 4190 X-1 was carried out in January of 2008 (proposal ID: 11012; PI: Roberts). This data has not currently been processed by the HLA pipeline, and so was reduced using tools from the IDL Astronomy Users Library[9]. This package allows the user to combine the separate detectors into a 'batwing' image, whilst drizzling is performed to account for cosmic rays.

2.4 Identification of counterparts

Although astrometric corrections are already performed by HLA pipeline, this only applies to $\sim$ 80 per cent of processed observations (see HLA for for more information). For our analysis to be successful we require the highest levels of accuracy in astrometry in order to minimise errors. We therefore check and improve astrometric corrections of each field using the the IRAF tools *CCFIND*, *CCMAP* and *CCSETWCS*, in combination with either the 2MASS or USNO 2.0 catalogues (depending on number of sources available in the field). This process also calculates the average astrometric (3 σ) error across the field. These errors are combined in quadrature with both the astrometry and positional errors from *Chandra* to provide the resulting error regions for each individual ULX listed in Table 2.3.

We find that 13 of the 96 observations used in our analysis do not contain enough catalogued objects in the optical/ultraviolet fields of view to allow for accurate astrometry corrections. In these cases we compare the field to an alternative corrected observation in a similar waveband. We match sources in these observations and perform relative astrometry corrections using the IRAF tools *IMEXAM* and *GEOMAP*. The tool *GEOXYTRAN* is then used to translate the position of the ULX to the relative field co-ordinates. For example, the ACS - HRC provided much greater detail of the optical/UV fields around the ULX NGC 2403 X-1, but the restricted field of view of this detector results in the lack of catalogued objects. No objects are visible from the 2MASS catalogue whilst only one for the USNO catalogue was visible. We therefore perform relative astrometry to the closest corrected waveband image, which in this case is F435W.

---

[9] `http://idlastro.gsfc.nasa.gov`

Table 2.3: *HST* observations details and corrected source magnitudes

Source	Observation ID	Instrument	Filter	Error RA$^{a(i)}$	Error Dec$^{a(ii)}$	C/P ID^{b}	Vegamag^{c}
NGC 598 ULX1	06038_02	WFPC2	F170W	0.791	0.813	0	–
	06038_02	WFPC2	F336W	0.813	0.879		–
	06038_02	WFPC2	F439W	0.909	0.905		–
	06038_02	WFPC2	F555W	0.775	0.783		–
	05464_05	WFPC2	F814W	0.683	0.712		–
NGC 55 ULX1	09765_03	ACS−WFC	F606W	0.708	0.713	1	23.2 ± 0.3
	09765_03	ACS−WFC	F814W	0.708	0.660		23.1 ± 0.5
NGC 4190 X-1	11012_02	WFPC2	F300W	0.551	0.551	1	25 ± 6
	11012_02	WFPC2	F450W	0.575	0.575		24 ± 2
	11012_02	WFPC2	F606W	0.558	0.558		25 ± 2
	11012_02	WFPC2	F300W	0.551	0.551	2	–
	11012_02	WFPC2	F450W	0.575	0.575		25 ± 3
	11012_02	WFPC2	F606W	0.558	0.558		27 ± 5
NGC 253 ULX1	05211_01	WFPC2	F336W	0.625	0.714	1	–
	10915_98	ACS−WFC	F475W	0.608	0.628		26 ± 2
	05211_01	WFPC2	F555W	0.770	1.089		–
	10915_98	ACS−WFC	F606W	0.607	0.621		–
	10915_98	ACS−WFC	F814W	0.597	0.619		–
	05211_01	WFPC2	F336W	0.625	0.714	2	–
	10915_98	ACS−WFC	F475W	0.608	0.628		25 ± 2
	05211_01	WFPC2	F555W	0.770	1.089		–
	10915_98	ACS−WFC	F606W	0.607	0.621		23.5 ± 0.7
	10915_98	ACS−WFC	F814W	0.597	0.621		–
NGC 253 ULX2	10915_98	ACS−WFC	F475W	0.608	0.627	1	21.7 ± 0.3
	10915_98	ACS−WFC	F606W	0.607	0.621		20.8 ± 0.2
	10915_98	ACS−WFC	F814W	0.597	0.619		19.6 ± 0.1
NGC 253 ULX3	05211_01	WFPC2	F336W	0.625	0.714	1	–
	10915_98	ACS−WFC	F475W	0.608	0.627		–
	06440_01	WFPC2	F502N	0.706	0.865		21 ± 5
	05211_01	WFPC2	F555W	0.592	1.089		–
	10915_98	ACS−WFC	F606W	0.607	0.621		–
	10915_98	ACS−WFC	F814W	0.597	0.619		–
NGC 253 XMM6	10915_97	ACS−WFC	F475W	0.600	0.626	1	26 ± 2
	10915_97	ACS−WFC	F606W	0.594	0.621		25 ± 1
	10915_97	ACS−WFC	F814W	0.586	0.596		23 ± 4
	10915_97	ACS−WFC	F475W	0.600	0.626	2	–
	10915_97	ACS−WFC	F606W	0.594	0.621		25.3 ± 0.8
	10915_97	ACS−WFC	F814W	0.586	0.596		23.6 ± 0.9
	10915_97	ACS−WFC	F475W	0.600	0.626	3	–
	10915_97	ACS−WFC	F606W	0.594	0.621		–
	10915_97	ACS−WFC	F814W	0.586	0.596		23 ± 3

Source	Observation ID	Instrument	Filter	Error RA$^{a(i)}$	Error Dec$^{a(ii)}$	C/P ID^{b}	Vegamag^{c}
NGC 253 XMM6	10915_97	ACS−WFC	F475W	0.600	0.626	4	–
	10915_97	ACS−WFC	F606W	0.594	0.621		–
	10915_97	ACS−WFC	F814W	0.586	0.596		24 ± 2
	10915_97	ACS−WFC	F475W	0.600	0.626	5	–
	10915_97	ACS−WFC	F606W	0.594	0.621		–
	10915_97	ACS−WFC	F814W	0.586	0.596		24 ± 1
M81 X-6	06139_01	WFPC2	F336W	0.647	0.560	1	22 ± 2
	10584_18	ACS−WFC	F435W	0.645	0.556		23.7 ± 0.1
	09073_01	WFPC2	F555W	0.647	0.557		24 ± 1
	10584_18	ACS−WFC	F606W	0.647	0.557		23.1 ± 0.7
	09073_01	WFPC2	F814W	0.648	0.561		21 ± 3
Hol IX X-1	09796_a3	ACS−HRC	F330W	0.631	0.556	1	20.6 ± 0.3
	09796_03	ACS−WFC	F435W	0.623	0.547		22.3 ± 0.3
	09796_03	ACS−WFC	F555W	0.554	0.519		22.5 ± 0.4
	09796_03	ACS−WFC	F814W	0.730	0.545		22.2 ± 0.3
NGC 4395 ULX1	09774_ab	WFPC2	F336W	0.770	0.687	1	22 ± 1
	09774_0b	ACS−WFC	F435W	0.502	0.579		CG
	09774_0b	ACS−WFC	F555W	0.502	0.579		CG
	09774_0b	ACS−WFC	F814W	0.502	0.577		CG
NGC 1313 X-1	09796_a1	ACS−HRC	F330W	0.660	0.649	1	22 ± 1
	09774_05	ACS−WFC	F435W	0.657	0.649		23.6 ± 1.0
	09774_05	ACS−WFC	F555W	0.667	0.610		24 ± 1
	10210_06	ACS−WFC	F606W	0.539	0.524		23.7 ± 0.8
	09774_05	ACS−WFC	F814W	0.702	0.597		24 ± 1
	09796_a1	ACS−HRC	F330W	0.660	0.649	2	24 ± 3
	09774_05	ACS−WFC	F435W	0.657	0.649		24 ± 1
	09774_05	ACS−WFC	F555W	0.667	0.610		25 ± 3
	10210_06	ACS−WFC	F606W	0.539	0.524		24.1 ± 1.0
	09774_05	ACS−WFC	F814W	0.702	0.597		25 ± 5
NGC 1313 X-2	09796_a2	ACS−HRC	F330W	1.078	0.936	1	21.6 ± 0.8
	09796_02	ACS−WFC	F435W	0.612	0.635		23.1 ± 0.4
	09796_02	ACS−WFC	F555W	0.671	0.621		23.3 ± 0.5
	09796_02	ACS−WFC	F814W	0.681	0.629		23.5 ± 0.6
	09796_a2	ACS−HRC	F330W	1.078	0.936	2	–
	09796_02	ACS−WFC	F435W	0.612	0.635		–
	09796_02	ACS−WFC	F555W	0.671	0.621		24.1 ± 0.7
	09796_02	ACS−WFC	F814W	0.681	0.629		–
IC 342 X-1	10579_b3	ACS−HRC	F330W	0.761	0.742	1	–
	10768_02	ACS−WFC	F435W	0.551	0.539		23.1 ± 1.0
	10768_02	ACS−WFC	F555W	0.541	0.532		22.3 ± 0.6
	10579_13	ACS−WFC	F606W	0.539	0.538		21.9 ± 0.4
	10768_02	ACS−WFC	F658M	0.547	0.537		22 ± 2
	10768_02	ACS−WFC	F814W	0.544	0.529		21.1 ± 0.2

Source	Observation ID	Instrument	Filter	Error RA$^{a(i)}$	Error Dec$^{a(ii)}$	C/P ID^{b}	Vegamag^{c}
IC 342 X-1	10579_b3	ACS−HRC	F330W	0.761	0.742	2	–
	10768_02	ACS−WFC	F435W	0.551	0.539		24 ± 2
	10768_02	ACS−WFC	F555W	0.541	0.532		24 ± 2
	10579_13	ACS−WFC	F606W	0.539	0.538		24 ± 2
	10768_02	ACS−WFC	F658M	0.547	0.537		–
	10768_02	ACS−WFC	F814W	0.544	0.529		24 ± 1
IC 342 X-2	10579_a5	ACS−HRC	F330W	0.555	0.611	1	–
	10579_15	ACS−WFC	F435W	0.551	0.607		25 ± 1
	10579_15	ACS−WFC	F606W	0.564	0.617		–
	10579_a5	ACS−HRC	F330W	0.555	0.611	2	–
	10579_15	ACS−WFC	F435W	0.551	0.607		24 ± 2
	10579_15	ACS−WFC	F606W	0.564	0.617		–
IC 342 ULX2	06367_03	WFPC2	F555W	0.667	0.672	0	–
	05446_0j	WFPC2	F606W	0.686	0.867		–
	06367_03	WFPC2	F656N	0.616	0.669		–
	06367_03	WFPC2	F675W	0.656	0.714		–
	06367_03	WFPC2	F814W	0.610	0.667		–
IC 342 X-6	08199_01	WFPC2	F555W	0.715	0.741	1	23.4 ± 0.8
	05446_0j	WFPC2	F606W	0.748	0.776		22 ± 1
	08199_01	WFPC2	F814W	0.662	0.747		22.6 ± 0.6
Circinus ULX1	07273_01	WFPC2	F502N	0.553	0.566	1	–
	07273_01	WFPC2	F547M	0.631	0.637		–
	06359_08	WFPC2	F606W	0.559	0.569		20 ± 6
	07273_01	WFPC2	F656N	0.590	0.618		–
	07273_01	WFPC2	F814W	0.549	0.561		–
Circinus ULX3	09379_64	ACS−HRC	F330W	0.554	0.568	0	–
	07273_01	WFPC2	F502N	0.553	0.566		–
	07273_01	WFPC2	F547M	0.631	0.678		–
	06359_08	WFPC2	F606W	0.559	0.569		–
	07273_01	WFPC2	F656N	0.590	0.618		–
	07273_01	WFPC2	F814W	0.549	0.561		–
Circinus ULX4	09379_64	ACS−HRC	F330W	0.554	0.568	1	15 ± 2
	07273_01	WFPC2	F502N	0.553	0.566		–
	07273_01	WFPC2	F547M	0.631	0.678		–
	06359_08	WFPC2	F606W	0.559	0.569		–
	07273_01	WFPC2	F656N	0.590	0.618		–
	07273_01	WFPC2	F814W	0.549	0.561		–
	09379_64	ACS−HRC	F330W	0.554	0.568	2	16 ± 2
	07273_01	WFPC2	F502N	0.553	0.566		–
	07273_01	WFPC2	F547M	0.631	0.678		–
	06359_08	WFPC2	F606W	0.559	0.569		–
	07273_01	WFPC2	F656N	0.590	0.618		15 ± 1
	07273_01	WFPC2	F814W	0.549	0.561		–

Source	Observation ID	Instrument	Filter	Error RA$^{a(i)}$	Error Dec$^{a(ii)}$	C/P ID^{b}	Vegamag^{c}
Circinus ULX4	09379_64	ACS−HRC	F330W	0.554	0.568	3	–
	07273_01	WFPC2	F502N	0.553	0.566		–
	07273_01	WFPC2	F547M	0.631	0.678		15.3 ± 0.3
	06359_08	WFPC2	F606W	0.559	0.569		–
	07273_01	WFPC2	F656N	0.590	0.618		16 ± 3
	07273_01	WFPC2	F814W	0.549	0.561		–
NGC 2403 X-1	10579_a3	ACS−HRC	F330W	0.649	0.700	1	23 ± 2
	10579_03	ACS−WFC	F435W	0.649	0.700		25 ± 1
	10579_03	ACS−WFC	F606W	0.637	0.640		24.5 ± 0.7
NGC 5128 ULX1	06789_a1	WFPC2	F555W	0.808	0.844	1	–
	10260_12	ACS−WFC	F606W	0.720	0.731		23.7 ± 0.7
	06789_a1	WFPC2	F814W	0.815	0.815		–
NGC 4736 XMM1	10402_06	WFPC2	F336W	0.846	0.768	0	–
	09042_80	WFPC2	F450W	0.807	0.816		–
	10402_06	WFPC2	F555W	0.830	0.774		–
	09042_80	WFPC2	F814W	0.739	0.693		–
Hol II X-1	10522_03	ACS−WFC	F502N	0.583	0.540	1	–
	10522_03	ACS−WFC	F550M	0.540	0.525		21.5 ± 0.3
	10522_03	ACS−WFC	F658M	0.540	0.525		–
	10522_03	ACS−WFC	F660N	0.628	0.528		21 ± 2
	10522_03	ACS−WFC	F814W	0.540	0.525		21.5 ± 0.2
M83 XMM1	10579_a1	ACS−HRC	F330W	0.548	0.539	1	–
	10579_11	ACS−WFC	F435W	0.546	0.538		26 ± 3
	10579_11	ACS−WFC	F606W	0.560	0.564		25 ± 2
M83 XMM2	09774_af	WFPC2	F336W	0.763	0.772	0	–
	09774_0f	ACS−WFC	F435W	0.619	0.666		CG
	09774_0f	ACS−WFC	F555W	0.591	0.606		CG
	09774_0f	ACS−WFC	F814W	0.582	0.669		CG
NGC 5204 X-1	09370_01	ACS−WFC	F220W	1.043	1.300	1	19.8 ± 0.5
	09370_01	ACS−WFC	F435W	1.066	1.086		22.37 ± 0.10
	08601_39	WFPC2	F606W	0.910	0.939		22.3 ± 0.8
	08601_39	WFPC2	F814W	0.919	0.874		23 ± 1
	09370_01	ACS−WFC	F220W	1.043	1.300	2	19.5 ± 0.4
	09370_01	ACS−WFC	F435W	1.066	1.086		20.8 ± 0.1
	08601_39	WFPC2	F606W	0.910	0.939		21.0 ± 0.8
	08601_39	WFPC2	F814W	0.919	0.874		20 ± 2
NGC 5408 X-1	08601_41	WFPC2	F606W	0.544	0.604	1	22.2 ± 0.6
	08601_41	WFPC2	F814W	0.544	0.603		23.1 ± 3
NGC 3034 ULX3	10776_24	ACS−WFC	F435W	0.667	0.600	0	–
	10776_24	ACS−WFC	F555W	0.636	0.594		–
	10776_24	ACS−WFC	F658M	0.602	0.588		–
	10776_24	ACS−WFC	F814W	0.606	0.605		–

Source	Observation ID	Instrument	Filter	Error RA$^{a(i)}$	Error Dec$^{a(ii)}$	C/P ID^b	Vegamag^c
NGC 3034 ULX4	10776_24	ACS−WFC	F435W	0.667	0.600	0	–
	10776_24	ACS−WFC	F555W	0.636	0.596		–
	10776_24	ACS−WFC	F658M	0.601	0.587		–
	10776_24	ACS−WFC	F814W	0.606	0.605		–
NGC 3034 ULX5	10776_24	ACS−WFC	F435W	0.667	0.600	1	23 ± 2
	10776_24	ACS−WFC	F555W	0.635	0.595		21.8 ± 0.8
	10776_24	ACS−WFC	F658M	0.601	0.587		–
	10776_24	ACS−WFC	F814W	0.606	0.605		–
	10776_24	ACS−WFC	F435W	0.667	0.600	2	21.9 ± 0.7
	10776_24	ACS−WFC	F555W	0.635	0.595		–
	10776_24	ACS−WFC	F658M	0.601	0.587		–
	10776_24	ACS−WFC	F814W	0.606	0.605		–
NGC 3034 ULX6	10776_24	ACS−WFC	F435W	0.745	0.686	0	–
	10776_24	ACS−WFC	F555W	0.716	0.683		–
	10776_24	ACS−WFC	F658M	0.686	0.675		–
	10776_24	ACS−WFC	F814W	0.691	0.690		–

Notes: ^{a}Combined error of the (*i*) right ascension and (*ii*) declination of the ULX. ^{b}Counterpart identification number, 0 is listed if no individual counterpart is available within the error region. ^{c}Absorption and Galactic extinction corrected Vega magnitudes of the counterpart for the given filter.

In the case of our most recent observation, NGC 4190, we find that we are unable to correct the astrometry of any field by matching to known catalogues. We therefore opt to take advantage of the increased field of view afforded us by SDSS, collecting an image of this region from their archive. The astrometry of this image is corrected using the 2MASS catalogue, and relative astrometry performed on each of the *HST* images. We note that where relative astrometry is required, the additional errors arising from this are also folded into our calculations. The resulting positional errors for all ULXs can be found in Table 2.3.

Elliptical error regions are plotted in all processed *HST* observations of the ULX fields, which can be seen in Figure 2.2. For each ULX in our sample we present a 25 × 25 arcsecs colour image (tri-colour wherever possible), and a finding chart (6 × 6 arcsecs) to mark the positions of each potential optical counterpart. To construct the colour images we select available wavebands for each part of the optical/UV spectrum. We use filter bands ranging from F656N to F814W to represent the red end of our range, we apply filter bands F475W to F606W for the green band, whilst F220W – F450W are blue. In each case where more than one band is available, we opt for a band that gives the clearest view of any potential counterparts. In some cases we find at least one colour band may not be available and so some are only in one or two bands. This work reveals that eight regions contain no optical counterparts to ULXs. Of the 23 remaining sources, 13 have a unique counterpart, whilst 10 have between two and five objects present within the positional error ellipse.

In those fields where counterparts are identified, we collate Vega magnitude zero points (Zpt) to allow for the derivation of *HST* filter dependent Vega magnitudes of each source. This type of magnitude is a synthetic system in which the magnitude is calculated comparatively to that of the star Vega. In this system, the magnitude of the star Vega is defined to be exactly zero in all *standard* filters. For observations made using the ACS instruments, we are able to take these values directly from Sirianni et al. (2005). In the case of observations taken by WFPC2, the HLA pipeline converts the units contained within the science field to electron s^{-1} (like ACS) rather than DN (Data Number), and hence the tabulated zero points given in the *HST* Data Handbook for WFPC2[10] must also be converted. This can be done simply by using a correction for the gain[11], using $Zpt =$ tabulated zero point $+2.5 \times log$(gain).

Aperture photometry is performed on all possible counterparts using GAIA and the collated zero points to find the Vega magnitude in each available filter band. Aperture corrections are applied to all fields, irrespective of instrument and detector, following the procedures laid down by Sirianni et al. (2005) (although values of corrections for WPFC2 observations are taken from the *HST* WFPC2 cookbook[12]).

---

[10] `http://www.stsci.edu/hst/wfpc2/Wfpc2_dhb/wfpc2_ch52.html#1933986`

[11] `http://www.stsci.edu/hst/wfpc2/Wfpc2_hand_current/ch4_ccd14.html#440723`

[12] `http://www.stsci.edu/hst/wfpc2/Wfpc2_dhb/wfpc2_ch52.html#1933986`

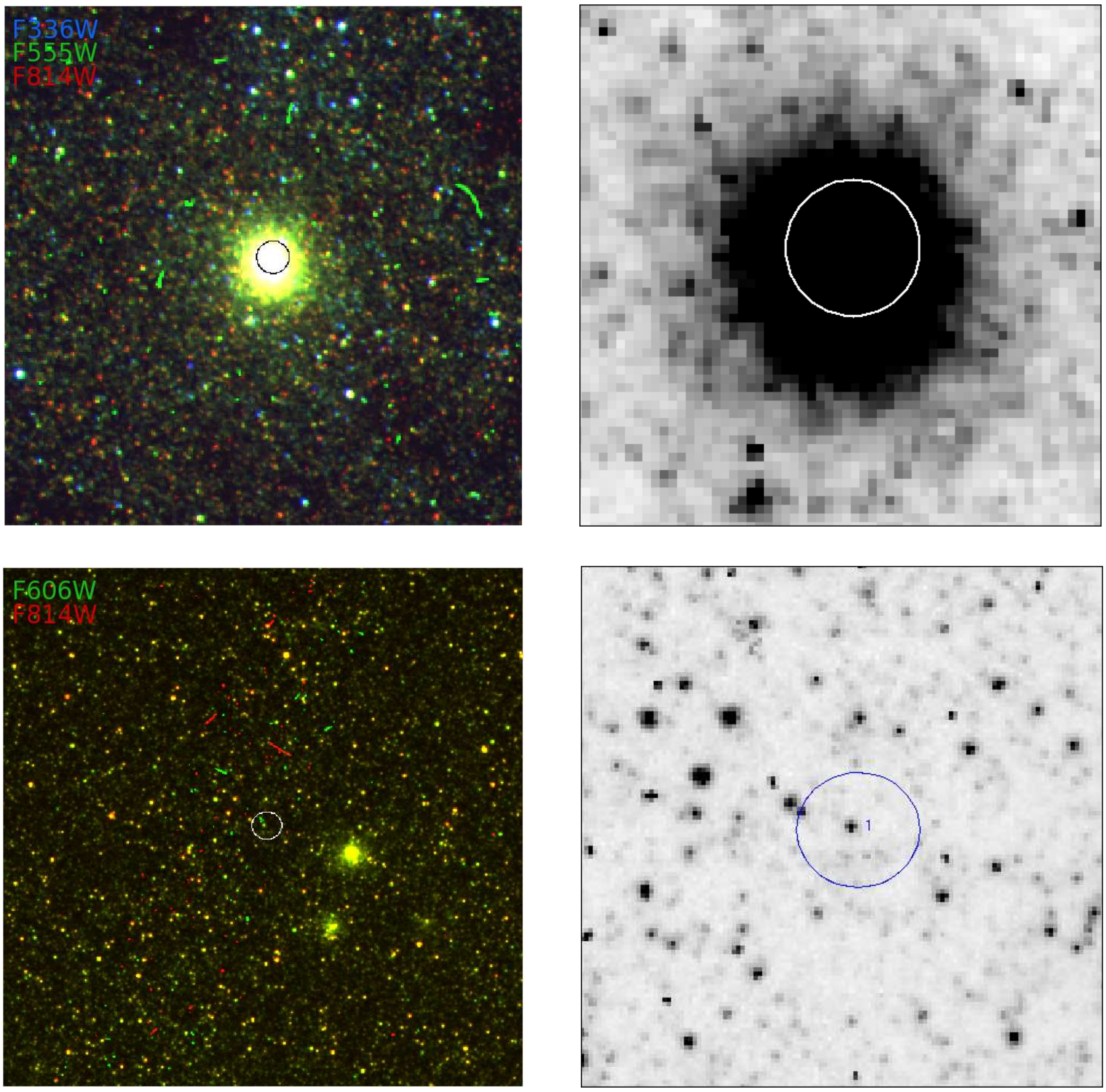

Figure 2.2: *HST* colour images (*left*) and finding charts (*right*) of the ULX locations. *Left panel*: Colour images are 25 × 25 arcseconds in size, overplotted with positional error ellipse and constructed using the following filter band pass where available; blue = F220W – F450W, green = F475W – F606W and red = F656N – F814W. *Right panel*: Finding charts are made from only one individual band, showing a regions 6 × 6 arcseconds, overplotted with the combined positional error ellipse for that band (specific wave bands given in brackets after source name, below). Potential counterparts are highlighted numerically with associated magnitudes given in Table 2.3. *Specific notes*: displayed ULX regions are, from top to bottom, NGC 598 ULX1 (F555W) & NGC 55 ULX1 (F814W).

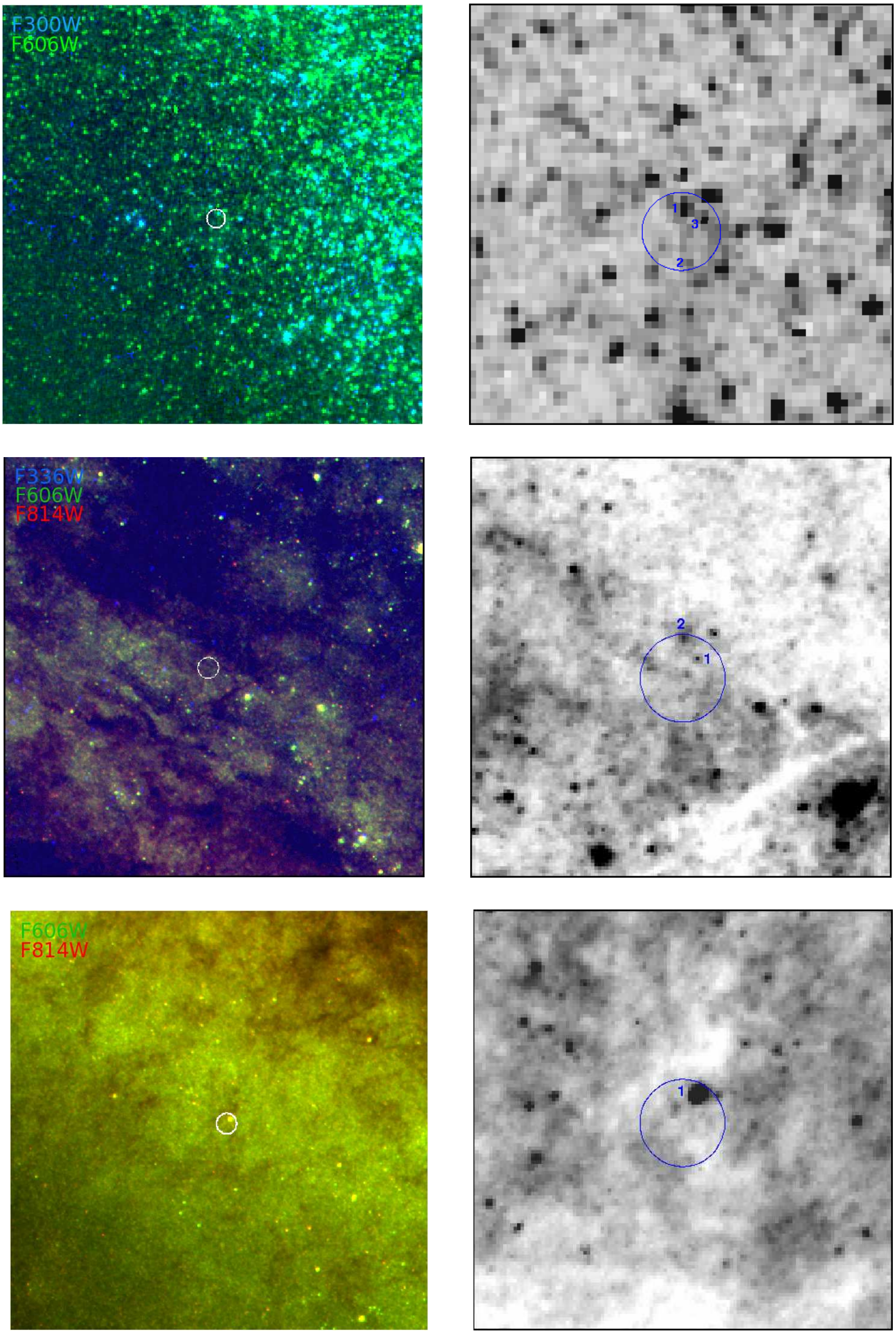

Figure 2.2: *continued, pg. 2* - Specific notes: displayed ULX regions are, from top to bottom, NGC 4190 X-1 (F606W), NGC 253 ULX 1 (F475W) & NGC 253 ULX2 (F606W).

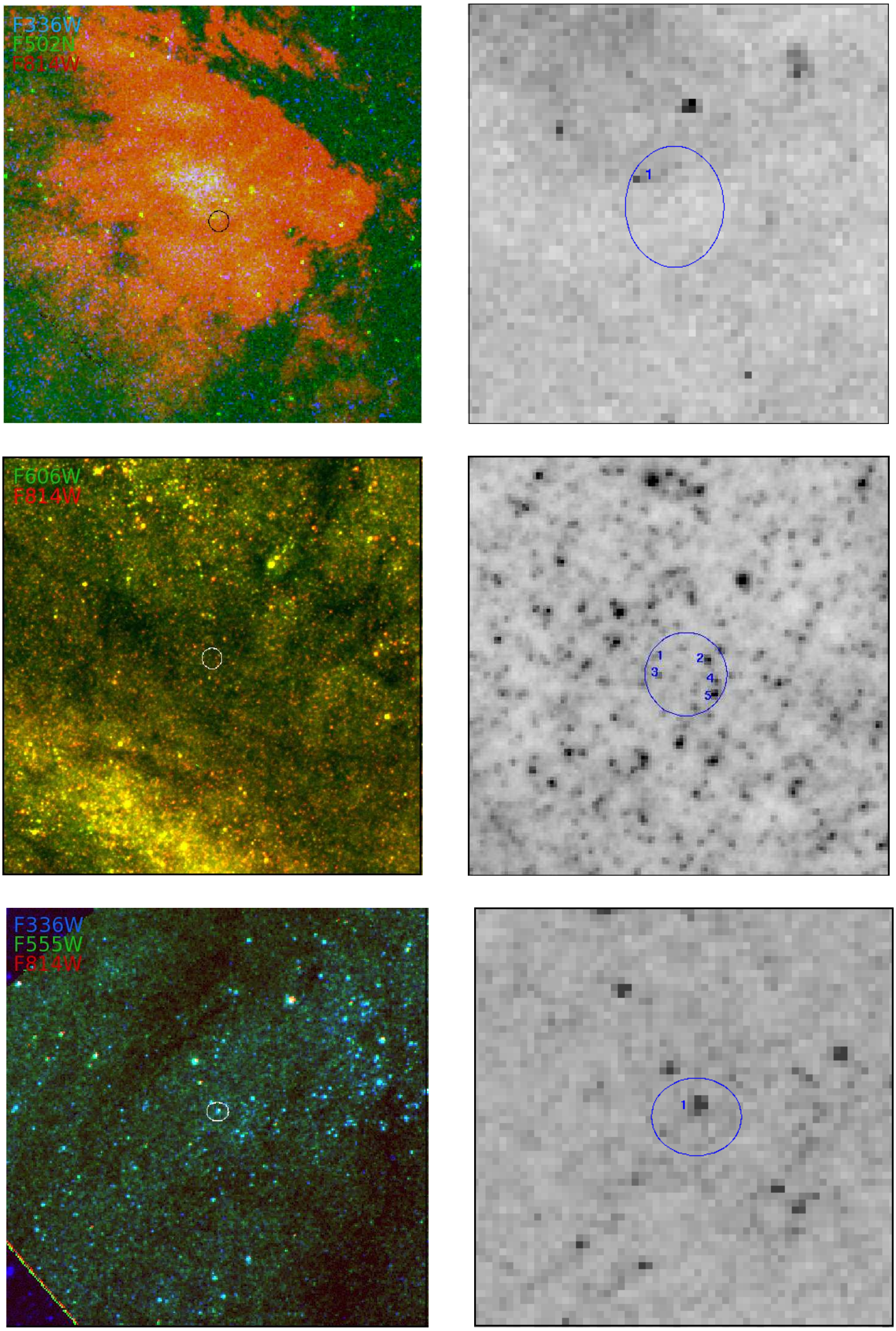

Figure 2.2: *continued, pg. 3* - Specific notes: displayed ULX regions are, from top to bottom, NGC 253 ULX3 (F502N), NGC 253 XMM6 (F814W) & M81 X-6 (F555W).

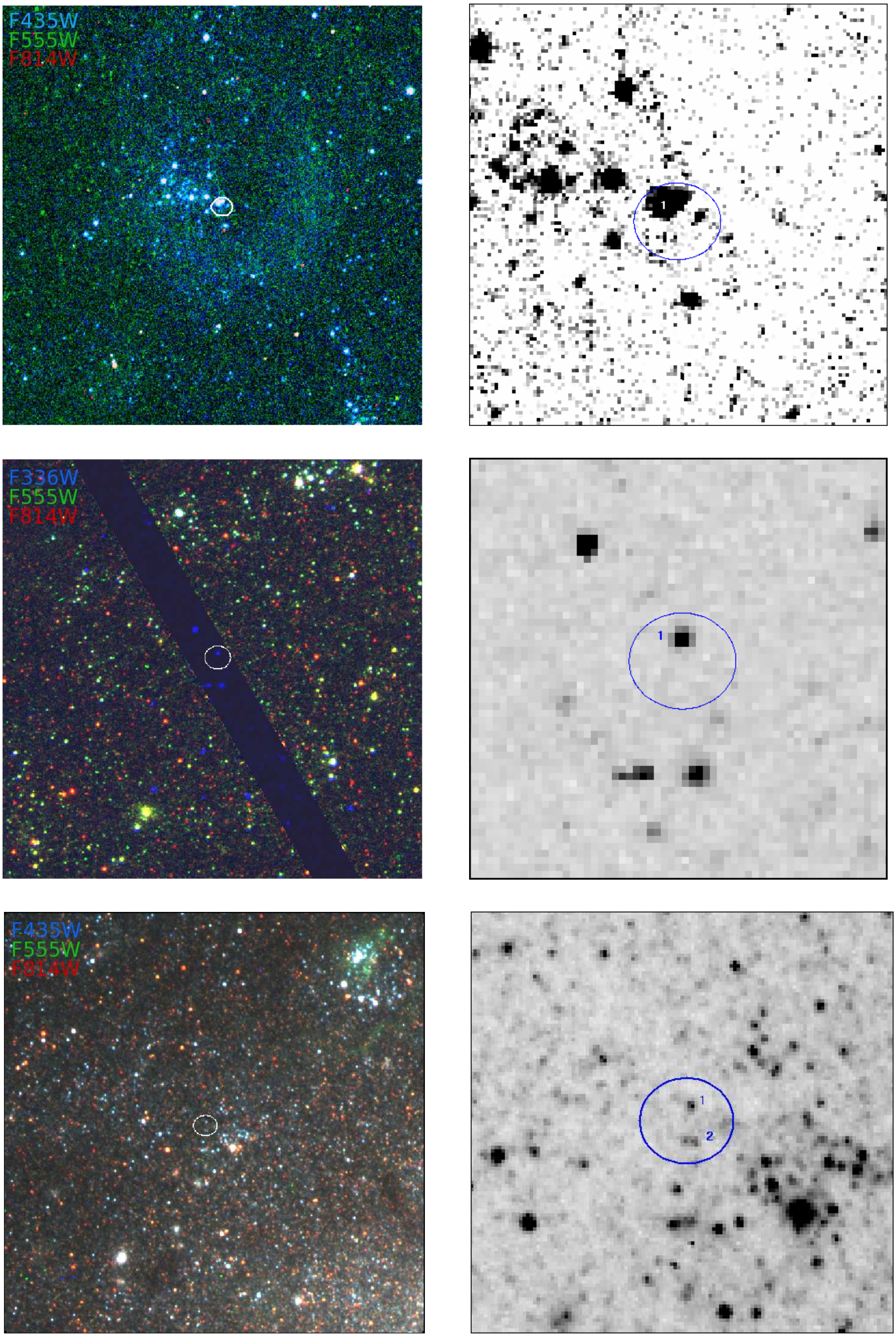

Figure 2.2: *continued, pg. 4* - Specific notes: displayed ULX regions are, from top to bottom, Holmberg IX X-1 (F555W), NGC 4395 ULX1 (F336W) & NGC 1313 X-1 (F555W).

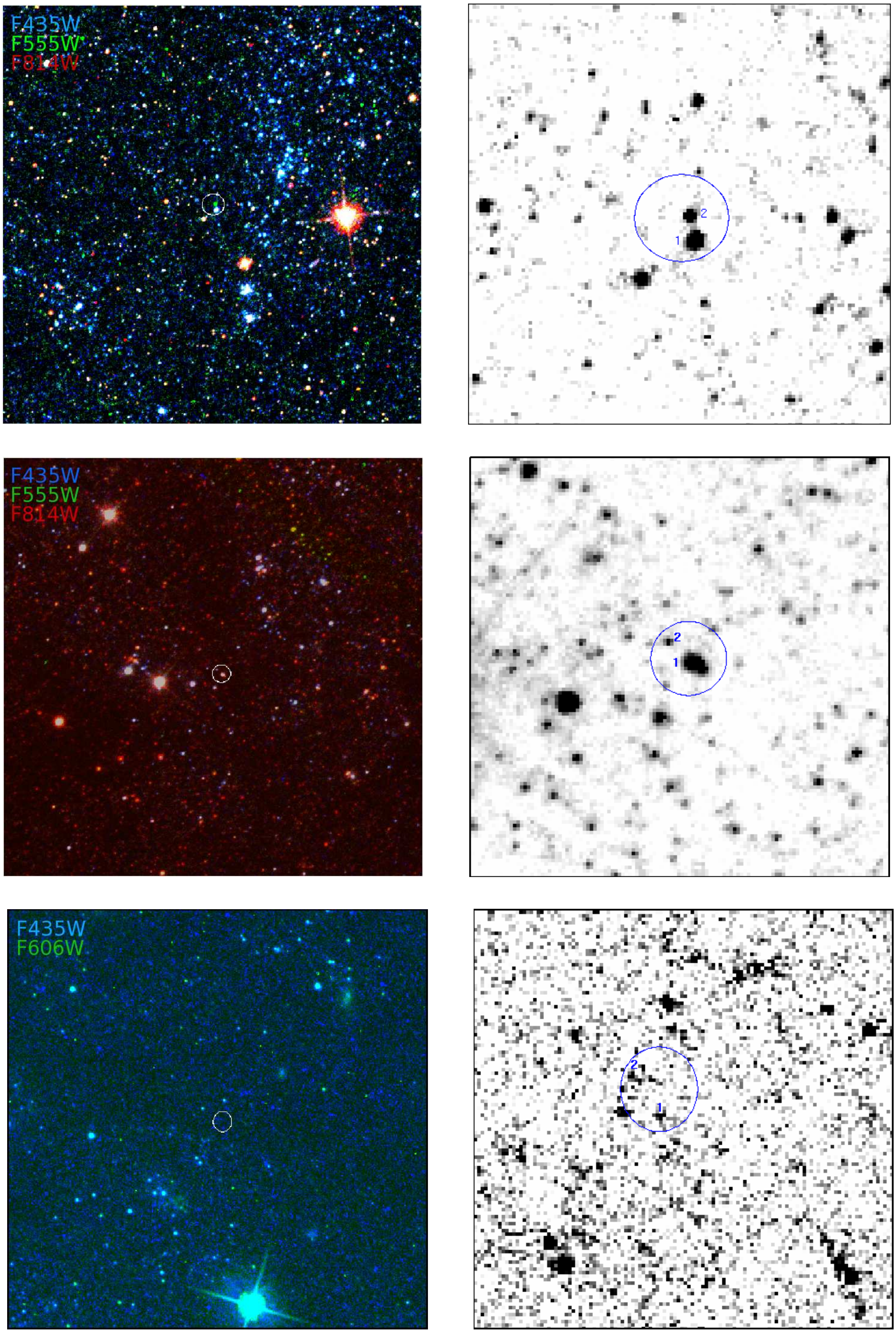

Figure 2.2: *continued, pg. 5* - Specific notes: displayed ULX regions are, from top to bottom, NGC 1313 X-2 (F555W), IC 342 X1 (F814W) & IC 342 X2 (F435W).

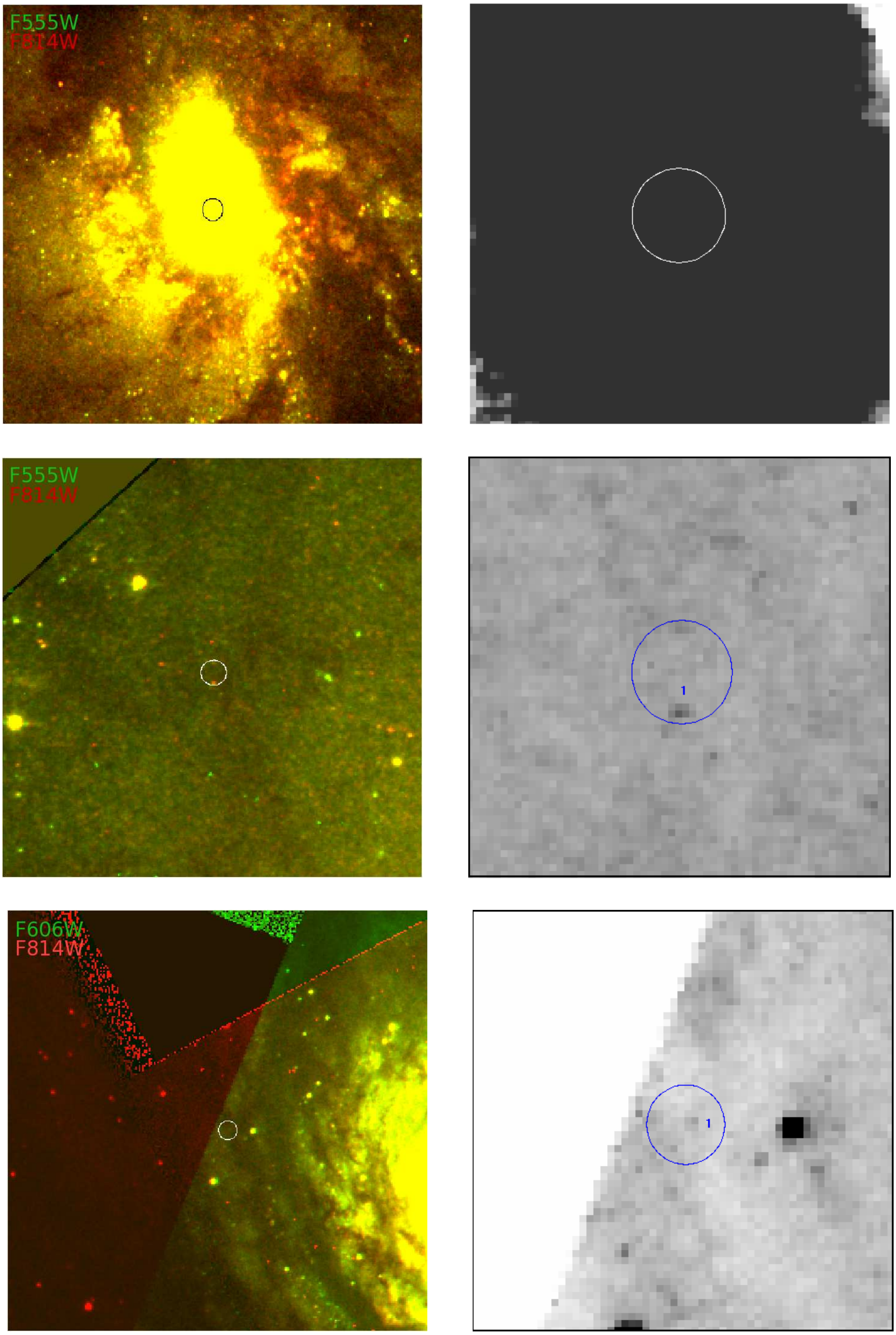

Figure 2.2: *continued, pg. 6* - Specific notes: displayed ULX regions are, from top to bottom, IC 342 ULX2 (F555W), IC 342 X6 (F555W) & Circinus ULX1 (F606W).

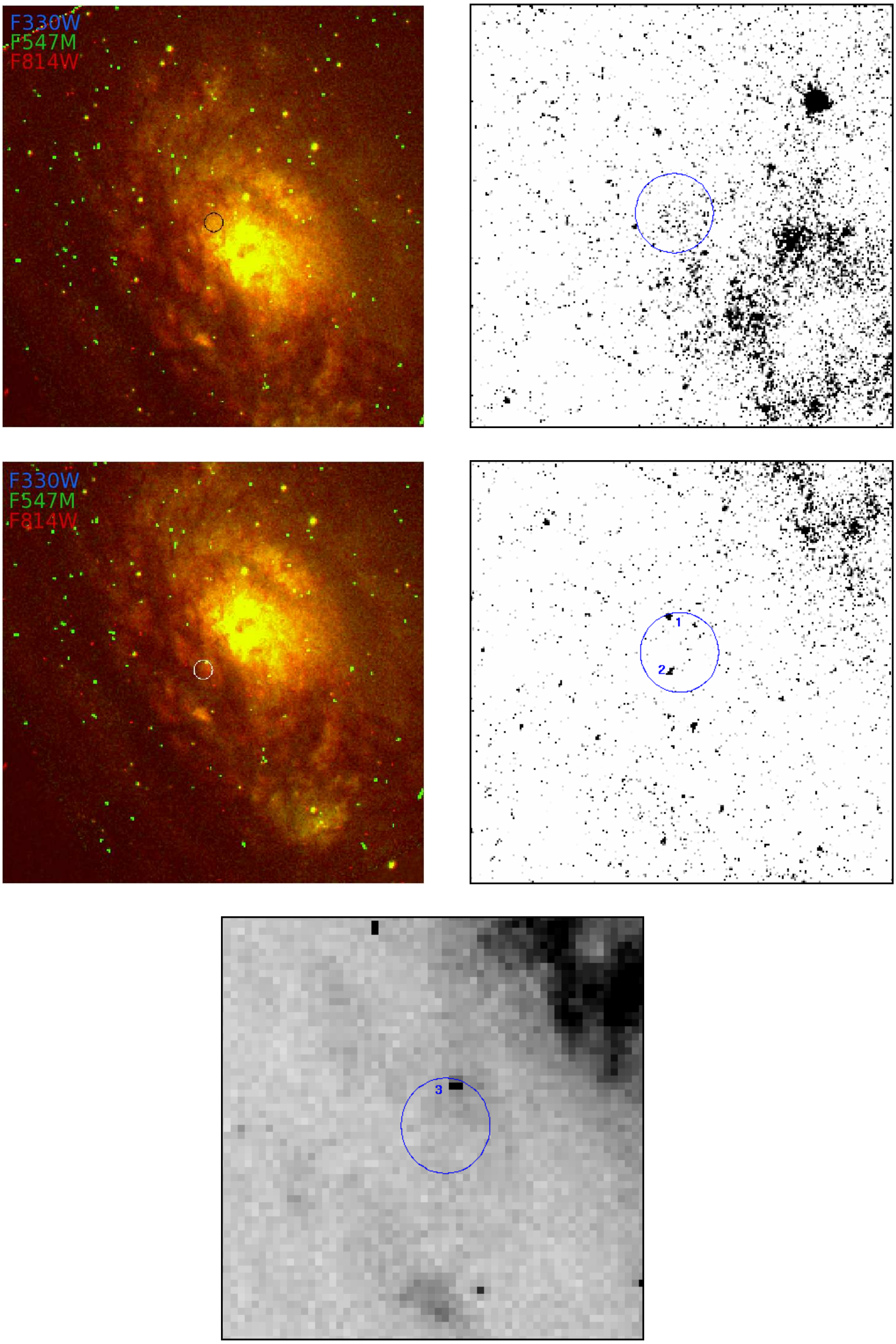

Figure 2.2: *continued, pg. 7* - Specific notes: displayed ULX regions are, from top to bottom, Circinus ULX3 (F330W), Circinus ULX4 (F330W & F547M). An additional finding chart is provided for Circinus ULX4, and one object was not visible in first selected band.

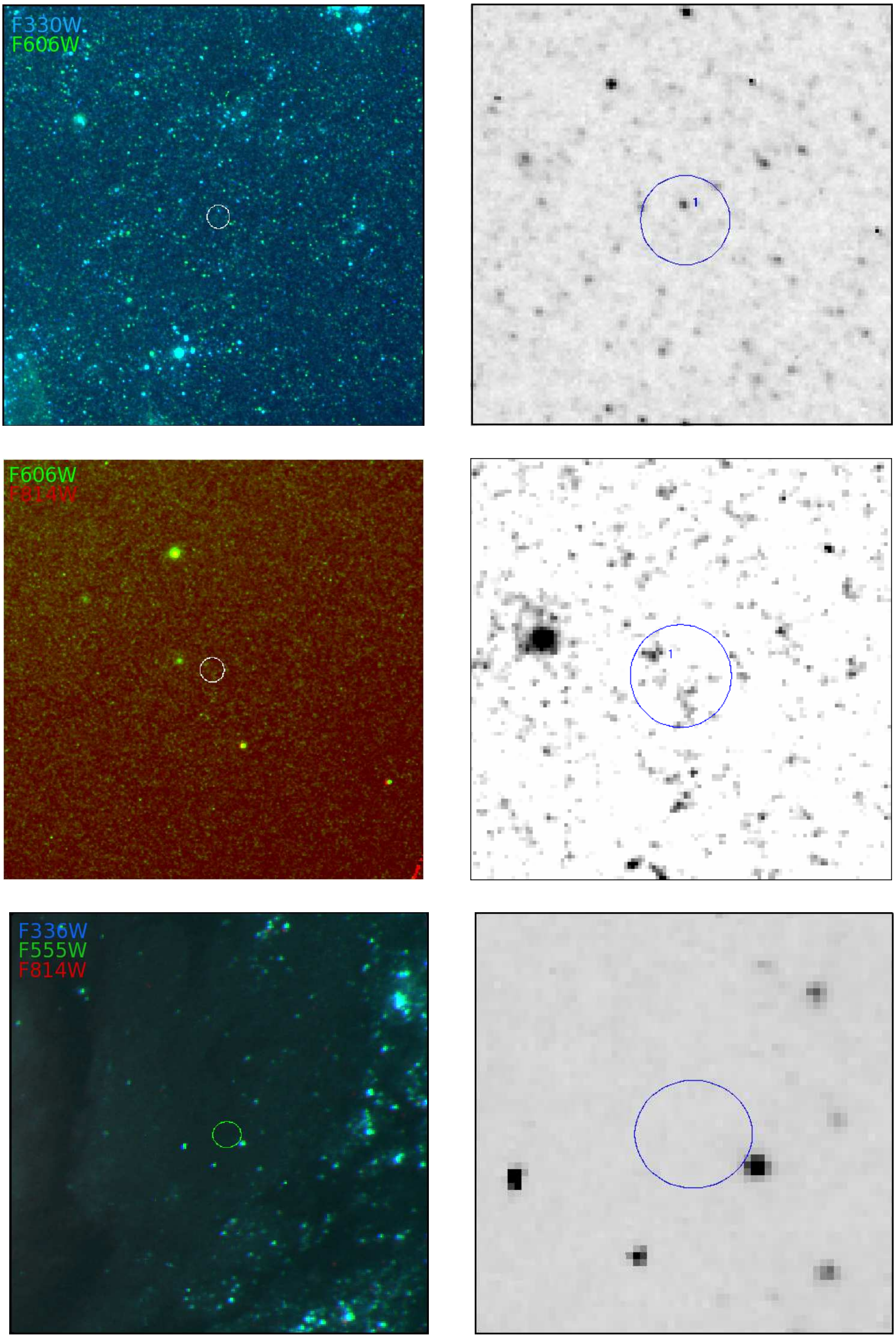

Figure 2.2: *continued, pg. 8* - Specific notes: displayed ULX regions are, from top to bottom, NGC 2403 X- 1 (F606W), NGC 5128 ULX1 (F606W) & NGC 4736 X-1 (F555W).

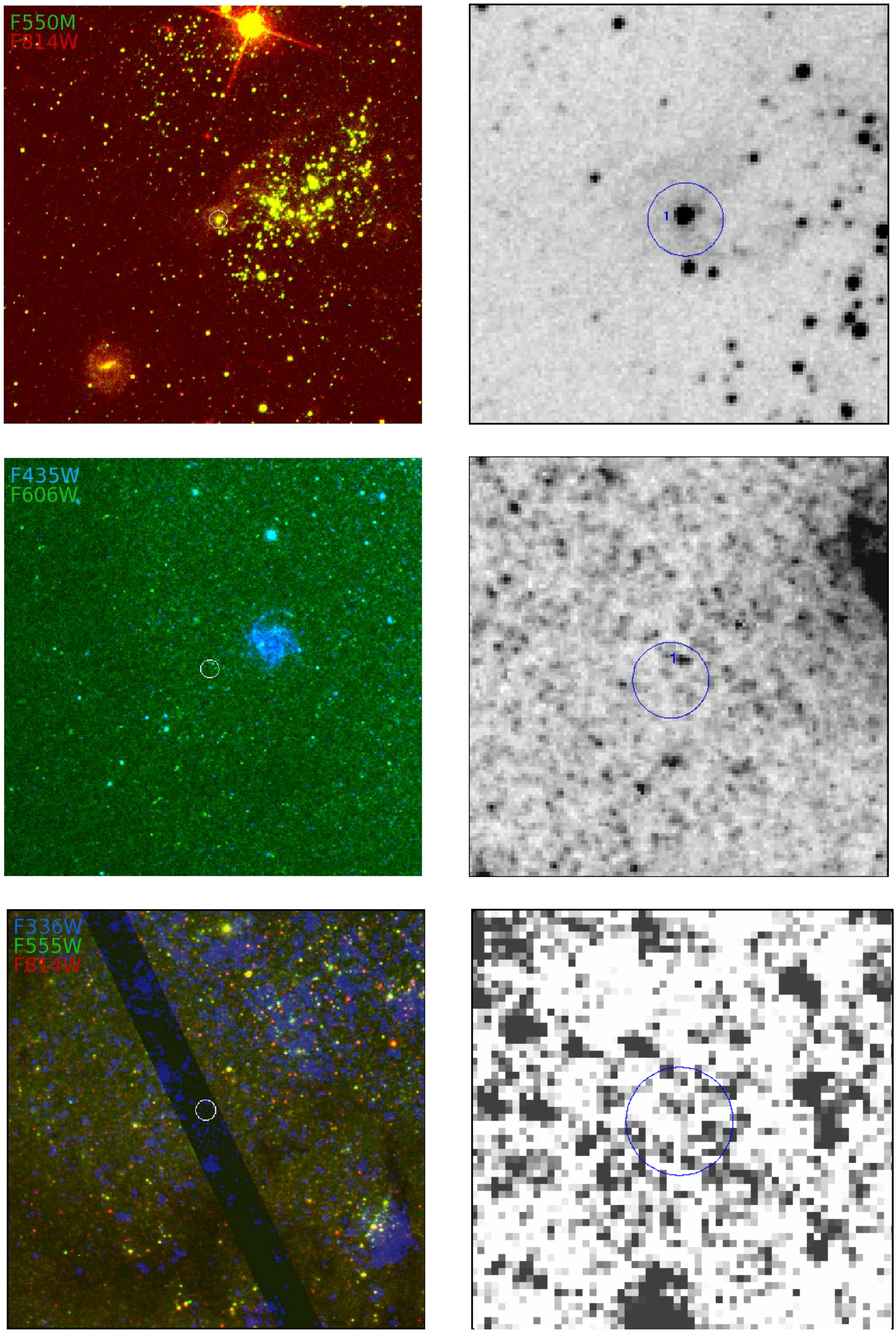

Figure 2.2: *continued, pg. 9* - Specific notes: displayed ULX regions are, from top to bottom, Holmberg II X-1 (F550W), M83 XMM1 (F606W) & M83 XMM2 (F336W).

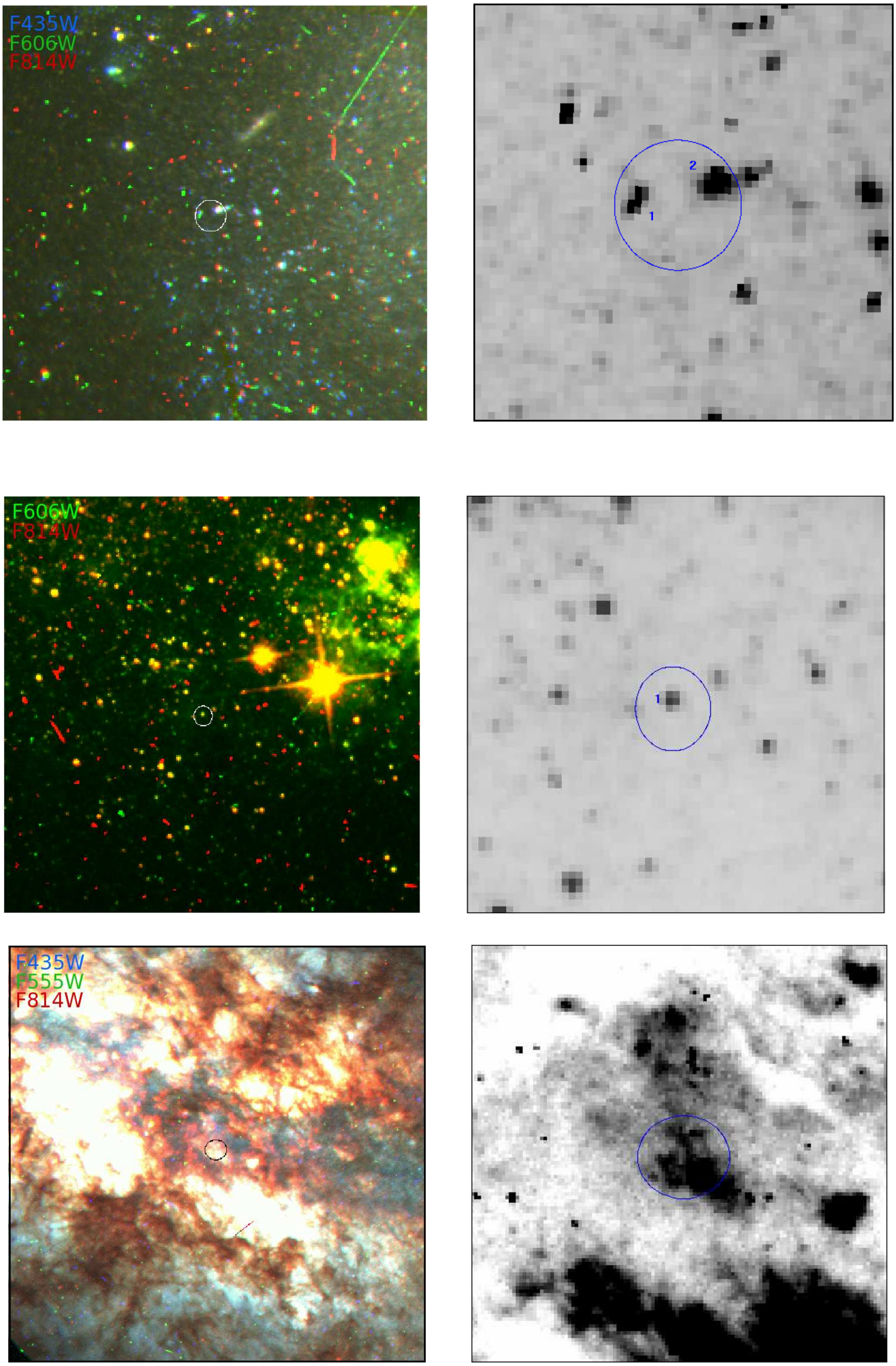

Figure 2.2: *continued, pg. 10* - Specific notes: displayed ULX regions are, from top to bottom, NGC 5204 X-1 (F606W), NGC 5408 X-1 (F606W) & NGC 3034 ULX3 (F435W).

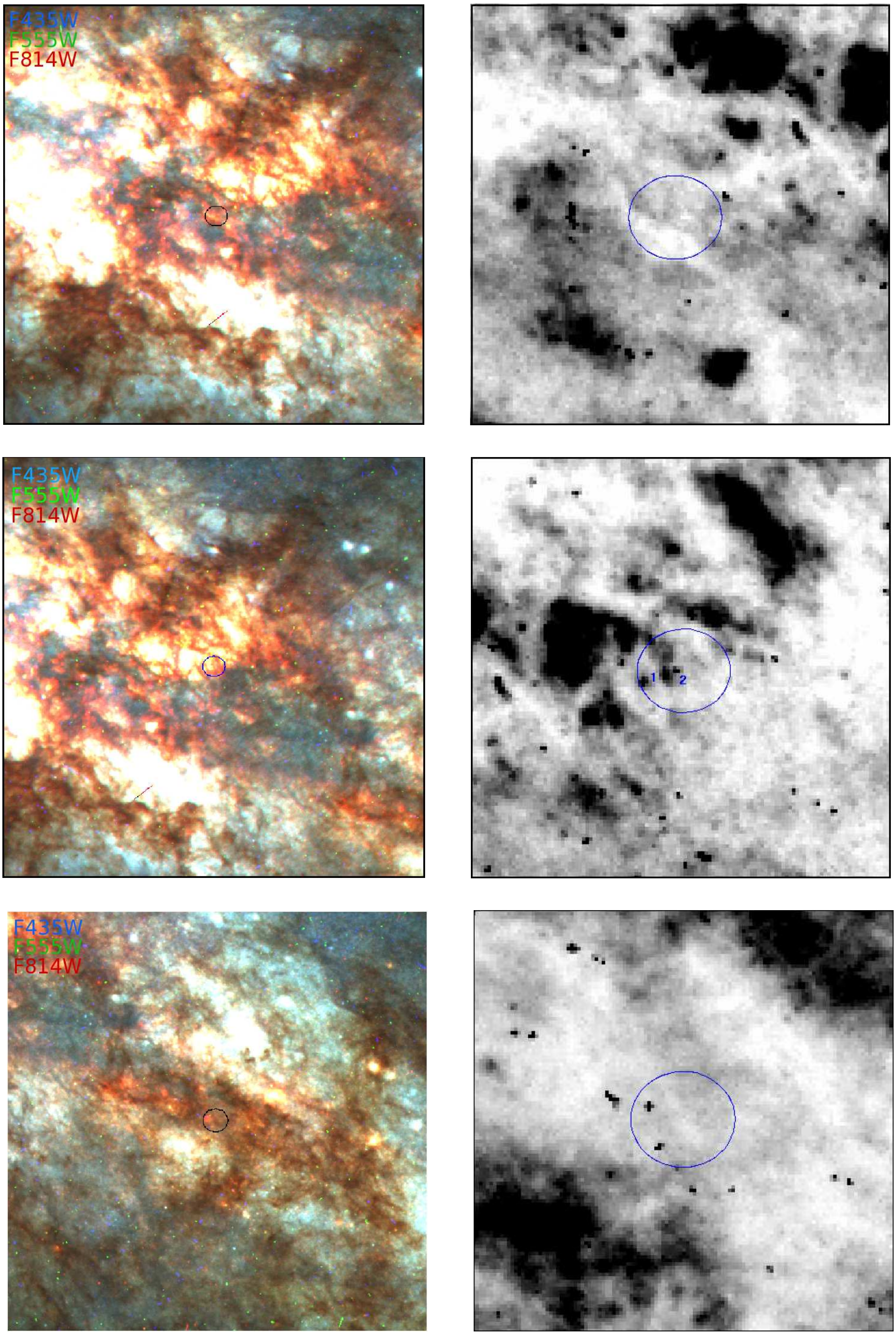

Figure 2.2: *continued, pg. 11* - Specific notes: displayed ULX regions are, from top to bottom, NGC 3034 ULX4 (F435W), NGC 3034 ULX5 (F435W), NGC 3034 ULX6 (F435W).

In an attempt to correct for reddening, Galactic extinction corrections were also applied in all cases, using $E(B-V)$ values listed in Table 2.1. These are used in combination with the filter specific extinction ratios gathered from different locations depending on instrument. Extinction ratios for WFPC2 data were taken from Schlegel, Finkbeiner & Davis (1998) wherever possible, but when values were not available we calculated these using SYNPHOT. The calculated values are found by folding a template spectrum through the instrumental response allowing for some foreground extinction using Cardelli laws (chosen for consistency with Schlegel et al. 1998). Although this correction is spectrum-dependent, we find that this dependence is only at a low level, and we therefore opt to use a 10,000 K blackbody as a first order estimate in order to obtain these corrections because the observed counterparts are of unknown type. For magnitudes calculated using ACS fields, filter-dependent extinction ratios are given by Sirianni et al. (2005). Again, because the extinction ratios are also dependent on stellar type (and no blackbody is available), we choose to use the corrections for an O5 V star, following the example of Roberts et al. (2008). Although this choice will affect the calculated magnitudes of our sources, the impact will be minimal in most bands, beginning to impact on magnitudes only marginally in the bluest bands (F435W and bluer). The aperture and Galactic extinction-corrected Vega magnitudes are given in Table 2.3.

2.5 Counterparts

Our analysis has detected the presence of 38 potential counterparts to 23 ultraluminous X-ray sources. As stated, one of the main reasons for this project is to identify possible candidates for follow-up using ground-based telescopes. The results of this study have led to several successful applications to the Gemini Telescopes to observe five potential counterparts and confirmed counterparts identified in other work. To date three of the observations have been made from our programmes, which are contained within Chapter 3.

2.5.1 Spectral typing from broad-band spectra

Here we find that many of the possible counterparts are too faint for spectroscopic follow-up (see Chapter 3), and so cannot be utilised in this way. We therefore attempt to explore the nature of these sources via other means, by attempting to type these stars. To do this we must compare their properties to known stellar types. One method of doing this is to convert the filter band magnitudes to UBVRI magnitudes to compare to known values (e.g. Soria et al. 2005, Ramsey et al. 2006, Roberts et al. 2008). There is a problem with this approach, highlighted by Sirianni et al. (2005): the filters used onboard *HST* are not an exact match to those used in other (standardised) photometric systems, and this can lead to large errors in typing (see Sirianni et al 2005 for more detailed discussion). They recommend instead working in systems based within the *HST* filters. If we wish to perform additional analysis of the data, we must therefore convert information relating to standard stellar types into the *HST* filter bands. To do this we fold a range of standard stellar spectra through the SYNPHOT tool *CALCPHOT*, a package that allows the user to calculate the photometric magnitudes that would be observed for a given stellar type with a given Johnson-Cousins band Vega magnitude (although other input options are available). In order to simplify our comparison process, we choose to normalise all our spectra to a V band magnitude of zero. We use the standard stellar templates associated with the SYNPHOT package, of which there are two available. These are stored in the form of two spectrophotometric atlases, one by Bruzual-Person-Gun-Stryker and the other by Jacoby-Hunter-Christian. We opt to use the former as the band pass coverage of this atlas has been extended to include the ultraviolet and infrared as opposed to the latter which has not, consistent with the wider waveband coverage required by our analysis. As a result our choice of stellar class is restricted to those within this atlas, which contains a wide range of types but very few giant and/or supergiants templates. The conversion is performed for all instrument/detector/filter combinations used in the analysis of our ULX fields, with the resulting values plotted in Figure 2.3. Our templates range from O to M, varying in size from main sequence to supergiants. The templates are grouped in colour, according to type as follows; magenta - O stars, blue - B type, cyan - A type stars, green - F stars, yellow - G type, orange - K stars and red - M type stars.

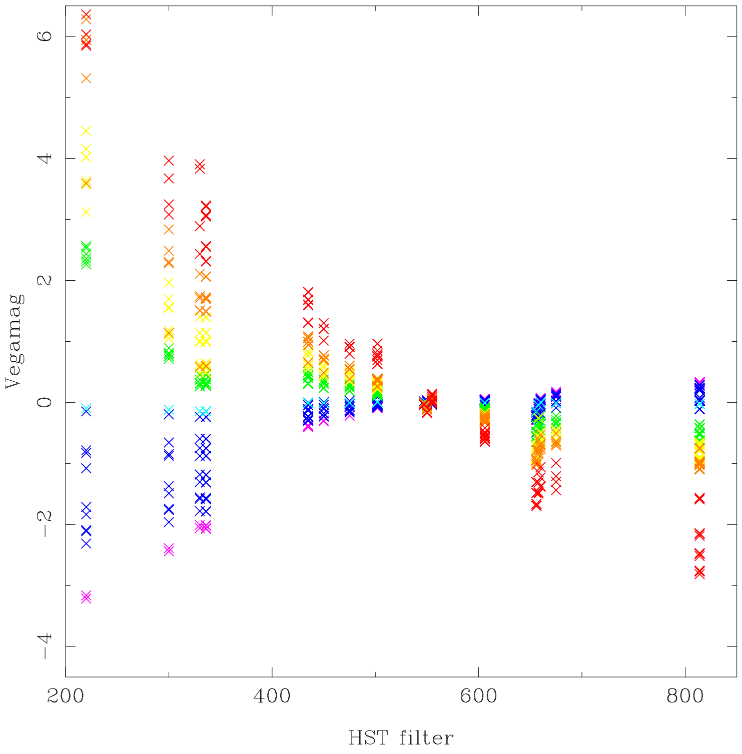

Figure 2.3: Photometric stellar templates for *HST* filter bands, constructed using the IRAF package SYNPHOT. The templates normalised to a V band Vega magnitude of zero, and are grouped according to type as follows; magenta - O stars, blue - B type, cyan - A type stars, green - F stars, yellow - G type, orange - K stars and red - M.

We compare the calculated magnitudes of all potential counterparts to the derived templates displayed in Figure 2.3, whenever more than one filter band is available. Simple χ^2 minimisation is performed to determine the best fitting stellar type. Some examples of the resultant fits can be seen in Figure 2.4. To do this we are required to apply an *offset* to the data, to shift derived magnitudes of our sample to a magnitude of approximately zero in the V band, a shift that is refined during χ^2 minimisation. This *offset* can also be considered to be the m_{555} of the source (which will be similar in value to similar m_V). Of the 38 counterparts identified, 14 have only a single filter band magnitude available for fitting. In some cases this is due to the presence of a chip gap in alternate observation, but in others this may be due to the depth of the exposures (see also Ptak et al. 2006). This fitting process results in the classification of the 24 remaining potential counterparts, covering the broad range of the types available. We note that in nine of these instances, fitting is performed where only two bands are available; similarly that six of our sample have three data points available for fitting, five contain four *HST* bands and four contain maximum of 5 data bins for comparison to standard stellar types. The resultant types and applied refined *offsets* are displayed in Table 2.4.

We now briefly consider the fits achieved by this process, although we note that the size of magnitude errors mean that caution is required. If we assume that these values are correct, our analysis indicates that the majority of these objects are not OB stars, as had been indicated previously (e.g. Liu et al. 2007, Copperwheat et al. 2007). We find that only nine of our 24 potential counterparts appear to have colours that are consistent with these types. Initial findings would indicate that only three are consistent with O type stars while six are similar to B type stars. The fits of the remaining 15 sources would suggest that we are observing five, three, zero, one and five are types A, F, G, K and M respectively, with one extraneous source (M81 X-6) which we will return to later (see Section 2.5.5). Our work also reveals that eleven appear most consistent with stars in the main sequence stars (V), while three are type IV sub-giants, six are giants (III) and two are supergiants (one type Ia and one Ib), and one designated O8 f.

As stated above, some of the error bars derived from Vega magnitude calculations are quite large, and so our sample can cover a wide range of possible stellar types (for example NGC 3034 ULX5 is best described by the template of a M2 giant, but covers a range of types from B through to M within the errors as can be seen in Figure 2.4). When looking at these ranges we find that twenty of our sample can be considered as having colours consistent with O/B type stars, with the remaining three sources being classified as late type sources (G, K & M) by colours. We tabulate the range of possible stellar types allowed within the errors of magnitudes for each source in Table 2.4.

Table 2.4: Typing of potential ULX counterparts

Source	C/P ID[a]	Type[b]	Type M_V[c]	Distance modulus[d]	m_{555}[e]	*offset*[f]	Δm_{555}	Possible types[h]	M_{555}[g]	Previous identification[i]
NGC 598 ULX1	0	–	–	24.771	–	–	–	–	–	nucleus(3)
NGC 55 ULX1	1	A1 V	+0.7*(1)	26.203	26.898	23.179	-3.719	O, B, A, early F	-3.0	–
NGC 4190 X-1	1	B9 V	+0.21(2)	27.236	27.431	24.812	-2.319	all	-2.4	–
	2	O5 V	-5.00(2)	27.236	22.200	25.560	-2.042	all	-1.676	–
NGC 253 ULX1	1	–	–	27.386	–	–	–	–	–	–
	2	M2 III	-0.6(1)	27.386	29.930	24.099	-2.831	all	-3.3	–
NGC 253 ULX2	1	M0 V	+9.0(1)	27.386	36.478	21.165	-15.313	M, late K	-6.2	–
NGC 253 ULX3	1	–	–	27.386	–	–	–	–	–	–
NGC 253 XMM6	1	M0 V	+9.0(1)	27.386	36.478	25.601	-10.877	all	-1.8	–
	2	M0 III	-0.2(1)	27.386	27.304	25.782	-1.522	M	-1.4	–
	3	–	–	27.386	–	–	–	–	–	–
	4	–	–	27.386	–	–	–	–	–	–
	5	–	–	27.386	–	–	–	–	–	–
M81 X-6	1	F5IV	+2.3(1)	27.657	29.982	23.261	-6.721	[See Section 2.5.5]	-4.4	O8 V(4,5)
Hol IX X-1	1	B4 V	-1.22(2)	27.670	26.429	22.253	-4.176	B	-5.4	OB(5,6)
NGC 4395 ULX1	1	–	–	27.782	–	–	–	–	–	–
NGC 1313 X-1	1	B2 III	-2.63(2)	27.841	25.180	23.707	-1.473	O, B	-4.1	–
	2	B9 IV	-0.17(2)	27.841	27.835	24.099	-3.736	O, B, A, F, G, K	-3.6	–
NGC 1313 X-2	1	B2 III	-2.63(2)	27.841	25.180	23.359	-1.821	O, early B	-4.5	OB(5,7)
	2	–	–	27.841	–	–	–	–	–	–

Source	C/P ID^a	Type^b	Type $M_V{}^c$	Distance modulus^d	$m_{555}{}^e$	*offset*^{f}	$\Delta m_{555}{}^g$	Possible types^h	$M_{555}{}^i$	Previous identification^i
IC 342 X-1	1	K0 IV	+3.2(1)	27.955	31.221	22.227	-8.994	K, G	-5.7	F8-G0 Ib(8), F0–F5 I(9)
	2	F6 V	+3.4*(1)	27.955	31.378	24.045	-7.333	O, B, A, F, G, K, early M	-3.9	–
IC 342 X-2	1	–	–	27.955	–	–	–	–	–	Y(9)
	2	–	–	27.955	–	–	–	–	–	–
IC 342 ULX2	0	–	–	27.955	–	–	–	–	–	–
IC 342 X-6	1	F7 IV	+2.3*(1)	27.955	30.282	23.069	-7.213	O, B, A, F, G, K	-4.9	–
Circinus ULX1	1	–	–	28.010	–	–	–	–	–	K5 or later(10)
Circinus ULX3	0	–	–	28.010	–	–	–	–	–	–
Circinus ULX4	1	–	–	28.010	–	–	–	–	–	–
	2	A5 V	+2.0*(1)	28.010	30.015	15.710	-14.305	B, A, F, G, early to mid K	-12.4	–
	3	A1 V	+0.7(1)	28.010	28.705	15.338	-13.367	all	-12.7	–
NGC 2403 X-1	1	B8 Ia	-5.67(2)	28.116	22.444	24.538	2.095	O, B, A, F, early K	-3.6	OB giant/ supergiant(9)
NGC 5128 ULX1	1	–	–	28.121	–	–	–	–	–	OB (11)
NGC 4736 XMM1	0	–	–	28.167	–	–	–	–	–	–
Hol II X-1	1	A3 III	-0.2*(1)	28.266	28.756	21.490	-7.266	B, A	-6.8	O4 V/B3 Ib(12)
M83 XMM1	1	A3 V	+2.0*(1)	28.360	30.358	25.486	-4.872	all	-2.9	–
M83 XMM2	0	–	–	28.360	–	–	–	–	–	–

Source	C/P ID^{a}	Type^{b}	Type $M_V{}^{c}$	Distance modulus^{d}	$m_{555}{}^{e}$	*offset*^{f}	$\Delta m_{555}{}^{g}$	Possible types^{h}	$M_{555}{}^{i}$	Previous identification^{j}
NGC 5204 X-1	1	O5 V	-5.00$^{(2)}$	28.406	23.370	22.743	-0.627	O	-5.3	O5V, O7III or B0 Ib$^{(13)}$
	2	F8 V	+3.4$^{*(1)}$	28.406	31.840	20.184	-11.656	–	-8.2	star cluster$^{(14)}$, O5 V + cluster$^{(13)}$
NGC 5408 X-1	1	O8 F	-4.83$^{*(2)}$	28.406	23.539	22.198	-1.341	O, B, A, F, G, K, early M	-6.2	B/A supergiant$^{(15)}$
NGC 3034 ULX3	0	–	–	28.580	–	–	–	–	–	–
NGC 3034 ULX4	0	–	–	28.580	–	–	–	–	–	–
NGC 3034 ULX5	1	M2 III	-0.6$^{(1)}$	28.580	28.108	21.610	-6.498	B, A, F, G, K, M	6.9	
	2	–	–	28.580	–	–	–	–	–	–
NGC 3034 ULX6	0	–	–	28.580	–	–	–	–	–	–

Notes: ^{a}Counterpart ID taken from Table 2.3. ^{b}Stellar type derived from χ^2 fitting of *HST* band stellar templates, created using SYNPHOT. ^{c}Absolute magnitude of identified stellar type in V band (taken from similar type if particular M_V is unavailable, sources are indicated by *). ^{d}Calculated distance modulus using values in Table 2.1. ^{e}Derived Vega magnitude in F555W band, assuming stellar type classification is correct. ^{f}*Offset* required to fit observed data to stellar types, this can also be considered to be the apparent magnitude in the F555W band ($\sim m_{555}$). This is found by χ^2 fitting. ^{g}Value $\Delta m_{555} = \textit{offset} - m_{555}$. ^{h}All possible types allowed within errors. ^{i}Absolute magnitude in *HST* band F555W, calculated using *offset* value. ^{j}Stellar types collated from work of other authors, where Y refers to identification without typing. Figures shown in brackets relate to following references: $^{(1)}$Zombeck (1990), $^{(2)}$Wegner (2006), $^{(3)}$Dubus et al. (2004), $^{(4)}$Liu et al. (2002), $^{(5)}$Ramsey et al. (2006), $^{(6)}$Grisé et al. (2005), $^{(7)}$Liu et al. (2007), $^{(8)}$Feng & Kaaret (2008), $^{(9)}$Roberts et al. (2008), $^{(10)}$Weisskopf et al. (2004), $^{(11)}$Ghosh et al. (2006), $^{(12)}$Kaaret et al. (2004), $^{(13)}$Liu et al. (2004), $^{(14)}$Goad et al. (2002), $^{(15)}$Lang et al. (2007).

2.5.2 Spectral types from magnitudes

We are able to glean yet more information about this sample by considering their magnitudes. We noted above that large error bars and a restricted typing catalogue means that our initial classification should be viewed with caution. However, we now use these to calculate apparent magnitude for such a source (assuming typing is correct). We will then be able to compare these to our observed magnitudes.

We collate the absolute magnitudes for our sample based on the stellar type classifications. By combining this with the distance modulus for each source (using values from Table 2.1), we are able to derive the apparent magnitude for a star of that class of object at the required distance. Exact absolute magnitudes for all star types are not given in Zombeck (1990) and Wegner (2006), so to compensate for this we use absolute magnitudes for the most similar star type available within the text. This will lead to discrepancies in magnitudes of at most 1 – 2, depending on type.

We use the absolute magnitude for the V band to allow for easy comparison to our fits, and fold this through *CALCPHOT* to derive the value for the *HST* band F555W (i.e. m_{555} for that object). We must also make an assumption about the instrument and detector to perform this calculation. Our original conversion of stellar templates were all normalised to a V band of zero, which results in a clustering of values in band F555W (see Figure 2.3). This indicates that the choice of instrument and detector will have minimal impact on our apparent magnitude (m_{555}) calculations. For the purpose of this analysis we choose to use the combination of ACS and WFC at this stage as more than 50 per cent of our *HST* fields are of this combination. The V band absolute magnitudes, distance moduli and apparent magnitudes for the F555W filter are given in Table 2.4.

One aspect that we have not considered thus far is reddening intrinsic to either the host galaxy or the region localised to the source itself. Such reddening would impact the colour classification of the source and therefore the derived magnitude of this system (m_{555}). NGC 253 is a bright galaxy that is oriented almost edge on to our line of sight, and the ULXs in the galaxy also reside in dusty regions (see Figure 2.2 (page 2 & 3)). Such regions could severely impact the photometry in each band leading to misidentification of source type. The stellar counterparts identified in IC 342 have high values of galactic foreground

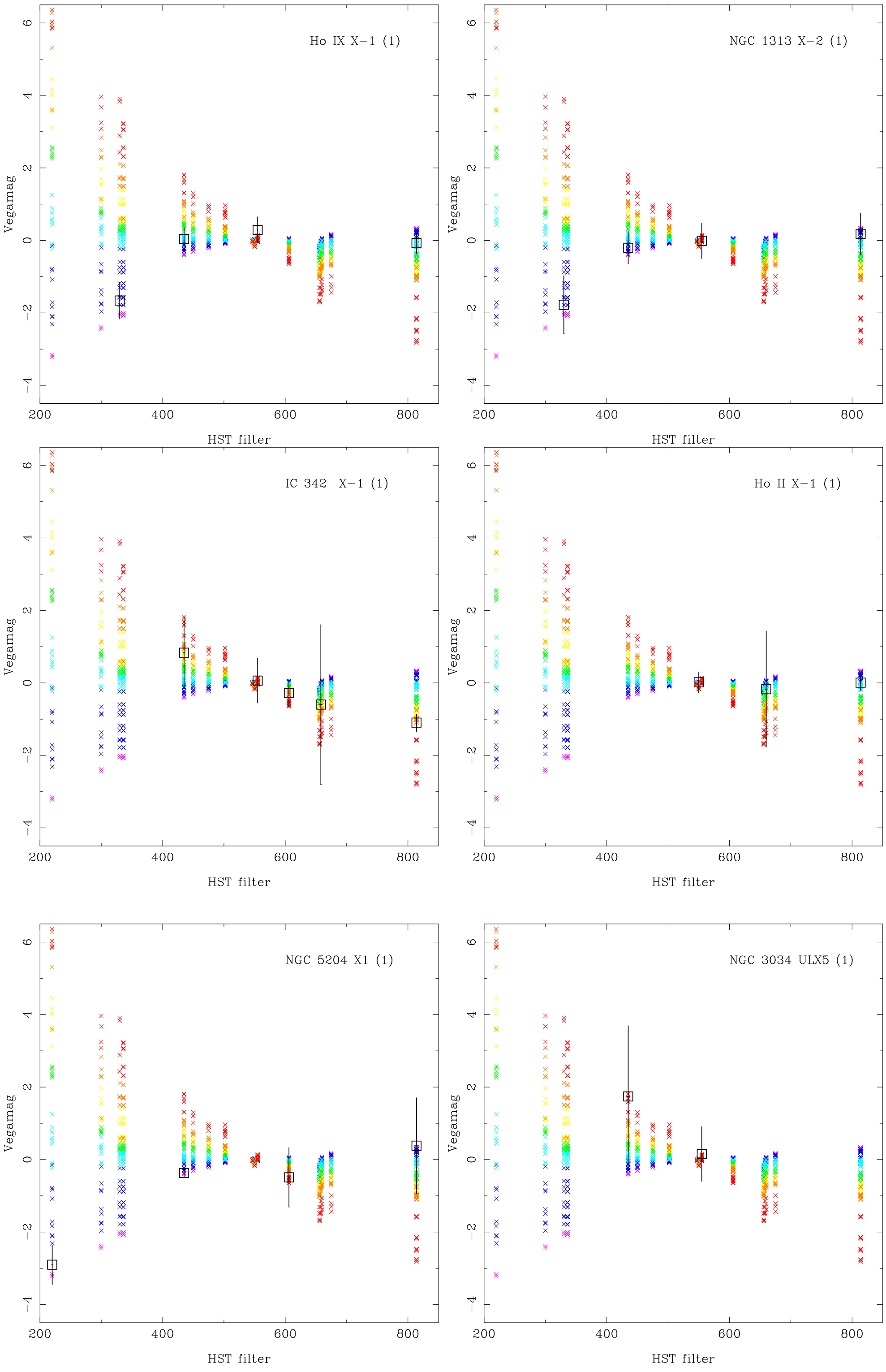

Figure 2.4: Vega magnitudes of six of our sample, plotted against the stellar templates taken from the Bruzual-Person-Gun-Stryker atlas. From here it is evident that a range of types and data quality is available within our sample. Some are well constrained, such as Holmberg IX X-1 (1), whilst others, such as NGC 3034 ULX5 (1), have such large errors as to cover the whole range of possible stellar templates.

extinction, but high values of X-ray absorption indicate an additional (possibly large) intrinsic reddening correction could be required[13] (Roberts et al. 2008). Such corrections could easily alter the stellar type observed. The Circinus galaxy appears behind the plane of our Galaxy, which would cause greater extinction factors to occur. Finally Holmberg II X-1 resides in the heart of a bright nebula, whose emission is found to be photoionised by the ULX, causing its He II to be an order of magnitude greater than similar nebulae found elsewhere (Kaaret et al 2004). Material from the region associated with the nebula could easily redden the emission of any stellar object residing within it. This would also affect the apparent magnitude of the object ($\sim$ *offset*), but to what extent the two relate is not yet clear.

We compare these apparent magnitudes with our calculated magnitudes, using the *offsets* gained from χ^2 fitting. We find that five of our sample display a large difference in these two values. The observed apparent magnitudes of Circinus ULX4 counterparts 2 and 3, NGC 253 ULX2 counterpart 1, NGC 253 XMM6 counterpart 1 and NGC 5204 X-1 counterpart 2 are over ten magnitudes brighter than would be expected for their derived stellar type. We also find that IC 342 X-1 counterparts 1 & 2, IC 342 X-6 counterpart 1, Ho II X-1 counterpart 1 and NGC 3034 ULX5 counterpart 1, appear brighter than expected by over 5 magnitudes. This difference may be partially explained by the mistyping caused by reddening, but given the range of types allowed in the fitting of these source, it appears more likely that we are looking at brighter objects. This implies that we are observing emission from O/B stars or later type bright/supergiants.

Of the fourteen sources yet to be considered we find that seven display similar apparent magnitudes to their *offsets* ($\Delta m_{555} \lesssim 2$), indicating that the classification of these objects may be approximately correct, whilst the six remaining sources (excluding the spurious source – M81 X-6) display a greater divergence. In four of these cases we were unable to collate the exact value of M_V for the specified source type. This could alter the derived apparent magnitude of the source by 1 – 2 magnitudes, resulting in a similarity of fit and possible confirmation of type. The result would be the possible classification of eleven sources.

An alternative suggestion may be that the colours are approximately correct, but that

---

[13] X-ray absorption has a more major impact in observations of IC 342 X-2.

we are observing giant/supergiant sources. The number of bright/supergiant templates available within our chosen atlas is limited (as mentioned above). To explore this possibility, we attempt to estimate the absolute magnitude of each of our sample. We now ignore previous classifications and derive the absolute magnitude for the F555W ($\sim$ V) band from the observed magnitude for each source. As we do not have a F555W observation for every source, we choose to use the *offset* value. Although this will have some dependance of the stellar type fitting, this should be minimal, and all types are normalised to around the same value in the band.

We combine the distance modulus of each source with the *offset* provided by χ^2 fitting to derive a value for M_{555}, the results of which are also given in Table 2.4. These calculations provide us with absolute magnitudes over the range $-1.4 < M_{555} < -12.7$. Comparing these values to the classifications provided by Zombeck (1990) indicates that we must be observing blue objects (OB stars) and/or giants/bright giants/supergiants over a range of types. We also note from Zombeck (1990), that the brightest supergiants have $M_V \simeq 8.2$. This would indicate that either the two possible counterparts of Circinus ULX4 are foreground stars situated within our own galaxy, or that the emission from the companion is brightened by emission from an accretion disc. Given that the Circinus galaxy is situated near the mid-plane of our Galaxy, the first suggestion is possibly more likely.

2.5.3 Accretion disc emission

The final point that should be considered when looking at the magnitudes and typing of these systems is the presence of an accretion disc. If we are in fact observing X-ray binary systems, optical radiation would be released from both the companion star and the accretion disc, and therefore the presence of such a disc could increase the emission and change the shape of the source spectra. There would also be an additional component from the X-ray irradiation of the companion star. In order to explore this further we would need to apply some of the current theoretical models which are designed to describe such systems. Attempts have been made to create such models (e.g. Copperwheat et al. 2005, 2007; Patruno & Zampieri 2008; Madhusudhan et al. 2008), which indicate that the most likely counterpart to a ULX would be high mass donor performing mass transfer via

Roche lobe overflow. Madhusudhan et al. (2008) combined the emission expected from the star with that caused by X-ray irradiation of the accretion disc (and star) in order to estimate the effective spectral type that would be observed as counterparts, finding a prevalence for O and B type stars. This is due to the additional components resulting in bluer and more luminous emission. In 2005, Copperwheat et al. introduced their irradiation models, and used them in combination with OB main sequence stars and four supergiants ranging from F to M, to explore the resulting emission from the system. They found that the emission was impacted greatly, observing a large increase in the observed magnitude (increase of $\sim 0.5 - 5$, depending on assumptions of disc and X-ray hardness and band). Such an increase in the absolute magnitude of these systems could help to explain some of the Δm_{555} values observed in our sample, possibly even including those in the Circinus galaxy. The authors followed this up with another paper in 2007, where the model was applied to a range of ULX data, finding companion stars to be main sequence or evolved giants/supergiants of spectral type B or later and noting that when irradiation models are considered counterparts appear older, larger and less massive than would be inferred without their application. Applying such models to this large data set would allow us to not only explore the nature of potential counterparts in more detail, but also start to explore their compact companions, and it appears to be an obvious next step for our sample.

2.5.4 Comparisons to previous studies

Table 2.4 also includes a note of any previous identifications and source classifications that have been published. Where more than one counterpart is present in our sample, we list the previous identification alongside the counterpart matching that referred to in the literature. Thirteen potential counterparts have been previously identified from our sample, one of which was that of NGC 598 ULX1. Dubus et al. (2004) indicates that NGC 598 ULX1 is associated with the nucleus of the galaxy, which is clearly the case as seen in Figure 2.2 (pg. 1). We are therefore unable to identify an individual counterpart – in agreement with the previous findings. IC 342 X-2 counterpart 1 was previous identified but no classifications were possible at that time. We find that we are still unable to classify with current archival data. M81 X-6 has also been previously classified, but as noted previously, this source will be discussed in the next section and so we do not consider it further at this time (see Section 2.5.5).

We find that of the ten cases remaining, five of our stellar type ranges are in agreement with previous results (Ho IX X-1 (1), NGC 1313 X-2 (1), NGC 2403 X-1 (1), NGC 5204 X-1 (1) & NGC 5408 X-1 (1); where bracketed values refer to counterpart ID). In two further cases, the authors attempt to take intrinsic reddening into account, altering their result. This occurs for IC 342 X-1(1) and Holmberg II X-1 counterpart 1. This highlights the aforementioned issue of reddening. We find these sources to be the type KO IV (IC 342 X-1 counterpart 1, possible types cover G – K range) and A3 III (Holmberg II (1), with errors covering B – A types), whilst previous work found these to be an F type supergiant (Feng & Kaaret 2008; Roberts et al. 2009) and an O/B type possible supergiant (Kaaret et al. 2004) respectively. This implies that reddening can have a large impact in the classification of such objects, a factor that requires further research on the environments of ULX.

Next we consider NGC 5204 X-1 (2), an object identified by Goad et al. (2002) to be a star cluster, using data from WFPC2. When Liu et al. (2004) revisited this source, and the data, they incorporate higher resolution data from the ACS HRC, which was able to resolve the source into two components, revealing the presence of an O5 V star and redder star cluster. The data we use combines the data both the previous studies, which may have lead to the alternate classification of an F8 V type star. As to data used comes from two observations, we will discuss this source further in the next section.

In the two remaining cases we find that we are unable to classify these sources. The first of these is NGC 5128 X-1. The counterpart to this source has been initially identified by Weisskopf et al. (2004), classifying this source as an OB star. Ptak et al. returned to the field in 2006, finding that they were only able to gain limits on the magnitude of the counterpart using their methods. Here we suffer similar problems to Ptak et al. (2006), in that our methods only allow us to place limits of the brightness of this source. We are therefore unable to constrain the magnitudes and are unable to classify the type of stellar object we are observing. From the literature we find that Weisskopf et al. (2004) performed their own data reduction to get the deepest correct image possible, while Ptak et al. (2006) used the WFPC2 associations providing slightly shallower images of the same field. This would suggest that the data retrieved from HLA is not maximised for depth of image, so if we wish to consider the fainter sources the data should be reduced accordingly. We do note however, that given the volume of data available in the HLA, it may be more useful at present to consider limits on the luminosity of these sources instead. We find the same problem with the faint counterpart to Circinus ULX1, where only limits on the magnitude are possible.

2.5.5 Possible optical variability?

Although every effort was made to gain a wide range of *HST* bands from single observational IDs, this was not always possible, as noted above. This occurred in 15 of the 31 ULX fields. In four cases we find that the error region contains no visible counterparts, while in the remaining eleven ULX error regions we observe sixteen potential counterparts, nine of which are were only detected in one observation. We find that, although Circinus ULX4 counterpart 2 was observed on two separate programmes, only one band magnitude was available in each. As a result we are unable to explore the variations of this source at present. This gives us six potential counterparts to consider; NGC 1313 X-1 (1) & (2), IC 342 X-6 (1), NGC 5204 counterparts 1 & 2 and finally M81 X-6. We therefore return to these fields to look for signs of variability in their emission of potential ULX counterparts.

This sample contains only one exposure of each band for each ULX. We are therefore unable to look for variations in the luminosity of an individual band by comparison to previous data using this current data set (unless we return to our sample to gain limits from all available fields, this falls outside the scope of this thesis). We note however the value of such an approach and suggest this as a possibility for future studies of this sample. Instead, we look for changes in the emission of these sources by comparing the observed magnitudes to the *HST* band stellar templates constructed earlier. Such a comparison would highlight variations in the source emission via a change in apparent stellar type. We highlighted in previous discussion that variations have been observed within a single observational ID, when an exposure of an individual field has been delayed for a period of days (NGC 5055 X-2 from Roberts et al. 2008). We therefore check all remaining fields to confirm consistency of observation dates within each observational ID. We find in all cases that exposures were taken in quick succession (within 24 hour period), so assume that the filter-band observed within each observational band will be consistent in emission.

To look for these changes we fit each of the observational IDs separately with the same χ^2 test as is outlined above, noting down any changes in the preferred stellar type.

NGC 1313 X-1 (1) & (2) are observed in five different energy bands, four of which have the same observational ID, which only allows for additional fitting of one observation. With the removal of the F606W band we find no change in the fitting of of counterpart 1, suggesting that there is little to no variation in the emission of this source. Counterpart 2 shows only a slight shift in spectral type. When fitting the wavebands contained within observation 09774_05, we find that this source is best explained as a B6 V star as opposed to B9 IV fit achieved using all available bands. Such changes do not significantly impact the range of stellar types that could be applied to this star (within errors), but variations like this have been noted before in NGC 1313 X-2 (1) by Mucciarelli et al. (2007) and NGC 5055 X-2 (Roberts et al. 2008, discussed earlier), with variations attributed to non-stellar processes (possibly from the accretion disc).

A similar but stronger shift is observed in the counterpart to IC 342 X-6. This ULX is observed in three bands, where two wavebands are contained within the same observation. Whilst fitting these two bands we find that that the best fit spectral type changes from F7 IV to G5V. In fact when we consider the *offset* required for fitting, we find a slight decrease of 0.262 magnitudes, and the range of possible types is cut from it's original O – K to A – K. The spectrum of this source appears to be reddened, or alternatively the other observation (05446_0j) may have taken place during a burst of blue emission that faded before the later observations. Such emission could be a result of variations in the accretion disc, or from variations in the X-ray emission resulting in a greater or lesser extent of X-ray re-ionisation. Further investigations into the variability of these systems may help us to explain this behaviour.

If we now consider the possible counterparts of NGC 5204 X-1, where four bands are available for fitting, we find that the two lower bands are from one observation (09370_01) whilst the higher are from another (08601_39). For each counterpart we now fit each observation. Counterpart one, originally best fit by an O5 V star, is now fit separately fit as an O5 V star in the lowest bands (F220W & F435W) and an O8 f in the higher wavelength bands (F606W & F814W), but cover a similar range of stellar template (within errors). The second potential counterpart of this source shows a more extreme change. This counterpart has previously been identified and discussed by both Goad et al. (2002) and Liu et al. (2004), as mentioned above, with identifications of a star cluster and an O5 V star & cluster respectively. Liu et al. (2004) suggested that only the higher resolution data could be used to disentangle the emission of these two sources due to their proximity to one another. We find that the complete data set is best fit by a template for an F8 V star, but that is not well described by any stellar type. If we now split the data according to observational IDs, we find that 09370_01 is fit by a B2 III star, with possible fits limited to B-type stars, whilst 08601_39 is represented by an F8 V spectral template but representative of types in the range late A and F stars. The difference in the stellar typing of these two observations are too extreme to be explained by an intermediate class of star, we must therefore turn to another suggestion. If we now compare our work with the findings of Liu et al. (2004) we are in agreement with the suggestion that the lower resolution redder WFPC2 are unable to separate the emission for the two components, so that the colours are probably due to contamination by cluster emission.

Finally we return to our spurious source, M81 X-6. Figure 2.5 shows the resulting magnitudes plotted against all available stellar templates, where we find that the observations of this source describes emission unlike that of any available template. This spectrum appears to be bright at both the red and the blue ends, with the faintest bands towards the centre. The plotted magnitudes are taken from three separate observations, each one denoted by a different symbol. The initial fit provided for this source is an F5 IV, whilst two of the separate observations (09073_01 & 10584_18) are fit by an M2 III and F7 IV respectively. However, if we incorporate the final data point we appear to be looking at an intrinsically blue source with a strong degree of reddening localised to the red end of the spectrum, or a two component spectrum, possibly explained by confused emission from two stars (c.f. NGC 5204 counterpart 2), or one red star and a bright accretion disc. One way to explore this further is to split the spectrum by wave band, fitting the F336W, F435W and F555W photometric magnitudes in the first instance and F555W, F606W and F814W in the second. By doing this we note a large difference on the stellar types observed, and gain fits for an O5V and M4V templates respectively, the two extremes of our available stellar templates. This is too large a discrepancy to be explained by variability,

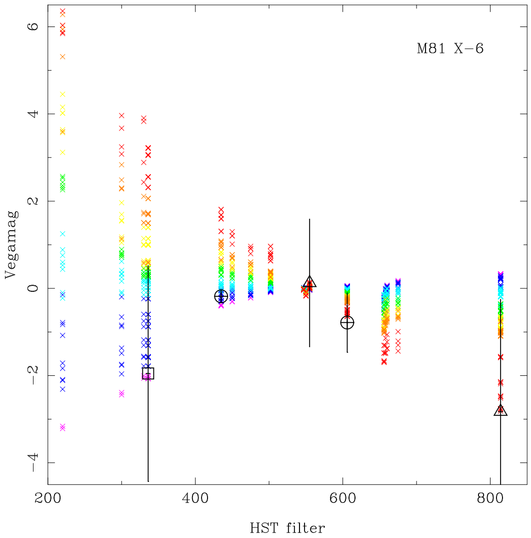

Figure 2.5: Vega magnitudes for M81 X-6, plotted against the stellar templates taken from the Bruzual-Person-Gun-Stryker atlas. The photometric magnitudes of this source has been collated over three observations, each one plotted using a different symbol. The lowest band, denoted by open squares, is from 06139_01, while 09073_01 is represented by open triangles and 10584_18 is marked by open circles.

and would seem to indicate some form of source confusion/contamination, either from some form of reddening component or by the combination of emission from two stars. To unlock the nature of this source we will need to return to the Hubble Legacy archive to gain further observations of this source, paying particular attention to any using the ACS - HRC in order to gain our clearest view of this source.

2.6 Summary

Here we present the findings of our survey of the optical counterparts to ultraluminous X-ray sources, that combines data from both the *Hubble* Legacy Archive and the *Chandra* space telescope. We collate information pertaining to those ULXs residing within 5 Mpc, and search for any potential counterparts. We find that from our initial sample of 45 ULXs, 14 have no archival data. In the remaining 31 cases we collated data from each telescope and correct the astrometry of the downloaded data. We find that while some ULXs show the presence of a unique optical counterpart, a number have either no or multiple counterparts. This analysis has revealed that 8 of our sample have no observed counterpart within the error region, although as Ptak et al. (2006) highlighted in some cases this will be due to insufficient depth in the exposures of these fields. The remaining 23 ULXs have a total of 38 potential counterparts, 24 of which are observed in multiple bands affording us the opportunity to attempt classification. We find that initial identifications of potential counterparts show no prevalence for a single stellar type. Classifications cover the wide range of types from blue OB stars to red M types, and range in size from main sequence to supergiants that are possibly reddened.

When considering the derived absolute magnitudes of these sources in the F555W filter band ($\simeq M_V$), the results are more suggestive of giants/bright giants/supergiants in the majority of cases, although some appear too bright to be explained by even the most luminous stars. The presence of such luminous objects indicates that, in some cases we are either observing foreground sources that are not related to the ULX, or that the stellar emission is brightened by emission from an irradiated accretion disc. Such emission could easily brighten the system by up to ~ 5 magnitudes (Copperwheat et al. 2007). When combining the results of best-fitting typing and absolute magnitude, we find a disparity. If instead we combine the range of possible stellar types with the derived absolute magnitude, this indicates that we are mainly observing OB type stars, along with a few later type bright giants/supergiants.

The results of this survey have also highlighted seven good candidates for optical spectroscopic follow-up, 5 of which have been successfully awarded time with the Gemini Observatory as part of our ongoing programme (NGC 1313 X-2 (1), GS-2005B-Q-30, PI: Roberts; NGC 5204 X-1 (1) & Ho IX X-1 (1), GN-2007B-Q-49, PI: Gladstone; NGC 4395 X-1(1), GN-2009A-Q-51, PI: Gladstone; NGC 253 ULX2 (1), GS-2009B-Q-8: PI: Gladstone). The two remaining good candidates Ho II X-1 (1) and NGC 5408 X-1 (1) have been awarded time on alternate programmes.

Now that this sample has been collated, it provides us with a population of potential ULX counterparts that can be used to further explore the nature of these systems. One option is to use this sample in conjunction with optical/irradiation models of ULXs (e.g. Copperwheat et al. 2005; Patruno & Zampieri 2008; Madhusudhan et al. 2008) to disentangle the emission from the different components of the spectrum (stellar and disc emission). We can also use these models to see what further information can be gleaned about the compact objects contained within these systems. Furthermore, we can use this sample to look for further signs of variability by returning to the archives to collate multiple exposures of the each field (wherever possible), to see how these systems change over time.

Chapter 3

Spectroscopy of the optical counterparts to ULXs

3.1 Introduction

Optical emission from ultraluminous X-ray sources, as discussed in Chapters 1 & 2, can potentially be composed of emission from the companion star, the accretion disc and the surrounding nebula. We would expect the spectrum of the companion star to be comprised of a continuum slope inset with various absorption and emission lines from the stellar atmosphere that aid in typing the object. Such data allows constrains to be placed on the evolutionary history of the star and in-turn, the binary system. Conversely, we would expect light from the accretion disc to contain few emission features (mainly high excitation lines) with an underlying blue continuum. Emission from a surrounding nebula could either be shock powered or X-ray photoionised, which would be indicated by the presence of either low or high excitation lines respectively.

Optical spectroscopy of ULXs could therefore provide us with the best means of understanding the nature of these sources. In particular, if distinct features are evident from either the accretion disc or the companion star, repeated observations of the system could provide radial velocity curve measurments that could be used to calculate of a mass function for the system. Such a calculation would allow us to place limits on the mass of the compact object, finally settling the long-running debate over black hole mass within ULXs, whilst emission from the surrounding nebula could help us to understand the geometry of these systems in more detail.

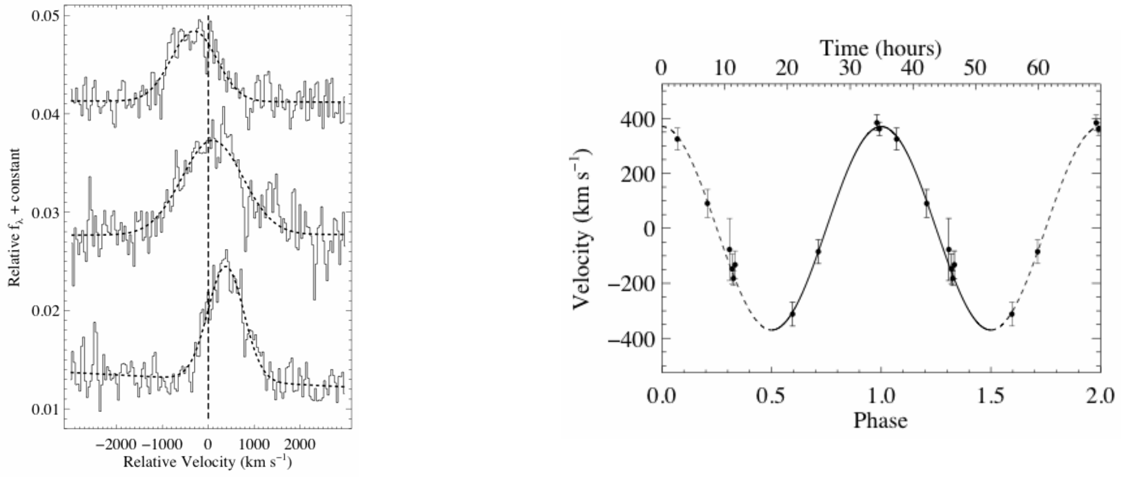

Figure 3.1: Data from the Wolf-Rayet/black hole X-ray binary IC 10 X-1. (a) Spectra of the He II 4686 Å line, de-redshifted and converted to velocity space, showing that the centroid clearly shifts with time. (b) Radial velocity curve of the He II line, relative to the [O III] 5007 Å line, two cycles are plotted for clarity. Here you can see the 34.93 hr period derived from 10 observations taken over a period of one month. Both figures are taken from Silverman & Filippenko (2008).

This is certainly not a novel approach for X-ray binary systems; one of the earliest of these studies (Cyg X-1) was discussed in Section 1.3.1. The interested reader is also referred to van Paradijs & McMintock (1995) or Charles & Coe (2006) for a more detailed discussion on the success of this method in Galactic systems.

A similar approach was recently undertaken for the analysis of an extra-galactic source. In this study a similar He II line was used to constrain the mass of the extragalactic X-ray binary IC 10 X-1, although in this case the He II line is emitted from the Wolf-Rayet companion (Prestwich et al. 2007; Silverman & Filippenko 2008). A series of 10 observations over a one-month period revealed shifts in the He II line (see Figure 3.1(a)), culminating in the radial velocity curve (Figure 3.1(b)). This provided a mass function of 7.64 $M_\odot$ that, when combined with estimates on the companion mass, gave a primary mass of 23 – 34 $M_\odot$. This is a very notable result as this is up to twice as massive as stellar black holes found in our own Galaxy.

Using the results from our optical counterparts survey, presented in the Chapter 2, we were able to highlight a number of sources available for spectroscopic follow-up. Some

Table 3.1: Gemini observations of optical counterparts.

ULX name	Source position[a] RA & Dec	Program ID	Start time[b]	Duration (s)
NGC 1313 X-2	03 18 22.34 -66 36 03.7	GS-2005B-Q-30	2005-10-08 06:12:50	9×1200
			2005-11-30 03:33:59	2×1200
Ho II X-1	08 19 30.20 +70 42 18.0	GN-2007B-Q-57	2008-01-13 09:57:07	4×1200
			2008-01-15 09:17:15	4×1200
Ho IX X-1	09 57 54.05 +69 03 47.3	GN-2008A-Q-49	2008-03-07 08:48:18	6×900
NGC 5204 X-1	13 29 38.60 +58 25 06.0	GN-2008A-Q-49	2008-07-03 06:41:13	4×720

Notes: [a]J2000 coordinates, [b]start time of observations in universal time (UT).

of these ULXs counterparts had already been identified, with time awarded to other programmes. However, successful applications have been made to the Gemini Observatory, with five of our applications for pilot observations of ULX counterparts being approved. To date, three of our optical counterpart candidates have been observed, which we present and discuss in the following work.

The spectrum of one futher candidate recently became available in the public archives of the Gemini telescope. This data was also collected from the archive to be included in our current work.

3.2 Observations

We use the Gemini Observatory to perform our observations. It consists of a pair of 8.1 metre diameter, altitude-azimuth mounted telescopes with one situated at the summit of Cerro Pachon in Chile (Gemini South) and the other on the summit of Mauna Kea on the island of Hawaii (Gemini North). Thus it offers astronomers the opportunity to observe the entire sky. Of the three observations to be considered from our programme, two were observed with Gemini North, namely Holmberg IX X-1 and NGC 5204 X-1, with the other, NGC 1313 X-2, was observed at Gemini South. We also retrieve one archival observation of Holmberg II X-1 (PI: Jifeng Liu), that was also taken with Gemini North. The details of these observations can been seen in Table 3.1.

Considering initially only those exposures taken as part of our study, each observation was taken using the Gemini Multi-Object Spectrograph (GMOS). The purpose of these pathfinder observations was to determine whether sufficiently strong emission/absorption features were evident in its ultraviolet/optical spectrum to allow for future observations to constrain the compact object mass. They were performed using the B600 grating to disperse the spectra and to optimise our sensitivity in the blue (where imaging data colours tells us sources are brightest). In each case the exposures were stepped in wavelength over a range of 10 Å, centred on the blaze wavelength of the grating (4610 Å). This procedure was used to compensate for chip gaps and to allow full spectral coverage. The overall set-up was designed to provide a spectral resolution of $\sim$ 1 Å per 2 pixel element, and a coverage of the 3250 – 6000 Å wavelength range (although signal-to-noise varies as listed below).

Our observation of NGC 1313 X-2 took place during semester 2005B on Gemini South, using the long-slit mode with a 1 arcsecond slit and 2 pixel binning in both the spatial and spectral directions. The total observation was split into 11 exposures of 20 minutes each, in order to allow for cosmic ray rejection. The exposure times were determined by the Gemini Integration Time Calculator, which indicated that such a configuration would provide a continuum signal-to-noise in excess of 5 over the range 3800 – 5050 Å.

The observations of the optical counterparts to Holmberg IX X-1 and NGC 5204 X-1 were carried out during 2008A semester on Gemini North. In each case we used the 0.75 arcsecond slit to approximately match the source PSF (in good observing conditions), while minimising the background and excluding the light from neighbouring sources. To achieve a continuum signal-to-noise in excess of 5 over the 3800 – 6000 Å range, we required a total observation time of 48 minutes for NGC 5204 X-1 (split into four twelve minute intervals for cosmic ray rejection), whilst an observation time of 90 minutes (split into six fifteen minute intervals) for Holmberg XI X-1was calculated to be sufficient to detect a continuum signal-to-noise > 5 over the range 4000 – 5250 Å.

The archival observation of Holmberg II X-1 was taken in January 2008, as part of semester 2007B. This programme was designed to look for absorption lines that could be used to confirm the O/B spectral typing of the counterpart or the presence of reprocessed emission from the accretion disc. As with our programme, the observations were made using GMOS, in long-slit mode, with the B600 grating. The PI decided, however, to centre their observations at a higher wavelength and to not step in wavelength. As a result the spectrum reaches to longer wavelengths, but retains chip gaps.

3.3 Data reduction and analysis

Data reduction was performed using the standard Gemini packages within IRAF. The first stage of this process was the reduction of the standard star. We used the GMOS package tasks to produce a normalised spectral flat field image, using the task *GSFLAT*. We also reduced, bias subtracted, and mosaicked the arc lamp exposures with *GSREDUCE*, *GSWAVELENGTH* & *GSTRANSFORM*. These calibration files were applied to the standard star exposures during reduction using the same tasks. Sky subtraction was applied, and the exposures co-added using the IRAF task *IMCOMBINE*. Finally the combined standard star image file is divided by the exposure time to create a two dimensional spectrum of the field. This step allows for calibration of observations irrespective of exposure length. A one-dimentional spectrum of the standard star was then extracted and compared to the archival spectrum of the same star, stored in the IRAF standard star directory. This provides a sensitivity function for the chip, to allow us to remove the instrumental response and to flux calibrate our observations.

A similar process was then applied to the exposures of each of our objects. The flats and arcs were processed using the GMOS package tasks *GSFLAT*, *GSREDUCE*, *GSWAVELENGTH* & *GSTRANSFORM*, which are then in-turn applied to the science exposures with *GSREDUCE* and *GSTRANSFORM*. The exposures were then combined and divided by the exposure time to allow for the application of the flux calibration file.

A portion of these two-dimensional fields can be seen in Figures 3.2, 3.3, 3.4 & 3.5. In each case we show an image of the ULX field, with the position of the ULX marked. We can also see that the nebula associated with each ULX is clearly visible. Each of these images have been taken from Pakull & Mirioni (2002). We also show an image of the two-dimensional spectra in which the wavelength is dispersed in the x direction, whilst y shows the spatial dispersal.

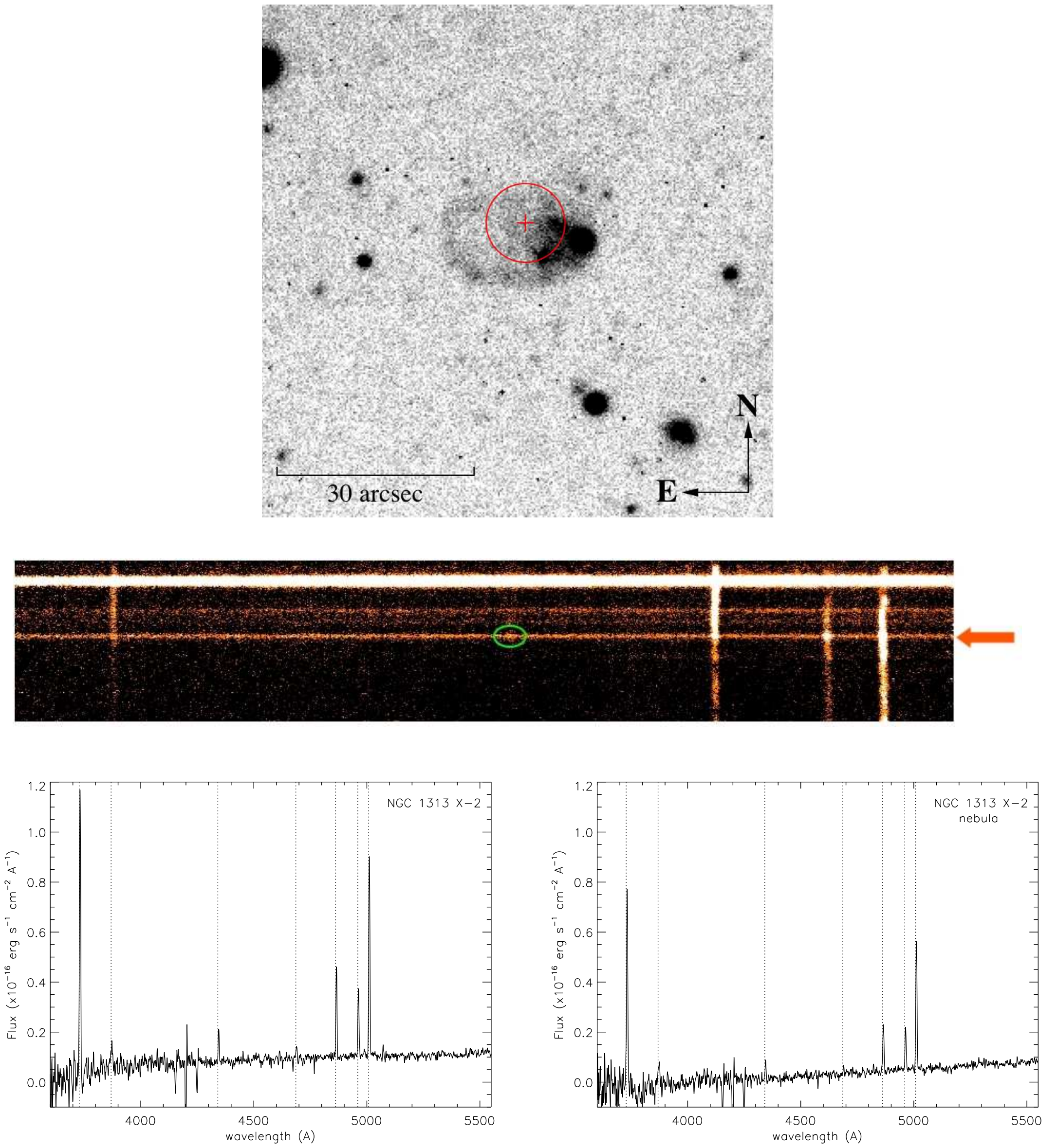

Figure 3.2: (*Top*) H_α image of the of the region around NGC 1313 X-2 (Pakull & Mirioni 2002), an alternative optical view of this ULX can be seen in Figure 2.2 (pg. 5). (*Centre*) Two dimensional spectrum of the source, (using a 1 arcsec slit) showing nebula lines and source emission. (*Bottom left*) One dimensional source spectrum for NGC 1313 X-2 marked with the positions of the [O II], [O III] doublet, H_β, H_γ and [Ne III] lines, along with the line associated with X-ray re-ionisation He II 4686 Å. (*Bottom right*) One dimensional spectrum of the nebula of NGC 1313 X-2, with same emission lines marked.

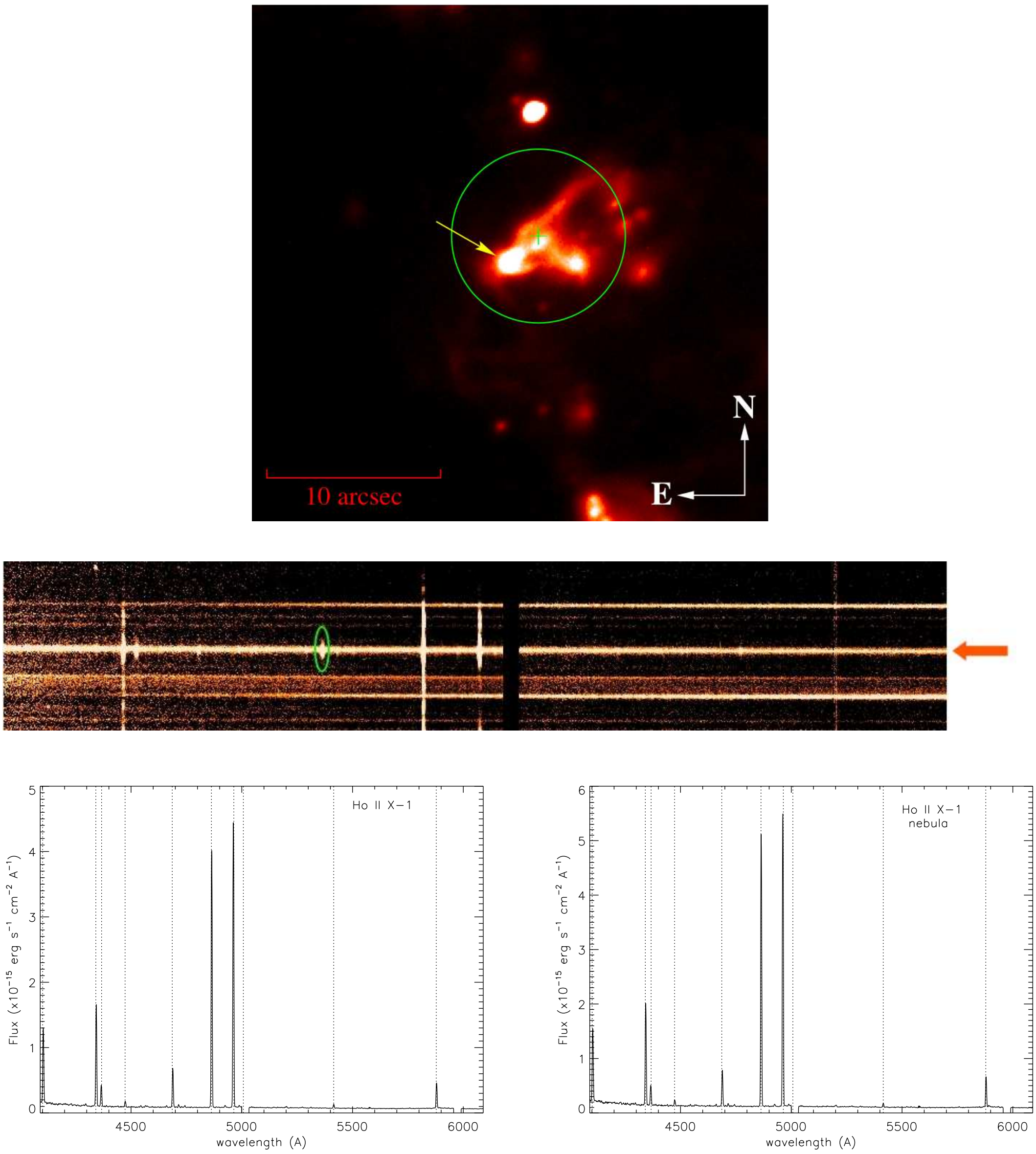

Figure 3.3: (*Top*) H$_\alpha$ image of the of the H II region HSK70 in the area of Ho II X-1 (Pakull & Mirioni 2002), an alternative optical view of this ULX can be seen in Figure 2.2 (pg. 9). (*Centre*) Two dimensional spectrum of the source, taken using a 1 arcsec slit, showing nebula lines and source emission. We note the presence of extended He II 4686 Å line, highlighted by an ellipse. This implies an extended He II region. (*Bottom left*) One dimensional source spectrum for Ho II X-1 marked with the positions of the H$_\beta$, H$_\gamma$, H$_\delta$, [O III] 4363 Å and the [O III] doublet, although unfortunately the 5007 Å line has been lost at the chip gap. We also highlight the locations of the He I 4471 & 5876 Å lines and the He II 4686 & 5413 Å line. (*Bottom right*) One dimensional spectrum of the nebula of Ho II X-1, with same emission lines marked. We can see from this that the 4686 Å line is also present in the nebula region.

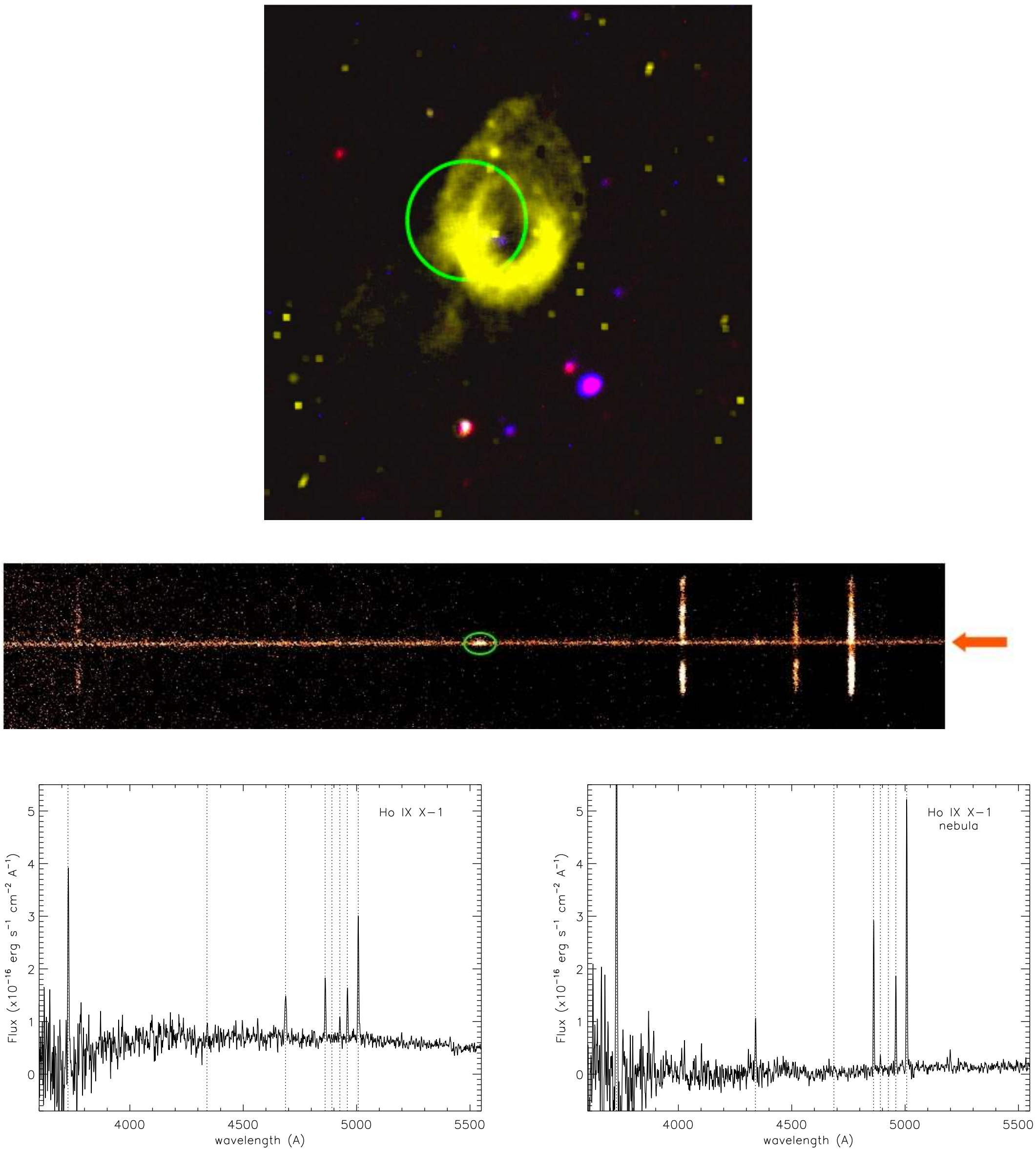

Figure 3.4: (*Top*) Optical image of the barrel-shaped nebula LH 9/10 surrounding Ho IX X-1, to demonstrate the strength of the nebula emission (Pakull & Mirioni 2002). An alternativee optical view of this ULX can be seen in Figure 2.2 (pg. 4). (*Centre*) 0.75 arcsec long slit mode slit two dimensional spectrum of the source showing strong nebula lines. We highlight the presence of a strong He II 4686 line (see ellipse), which is confined to the source region (not extended). (*Bottom left*) One dimensional source spectrum for Holmberg IX X-1, with the positions of the [OII], [OIII] doublet, H_β, H_γ and HeII 4686 lines marked. We also mark the position of two further lines, one seen in the source spectrum at 4926 Å, and one in the spectrum of the nebula at 4891Å. Each of these lines are discussed further in the text. (*Bottom right*) One dimensional spectrum of the nebula of Ho IX X-1, with the same emission lines marked.

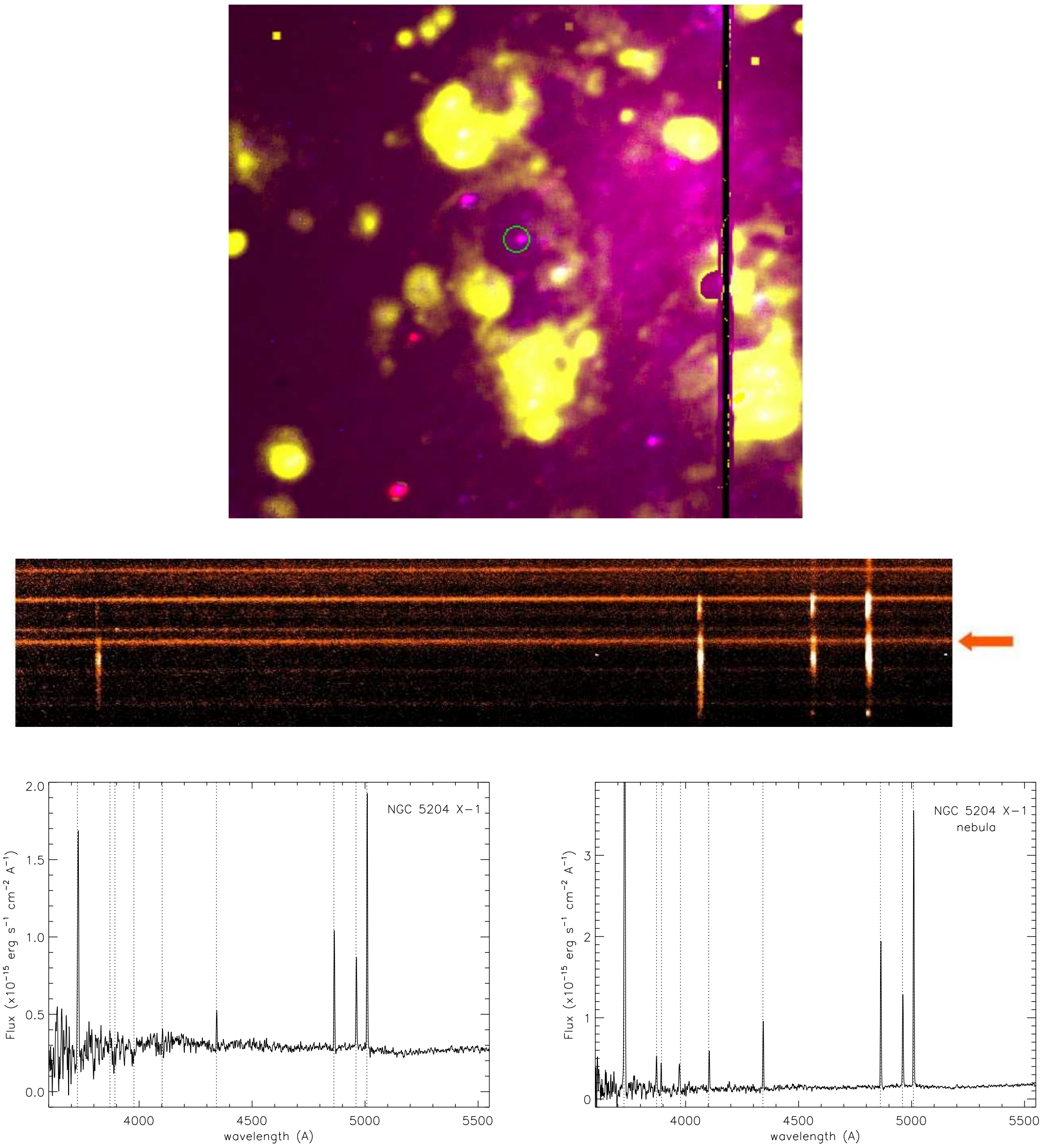

Figure 3.5: (*Top*) Optical image of the area surrounding NGC 5204 X-1, showing clearly the nebula surrounding this source (Pakull & Mirioni 2002). An alternative optical view of this ULX can be seen in Figure 2.2 (pg. 10). (*Centre*) 0.75 arcsec long slit mode two dimensional spectrum of the source showing strong nebula lines. (*Bottom left*) One dimensional source spectrum for NGC 5204 X-1, with the positions of the [O II], [O III] doublet, H_β, H_γ, H_δ, H_ϵ, H_ζ and [Ne III] lines marked. (*Bottom right*) One dimensional spectrum of the nebula of NGC 5204 X-1, with same emission lines marked.

Looking initially at the the two-dimensional spectral field, we see the counterpart is centred (and highlighted by an arrow). Whilst Ho IX X-1 appears reasonably isolated, Ho II X-1, NGC 1313 X-2 and NGC 5204 X-1 show other sources very nearby. The extended emission of the nebular lines are clearly visible in the spatial dispersion direction.

As a final step in our data reduction, we extract and plot a one-dimensional spectrum for each source, which are also shown in Figures 3.2, 3.3, 3.4 & 3.5. Alongside this, we plot a neighbouring region taken from either just above or just below the source. This region is of the same spatial size as the source extraction region, and allows us to compare the source emission with the emission lines from the surrounding area, which will mainly be emission from associated nebula. From this we are able to disentangle the source emission from that of the nebula.

We find that in each case the spectra are reasonably devoid of absorption features, but that a range of emission features are present. We also find that many of the emission lines are common to each field, for example the [O III] doublet (although the 5007 Å line is unfortunately positioned on the chip gap in Ho II X-1).

He II emission is visible in three of the sample. These are NGC 1313 X-2, Ho II X-1 and Ho IX X-1. In NGC 1313 X-2 & Ho IX X-1 it is restricted to the source track. As this emission is spatially associated with the source it is possible that it is the result of X-ray reprocessing in the accretion disc. Therefore measurements of this line could potentially be used to construct radial velocity curves of this source. As a result of this find, we have applied for a series of follow-up observations for these two sources and have been awarded ~ 50 hours of band one time, in semester 2009B, to pursue radial velocity curves, and so mass measurements of these sources.

In the case of Ho II X-1, we find we can see that this line is extended in the spatial direction, covering a region of ~ 3.9 arcseconds. At a distance of 4.5 Mpc (as listed in Chapters 2 & 5) this represents a region 85 parsecs in diameter. However, we note that authors have also quoted alternative distances to this source. Lehmann et al. (2005) quote a distance of 3.2 Mpc, whilst Kaaret, Ward & Zezas (2004) use 3.05 Mpc. This would result in a size scale of 61 & 58 Mpc respectively. At any quoted distance, a region of this size is too large to be explained by an emission from an accretion disc. We therefore discuss an alternative explanation below.

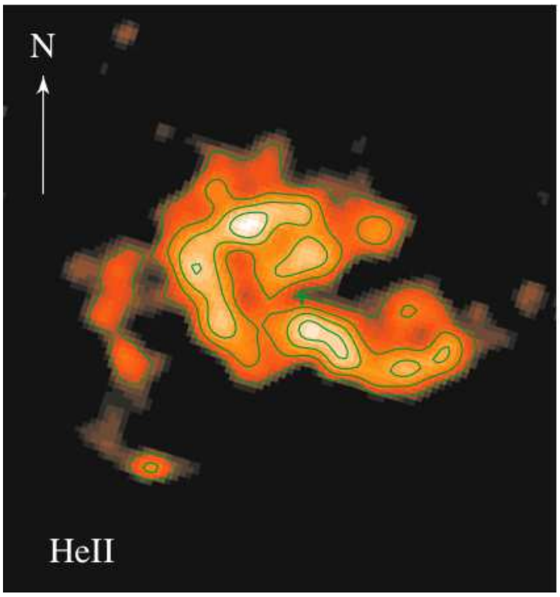

Figure 3.6: False-colour He II image of the region surrounding Ho II X-1, smoothed by a Gaussian filter with a FWHM of 0.24 arcsecs, taken from Kaaret et al. (2004). The arrow points Northwards and is 1 arcsec in length (∼ 15 parsecs), and contour levels are $\{2,3,4,5\} \times 10^{39}$ erg cm^{-2} s^{-1} arcsec^{-2}.

The extent of the He II emission in Ho II X-1 is more easily explained if the high excitation lines for He II are being emitted from the nebula. It has already been shown that the extended emission of [O II], [O III] and parts of the Balmer series (H_β, H_γ, H_δ, H_ϵ, H_ζ) are associated with the surrounding nebula (e.g. Pakull & Mirioni 2002, Abolmasov et al. 2007, Kaaret & Corbel 2009). The nature of this He II emission has been discussed previously, and the extended structure highlighted in papers by Kaaret, Ward & Zezas (2004), Lehmann et al. (2005) and Abolmasov et al. (2007). In each case the authors present a similar explanation, noting that emission feature is best described as a high-excitation nebula powered by the X-ray emission of the ULX.

The morphology of this region has been explored by both Kaaret et al. (2004) using data from the *Hubble Space Telescope* Advance Camera for Surveys (imaging was taken for a number of important lines with the He II emission image shown in Figure 3.6). Lehmann et al. (2005) took data using integral field spectroscopy at Calar Alto in Andalusia, Southern Spain, and at the SAO in Russia. Using each of these methods (and instruments), the authors find that the He II region extends over a region of 15 × 26 and 21 × 47 arcseconds respectively, with our results suggesting this region might extend slightly further. Their investigations also revealed that the overall emission from the H II region was consistent with the expected behaviour of a high-excitation region, with the highest excitation emission being concentrated around the source of X-rays around the location of the ULX. The morphology of this region also suggests that this is not powered by beamed X-ray emission, but instead is quasi-isotropic. Such a result indicates that the source of the X-ray emission must come from an intermediate mass black hole or a super-Eddington flow with little or no beaming.

Although this source is interesting and deserves further investigation, the fact that the He II emission is spatially extended (and not localised to the accretion disc) means that it cannot help in our current radial velocity curve project. Therefore we do not consider this ULX counterpart further within this chapter.

We now investigate the one dimensional spectrum for each source, and a nebular spectrum from a neighbouring region, to maximally exploit our current data. We note that as the nebula surrounds the source, nebular lines are present in both spectra, but by comparison of the two spectra we are able to look for features that are present in only the source (or nebula) spectrum. As mentioned above, we find that the spectrum of each source appears to be *almost* devoid of line emission, except the He II lines, and no significant absorption lines are observed. This implies that we may be seeing a spectrum that is dominated by an accretion disc. We therefore approach the analysis of these sources, and their environments, in two ways. We will explore the line emission (mainly from the nebula) to look for clues as to the nature of gas and dust interaction as a result of the ULX. This will allow us to look for information on metallicity of the regions, temperature, ionisation and other information that can be gleaned from observations of such a system. We will also attempt to investigate the underlying source continuum of the ULX counterpart, to see what information can be gained about the source.

3.3.1 Emission lines

The spectrum of each source was searched for both emission and absorption features using the IRAF package *SPLOT*. A number of emission lines are observed in each case. These are listed in Table 3.2 and are discussed below. As stated above, no significant stellar absorption lines were found. We also note that the three line features observed in NGC 1313 X-2 in both the source and neighbouring region spectra, at around 4200 Å, are due to a bad column on the chip. This is visible as three distinct lines as a result of the shift in wavelength applied to cover chip gaps.

We find that all the observed spectra contain the [O III] doublet (4959 & 5007 Å), and one of the [O II] 3727/3729 Å doublet. In each case we observe only the 3727 Å line, which is usually observed in an 11:2 ratio with $\lambda3729$. In all cases, the combined continuum and noise level at this wavelength is too high to allow for the detection of this secondary line. It is also possible that, at this resolution, this feature has become blended with the other [O II] feature. A portion of the Balmer series is also present. In all cases we observe the H_β and H_γ lines, but in the nebular spectrum of NGC 5204 X-1 we are also able to see H_δ, H_ϵ and H_ζ.

Of the other lines identified, one is of an unknown origin. We find an emission line in the source spectrum of Ho IX X-1 at 4926 Å. Two possible options have been identified to explain the data. The first is that we are observing the He I 4922 Å line that has been redshifted by 4 Å. As the apparent redshift of emission line remains approximately zero for the other measured lines in this source, this would suggest that the origin of this line emission would need to be associated with an alternative emission region travelling at ~ 250 km s^{-1} in comparison to the rest of the field. Such regions may be consistent with outflows from the central object (e.g. SS 433, Boumis et al. 2007), although there is a caveat to this. The He I 4922 Å is observed as a doublet with the He I 5016 Å, in a 2:1 ratio. At this level of data quality, this line should be clearly observed within the spectrum of this nebula. The non-detection of an emission line at ~ 5020 Å throws this interpretation into doubt.

Table 3.2: Optical emission lines from the ULX counterparts contained within our sample.

Line details	NGC 1313 X-2	NGC 1313 X-2 nebula	Ho IX X-1	Ho IX X-1 nebula	NGC 5204 X-1	NGC 5204 X-1 nebula
[O II] 3727 Å	3732.02±0.09 $7.2\pm0.3\times10^{-16}$ 460±20	3732.4±0.1 $4.9\pm0.3\ \times10^{-16}$ 430±20	3728.8±0.5 $2.5\pm0.5\times10^{-15}$ 400±80	3727.7±0.3 $4.2\pm0.5\times10^{-15}$ 440±60	3730.28±0.08 $2.02\pm0.06\times10^{-14}$ 420±20	3730.32±0.08 $2.10\times10^{-14}\pm0.07$ 410±20
[Ne III] 3869 Å	3872.6±10 $1.7\pm0.6\times10^{-17}$ 500±100	3872.4±1.0 $\pm0.31.0\times10^{-16}$ 900±100	– – –	– – –	– – –	3870.5±0.9 $2.0\pm0.7\times10^{-15}$ 500±100
H_ζ 3890 Å	– – –	– – –	– – –	– – –	– – –	3891.2±0.6 $8\pm3\times10^{-16}$ 230±80
H_ϵ 3970 Å	– – –	– – –	– – –	– – –	– – –	3972.3±0.6 $1.1\pm0.3\times10^{-15}$ 300±80
H_δ 4102 Å	– – –	– – –	– – –	– – –	4104.4±0.3 $9\pm2\times10^{-16}$ 230±40	4104.4±0.3 $1.4\pm0.3\times10^{-15}$ 260±50
H_γ 4341 Å	4345.0±0.1 $6.9\pm0.5\times10^{-17}$ 320±20	4344.9±0.2 $4.5\pm0.5\times10^{-17}$ 340±40	4341.0±0.6 $2.5\pm0.8\times10^{-16}$ 280±70	4340.6±0.4 $4\pm1\times10^{-16}$ 350±70	4343.34±0.10 $1.9\pm1\times10^{-15}$ 230±10	4343.5±0.1 $2.7\pm0.1\times10^{-15}$ 240±10
He II 4686 Å	4688.9±0.3 $3\pm1\times10^{-17}$ 360±50	4690.1±0.3 $1.5\pm0.3\times10^{-17}$ 190±40	4687.0±0.3 $6.6\pm0.3\times10^{-16}$ 460±40	– – –	– – –	– – –
H_β 4861 Å	4865.69±0.049 $2.01\pm0.03\times10^{-16}$ 312±6	4865.62±0.07 $1.32\pm0.04\times10^{-16}$ 340±10	4861.7±0.1 $8.1\pm0.4\times10^{-16}$ 280±20	4861.58±0.06 $1.28\pm0.05\times10^{-15}$ 280±10	4863.86±0.03 $4.25\pm0.07\times10^{-15}$ 219±4	4864.04±0.024 $7.04\pm0.09\times10^{-15}$ 21±3

Line details	NGC 1313 X-2	NGC 1313 X-2 nebula	Ho IX X-1	Ho IX X-1 nebula	NGC 5204 X-1	NGC 5204 X-1 nebula
O II 4891 Å(?)	– – –	– – –	– – –	4891.1± 0.5 $6{\pm}2{\times}10^{-17}$ 255±5	– – –	– – –
Unknown line in Ho IX	– – –	– – –	4926.0±0.3 $13{\pm}3{\times}10^{-16}$ 220±50	– – –	– – –	– – –
[O III] 4959 Å	4962.88±0.06 $1.62{\pm}0.04{\times}10^{-16}$ 320±6	4963.59±0.07 $1.15{\pm}0.04{\times}10^{-16}$ 330±10	4959.6±0.1 $6.5{\times}10^{-16}{\pm}0.4$ 260±20	4959.33±0.09 $7.8{\pm}0.4{\times}10^{-16}$ 240±10	4961.65±0.04 $3.25{\pm}0.06{\times}10^{-15}$ 239±5	4961.68±0.03 $4.67{\pm}0.08{\times}10^{-15}$ 221±4
[O III] 5007 Å	5011.04±0.02 $4.95{\pm}0.04{\times}10^{-16}$ 317±2	5011.51±0.03 $3.49{\pm}0.03{\times}10^{-16}$ 339±4	5007.34±0.06 $1.71{\pm}0.04{\times}10^{-15}$ 323±7	5007.16±0.03 $2.39{\pm}0.04{\times}10^{-15}$ 250±5	5009.4±0.02 $8.77{\pm}0.07{\times}10^{-15}$ 220±2	5009.58±0.01 $1.375{\pm}0.009{\times}10^{-14}$ 207±1
N I 5198/5200 Å	– – –	– – –	– – –	5199.0±0.4 $1.2{\pm}0.3{\times}10^{-16}$ 170±60	– – –	– – –
H_γ/H_β [a]	0.34±0.02	0.34±0.03	0.31±0.10	0.31±0.08	0.4±0.2	0.39±0.02
$E(B-V)_H$ [b]	0.73±0.4	0.74±0.07	1.0±0.3	0.9±0.2	0.14±0.06	0.43±0.02
N_H [c]	$2.50{\times}10^{21}{\pm}0.2$	–	$1.62{\times}10^{22}{\pm}0.09$	–	$5.0{\times}10^{20}{\pm}1.0$	–
$E(B-V)_{Xb}$ [d]	0.43±0.3	–	0.28±0.02	–	0.09±0.02	–
$E(B-V)_{Xr}$ [e]	0.59±0.5	–	0.36±0.02	–	0.07±0.01	–

Notes: The three numbers listed are the observed wavelength (Å), the flux (erg s^{-1} cm^{-2})and the FWHM (km s^{-1}) of the emission line. Specific notes: [a]Balmer decrement taken from the H_β and H_γ emission lines, [b]extinction value derived form the Balmer decrement, [c]X-ray absorption derived from fits of a physically motivated model (Galactic absorption included), taken for each ULX from Section 5.4.6, [d]extinction value calculated using the value for X-ray absorption, derived using ratio from Bohlin, Savage & Drake (1978), [e]extinction value calculated using the value for X-ray absorption, derived using equation from Reynolds et al. (1997).

Another possible explanation arises from studies of quasars and high Eddington ratio emitting supermassive black holes. The spectrum of such sources show similar emission lines, with many exhibiting the [O III] doublet, [O II] doublet and a section of the Balmer series (e.g. Hu et al. 2008). There is also evidence for the highly photoionised He II 4686 Å line (e.g. Boroson 2002). The spectra of these systems also includes a Fe II 4924 Å line, which could explain the observed emission (with a 2 Å offset). In these systems this emission is linked to the broad line regions. If we now scale this down to a ULX, and combine this with current theories on the nature of these systems, it could indicate that we are observing emission from an outflowing wind. This would account for the slight redshift in this emission line (in comparison to other lines in the spectrum). Such an outflow could be driven by the radiation instability at Eddington or super-Eddington rates. This would also lend further support to the suggestion that these systems are powered by stellar mass black holes.

There is also a problem with this theory; once again the suggested line is part of a doublet, with the other member of this pair located at 5018 Å. It is noted that this line is usually blended with the higher of the [O III] doublet lines, and so is not always detected (for example see figure 1 in Hu et al. 2008). This should not be the case here as we are observing much narrower emission lines, and so the 5018 Å line should be clearly resolved. Another issue is that these two emission lines are usually paired with two broad emission humps, peaking at a similar flux, but centred around 4510 and 5250 Å. Neither of these features are present above the continuum level. We are therefore unable to explain the emission of this line at present.

We also note the presence of a possible O II emission line in the nebula of Ho IX X-1. It is positioned at 4891 Å. This line is unconfirmed at present, but has been noted for its previous associations with planetary nebula (e.g. Meinel, Aveni & Stockton 1981).

Balmer decrement and extinction

The first stage in our analysis is to look for signs of reddening intrinsic to either the host galaxy or the region of the ULX. To do this we use the Balmer decrements to provide a value for the extinction of this source. This will be compared to Galactic values and extinction values derived from the dust-to-gas ratio.

The Balmer decrement provides a classic method for determining the amount of dust extinction for a source, by using the relative ratios of the Balmer lines in the source spectrum. Here we also apply the same method to the emission lines observed in the neighbouring regions, to see if the reddening is constant across the ULX nebula.

The standard approach is to use a combination of the H_α/H_β H_γ/H_β & H_δ/H_β ratios to calculate E(B – V) for the source. Unfortunately the H_α lies outside our band pass and H_δ is too weak in the majority of cases as it is lost in the continuum and noise. We are only able to take measurements of this line in NGC 5204 X-1. We are, however able to calculate values E(B – V) using just the H_γ/H_β ratio for each field (Reynolds et al. 1997). This is done using the following equation:

$$E(B-V) = a\log\left(\frac{R}{R_{intr}}\right)$$

where R is the Balmer decrement, R_{intr} is the intrinsic Balmer decrement, and a is a constant defined by the standard interstellar extinction curve of Osterbrock (1989). The intrinsic Balmer decrements for H_γ/H_β and H_δ/H_β are 0.474 and 0.262 respectively, whilst $a_{\gamma/\beta} = -5.17$ and $a_{\delta/\beta} = -3.52$ (Reynolds et al. 1997).

The E(B – V) values, derived from H_γ/H_β, are listed at the bottom of Table 3.2. We also calculate the E(B – V) using H_δ/H_β from the nebula of NGC 5204 X-1, and obtain a value of 0.44 ± 0.04. This is similar to the value derived for the H_γ/H_β. When we calculate the H_δ/H_β extinction values for the source spectrum, we obtain a value of 0.32 ± 0.02, which is more than twice that of the H_γ/H_β value. This still indicates the presence of large variation in absorption across the field but also suggests a possible variation in inonisation. For consistency within our sample, we will only consider the E(B – V) values calculated using the H_γ/H_β ratios in the remainder of this text.

If we look again at the extinction values for NGC 5204 X-1, and its associated nebula, we find a large difference. The extinction in the neighbouring region has increased by more that a factor of 3. This would suggest that the variation in extinction is intrinsic to the system, and may not be related to the wider galaxy. Previous studies of this source, and its environment have revealed an apparent cavity in the surrounding interstellar medium (Roberts et al. 2001). A cavity centred on the ULX could account for the varied extinction coefficients across such a small region of the NGC 5204, if interaction between the inter-stellar medium, the nebula and (possibly) outflows from the ULX resulted in denser patches of material surrounding the source, which has minimal impact along the line of sight.

We now compare the calculated extinction values with the Galactic values that were listed in Chapter 2 (see Table 2.1). We see that the Galactic E(B – V) are 0.110, 0.079 & 0.013 for NGC 1313 X-2, Ho IX X-1 & NGC 5204 respectively. As we noted in Chapter 2 the Galactic extinction can only give a lower limit to the total extinction. We find in each case there appears to be a remarkable difference in the Galactic and total extinction values. This suggests that there is a large amount of extinction intrinsic to the host galaxy or the ULX environment (c.f. NGC 5204 discussion above).

There is another approach that can be used to gain an estimate on the total extinction column observed in the direction of the source. It is calculated by combining the observed X-ray absorption of the source and a gas-to-dust ratio. Here we initially consider the N_H/E(B – V) relation presented by Bohlin, Savage & Drake (1978). In order to calculate this we require values for the X-ray absorption of each source. We obtain these values from fits of physically motivated models to high quality X-ray data of each of these sources (see Chapter 5). Using these values, we are able to calculate $E(B-V)_{Xb}$. Bohlin et al. (1978) carried out this research using the *Copernicus* satellite, and considered stars locally within our galaxy. Later work by Bouchet et al (1985) focused on the SMC, finding the gas-to-dust ratio to be higher than the Galactic value. If we now apply this ratio, we find that our extinction estimates are reduced to 0.01 – 0.05. In some cases this is lower than the Galactic values, we therefore do not consider this relation further. However, a further cold gas-to-dust ratio was discussed in Reynolds et al. (1997). In this case $N_H = 2.14 \times 10^{20} + 3.91 \times 10^{21} E(B-V)$ cm^{-2}. The extinction values calculated using this method are also listed at the bottom of Table 3.2, and are labelled with $E(B-V)_{Xr}$. We find in each case that these are similar to those calculated using Bohlin et al. (1978).

If we now compare the E(B – V) values derived from difference methods, we find that the extinction calculated from the Balmer decrement is higher than those derived using the gas-to-dust ratio. This implies that the gas-to-dust ratio found within our own Galaxy is different to those in the host galaxies of the ULXs (or in the area local to the ULX). There are two possible reasons for this. Either the gas-to-dust ratio in each of these galaxies is lower than that observed locally, or this is a result of something intrinsic to the ULX environments. If we consider once again the large variation in extinction observed between NGC 5204 X-1 and its environment, this could be further evidence of an interaction between the ULX and the surrounding inter-stellar medium, possibly fuelled by outflowing material from the ULX. Such massive outflows do not occur in the standard accretion states and so this would indicate that we are not looking at an IMBH, but are observing a stellar mass black hole in a super-Eddington accretion state.

Another method used to determine the amount of reddening observed in the spectrum is to calculate the value of A_v. This term can then be used in combination with a wavelength dependent term (defined by a chosen reddening law) to correct spectra for the effects of reddening. It can once again be determined by the use of the Balmer decrement, or alternatively Paschen lines, in ratio with Hydrogen lines. Unfortunately all the Paschen lines lie outside our band pass, we are therefore left with only the Balmer decrement term (Ward et al. 1987). This is

$$A_v = 6.67\log\left(\frac{H_\alpha}{2.85H_\beta}\right)$$

Once again we are unfortunate in the fact that H_α falls outside our band pass. So we are therefore unable to determine this reddening parameter from this data.

Density, temperature, abundance and metallicity

There are a number of standard line ratios that can be (and have been) applied to the spectra of ULXs and their associated nebulae (e.g. NGC 5408, Kaaret & Corbel 2009). The first of these diagnostics uses the [O II] λ3727/3729 or [S II] λ6716/6731 line ratios to estimate the electron density of the region (Osterbrock & Ferland 2006). As we state above, we are unfortunately unable to detect the [O II] 3729 Å line, and our coverage does not extend to the [S II] lines. We are therefore unable to to use these standard density indicators with our current sample.

To estimate the electron temperature of the nebula, the standard approach is to use a ratio of the [O III] lines ($(f_{\lambda 4959} + f_{\lambda 5007})/f_{\lambda 4363}$) (Osterbrock & Ferland 2006). Some other line ratios can also be used in the same way, for example [Ne III] lines ($(f_{\lambda 3869} + f_{\lambda 3968})/f_{\lambda 3343}$) or [S III] lines ($(f_{\lambda 9531} + f_{\lambda 9069})/f_{\lambda 6312}$). Unfortunately the [S III] lines

Table 3.3: Values of abundance related line ratios and the R_{23} diagnostic.

Source	[O III]/H_β	He II/H_β	R_{23}	[OII]/[OIII]
NGC 1313 X-2	2.46	0.15	6.85	1.45
NGC 1313 X-2 nebula	2.64	–	7.23	1.40
Ho IX X-1	2.11	0.81	6.00	1.46
Ho IX X-1 nebula	1.87	–	5.75	1.75
NGC 5204 X-1	2.06	–	7.58	2.30
NGC 5204 X-1nebula	1.95	–	5.60	1.53

lie outside our current band pass, as does one of the emission lines required for the [Ne III] line ratio. This leaves just the ratio of [O III] lines. Osterbrock & Ferland (2006) do note, however, that there can be difficulty in observing the [O III] 4636 Å emission line. This problem is confirmed by the non-detection of this line in our current sample of ULX spectra. We are therefore unable to derive a temperature in this way. Osterbrock & Ferland (2006) go on to note that when this occurs, it has become convention to adopt the empirical relationships derived form H II regions, to allow for the comparison of similar systems. This has lead to the use of [O III]/H_β and He II/H_β line ratios in ULX nebulae, and the R_{23} diagnostic. We shall, therefore consider each of these in turn (see Table 3.3 for derived values).

The first of these line ratios is [O III]/H_β, and can provide information of the abundance and metallicities of the region, including the O^{++}/H^{+} ratio. To do this effectively, we would need to incorporate information on the temperature of the system. One solution to this is to perform a comparative exercise with similar source, using ratios from other surveys of ULX populations. A study by Abolmasov et al. (2007) suggested that sources with an [O III]/H_β ratio of 3 – 7 would be classified as group A, whilst those with lower ratio would be classified as group B. Those in group A are said to show signs of photoionisation that would require the presence of a strong extreme ultraviolet or X-ray source, whilst those in group B are more likely to be shock ionised. If we now compare our sources to this criteria we find that in each case this line ratio would fit into group B, suggesting that the emission is shock-ionised. An alternative approach is to combine this information with the [O II]/[O III] ratio to extract the information required to classify the region. Using Baldwin, Phillips & Terlevich (1981), we are able to see that this approach also indicates that we are observing some evidence of shock ionisation.

It is interesting to note that our sample overlaps with that of Abolmasov et al. (2007), is that both studies include Ho IX X-1 & NGC 5204 X-1. Abolmasov et al.'s (2007) study indicated that NGC 5204 X-1 was included in their group A classification, whilst Ho IX X-1 was classified as group B. This would indicate that NGC 5204 X-1 was powered by photoionisation. However, the nebula of this source may have an irregular structure, 'bright' patches have also been observed in the in the [O II] flux maps of the systems (see figure 6 in Abolmasov et al. 2007). These patches could easily complicate the emission from this system, and the resulting spectrum would be dependant on slit orientation and 'patches' observed. We therefore propose that the structure of this nebula, and the surrounding interstellar medium, could show a combination of both shock and photoionisation. To clarify this matter, and confirm the structure and nature of this region, we would require high quality IFU data of the regions, covering a wider band pass. This would allow a detailed survey, across the nebula, using the complete classification systems of Baldwin et al. (1981).

The He II/H_β allows us to explore further the ionisation of the source, by comparing the relative intensity of the ionising flux required to produce these two lines. It therefore gives an indication of the amount of UV flux that is present in the system. As noted earlier, the He II line is only present in the spectrum of two of our sample. Therefore, we are only able to consider this line ratio for the source spectra of NGC 1313 X-2 and Ho IX X-1 (see Table 3.3).

Initially we consider NGC 1313 X-2, finding that it has a He II/H_β ratio of ~ 0.15. This is comparable to the results observed elsewhere (e.g. Ho II ~ 0.22, Kaaret, Ward & Zezas 2004; NGC 5408 X-1 ~ 0.38, Kaaret & Corbel 2009; a survey revealed He II/$H_\beta \sim 0.04 - 0.17$ across four sources, Abolmasov et al. 2007; NGC 6946 X-1 ~ 0.2, Abolmasov et al. 2008). If we now consider the ratio gained from Ho IX X-1, we find HeII/$H_\beta \sim 0.81$. Such a result is extremely high when compared to ratios for other sources. This may be due to the origin of the line emission, which in most cases has been attributed to the nebula surrounding the ULX. In this case we are likely observing emission associated with the accretion disc. As the accretion disc is located much closer to the origin of the X-rays, a greater proportion of high energy photons would be incident upon the source, and this could therefore power a much higher ionisation ratio.

Finally we attempt to apply the R_{23} diagnostic to our sample, following the method of Kewley & Dopita (2002). This indicator was first suggested by Pagel et al. (1979), as a method of gaining further insight into the nature of H II regions, when the standard line ratios were unattainable. This diagnostic is defined as

$$R_{23} = \frac{[\mathrm{O\,II}]\lambda3727 + [\mathrm{O\,III}](\lambda4959 + \lambda5007)}{H_\beta}$$

This ratio is sensitive to abundance, and can also give an indication of the metallicity of the region and a range of possible temperatures. Using this we find that R_{23} covers the range 5.6 – 7.2, indicating that in each case we are observing sub-solar metallicities (Kewley & Dopita 2002). Sub-solar metallicities are also in good agreement with the findings of other multi-wavelength studies of ULXs and their environments (e.g. Mapelli, Colpi & Zampieri 2009). This also indicates the presence of a moderate oxygen abundance and an average electron temperature in the range $7 - 10 \times 10^3$ K (Pagel et al. 1979). When comparing this ratio value to that provided by other authors, we find that our results are similar (e.g. NGC 5408 X-1, $R_{23} \simeq 5.4$, Kaaret & Corbel 2009; NGC 6946 X-1, $R_{23} \simeq 9$, Abolmasov et al. 2007).

3.3.2 Continuum emission

We now consider the continuum emission for each of our sample. There are four possible scenarios available to explain the observed continuum of these source. The first is that we are looking at stellar emission from the secondary star residing in an X-ray binary system. A spectrum such as this would be similar to that observed in Galactic high mass X-ray binary systems, where emission is dominated by the secondary star, although irradiation of the stars surface may lead to $\lesssim$ 10 per cent variation in the optical light curve and some small changes in the spectrum (see Chapter 1 and van Paradijs & McClintock 1995). The second option is that the accretion disc within the X-ray binary system has become the dominant optical emission source within the binary system, in which case we expect to observe the low energy tail of the disc. The spectra of such a source should be easily fit by a power-law slope $\simeq$ -3 (e.g. Greenhill, Giles & Coutures 2006). The third possibility is that the stellar and disc emission are comparable, and we are therefore observing two component spectra. Such an effect would also be observed if the emission from the system was contaminated by another source of similar magnitude in the vicinity of our system. The final option is that we observing emission from an object that is not associated with the ULX. This could either be an object in the vicinity of the ULX, located within its positional error circle, but which is not the binary counterpart, or it could be a foreground or background interloper that is unfortunately positioned in our line of sight.

In order to explore the continuum emission of the source we would ideally de-redden the spectra and perform local background subtraction. As we were unable to calculate a value for A_v using the Balmer decrement (although this can be found for E(B – V) values), the first of these becomes difficult. We therefore opt to fit only over the range 5000 – 6000 Å, to minimise the effects of reddening processes. We perform local background subtraction using a region of the same spatial size to removed emission from the nebular and ULX environment. This provides us with a first order approximation of the source spectrum.

Following the example of Kaaret & Corbel (2009), a power-law is then fit to the continuum slope. The best fitting spectral index was found to be -4.0 ± 0.3, -4.8 ± 0.2 & -2.7 ± 0.3 for NGC 1313 X-2, Ho IX X-1 & NGC 5204 X-1 respectively. The first two of these (NGC 1313 X-2 & Ho IX X-1) are very steep, steeper than would be expected for emission from an accretion disc, whilst the spectrum of of NGC 5204 X-1 shows a similar slope over the 5000 – 6000 Å range. This would indicate that the spectrum of NGC 1313 X-2 and Ho IX X-1 are not that of a standard optically thick geometrically thin accretion disc.

In order to compare our spectra to stars, it would be standard practice to try and fit these with stellar templates to match the absorption lines and the continuum emission. As our spectrum is devoid of absorption lines, we approach this in a slightly different manner. We instead collate the spectra of a range of O and B type stars and fit a power-law to their spectra, also over the 5000 – 6000 Å range. This reveals that the spectral index for these stellar types lies in the range $\sim$ -2.4 – -3.2. If we now combine this with the results from the ULX spectra, we find that NGC 5204 X-1 could be equally explained by the presence of an OB star, while NGC 1313 X-2 and Ho IX X-1 are still too steep to be explained by emission from an individual OB star. As an aside, on inspection of the stellar templates we also find that the main absorption features found in OB type stars are coincident with the emission lines found in the associated nebula. We therefore suggest that any stellar absorption features could have been washed out by the nebula rather than the presence of an accretion disc.

The steepness of the slope would indicate that in each case, we are not looking at a pure stellar spectrum. This rules out the possibility that we are observing a neighbouring object that is not contained within the binary system. If we consider the possibility that these objects are not associated with the ULX, but are in fact foreground/background objects. We must rule out the possibility that we are observing a foreground star, because as we have said above, we are not looking at a pure stellar spectrum. However, at present we cannot rule out the possibility that we are observing a background source of non-stellar origin.

If we now consider the optical emission from an X-ray binary system, the steep spectral slope in the continuum of these sources is still difficult to explain. We know that the optical tail of a standard Shakura – Sunyaev disc can be modelled by a power-law with a slope of -3, but if we are observing a stellar mass black hole in a super-Eddington accretion state we speculate that we might not expect to see the same emission. Further investigation, with higher quality data, will be required to settle this. We, therefore, await the arrival of our new observations in order to explore these sources in more detail.

Future work

To explore these sources in more detail we can apply a reddening correction to the spectrum of each source, using the derived E(B-V) values. Initially we do this for only one source to demonstrate its potential. In Figure 3.3.2 we show both the observed (black) and intrinsic (magenta) spectrum of Holmberg IX X-1 plotted using differing y axis scales (magenta - left, black - right). This is done using the tool *CCM_UNRED* from the IDL astronomy Library[1]. This uses the reddening curve of Cadelli, Clayton & Mathis (1989), which is used in combination with the the E(B − V) values from Table 3.2. We can see a dramatic difference in the shape of the spectrum, and with reddening accounted for we are able to see the intrinsic underlying continuum of the source. The resulting spectrum appears similar to young stellar spectral types. To test this further, we can then be compare this to a

---

[1] More information on *CCM_UNRED* can be found out `http://idlastro.gsfc.nasa.gov`.

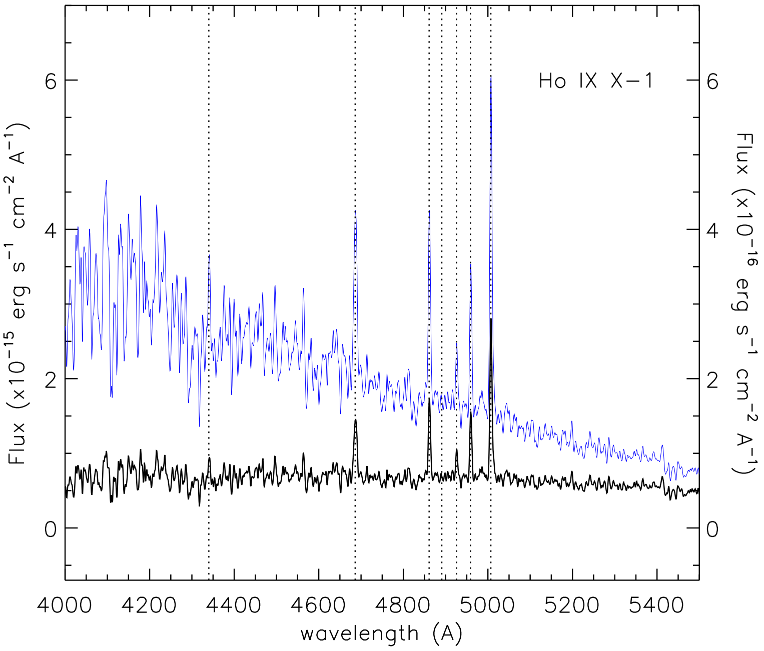

Figure 3.7: One dimensional source spectrum of Holmberg IX X-1; observed spectrum is shown in black in accordance with right hand y-axis, while the magenta spectrum is the intrinsic spectrum on the source plotted using the scale on the left hand y-axis..

range of stellar templates using a method similar to that outlined in Chapter 2, to explore the nature of these systems. As mentioned earlier in both this chapter, and the previous chapter, we would also expect to see emission from the accretion disc. Therefore, we can also compare the spectrum of this source to that of an accretion disc. This will allow us to further explore these systems and begin to understand more about their geometry.

3.4 Summary

The primary aim of the work contained within this chapter was to search the spectra of identified ULX counterparts in the hopes of identifying features that would allow us to obtain radial velocity curve measurements of ULXs in order to settle the mass debate. We find that two of the spectra contain the high ionisation line He II, which may be associated with the emission from an accretion disc. This emission line has been linked with X-ray re-ionisation for many years, and has been used repeatedly for radial velocity studies in Galactic X-ray binary systems (van Paradijs & McClintock 1995; Charles & Coe 2006). The identification of these lines has allowed us to successfully apply for further time on the Gemini telescopes for a multi-observation spectroscopic study of these two candidates (NGC 1313 X-2 & Ho IX X-1).

In order to gain more information on the nature of these systems we have explored their spectra further, whilst comparing this emission to a neighbouring spatial region. The aim of this comparison was to disentangle source emission from that of the associated nebulae. We find in all cases that the emission appears devoid of intrinsic absorption features, but we explore both the emission line features and the continuum of each source.

Emission line ratios have been examined in order to investigate the environment of the ULX, and any features associated with the source. We observe high excitation He II lines in the source spectra of two of our sample, as is outlined above. When the emission from these lines is combined with measurements of H_β, we find evidence of a small amount of photoionisation in the spectrum of NGC 1313 X-2, while a striking amount is observed in seen in Ho IX X-1. We speculate that the high levels of photoionisation are due emission from an accretion disc. However, the [O III]/H_β & [O II]/[O III] ratios show some evidence for shock ionisation within the nebular of our three systems. This indicates that the emission from these systems comes from separate regions of photo and shock ionisation, as can be seen in some galaxy centres (e.g. Maxfield et al. 2002). Finally, the R_{23} ratio indicates that we are observing a region of sub-solar metallicity, and an electron temperature of 7,000 – 10,000 K.

When we consider the Balmer decrement, we find that extinction can be highly variable across the field. This is most prominent in the spectrum of NGC 5204 X-1, where extinction can vary by $\sim$ factor 3 across the nebula. We speculate that this could be due to an interaction between the ULX and the surrounding inter-stellar medium, possibly fuelled by outflowing material from the ULX. If this is the case, it would indicate that we are observing stellar mass black holes accreting at super-Eddington rates.

When exploring the continuum emission of these sources we find that the spectrum of NGC 5204 X-1 is well fit by a power-law with a spectral index of -2.7 ± 0.3 in the

5000 – 6000 Å range. This slope can be explained by either a stellar object of type OB or by a standard accretion disc. However we find that NGC 1313 X-2 and Ho IX X-1 are well fit by a slope of $\gtrsim$ -4. The only certainty in this case is that this cannot be explained by purely stellar emission. This slope might also indicate that we are not looking at a standard accretion disc, so we speculate that the steep slope could be a result of a super-Eddington accretion in the system. Further analysis would need to be performed with higher quality data to resolve this.

Chapter 4

The ULX population in NGC 4485 and NGC 4490

4.1 Introduction

NGC 4485 and 4490 are, at a distance of only ~ 7.8 Mpc, amongst the handful of nearest interacting pairs of late type galaxies. At this distance their separation is a mere ~ 8 kpc. Their closest encounter occurred about 0.4 Gyr ago and has produced tidal features in both galaxies (Elmegreen et al. 1998). NGC 4490 shows evidence for a high star-formation rate pre-dating the encounter, that drove an outflow of H I gas. The passage of NGC 4485 through this extended cloud is now stripping the smaller galaxy's own interstellar medium through ram pressure stripping (Clemens, Alexander & Green 2000). H_α imaging shows the ongoing star-formation to be predominantly located in the tidal arms between the galaxies, with additional activity to the west of the nucleus of NGC 4490, and in a northern spiral arm (Thronson et al. 1989). Previous X-ray observations of these galaxies have shown that the galaxies are relatively bright in X-rays, as a result of the ongoing star-formation (Read, Ponman & Strickland 1997; Roberts et al. 2002, this paper is referred to hereafter within this chapter as RWWM02), and most remarkably, this pair of small galaxies is host to a relatively large population of six ultraluminous X-ray sources (ULXs), compared to a typical galaxy hosting < 1 (Liu, Bregman & Irwin 2006). In fact, within 10 Mpc the only comparable systems for hosting ULXs are M82 and M51, making the NGC 4485 & 4490 pair one of the key targets for studying populations of these extraordinary X-ray sources. As few large populations of ULX populations exist, many studies to date

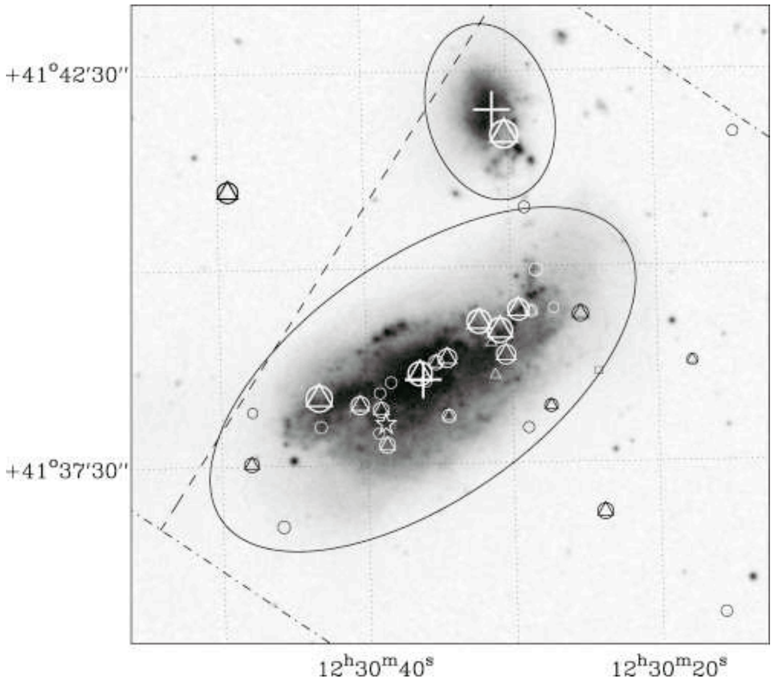

Figure 4.1: DSS-2 blue image of NGC 4485 & 4490 with Chandra X-ray source detections overlaid (taken for RWWM02). Source detections are marked as follows: soft band (0.3 – 2.0 keV) by open circles, hard band (2 – 10 keV) by open triangles, the optical nucleus of each galaxy is denoted by a large cross, and the position of SN 1982F by an open star. It should be noted that the size of each marker scales logarithmically with the source count rates. Finally, the D_{25} ellipses are shown by a solid line while the limits of the ACIS-S array and the divide between the S2 and S3 chips (S2 to the top left) are also shown by dot-dashed and dashed lines, respectively.

have focused on individual sources, a discussion of which can be seen in the Introduction. This galaxy therefore provides us with an excellent opportunity to explore a large data set with few observations.

To date, X-ray spectral analysis has been unable to uniquely determine the nature of ULXs. One option is to turn to a broader band pass in an attempt to find counterparts to these sources (see Chapters 2 & 3 for more details). Alternatively, others have chosen to carry out X-ray variability studies on these highly luminous systems, to compare to the known variability characteristics of stellar mass sources and AGN on both short and long time-scales. The analysis of temporal variability for both stellar and supermassive black holes via power spectral densities (PSD) has shown a scaling by mass and accretion rates of the PSD break time-scales (e.g. McHardy et al 2006). Unfortunately very few ULXs show much variability power, but some measurements have been made, for example Soria et al (2004) detected a break at 2.5 mHz in the PSD of NGC 5408 X-1, which they interpreted as indicating a mass of $\sim 100\ M_{\odot}$. In fact, intra-observational studies have revealed that only $\lesssim 15$ per cent of ULXs exhibit measurable short-term variability (Swartz et al 2004; Feng & Kaaret 2005).

Problems arise when extending variability studies to longer time-scales because few sources have been regularly observed. Unlike their Galactic stellar mass counterparts or the brighter quasars, which can be monitored daily by instruments such as the All Sky Monitor on board the *Rossi X-ray Timing Explorer*, analysis can only be carried out using pointed observations. This leads to large gaps in the light curves, making it difficult to track the trends of these systems. However, findings to date show that ULXs tend to be persistent over time-scales of $\gtrsim 10$ years (e.g. Roberts et al. 2004). One avenue that remains under-explored is that of spectral variability. These studies suffer from the same windowing issues discussed above, making it difficult to observe spectral evolution in detail. Some studies have been performed, such as the investigation into the X-ray source population of the Antennae performed by Fabbiano et al (2003). This, along with other studies, found that the majority of ULXs display a general hardening as the luminosity of the system increases (e.g. Homberg II X-1, Dewangan et al. in 2004; NGC 5204 X-1, Roberts et al. 2006).

In 2002, Roberts et al. published results from a 20 ks *Chandra* ACIS-S observation of the interacting galaxy pair NGC 4485 and NGC 4490. Initially their work entailed a study of the general X-ray emission from the pair, considering the emission from both diffuse and discrete sources. A total of 29 discrete sources were found to be coincident with NGC 4490 and one with NGC 4485, with luminosities ranging from $\sim 2 \times 10^{37}$ to 4×10^{39} erg s^{-1} (see Figure 4.1). Of these, six were identified as emitting at ultraluminous rates.

Table 4.1: Recent X-ray observations of NGC 4485 and NGC 4490.

Label	Observatory	Detector	Obs ID	Mode
C1	*Chandra*	ACIS-S	1579	FAINT
X1	*XMM-Newton*	EPIC	0112280201	Full Field
C2	*Chandra*	ACIS-S	4725	VFAINT
C3	*Chandra*	ACIS-S	4726	VFAINT

Label	Date	Time[a]	Exposure[b]	Aimpoint[c]	
			(ks)	RA	Dec
C1	2000:11:03	01:24:04	19.7	$12^h\ 30^m\ 31^s.2$	$+41^o$ 39' 00"
X1	2002:05:27	07:15:20	12.8	$12^h\ 30^m\ 30^s.28$	$+41^o$38'53".8
C2	2004:07:29	20:44:43	39.0	$12^h\ 30^m\ 31^s.2$	$+41^o$ 39' 00"
C3	2004:11:20	06:30:59	40.1	$12^h\ 30^m\ 31^s.2$	$+41^o$ 39' 00"

Notes: [a]Exposure start time in universal time (UT). [b] Instrument ontime (for EPIC we quote the pn value). [c]J2000 coordinates.

Here we revisit the data presented within RWWM02, combining this with information from subsequent *Chandra* and *XMM-Newton* observations in order to better explore the behaviour of these ULXs on both short and long time-scales.

4.2 Observations and Data Reduction

The NGC 4485/4490 galaxy pair has been observed by *Chandra* on three occasions, the first of which was reported in RWWM02, with two subsequent deeper observations taken during 2004. A search of the *XMM-Newton* archive revealed one further observation taken in 2002. Details of these observations can be seen in Table 4.1. (For simplicity, the observations will be labelled as shown in this table throughout the rest of this chapter.)

4.2.1 Chandra observations

Chandra observations were performed with the Advanced CCD Imaging Spectrometer (ACIS), using the S-array. The first observation (C1) was positioned on the standard aimpoint for the back-illuminated S3 chip, although a Y offset of -2.0 arcmins was used during subsequent observations to centralise the galaxy pair on the S3 chip. The later observations were also performed with the telemetry in VFAINT mode to optimise the detection of the faint extended diffuse emission component in the galaxies detected by RWWM02. Data reduction was carried out using the CIAO software, version 3.3.0.1, and standard *Chandra* data analysis threads[1]. The three observations were filtered by energy, rejecting events with energies outside the range 0.3 – 10.0 keV. The source spectra and light curves were extracted for each source using the CIAO tasks *PSEXTRACT* and *DMEXTRACT*, taking data from circular apertures, 5 pixels in diameter (thus encircling > 90 per cent of the source energy) and centred on each ULX.

Background spectra were extracted via an annulus encircling the source (8 to 16 pixels in diameter). Background light curves were extracted from circular regions, the same size as the source region, positioned in a source-free region near each ULX. The response and ancillary response files, necessary for spectral analysis, were created automatically by the standard *Chandra* tasks.

4.2.2 XMM-Newton observation

Data from the *XMM-Newton* observation of the NGC 4485/4490 pair was collected from the *XMM-Newton* Science Archive (XSA[2]) and reduced using the SAS software (version 7.0.0[3]). Here we utilise data from the *XMM-Newton* European Photon Imaging Camera (EPIC), which was operated in full-field mode with a medium optical filter in place for all three cameras during the observation. This observation was affected by a background flare that was removed using a good time intervals (GTI) file, created using a full-field background light curve extracted from the pn camera data. This reduced the total ontime to 12.8 ks. The same GTI file was used for both the pn and MOS instruments to allow

---

[1] For *Chandra* threads, published by the *Chandra* X-ray Center, see `http://asc.harvard.edu/ciao`.

[2] *XMM-Newton* Science Archive can be found at `http://xmm.esac.esa.int/xsa`.

[3] For details of the *XMM-Newton* Science Analysis Software see `http://xmm.esac.esa.int/sas`.

for the direct co-addition of light curves. As a final check for unscreened flares we visually inspected the time filtered full-field light curves for each MOS detector, and no additional flares were observed.

Source spectra and light curves were extracted from circular regions centred on the individual ULXs in each detector. We used a region 16 arcseconds in radius where possible, to enclose as many source counts as possible, whilst minimising the contribution from other components within the galaxies. The encircled energy fraction for such regions is ~ 70 per cent for both MOS and pn detectors. Where cross-contamination was likely due to the close proximity of these and other bright sources, data was extracted from a smaller circular region of 8 or 12 arcseconds in radius (dropping the encircled energy fractions to $\sim 50-60$ per cent; specific details of the regions used for individual sources are discussed below). We selected the best quality data (FLAG = 0) in each case and screened with PATTERN ≤ 4 for pn and PATTERN ≤ 12 for MOS, with light curves extracted in the 0.3 – 10.0 keV band. The response and ancillary response files were created automatically by the standard *XMM-Newton* tasks.

Background spectra and light curves were extracted from circular regions for every source. Regions were identical in size to source data extraction regions for light curves, but larger regions were used for spectra. Every effort was made to position these on the same chip as the source at a similar off-axis angle and distance from the read out nodes, though this was not always possible for the spectral regions. When necessary additional background regions were used to provide background data with average detector characteristics similar to the source data.

4.3 ULX properties

Our source selection was based on the ‘bright’ sample criteria set out by RWWM02, that is to say we selected sources that have observed X-ray luminosities of 10^{39} erg s^{-1} and above (i.e. objects ultraluminous in nature). The authors identified a total of six ULXs within these two galaxies that are listed in Table 4.2. It should be noted that the nomenclature for ULXs used here follows that of RWWM02, who used the official IAU designations for *Chandra* sources incorporating the source position in J2000 coordinates. Each observation

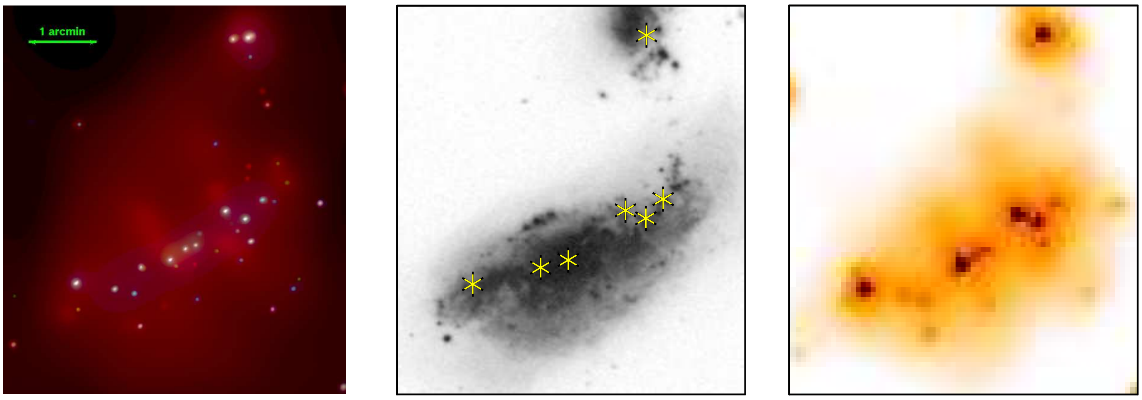

Figure 4.2: X-ray and optical views of the galaxy pair NGC 4485/4490. Each panel is shown on the same spatial scale to facilitate direct comparison, and North is up in all three panels. (*left*) Three-colour *Chandra* image. We combined data from all three *Chandra* ACIS-S observations using standard CIAO threads. We combine the data using MERGE and create the image using the DS9 thread. The data is adaptively smoothed using the CSMOOTH algorithm. The colours represent emission in the 0.3 – 1 keV (red), 1 – 2 keV (green) and 2 – 8 keV (blue) bands. The figure shows that the numerous luminous point sources within NGC 4490 (and NGC 4485) are clearly embedded in an extended, soft X-ray emission component that is present in both the disc and halo regions of the main galaxy. (*centre*) Optical image of the galaxies. We display the Digitised Sky Survey blue data, and mark the positions of the seven ULXs detailed in this paper using yellow asterisks. (*right*) *XMM-Newton* data for the galaxies in the 0.3 – 10.0 keV band. The raw (i.e. not exposure-corrected) imaging data from all three EPIC cameras is co-added, and then smoothed using CSMOOTH, before being displayed on a log heat scale.

was also checked to identify any previously unobserved ULXs that had emerged since the original study had been carried out. One additional source was found (in observation C3), which we refer to hereafter as CXOU J123038.3+413830 using the above nomenclature[4]. The seven ULXs (where detected) had ACIS-S/combined EPIC count rates of 0.009 – 0.076/0.018 – 0.105 count s^{-1}, resulting in 290 – 2070 counts in total being accumulated per source per observation. We highlight their positions relative to the optical extent of the galaxies using Digitised Sky Survey data, which we display alongside *Chandra* and *XMM-Newton* images constructed from the observations studied herein, in Figure 4.2.

The spectra and light curves for the seven sources were extracted and analysed for each observation, providing their data was sufficiently good to allow spectral analysis. This was only possible for CXOU J123038.3+413830 during observation C3. Conversely CXOU J123029.5+413927 had sufficient data for spectral analysis in all but the *XMM-Newton* observation (X1). The source spectra and light curves for CXOU J123030.8+413911, CXOU J123029.5+413927 (light curves only) and CXOU J123032.3+413918 were extracted from X1 using a region of only 8 arcseconds radius due to the close proximity of these three sources to one another. During the X1 observation, CXOU J123030.6+414142 was unfortunately positioned close to a pn chip gap. We therefore used a polygonal region to optimise our extraction of the pn source data. Circular apertures (radius 16 arcseconds) were viable for this source in each MOS detector. Similarly, pn data from CXOU J123042.3+413818 was extracted from a 12 arcsecond radius region due to the proximity of a chip gap, whilst its MOS data was extracted from a full 16 arcsecond radius aperture.

4.3.1 X-ray spectra

All the ULX X-ray spectra were grouped to a minimum of 20 counts per bin and then fitted using simple (absorbed single component) models in XSPEC version 11.3.1. The spectral fitting was carried out in the 0.3 – 10.0 keV range for all instruments. When fitting models to the spectra from *XMM-Newton*, the pn and MOS data were analysed concurrently to gain the best fit. A constant multiplicative factor was applied to allow for

---

[4] Fridriksson et al. (2008) also noted the emergence of this source and one other possible ULX, CXOU J123035.1+413846. We extracted a spectrum for the latter finding an observed luminosity of $<10^{39}$ erg s^{-1} in the 0.3 – 10.0 keV band, so it is not considered further in our analysis.

calibration differences between cameras. The pn constant was fixed at unity, whilst the constants for each of the MOS detectors were left as free parameters and, for the majority of sources, they agree to within 10 per cent (larger discrepancies are only present where disparate extraction regions were necessary; see above).

Each model included two absorption components; a fixed column of 1.81×10^{20} cm^{-2} representing the known absorption column along the line of sight to NGC 4485/4490 in our own Galaxy (from the Leiden, Argentine and Bonn Survey; Kalberia et al 2005), and a second component left free to vary that represents absorption within the host galaxy. These absorption columns were modelled using the TBABS model (Wilms, Allen & McCray 2000). In our initial fits it acted on either a power-law continuum (PO in XSPEC syntax) or a multi-colour disc blackbody model (DISKBB; Mitsuda et al. 1984), similar to RWWM02. We did attempt more complicated models, for example two component models such as an absorbed disc plus power-law model, but no statistically significant improvement was achieved in the fitting of any of the data, and so they are not discussed any further in this chapter.

The results of our fitting for the two models (absorbed power-law continuum and absorbed multicolour disc blackbody; hereafter referred to as the PL and MCDBB models respectively) are shown in Table 4.2. This also includes a luminosity for each ULX, the luminosity and its errors were calculated using the best fitting model to the data. For *Chandra* data this calculation proved straightforward, but for the concurrently fit *XMM-Newton* data sets we estimated the model flux from the pn data only. As CXOU J123030.6+414142 was unfortunately positioned close to a chip gap in the pn detector, we derived its luminosity using an average of the two MOS detectors. The errors quoted throughout Table 4.2 are the 90 per cent errors for one interesting parameter.

Table 4.2: Spectral modelling of the ULXs in NGC 4485 and NGC 4490

Source Name	Obs	TBABS * PO				TBABS * DISKBB			
CXOU		$N_H{}^a$	Γ	χ^2 / DoF	Luminosity^b	$N_H{}^a$	$kT_{in}{}^c$	χ^2 / DoF	Luminosity^b
J123029.5 + 413927	C1	5^{+2}_{-1}	$3.9^{+0.9}_{-0.8}$	**6.3/10**	$0.9^{+0.1}_{-0.8}$	$3.0^{+0.7}_{-0.6}$	$0.8^{+0.2}_{-0.1}$	6.4/10	$0.86^{+0.03}_{-0.6}$
	X1	...	...	...	...	...	...	...	...
	C2	$3.3^{+1.0}_{-0.7}$	$2.5^{+0.6}_{-0.4}$	**33.1/18**	$1.0^{+0.02}_{-0.7}$	2.2^{*}	1.3^{*}	38.6/18	0.9^{*}
	C3	2.1^{*}	2.0^{*}	**26.7/13**	0.7^{*}	1.4^{*}	1.4^{*}	29.0/13	0.6^{*}
J123030.6 + 414142	C1	$0.37^{+0.08}_{-0.07}$	$1.72^{+0.07}_{-0.1}$	61.1/59	$4.0^{+0.4}_{-0.7}$	0.16 ± 0.05	$1.4^{+0.2}_{-0.1}$	**46.8/59**	$3.6^{+0.2}_{-0.7}$
	X1	0.41 ± 0.1	2.1 ± 0.2	**35.9/38**	$2.1^{+0.6}_{-1}$	0.09 ± 0.08	$1.2^{+0.2}_{-0.1}$	39.5/38	$1.9^{+0.3}_{-1}$
	C2	$0.36^{+0.7}_{-0.6}$	2.0 ± 0.1	84.1/66	$2.4^{+0.3}_{-0.4}$	$0.14^{+0.05}_{-0.04}$	1.2 ± 0.1	**77.1/66**	$2.12^{+0.07}_{-0.3}$
	C3	0.40 ± 0.07	$1.87^{+0.1}_{-0.06}$	70.2/69	$2.6^{+0.3}_{-0.5}$	0.14 ± 0.05	$1.4^{+0.1}_{-0.10}$	**55.3/69**	$2.2^{+0.1}_{-0.3}$
J123030.8 + 413911	C1	$1.1^{+0.4}_{-0.3}$	1.8 ± 0.3	**24.2/29**	$2.5^{+0.4}_{-1}$	0.5 ± 0.2	$1.7^{+0.4}_{-0.3}$	28.8/29	$2.3^{+0.2}_{-2}$
	X1	$1.2^{+0.3}_{-0.2}$	$1.8^{+0.3}_{-0.2}$	**28.3/32**	$2.8^{+0.9}_{-2}$	0.7 ± 0.2	$1.6^{+0.3}_{-0.2}$	32.2/32	$2.5^{+0.6}_{-3}$
	C2	2.0 ± 0.3	2.4 ± 0.2	**55.9/53**	$2.6^{+0.4}_{-1}$	1.2 ± 0.2	1.2 ± 0.1	60.5/53	$2.4^{+0.1}_{-0.5}$
	C3	1.5 ± 0.2	2.2 ± 0.2	**64.4/59**	$2.4^{+0.3}_{-0.7}$	0.9 ± 0.1	1.3 ± 0.1	65.5/59	$2.3^{+0.07}_{-0.5}$
J123032.3 + 413918	C1	0.6 ± 0.2	1.7 ± 0.3	**12.8/21**	$1.7^{+0.2}_{-0.6}$	$0.3^{+0.1}_{-0.3}$	$1.5^{+0.5}_{-0.2}$	14.2/21	$1.5^{+0.2}_{-1}$
	X1	1.0 ± 0.1	2.2 ± 0.2	57.4/47	$2.8^{+0.9}_{-1}$	0.5 ± 0.1	1.2 ± 0.1	**47.3/47**	$2.7^{+0.3}_{-0.9}$
	C2	1.0 ± 0.2	2.0 ± 0.2	72.6/59	$3.2^{+0.4}_{-1}$	0.5 ± 0.1	$1.4^{+0.2}_{-0.1}$	**67.0/59**	$2.9^{+0.1}_{-0.5}$
	C3	0.9 ± 0.1	1.9 ± 0.1	88.1/64	$2.5^{+0.3}_{-0.5}$	$0.53^{+0.10}_{-0.08}$	$1.5^{+0.2}_{-0.1}$	**83.8/64**	$2.4^{+0.1}_{-0.7}$
J123036.3 + 413837	C1	$0.6^{+0.3}_{-0.2}$	1.7 ± 0.3	**20.5/22**	$1.7^{+0.3}_{-0.1}$	0.3 ± 0.2	$1.4^{+0.5}_{-0.2}$	23.3/22	$1.5^{+0.1}_{-1}$
	X1	$0.58^{+0.1}_{-0.09}$	$2.06^{+0.1}_{-0.07}$	84.7/66	$2.7^{+0.7}_{-1}$	$0.23^{+0.07}_{-0.06}$	1.3 ± 0.1	**77.3/66**	$2.6^{+0.4}_{-0.8}$
	C2	$0.8^{+0.4}_{-0.2}$	$2.5^{+0.5}_{-0.3}$	**10.7/13**	$0.40^{+0.08}_{-0.3}$	0.2 ± 0.2	$1.0^{+0.3}_{-0.2}$	18.9/13	$0.39^{+0.06}_{-0.2}$
	C2	1.3 ± 0.2	2.5 ± 0.2	72.9/62	$2.1^{+0.3}_{-0.5}$	0.7 ± 0.1	1.03 ± 0.08	**54.9/62**	$1.94^{+0.06}_{-0.2}$

Source Name	Obs	TBABS * PO				TBABS * DISKBB			
CXOU		${N_H}^a$	Γ	χ^2 / DoF	Luminosity^b	${N_H}^a$	${kT_{in}}^c$	χ^2 / DoF	Luminosity^b
J123038.3 + 413830	C1	...	...	...	...	...	...	...	...
	X1	...	...	...	...	...	...	...	...
	C2	...	...	...	...	...	...	...	...
	C3	$1.8^{+0.4}_{-0.3}$	$2.6^{+0.3}_{-0.2}$	41.5/35	$1.2^{+0.2}_{-0.5}$	1.1±0.2	1.1±0.1	**35.8/35**	$1.2^{+0.04}_{-0.3}$
J123043.2 + 413818	C1	1.3±0.2	2.3±0.2	46.6/40	$2.91^{+0.4}_{-0.09}$	$0.8^{+0.2}_{-0.1}$	1.2±0.1	**38.6/40**	$2.7^{+0.1}_{-0.5}$
	X1	$1.1^{+0.2}_{-0.1}$	2.7±0.2	59.3/54	$2.2^{+0.6}_{-1}$	$0.47^{+0.1}_{-0.09}$	$0.97^{+0.09}_{-0.08}$	**51.7/54**	$2.1^{+0.3}_{-0.7}$
	C2	1.3±0.2	2.7±0.2	83.6/58	$1.9^{+0.2}_{-0.6}$	0.7±0.1	$0.94^{+0.08}_{-0.07}$	**68.4/58**	$1.75^{+0.05}_{-0.2}$
	C3	$1.1^{+0.2}_{-0.1}$	2.2±0.1	87.2/79	$3.1^{+0.3}_{-0.6}$	$0.58^{+0.10}_{-0.09}$	1.32±0.1	**82.0/79**	$2.9^{+0.1}_{-0.3}$

Notes: the data quality was insufficient for spectral fitting in the *XMM-Newton* observation of CXOU J123029.5+413927. CXOU J123038.3 + 413830 is the new transient source, not previously observed as a ULX, that appears only in the most recent observation. We embolden the χ^2/degrees of freedom (DoF) for the best fitting model for each source observation. Specific notes: ^{a}Absorption column in units of 10^{22} atoms cm^{-2}. ^{b}Observed luminosity in the 0.5–8.0 keV band in units of 10^{39}erg s^{-1}. ^{c}Disc temperature in keV. *The best fitting models to this data gave a reduced χ^2 greater than 2, therefore we did not place constraints on the parameter errors.

The simple absorbed single component models as shown in Table 4.2 provide acceptable fits to the majority of the data (model rejection probabilities, based on the χ^2 fit, of $P_{\rm rej} < 95$ %). Only three best-fits were statistically poor models of the data; both the latter *Chandra* observations of CXOU J123029.5+413927 (with rejection probabilities of $P_{\rm rej} > 98.4$ %), and a very marginal rejection of the best fit to CXOU J123032.3+413918 in observation C3 ($P_{\rm rej} = 95.1$ %). We show examples of the spectral quality of our data in Figure 4.3, where data for two of the ULXs is shown over all four observation epochs. Clearly, the spectra and luminosity of the ULXs vary with time. We discuss this spectral variability further below.

The best-fitting parameters to the models are in the range $\Gamma \sim 1.7 - 2.7$ for the PL model, and $kT_{\rm in} \sim 0.8 - 1.7$ keV for the MCDBB model. As these two models are also commonly used to describe Galactic black holes, it is worth considering the comparative fits gained, although caution should be taken when doing this as the different band pass of *Chandra* to those instruments generally used to study Galactic black holes may be a contributory factor in differing results (see Section 4.4.1 for further discussion). Here we find that the observed values for PL photon index are in most cases a little on the low side for the steep power-law state (a.k.a. very high state) as described by McClintock & Remillard (2006), which is defined by a $\Gamma > 2.4$ power-law continuum, and in many cases are similar to the $\Gamma \sim 1.7 - 2.1$ slopes seen in the hard state. However, this range of power-law slopes is very typical for *Chandra* observations of ULXs (Swartz et al. 2004, Berghea et al. 2008). In a similar vein, the MCDBB inner disc temperatures are generally a little high compared to Galactic black holes in the thermal-dominated (high/soft) state which generally possess disc temperatures $kT_{\rm in} \sim 0.7 - 1.1$ keV (although higher temperatures have been seen, particularly in the steep power-law state cf. McClintock & Remillard 2006). They are however very similar to those measured in other ULXs modelled by a MCDBB (e.g. Makishima et al. 2000). The range of spectral properties therefore appear typical of the ULX class in general.[5]

---

[5] An explicit comparison of our fits to the data from C1, and the published fits from RWWM02, reveal that our parameter values ($\Gamma, kT_{\rm in}$) match very closely. However, there is a trend for our new absorption values to be ~ 30 per cent higher (although in many cases there is reasonable agreement with the previous measurements within the errors). This difference is likely attributable to a combination of considering data

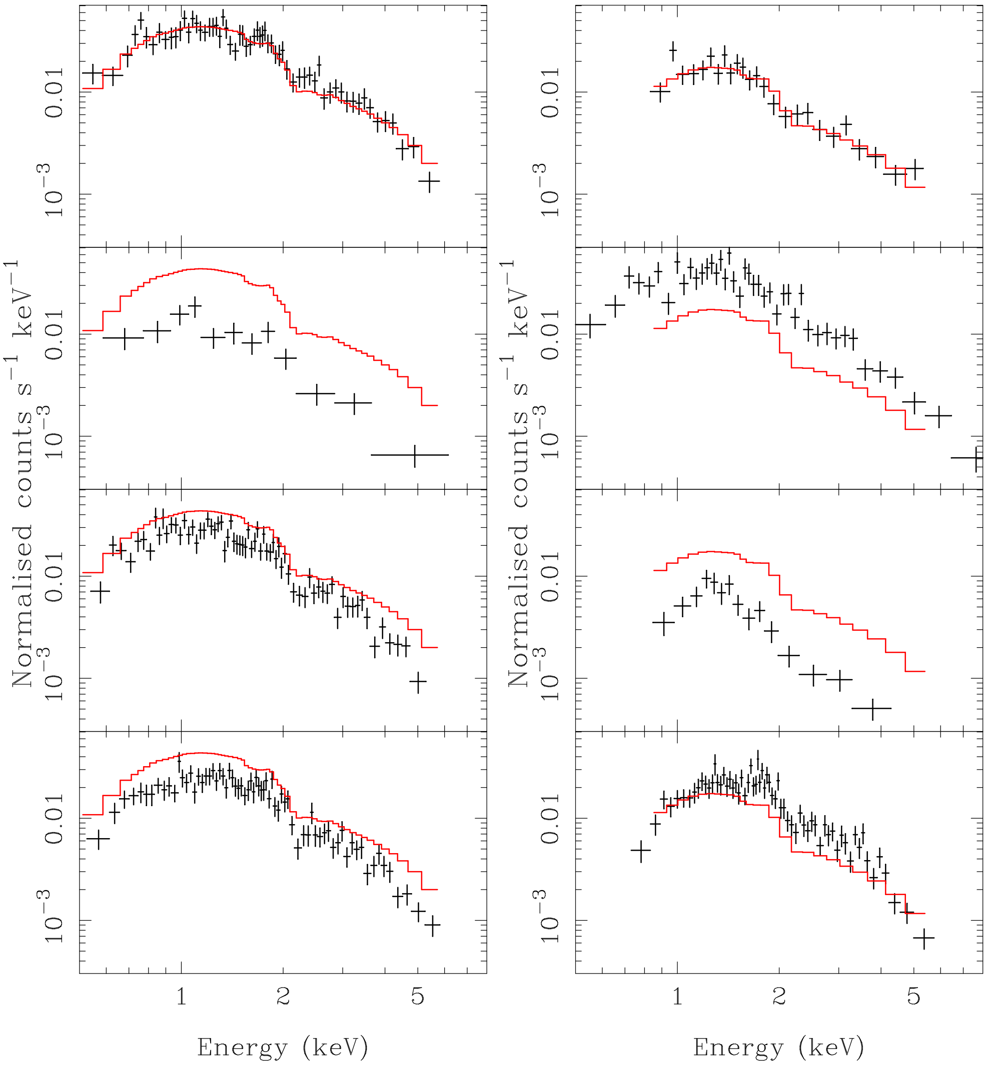

Figure 4.3: Example X-ray spectra from two ULXs. We show the spectral data for CXOU J123030.6+414142 (left) and CXOU J123036.3+413837 (right) over all four observations, which are ordered top - bottom in chronological order (i.e. C1, X1, C2, C3). In each panel we show the spectral data points in black (NB. for clarity we omit EPIC-MOS data, showing only EPIC-pn data in the second panel down). For ease of direct comparison we display the best fitting power-law continuum model to the C1 data in red in all subsequent panels. Clearly both sources display considerable spectral and luminosity variability.

4.3.2 Spectral variability

As the previous section shows, we have multiple detections of the ULXs in the NGC 4485/4490 system, each with sufficient data quality to examine their individual X-ray spectra. This therefore provides an excellent data set with which to begin to examine the variation in the X-ray spectra of these ULXs over time, as amply demonstrated in Figure 4.3. In particular, five ULXs have a complete set of spectral fits, i.e. an acceptable - or only marginally rejected - best-fitting spectrum in each epoch, which we base this analysis on. We do not discuss either the new transient ULX CXOU J123038.3+413830 (with only one spectral data set), or the candidate supernova remnant (SNR) CXOU J123029.5+413927, in the following work.

A first interesting trend to consider is which models provide a best fit to the data. Initially we consider the best fitting model to be that with the lowest χ^2/DoF (although we note that in some instances $\Delta\chi^2$ between the models is marginal). On the whole, these ULXs are more frequently better fit by the MCDBB model than the PL model (12/20 data sets). One source is consistently best fitted by each model; CXOU J123030.8+413911 is always better fitted by the PL model, whereas CXOU J123043.2+413818 is better fitted by the MCDBB in the four observations. The other three can all be best fit by both models in one or more observations. However, one trend appears in these three sources; *the PL provides the better fits exclusively at lower observed luminosity*, *whereas the MCDBB fits to the higher luminosity data*. An obvious interpretation of this change in spectral shape is that it could be an indication for a spectral state transition. Given the potential importance of this result, we have investigated it further. As so few of the spectral fits are rejected on the basis of the χ^2 statistic, the vast majority of fits constitute acceptable interpretations of the data so we could not simply use the χ^2 statistic to distinguish models. Instead, we turn to Bayesian Information Criterion analysis (Jefferys 1961; Schwarz 1978). This provides a measure of whether one model should be considered a superior description of the data, when compared to another. We calculate values in the range 0.48 – 7.82 for the majority of our comparisons between models for the same epoch data. Many line in

---

below 0.5 keV - which RWWM02 did not - and the improvements in calibration made over the intervening years.

the range of ‘positive’ evidence by the Bayesian Information Criterion (2 – 6; cf. Kass & Raftery 1995), with marginally ‘strong’ evidence in only two cases. Hence we cannot strongly distinguish which model provides a statistically superior fit for most data.

Despite the lack of a strong distinction between the two models in most sources, we do find that the parameterisations of these models vary between observations. This is perhaps not unexpected, given that it is a trend observed in other ULXs (e.g. NGC 2403 Source 3, Isobe et al. 2009). We have investigated this in Figure 4.4, where we plot the derived parameters for each model (the power-law photon index Γ, and the inner accretion disc temperature $kT_{\rm in}$, as listed in Table 4.2) against the 0.5 – 8 keV luminosity of the source derived from that model. We show this for both the observed luminosity, and for an intrinsic luminosity calculated in the same band by simply setting the absorption acting on the model to zero. In each plot we show the data points for which that model is the better fitting by solid error lines, and use dashed errors for the worse fitting model (based on χ^2 fitting results). Each separate ULX is distinguished via individual colours and symbols (see the Figure caption for a key). The Figure is plotted showing 1 σ errors on the source parameters; clearly there are statistically significant changes in luminosity and/or parameterisation for each source over the course of our observations.

What is immediately obvious from comparing the two pairs of panels in Figure 4.4 is that the models react rather differently to the removal of an absorption column. The removal of an absorption column for the MCDBB model leads to little movement in the relative positions of the data points, only a general movement to higher luminosities (with the latter as would be expected from correcting to an intrinsic luminosity). However, the power-law continuum data points react rather more dramatically, with the data with softer intrinsic slopes (higher values of Γ) having a much larger apparent correction from observed to intrinsic luminosity than those data sets with harder slopes. This is rather well-demonstrated by the data for CXOU J123030.8+413911 (red squares, the only source always best-fitted by the power-law model), which appears to vary its spectral slope with little or no contemporaneous change in observed luminosity; however when the correction is made for the modelled absorption, it shows a clear trend of becoming softer as its luminosity increases. A pertinent question is therefore whether this latter relationship is a physically correct interpretation of the data, or whether this is some sort of artefact of

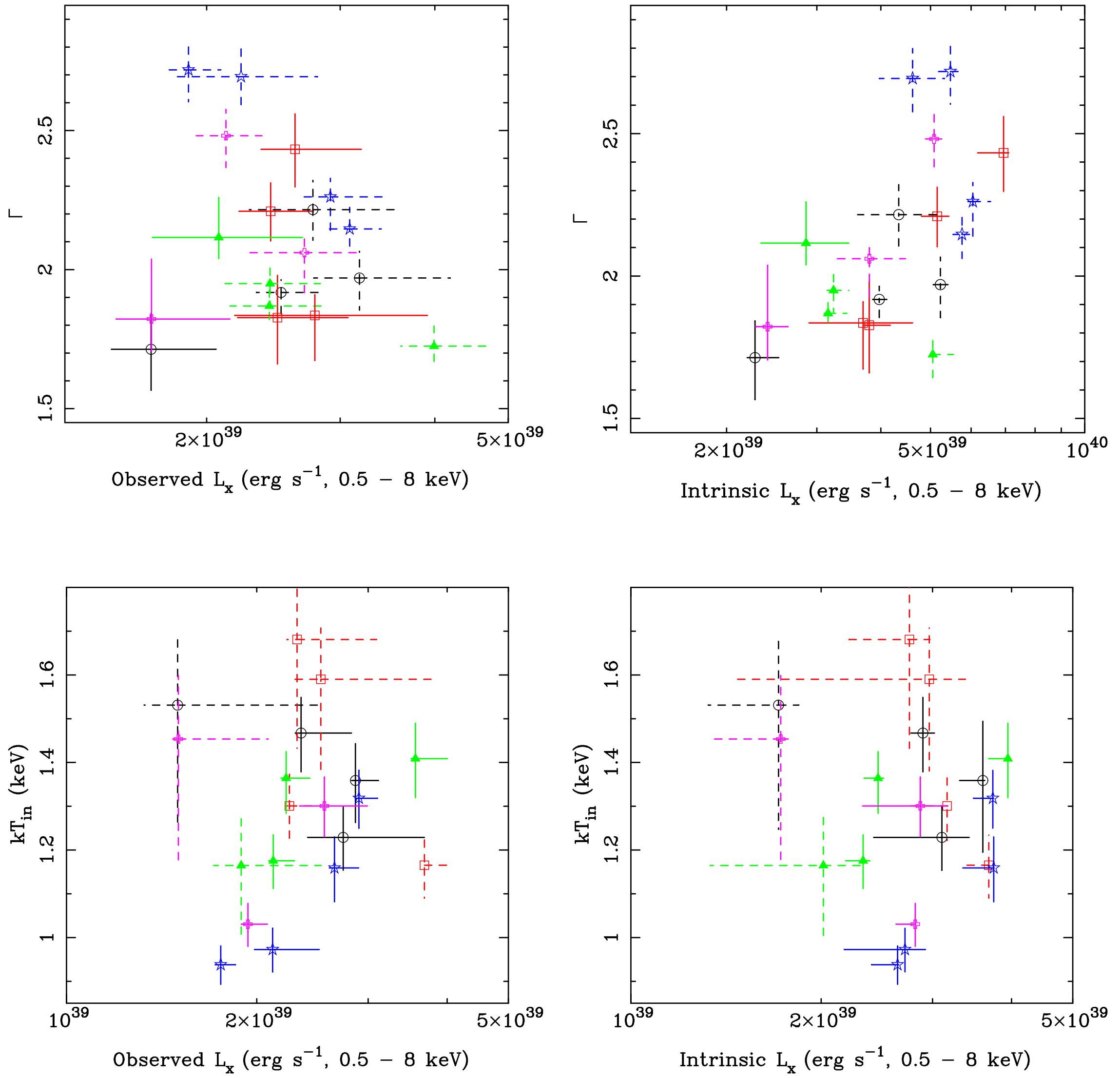

Figure 4.4: Variation of the spectral parameters in five ULXs in the NGC 4485/4490 system. (*Top row*) We show the best fitting parameter for the power-law continuum model, Γ, against the 0.5 – 8 keV luminosity derived from that model for two cases: (*left panel*) the observed luminosity and (*right panel*) the intrinsic luminosity. (*Bottom row*) The same, but for the inner accretion disc temperature $kT_{\rm in}$ in the MCDBB model. We plot each pair of panels on the same scale for ease of comparison. For ULXs best fitted by the spectral model that is the subject of each panel, we plot the error bars as solid lines. Where the ULX is better fit by the other model, we plot dashed error bars. Each ULX is delineated by a different colour/symbol combination. These are: green filled triangles - CXOU J123030.6+414142; red open squares - CXOU J123030.8+413911; black open circles - CXOU J123032.3+413918; magenta open plusses - CXOU J123036.3+413837; blue open stars - CXOU J123043.2+413818.

the fitting process.

We have examined this question by plotting the best fitting values of the power-law photon index (Γ) against the fitted absorption column density ($N_{\rm H}$) in Figure 4.5. If there were no relation between the two one would see a simple scatter plot, with the column independent of the power-law slope. However, at least in the case of CXOU J123030.8+413911, the measured column density is clearly increasing concurrently with Γ. This suggests that one of two scenarios is occurring: either there is a physically real increase in absorbing column, local to the ULX, that occurs simultaneously with a steepening of the spectral slope and increase in intrinsic luminosity; or that the spectral fitting process is artificially inferring higher columns that go hand-in-hand with steeper slopes in some observations. The latter is not so far-fetched; as the column is inferred from the low-energy turn-over of the power-law spectrum, one might expect some degeneracy between the slope being turned over and the amount of material required to produce the turn-over, particularly within the limited band-pass of the *Chandra* data where we see few data points above $\sim$ 5 keV to really constrain the slope of the power-law tail (cf. Figure 4.3).

The other four sources all behave somewhat differently from CXOU J123030.8+413911. Two sources - CXOU J123030.6+414142 and CXOU J123043.2+413818, plotted in Figures 4.4 & 4.5 as green triangles and blue stars respectively - appear to consistently harden their spectra as their luminosity increases. Interestingly these two sources are predominantly better fit by a MCDBB model (albeit with the caveats discussed above about distinguishing the models), and we note that this behaviour is quite consistent with accretion discs becoming hotter as their luminosity increases, as is seen in Galactic black hole X-ray binaries[6]. On the other hand, the behaviour of the remaining two sources is less clear cut. CXOU J123032.3+413918 (plotted as black circles) is mainly better fit by a MCDBB model; in this model it appears not to vary substantially (less than $\sim$ 30 per cent, with large errors) in luminosity or disc temperature, but when better fit by a power-law model it appears slightly harder in spectrum (although again with large errors). CXOU J123036.3+413837 (magenta open plusses) behaves similarly - again it

---

[6] Indeed, standard accretion disc spectra are known to show a relationship of $L_{\rm X} \propto T^4$, e.g. Done, Gierliński & Kubota (2007).

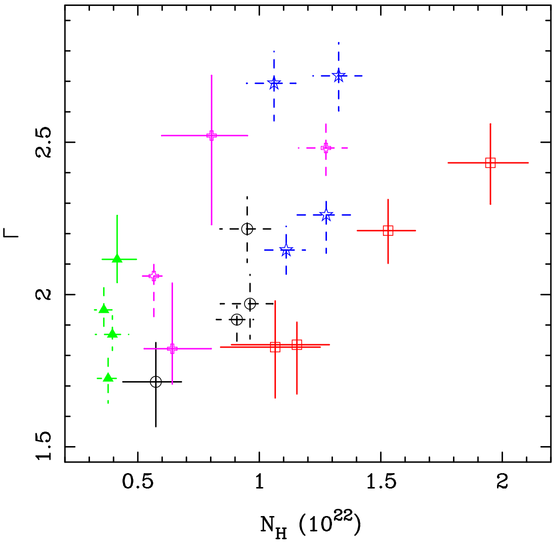

Figure 4.5: A comparison between the fitted values of the power-law photon index Γ and the absorption column $N_{\rm H}$ for the power-law model. ULXs are denoted by the same colour/symbol combination as in Figure 4.4.

appears harder in the power-law state than when it possesses a MCDBB-dominated spectrum, although in this case there is a wider difference in the parameters of the data points for the MCDBB spectrum. Interestingly, though, these two disc-dominated spectra appear to follow the same more luminous/harder trend as CXOU J123030.6+414142 and CXOU J123043.2+413818. So, although we are unable to strictly distinguish which model provides the preferable fit to the data, it does appear as though those sources slightly better fitted by a MCDBB model are behaving in a fashion consistent with that expected of sources dominated by an accretion disc. We discuss this interesting result further in the next section.

4.3.3 Short-term X-ray variability

Following the method of RWWM02, light curves for each source observation were binned to ∼25 and ∼100 counts per bin to allow simple tests on variability to be carried out. Initially these tests were performed by fitting the background-subtracted light curves to a constant flux (the average for that observation) then examining the fit with a χ^2 test.

It was necessary to cut the (co-added pn and MOS) light curves in two to remove a large flaring event from the observation, therefore the *XMM-Newton* data initially provides two light curves for each source. As a further test the *XMM-Newton* light curves were reassembled (excluding the flaring event) and the light curves were re-tested. A separate test on the light curves was carried out by investigating the excess variance of each data set. However, no statistical signs of short-term variability were detected by any test in any light curve. We note that none of the seven ULXs we have in common with the work of Fridriksson et al. (2008) showed short-term variability in their analysis either, when tested using a one-sided Kolmogorov-Smirnov test.

4.3.4 Long-term X-ray variability

Fridriksson et al. (2008) examine the long-term variability of the ULXs in NGC 4485/4490, and detect significant flux variability in all but one of the ULXs (that one being CXOU J123030.8+413911). Here we also derive long-term light curves, albeit using generally more conservative techniques, which we present in Figures 4.6 and 4.7. We expand on the long-term lightcurves presented in RWWM02 (based on *ROSAT* data, and *Chandra* data from observation C1 alone), which we limit to the 0.5 – 2.0 keV band as this is the only band in common for all the instruments. The luminosities we quote are therefore generally lower than seen elsewhere. We also include limits where sources are undetected (calculated as per RWWM02). Finally, we display the 1 σ errors for the luminosities derived from spectral modelling of the *Chandra* and *XMM-Newton* data (the errors on the *ROSAT* data are more standard counting errors, due to the lack of spectral information in this data).

Long-term light curves for the six previously-known ULXs are shown in Figure 4.6, which is a simple extension of figure 5 in RWWM02. The light curve for the new transient ULX (CXOU J123038.3+413830) is in Figure 4.7, and shows it would have been clearly detectable in earlier *ROSAT* PSPC, *Chandra* and *XMM-Newton* data. Of the other ULXs, CXOU J123030.8+413911 was itself deemed a transient in RWWM02 due to its non-detection by *ROSAT*; however it has apparently remained in outburst at roughly the same flux level in observations spanning $\sim$ 4 yrs after its discovery. The flux of CXOU J123043.2+413818 has remained similarly stable, though this is over a longer $\sim$ 15 year time scale. At first glance this may appear to contrast with the findings of Fridriksson

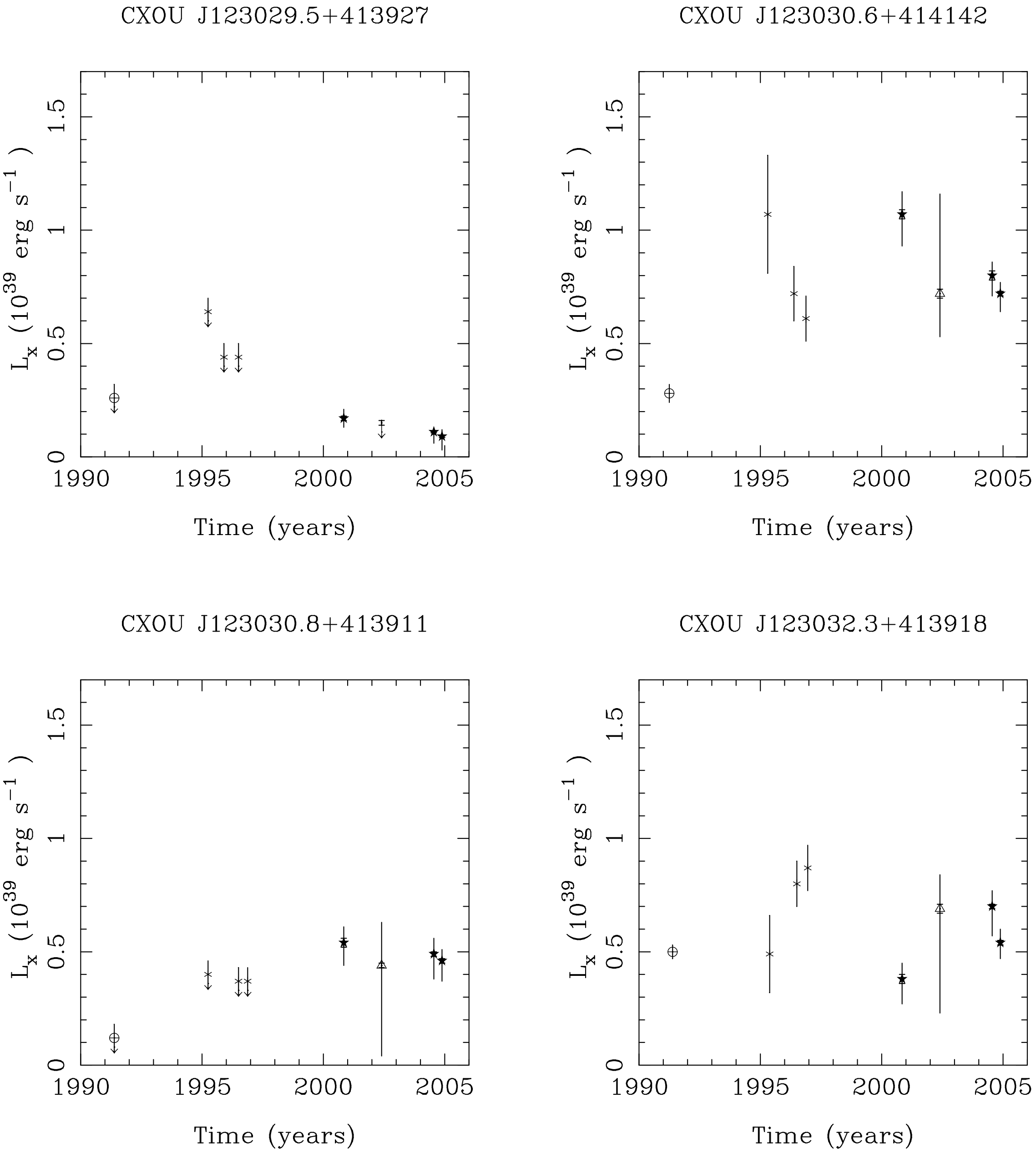

Figure 4.6: Extended long-term light curves of the six ULXs identified in NGC 4485 and NGC 4490. Results shown are from *ROSAT* PSPC and HRI instruments (represented by open circles and asterisks respectively), *Chandra* ACIS-S (filled pentagram) and *XMM-Newton* EPIC camera (open triangle) in the 0.5 – 2 keV band, using the best fitting single component models (either absorbed power-law or multi-colour disc blackbody). Data from the earlier missions have been taken from the RWWM02 paper, whilst more recent results have been calculated in this work. Errors have also been derived using a similar method to RWWM02 for *ROSAT* PSPC and HRI instruments for each new observation, these are also shown. Upper limits are represented by downwards arrows.

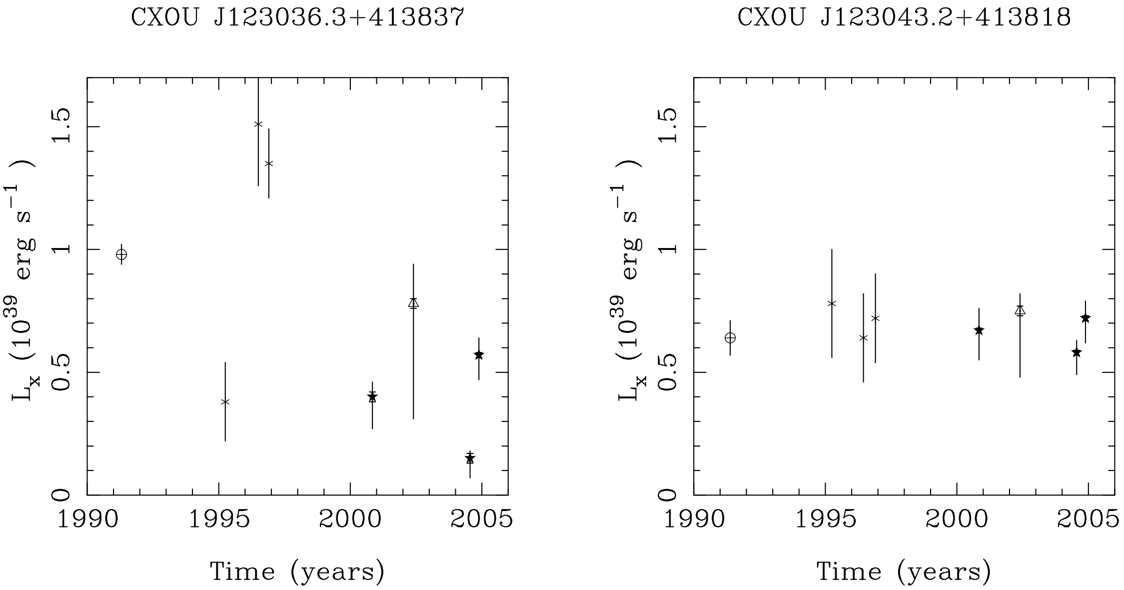

Figure 4.6: *continued.*

et al. (2008), but this difference is predominantly due to band pass selection. They note significant variations in hard colour that by their definition covers the 1 – 7 keV band; we however consider the 0.5 – 2.0 keV band common to all instruments contributing data. To further test our result, we apply the same significance parameter ($S_{\rm flux}$) used by the authors. They define a source as variable if $S_{\rm flux} > 3$, where

$$S_{flux} = max_{ij} \frac{|F_i - F_j|}{\sqrt{\sigma_{F_i} - \sigma_{F_j}}}$$

We find that $S_{\rm flux} = 1.3$ for CXOU J123043.2+413818, confirming the lack of variability. The three other brighter ULXs have displayed higher variability amplitudes over the $\sim$ 15 years covered by the observations, though have remained detectable throughout this time (CXOU J123030.6+414152, $S_{\rm flux} = 6.2$; CXOU J123032.3+413918, $S_{\rm flux} = 3.6$; CXOU J123036.3+413837, $S_{\rm flux} = 12.2$). We discuss the remaining source (CXOU J123029.5+413927) below in Section 4.4.2.

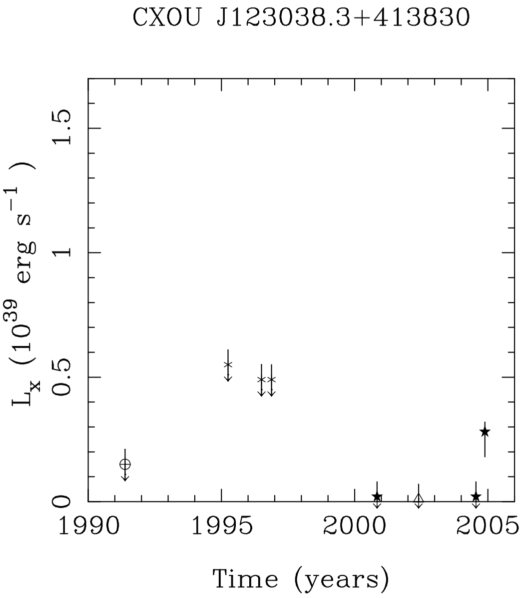

Figure 4.7: Extended long-term light curve for the new transient ULX, CXOU J123038.3+413830. Symbols are as per Figure 4.6.

4.4 Discussion

4.4.1 Spectral state changes in ULXs?

In the previous section we consider the properties of the ULXs separately. We show that most are adequately fit by two simple spectral models (a power-law continuum or a MCDBB). Although there are apparent trends (based on a superior χ^2 fit) in the best fitting model to the data with the luminosity of the ULX at a given epoch, we show that statistically we cannot strongly distinguish a best fitting model on this basis alone. Interestingly, though, the best fitting parameters do give some support to the initial distinction based on the χ^2 fit - those models better fitted by a MCDBB do appear to behave in a way consistent with this (increasing in disc temperature as their luminosity increases). No temporal variability is evident on short (intra-observation) time-scales for any source contained within NGC 4485/4490. However, strong variability is seen over longer (∼ years) time-scales in most of the ULXs.

When we consider the spectral and temporal behaviour of the ULXs together, we find that these ULXs appear rather heterogeneous, an unsurprising result given previous multi-epoch observations (e.g. Fabbiano et al. 2003a, Roberts et al. 2004, Zezas 2006). We initially consider only the five sources discussed in Section 4.3.2, examining both the long-term light curves and spectral variability of each source to see if and how they are related. We find that the two sources remaining reasonably constant in their long-term light curves display very different spectral evolution behaviours over time. We find that CXOU J123043.2+413818 follows a similar spectral evolution to a disc, loosely following $L_{\rm X} \propto T^4$ on the parameter-luminosity plot, whilst CXOU J123030.8+413911 appears to show the opposite trend, with $kT_{\rm in}$ decreasing as the luminosity increases. Although we cannot statistically separate model preference, it is interesting to note that each source is consistently better fitted by a particular model. While CXOU J123043.2+413818 varies in a disc-like manner, it also retains a lower χ^2 fit for MCD, whilst CXOU J123030.8+413911 is better fitted by a PL-type shape. We reiterate that we cannot offer a statistical distinction between these two models for either source, but suggest that this secondary evidence supports the initial distinction made by χ^2 fits.

More interestingly, we find that the spectral fits to the other three sources, CXOU J123030.6+414142, CXOU J123032.3+413918 and CXOU J123036.3+413837, appear to show them transiting between these two models, which could potentially be used as a test of our secondary evidence. If we consider their changing spectral behaviour we find that those observations better modelled by a MCDBB appear to vary in a disc-like fashion in the majority of cases, while those modelled by a PL tend to leave the $L_{\rm X} \propto T^4$ track. We also note that the long-term light curves of each of these sources vary substantially; crucially these flux variations correlate with apparent spectral state, with observations at low luminosities appearing to possess a PL-type shape, with spectra switching to a MCDBB-type state at higher luminosities. Again, despite the lack of statistical evidence for a distinction between the models, this behaviour does appear to support the χ^2 fitting. If we do accept the changes in spectral shape, then the most obvious explanation of the behaviour of the ULXs is that they can reside in different spectral states, delineated by the PL and MCDBB spectra, and that in some cases we are observing sources that have undergone a transition from a PL-type to MCDBB-type state (or vice-versa). As this is an extremely interesting result, we now consider the physical implications of such behaviour on our understanding of these systems.

A further reason to think that there may be some physical basis for the two spectral types we see in the NGC 4485/4490 ULXs is that they have been seen in other ULXs before. Mizuno et al. (2007) suggested (based on observations of two ULXs in NGC 1313) that the PL-type state may be representative of the very high state observed in Galactic black hole X-ray binary systems, whilst the MCDBB-type state may be more suggestive of the theoretically predicted 'slim disc' model (e.g Watarai et al. 2001). The latter is supported by observations fit by the p-free model (e.g. Vierdayanti et al. 2006). The p-free model assumes that the disc temperature scales as r^{-p}, where r is the radius and p is a free parameter. In the case of a standard disc the value of p would be fixed at 0.75 but if the p-value decreases, softer energies become more enhanced, and the spectrum becomes more representative of a slim disc. In the case of the MCDBB-type spectra of M81 X-9, the best fitting parameters reduce the p-value to 0.6, significantly smaller than a standard disc value (Miyawaki et al. 2006), supporting the existence of an ultraluminous slim disc state (although we note that problems begin to arise for this model in the higher quality data regime, see Chapter 5). Kuncic et al. (2007) made similar associations for the PL-type state, but suggested that this could also be representative of a system with some kind of outflow. The authors did this by demonstrating that a disc modified with jet emission could also explain the observed spectral shape. Soria & Kuncic (2008) developed this work further, presenting the idea that the PL-type state could be explained by a black hole in the hard state with an associated jet that persisted up to $\sim$ Eddington rates, where an outflow-dominated or a slim disc state would be formed. This allows for the possibility of direct transition from a hard PL-type state to a super-Eddington state.

The suspected change in state that we observe is consistent with those found previously and we argue that, although the PL-like spectrum observed appears similar to that of an accreting black hole in the low/hard state, we are probably observing sources residing in the very high state (VHS; a.k.a. steep power-law state, McClintock & Remillard 2006). The spectrum of the VHS is empirically characterised by a hot disc and a steep power-law in the 3.0 – 20.0 keV band. It should be noted that the power-law component is used as a proxy to describe optically-thin Comptonisation, however a spectrum resulting from this process is subtly curved with a shallower slope at lower energies. Here we observe only the lower 0.3 – 10.0 keV energy range, although the relatively poor high energy sensitivity of the *Chandra* ACIS-S means we only have constraints up to $\sim$ 5 keV. Hence we observe only the shallower section of the Comptonised component. This should then also be combined with emission from the 1 – 2 keV disc component seen in the VHS (although data quality is insufficient at present to separate these components). This amalgamation of components could potentially act to flatten the slope of the spectrum below 5 keV, resulting in the range of power-law photon indices observed. As the mass accretion rate (and so the observed luminosity) is increased, it is likely that a change in the accretion structure of the system occurs that invokes a change in spectrum to the MCDBB-like state. The observed curvilinear structure of such a state would be representative (in our modest spectral quality regime) of a slim disc, or an optically-thick Comptonising corona masking the inner radii of the disc (Done & Kubota 2006; Stobbart et al. 2006). We note that in each of these model scenarios the disc temperature increases with luminosity (Roberts et al. 2006; Vierdayanti et al. 2008).

The detection of this possible change in state (from PL to MCDBB-type or vice-versa) has previously been noted in other ULX studies. The clearest transition to date was reported in M81 X-9 by Miyawaki et al. (2006), with a transitional luminosity of 1.5 $\times 10^{40}$ erg s^{-1}. Multiple spectra of NGC 1313 Source B were also analysed by the authors but results in this case were not as clear as M81 X-9. The tendency towards MCDBB-like spectra with increasing luminosity was apparent, although a precise transition was not evident, occurring within the range $\sim 5 - 9 \times 10^{39}$ erg s^{-1}. Similar transitions, from a PL-type state to a MCDBB-type state, have also occured in IC 342 X-1 and X-2 at around 10^{40} erg s^{-1} (although with only two observations analysed, it is impossible to give a precise transition luminosity; Kubota et al. 2001).

Soria & Kuncic (2008) proposed that the transition between states would occur at around the Eddington limit, if we assume little beaming. Based on this proposition, the observations reported provide a potential diagnostic to these systems, and allow us to place constraints on the masses of the black holes contained within the ULXs in NGC 4485/4490. Firstly we note that it is certainly not necessary to invoke an intermediate mass black hole to achieve the observed luminosities of these systems ($\lesssim 4 \times 10^{39}$ erg s^{-1}), indicating that these sources need be no more than large stellar mass compact objects ($\lesssim 30\ M_{\odot}$ if they obey the Eddington limit). Secondly, if this apparent state change is occurring at the Eddington limit, the luminosity at which a transition is observed would give a rough estimate on the mass of the system. Although we cannot observe a distinct change in state at this level of data quality, the variable ULXs in NGC 4485/4490 appear to change state at $\sim 2 \times 10^{39}$ erg s^{-1}, which would mean that these systems are host to $\sim$10 – 15 $M_{\odot}$ black holes, i.e. standard stellar mass black holes. Following this argument CXOU J123030.8+413911, which continues to reside in the PL-type state up to a luminosity of 2.8×10^{39} erg s^{-1}, could therefore contain a more massive black hole. Interestingly, if we were to extrapolate this argument to other sources where transitions have been reported, with observed transitional luminosities ranging from 2 – 15×10^{39} erg s^{-1} (including our current sample), the primaries of ULXs would range in mass up to no more than $\sim$100 $M_{\odot}$ (M81 X-9, in agreement with Tsunoda et al 2006).

The implications of this argument are in agreement with evidence emerging from other observations of ULXs, a review of which was compiled by Roberts (2007). For example, when high quality X-ray spectra are available, a break emerges above 2 keV (Stobbart et al. 2006), which should not be present in the X-ray spectrum of large, $\sim$ 1000 $M_{\odot}$ intermediate-mass black holes. This feature is more indicative of some form of extreme accretion onto a smaller compact object. Optical evidence also appears to be converging on similar mass estimates, for example irradiation models describing the optical emission of ULXs have been used to constrain the mass of the black hole for several sources, generally imposing the limit $M_{BH} \lesssim 100$ $M_{\odot}$ (Copperwheat et al. 2007). Recent developments in theory have shown that it is possible to create black holes with $M_{BH} \lesssim 100$ $M_{\odot}$, in young stellar populations with either low metallicity stars (Fryer & Kalogera 2001, Heger et al. 2003), or with the merging of binaries (Belczynski et al. 2006). With evidence from both observation and theory converging on large stellar mass objects, timely evidence came when Prestwich et al. (2007) found such an object. Repeated optical exposures of the Wolf-Rayet black hole binary known as IC 10 X-1 culminated in a radial velocity curve, providing a primary mass estimate of 23 – 34 $M_{\odot}$, the largest stellar mass black hole found to date (see also Silverman & Filippenko 2008). Hence it is looking an increasingly realistic proposition that a large fraction of the ULX population are powered by black holes not substantially larger than those we already know of in our own Galaxy.

4.4.2 The candidate SNR CXOU J123029.5+413927

CXOU J123029.5+413927 was identified as a possible supernova remnant due to its high absorption column, soft underlying continuum and its coincidence with the radio source FIRST J123029.4+413927 (RWWM02). Mid-infrared studies of NGC 4485/4490, carried out by Vázquez et al. (2007) using the *Spitzer Space Telescope*, found that five of the ULXs showed high ionisation features that are found in AGN. Conversely the mid IR spectrum of CXOU J123029.5+413927 showed emission more indicative of star forming regions. This, with the addition of a weakly detected [O VI] 25.91 μm emission line, a line that is recognised as a strong feature in SNRs (Morris et al. 2006; Williams et al. 2006), supports the previous classification. If it is a SNR then it is obviously amongst the brightest of its class - X-ray luminosities in excess of 10^{39} erg s^{-1} are seen in a number of young SNRs (Immler & Lewin 2003), although typical older SNRs are 2 – 3 orders of magnitude fainter in X-rays (e.g. Pannuti et al. 2007). However, in contrast to previous evidence, analysis by Fridriksson et al. (2008) reported a 30 per cent drop in luminosity for this source in the four months between the second and third *Chandra* observations, behaviour that is more typical of an X-ray binary source.

A compelling argument on the nature of this source is discovered when looking at the light curve of this source. We find that previous observations place its detonation (or at least the epoch at which its X-ray emission brightened) some time after the 1991 *ROSAT* observation, which would imply that we may be observing a very young SNR. The calculated rate of decay of X-ray flux within the light curve gives further insight. Studies performed using data from early X-ray telescope missions showed that this decay proceeds as $L_{\rm X} \propto t^{-s}$ with index $s = 1$ (e.g. Chevalier & Fransson 1994); however the flux and temperature calculations performed in these earlier studies could have been contaminated by diffuse emission due to the poorer resolution of these satellites. More recent studies with *Chandra* and *XMM-Newton* have demonstrated that the decay observed within the light curve of a young SNR has an index $s \sim 3$ (e.g. $L_{\rm X} \propto {\rm t}^{-2.7}$ in Immler & Kuntz 2005, ${\rm t}^{-3}$ in Temple, Raychaudhury & Stevens 2005, ${\rm t}^{-3.9}$ in Aretxaga et al. 1999). The rate of decay observed in the light curve of CXOU J123029.5+413927 is found to be $L_{\rm X} \propto t^{-0.3}$, a decay rate that is far shallower than young SNRs. Therefore this source *could* simply be an X-ray binary system, as suggested by Fridriksson et al. (2008). An alternative to this could be a young SNR with an additional roughly constant component, diluting the emission and affecting the observed decay rate. This component could be an X-ray binary system, although it is notable that it hasn't produced the high ionisation nebulae as seen around the other ULXs in NGC 4490 by Vázquez et al. (2007). Much deeper observations would be required in order to test either hypothesis.

4.5 Summary

Multiple observations of the interacting galaxies NGC 4485 & 4490 have afforded us the opportunity to study its large ULX population, and in particular to see how their emission evolves over time. We have found that the population is unanimous in its lack of short-term temporal variability, but long-term spectral and temporal variations have given a possible insight into the mass of black holes contained within them. Observations have revealed that sources exhibiting large scale temporal variation (excluding CXOU J123029.5+413927) may change spectral shape from that of a PL-type to a MCDBB-type as their luminosity increases. If real - and there is some uncertainty here, as we cannot strongly differentiate between fits with PL and MCDBB models based on the current data – this change in spectral shape/state occurs at $\sim 2 \times 10^{39}$ erg s^{-1} for the ULXs in this system. We propose that this state change is from the VHS to an ultraluminous state, a transition that occurs at around the Eddington limit. If this is the case it would imply that *the majority of the ULX population residing in this interacting galaxy pair are stellar mass black holes of around 10 – 15* $M_{\odot}$.

The analysis of the possible spectral transitions has culminated in a testable hypothesis that can potentially be applied to other ultraluminous X-ray sources, for example the newly observed transient source CXOU J123038.3+413830. This object has only been observed once to date and so it is impossible to tell at present any more than its current preferred state, a MCD-type state. The observed luminosity of this source is much lower than the transitional luminosity noted for the majority of sources in our current source population. Extrapolating from our above arguments would suggest that this system contains a compact object of lower mass. Further observations are obviously required to constrain the nature of this source and indeed to continue our study of the behaviour of the whole ULX population of NGC 4485 & 4490.

4.6 Addendum - New *XMM-Newton* Data and Results

The previous sections of this chapter were accepted for publication by the Monthly Notices of the Royal Astronomical Society as Gladstone & Roberts (2009). However, we subsequently received two further proprietary *XMM-Newton* observations of these systems (Programme: 055630; PI: Gladstone). We therefore return to this interacting galaxy pair to explore further the spectral evolution of these sources and to begin to test the theories and ideas put forward during our previous analysis.

4.6.1 *XMM-Newton* observations and data reduction

The interacting galaxy pair, NGC 4485 & 4490, was observed twice by the *XMM-Newton* telescope in 2008, the details of which are listed in Table 4.3. For simplicity we continue our nomenclature for observations, labelling these observations X2 and X3, and using these throughout the rest of this work.

These new observations were reduced using the SAS software (version 8.0.0). We utilise data from *XMM-Newton* EPIC, which was operating in full-field mode using the medium filter. Unfortunately each of our observations were severely affected by background flaring. In the case of X2, background flaring caused periods of data to be lost resulting in multiple exposures within each MOS detector.

We find that the second exposure in both MOS detectors was so heavily contaminated as to make it unusable. We therefore only use the first MOS exposure along with the pn data in our analysis. The data from observation X2 was cleaned to remove any residual flaring by constructing a good time interval (GTI) file from the pn data using a full-field 10 – 15 keV background light curve and count rate criteria (< 1.5 cnt s^{-1}). As a result the exposure for the pn detector was reduced to 21.9 ks, although slightly less is available in each of the MOS detectors (by ~ 40 s). We find that this difference is small because the majority of pn data obtained during the time frame of each MOS exposure 2 is removed during cleaning. The same GTI file was used for both the pn and MOS instruments to allow for the direct co-addition of light curves (pn data was cropped to account for the lost time in in MOS due to the loss of the second exposure). As a final check, we visually inspected the time filtered full-field light curves for each MOS detector,

Table 4.3: New X-ray observations of NGC 4485 and NGC 4490.

Label	Observatory	Detector	Obs ID	Mode
X2	*XMM-Newton*	EPIC	0556300101	Full Field
X3	*XMM-Newton*	EPIC	0556300201	Full Field

Label	Date	Time^a	Exposure^b (ks)	Aimpoint^c	
				RA	Dec
X2	2008:05:19	08:52:45	21.9	12^h 30^m 36^s	+41^o 38' 41"
X3	2008:06:22	06:14:13	3.18	12^h 30^m 36^s	+41^o 38' 41"

Notes: ^{a}Exposure start time in universal time (UT). ^{b}Sum of GTI file. ^{c}J2000 coordinates.

and no additional flares were observed. Source spectra and light curves were extracted from X2 using circular regions centred on the individual ULXs in each detector, following the procedures described in Section 4.2.2 & 4.3.

If we now consider X3, we find that heavy flaring took place throughout the entirety of the observation, which resulted in the loss of the majority of the data from this observation (only $\sim$ 3.2 ks remained after cleaning). The resulting spectra are of too low quality to be able to perform reasonable spectral analysis in all cases. Whilst the short term light curves of each of our sample will be washed out by the background emission, we are at least able to extract enough information from X3 to extend the baseline of our long-term light curves for each ULX.

4.6.2 ULX properties

Seven ultraluminous X-ray sources were discussed in Sections 4.3 to 4.4. Here we find that the newest ULX transient detected (CXOU J123038.3+413830) appears to have once again faded below the detection limits of our new observations. As this source only just peaked inside the ULX luminosity range during the observation C3, it indicates that this transient source may be similar to X-ray binaries within our own Galaxy, for example a low mass X-ray binary observed during outburst (see Chapter 1 for discussion of these systems) or a Be X-ray binary observed during a burst. While we note that the majority of compact objects in Galactic Be X-ray binary systems have so far been identified as neutron stars (42/64, with the nature of the remainder unknown), we point out that current evolutionary scenarios predicts that a low number of these sources will contain black holes (Belczynski & Ziolkowski 2009). If CXOU J123038.3+413830 is a Be X-ray source, then given the luminosity of this source at the observed peak, it would be more likely that this was a system containing a black hole. We are therefore unable to study this source further during the extended exploration of this ULX population, but we suggest searching databases of alternative X-ray telescopes to look for further evidence of outburst in order to confirm its nature.

The six remaining ULXs have combined EPIC count rates of 0.053 – 0.240 count s^{-1}, resulting in 1157 – 5120 counts in total being accumulated per source (for X2 only), providing us with the best quality data currently available for the sources in this galaxy pair. We note that CXOU J123030.6+414142 fell near to the pn chip gap once again, but at a great enough distance to allow for the use of a circular extraction region. However, due to the proximity to a new nearby source we are forced to use a reduced radius of 12 arcsecs in all detectors.

ULX X-ray spectra are grouped to a minimum of 20 counts per bin and fitted using the same simple (absorbed single component) models discussed earlier using XSPEC version 11.3.1, in order to compare these results with those of our previous analysis. EPIC pn and MOS data are once again analysed concurrently using a constant multiplicative factor to gain the best fit, with spectral fitting carried out in the 0.3 – 10.0 keV energy range. The resulting fits are given in Table 4.4 with errors quoted to 90 per cent for one interesting parameter.

Table 4.4: Spectral modelling of the ULXs in NGC 4485 and NGC 4490 in observation X2.

Source Name	TBABS * PO				TBABS * DISKBB				BIC
CXOU	${N_H}^a$	Γ	χ^2 / DoF	${L_\mathrm{X}}^b$	${N_H}^a$	${kT_{in}}^c$	χ^2 / DoF	${L_\mathrm{X}}^b$	
J123029.5 + 413927	1.9±0.4	$2.3^{+0.2}_{-0.1}$	81.44/52	$1.0^{+0.7}_{-0.4}$	0.9±0.2	$1.4^{+0.2}_{-0.1}$	**61.42/52**	$1.0^{+0.8}_{-0.3}$	8.22
J123030.6 + 414142	$0.31^{+0.05}_{-0.04}$	$1.97^{+0.10}_{-0.09}$	**104.29/111**	$2.6^{+0.6}_{-0.4}$	0.07±0.03	$1.31^{+0.10}_{-0.09}$	120.36/111	$2.5^{+0.5}_{-0.3}$	6.98
J123030.8 + 413911	1.3±0.2	$1.9^{+0.2}_{-0.1}$	**68.93/76**	$3.2^{+1}_{-0.8}$	0.8±0.1	$1.7^{+0.2}_{-0.1}$	80.05/76	$3.1^{+0.5}_{-0.3}$	4.82
J123032.3 + 413918	0.7±0.1	$2.0^{+0.2}_{-0.1}$	**56.37/58**	$2.0^{+0.9}_{-0.6}$	$0.29^{+0.08}_{-0.7}$	$1.4^{+0.2}_{-0.1}$	73.58/58	$1.9^{+0.8}_{-0.3}$	7.42
J123036.3 + 413837	0.76±0.06	$2.26^{+0.08}_{-0.07}$	279.00/227	$4.6^{+0.8}_{-0.6}$	0.35±0.03	1.23±0.05	**196.23/227**	$4.6^{+0.5}_{-0.3}$	35.95
J123038.3 + 413830	...	...	...	...	...	...	...	...	
J123043.2 + 413818	$0.8^{+0.2}_{-0.1}$	$2.22^{+0.10}_{-0.2}$	76.53/63	$2.2^{+1}_{-0.6}$	$0.37^{+0.1}_{-0.09}$	$1.19^{+0.1}_{-0.10}$	**57.59/63**	$2.1^{+0.7}_{-0.2}$	8.7

Notes: We embolden the χ^2/degrees of freedom (DoF) for the best fitting model for each source observation. Specific notes: ^{a}Absorption column in units of 10^{22} atoms cm^{-2}. ^{b}Observed luminosity in the 0.5–8.0 keV band in units of 10^{39}erg s^{-1}. ^{c}Disc temperature in keV. ^{d}Bayesian Information Criterion value (using Schwarz method).

We find that single component models provide an acceptable fit ($P_{\rm rej} < 95$ %) in the majority of cases. There are only three instances in which the rejection probabilities exceed this, the first of which is the possible SNR. In this case the χ^2 minimisation shows preference for a MCDBB and the PL is rejected on null hypothesis grounds (an interesting point that will be discussed in more detail in Section 4.6.5). The second is the near nuclear source in NGC 4490, which is also the most variable. This source is best fit by a MCDBB when we consider χ^2 minimisation, but also rejects a PL fit based on the null probability. Finally, the third is CXOU J123032.3+413918, a source that we would describe as having a PL-like spectra, while a MCDBB fit is statistically rejected by the null hypothesis value. We will return to this point further in the next section.

4.6.3 Implications for spectral variability

Here we combine the results shown in Table 4.4 with those of our previous analysis (Table 4.2) to further explore the spectral evolution of these systems. We will discuss the potential SNR (CXOU J123029.5+413927) in a later section (Section 4.6.5) and so do not consider it further here.

Our previous analysis highlighted a series of possible trends and ideas, we therefore ask a number of questions of this continued analysis. Can we statistically differentiate between models in this new data? Does the new data continue to exhibit a PL-like spectrum at lower luminosities, changing to a MCDBB-type spectrum at higher luminosities? Do those sources that showed preference for only one type of spectral shape throughout all previous observations change shape in X2? Do MCDBB-like spectra continue to evolve in a disc-like manner?

To answer the first of these questions, as to whether we can statistically differentiate between models, we return to Bayesian Information Criterion to look for evidence of a statistical improvement in the fit of one model over another. We find that two of our sample show 'positive' evidence of model superiority, whilst two show 'strong' evidence of model preference. In each case this is in agreement with the findings highlighted in Table 4.2 using χ^2 minimisation criteria. However, we find that CXOU J123036.3+413837 has a BIC value of 35.95, providing 'very strong' evidence of model superiority (very strong $\gtrsim$ 10; Kass & Raftery 1995).

If we now include the null hypothesis testing highlighted above, we find that in two of the five cases, the model that more poorly describes the data can be rejected statistically using the highest quality data currently available for these sources. The combination of these results, give further support to our original supposition. For example CXOU J123032.3+413918 shows a PL-like spectra when we based model choice on χ^2 minimisation, the BIC value for this model is 7.42 giving further 'strong' statistical support to the a PL over a MCDBB model, and finally a MCDBB can be statistically rejected via null probability.

We now consider our second question: is the potential change in state still evident when the new data is incorporated? We find that 4/5 ULXs that we consider in this section, continue to show a preference for a PL-like structure at lower luminosities, whilst the spectra switches to a MCDBB-like shape at higher luminosities. However, we find that our most recent observation of CXOU J123030.6+414142 appears to deviate from this trend. If we consider briefly all observations of this source presented within this chapter, we find that this source is best represented by a PL in observations X1 & X2, whilst being best fit by a MCDBB in C1, C2 & C3. The spectrum extracted from X2 exhibits this PL-like spectral shape at a luminosity of $2.6(^{+0.6}_{-0.4}) \times 10^{39}$ erg s^{-1}, which is brighter than two of the previous MCDBB-like spectra (although similar within errors). Such an observation may raise questions about our previous findings, and the nature of these systems. One possible solution is that we are observing this source whilst it it undergoes the process of hysteresis, where the transitional luminosity is typically higher on the rise to outburst than on the decline. If we are observing this source during a transition, it is possible that the luminosity of this source is not a good indication of state. In either case data of greater quality and/or more numerous observations are required to answer this.

We now explore the third and fourth questions. These were: do those sources that showed preference for only one type of spectral shape throughout all previous observations change shape in X2 and do the MCDBB-like spectra continue to evolve in a disc-like manner? To examine how the spectra in these systems evolve over time, we combine the output from our analysis of X2 with the results found earlier in this chapter (see Figure 4.8). We fold in the new values for both Γ and $kT_{\rm in}$ with the observed and intrinsic luminosities for the 0.5 – 8.0 keV band pass (listed in Tables 4.2 & 4.4) to create new parameter verses luminosity plots for each model used. Again we plot those with the lowest value of χ^2 per degrees of freedom (best fit model) with a solid line, whilst those plotted with a dashed line refer to the model with the highest χ^2/DoF in respective parameter figures.

Considering initially CXOU J123043.2+413818, represented by blue open stars, we find that this object continues to show a MCDBB-like spectrum. The best fitting parameters for X2 falls along the same line observed previously, showing a rise in inner disc temperature as the luminosity increases, similar to that of a disc in the $kT_{\rm in}$ vs. $L_{\rm X,observed}$ plot, a trend that continues when we consider the intrinsic luminosity of the system.

We find that CXOU J123030.8+413911 (red open squares), continues to follow the trend observed previously by exhibiting a PL-type spectral shape irrespective of luminosity. This source reaches a new peak in the observed luminosity at 3.2×10^{39} erg s^{-1}, retaining a PL-like spectrum above the $\sim 2 \times 10^{39}$ erg s^{-1} limit suggested in previous work, but we note that this source has already been observed above this, and possible explanations discussed in Section 4.4.1. This source appears to display a lack of correlation between the observed luminosity and the photon index, but once the absorption is removed a correlation becomes evident.

We find that the spectra best represented by a MCDBB continue to show a disc like evolution in the majority of cases, whilst those observations described as PL-like continue to deviate for the $L \propto T^4$ track. We can now statistically distinguish between models in X2, and we note that a difference in spectral evolution continues with the addition of data from X2. This supports the original supposition of separate spectral states.

We note that one of our sample has been removed from the parameter–luminosity plots shown in Figure 4.8, this is CXOU J123036.3+413837. We find that we are unable to display all the data in Figure 4.8, whilst still allowing the trends of other sources to be evident, therefore we plot this source separately in Figure 4.9. This is the most variable source in our sample, with luminosities ranging over an order of magnitude in luminosity, from 0.4(C2) $-$ 4.5(X2) $\times 10^{39}$ erg s^{-1}. If we consider initially those observations best fit by a MCDBB, we find a loose correlation of inner disc temperature in relation to the observed luminosity. Now looking at parameters derived for the PL-like spectra, we find that this source follows a trend that are more similar to MCDBB-type spectra, the spectra

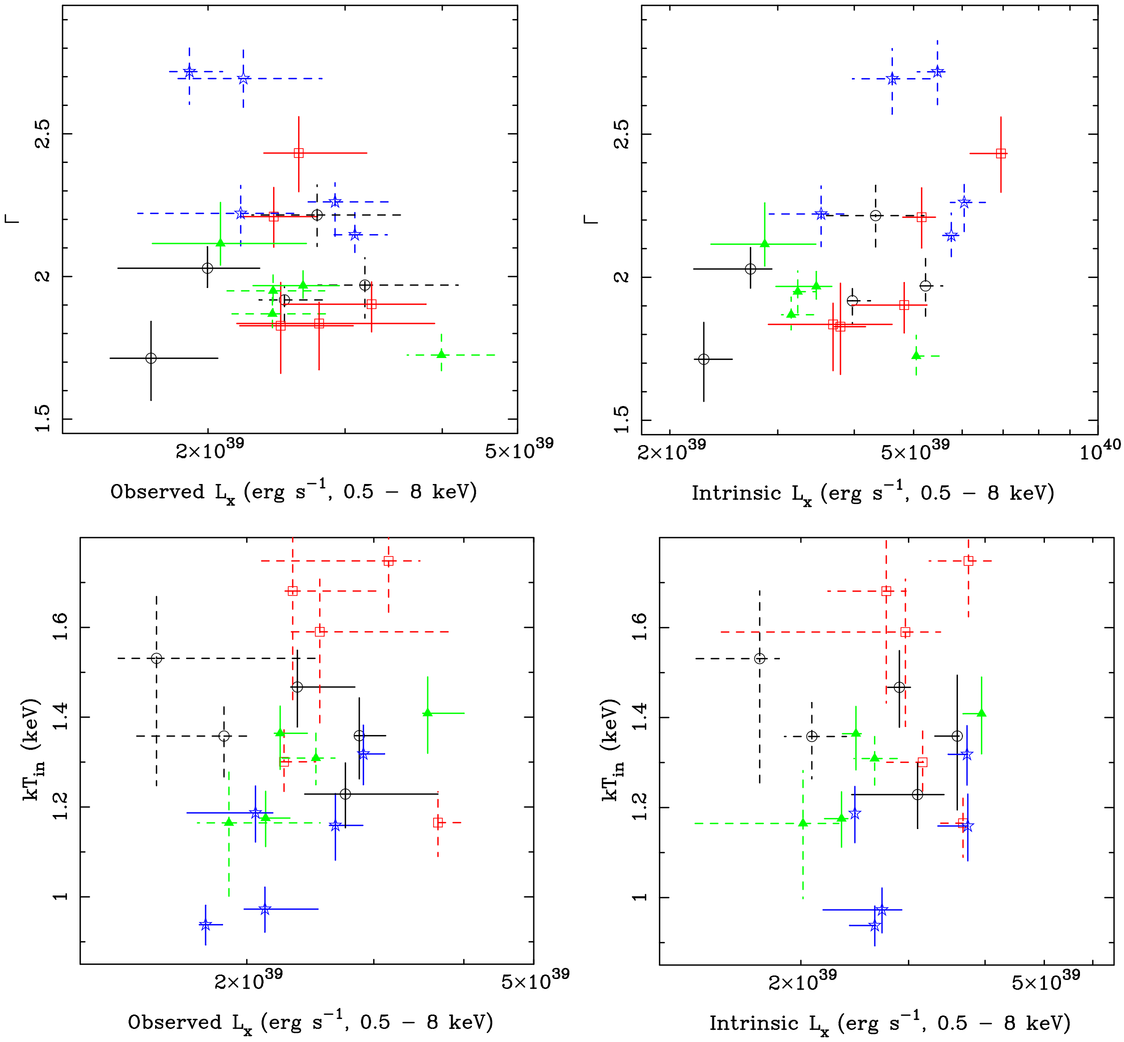

Figure 4.8: Spectral parameters in five ULXs in the NGC 4485 & NGC 4490 system, plotted against both the observed (*left panel*) and intrinsic (*right panel*) luminosity over the 0.5–8.0 keV energy range. Each ULX represented by a different colour/symbol combination as in Figure 4.4. These are: green filled triangles - CXOU J123030.6+414142; red open squares - CXOU J123030.8+413911; black open circles - CXOU J123032.3+413918; blue open stars - CXOU J123043.2+413818.

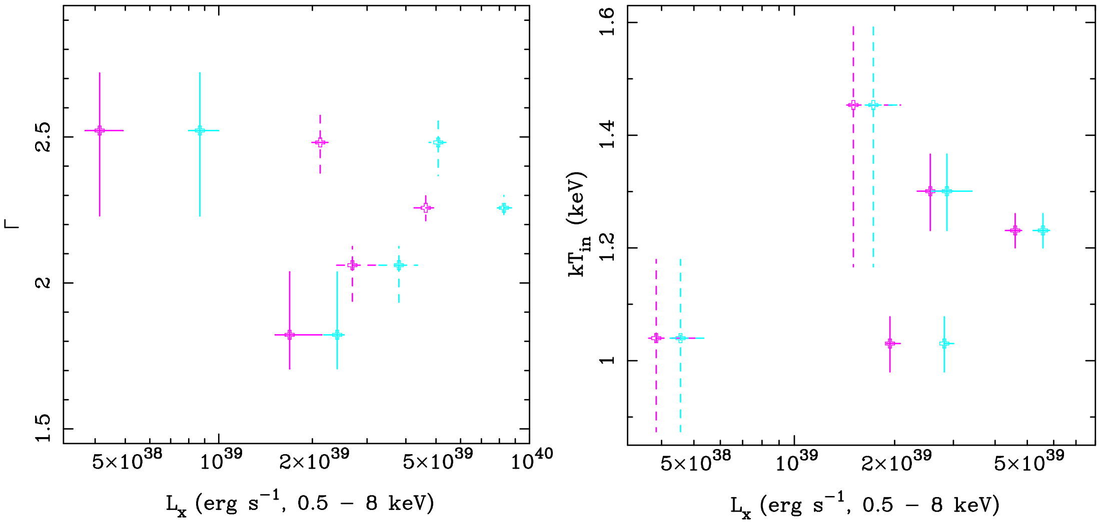

Figure 4.9: Spectral parameters for CXOU J123036.3+4113837, plotted against both the observed (*magenta*) and intrinsic (*cyan*) luminosity over the 0.5 – 8.0 keV energy range.

harden with increasing luminosity (although over a much larger luminosity range). One possible explanation for this difference is rooted in the fact that observations of this source cover a wide range of luminosities. This range allows for the possibility that we may be looking at more than two possible spectral states. At the lowest luminosities, this source is emitting well within the range observed from standard Galactic X-ray binary systems, and may therefore be residing in a standard accretion state, whilst all other observations of this source occur where it emits in the ultraluminous range ($> 10^{39}$ erg s^{-1}), and so may be residing in the states discussed in Section 4.4.1. If this is the case the PL-like observations could reflect two separate accretion states and so we would not necessarily expect the two PL-like observations to correlate in this parameter space. We also note that with such high variability, this source clearly stands apart from the rest of our sample. Again, further observations are required to clarify the range of spectral states observed in this source, and its implications for our overall results.

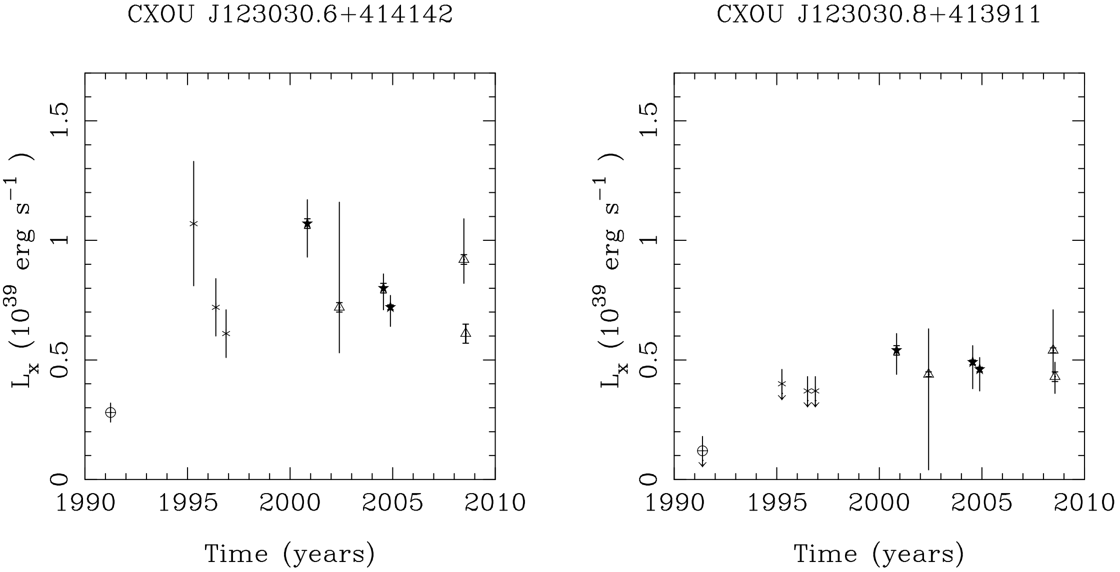

Figure 4.10: Extended long-term light curves of six ULXs studied in NGC 4485 and NGC 4490. Results shown are from *ROSAT* PSPC and HRI instruments (represented by open circles and asterisks respectively), *Chandra* ACIS-S (filled pentagram) and *XMM-Newton* EPIC camera (open triangle) in the 0.5 – 2.0 keV band, using the best fitting single component models (either absorbed power-law or multi-colour disc blackbody). Errors have also been derived using a similar method to RWWM02 for *ROSAT* PSPC and HRI instruments for each new observation, these are also shown. Upper limits are represented by downwards arrows.

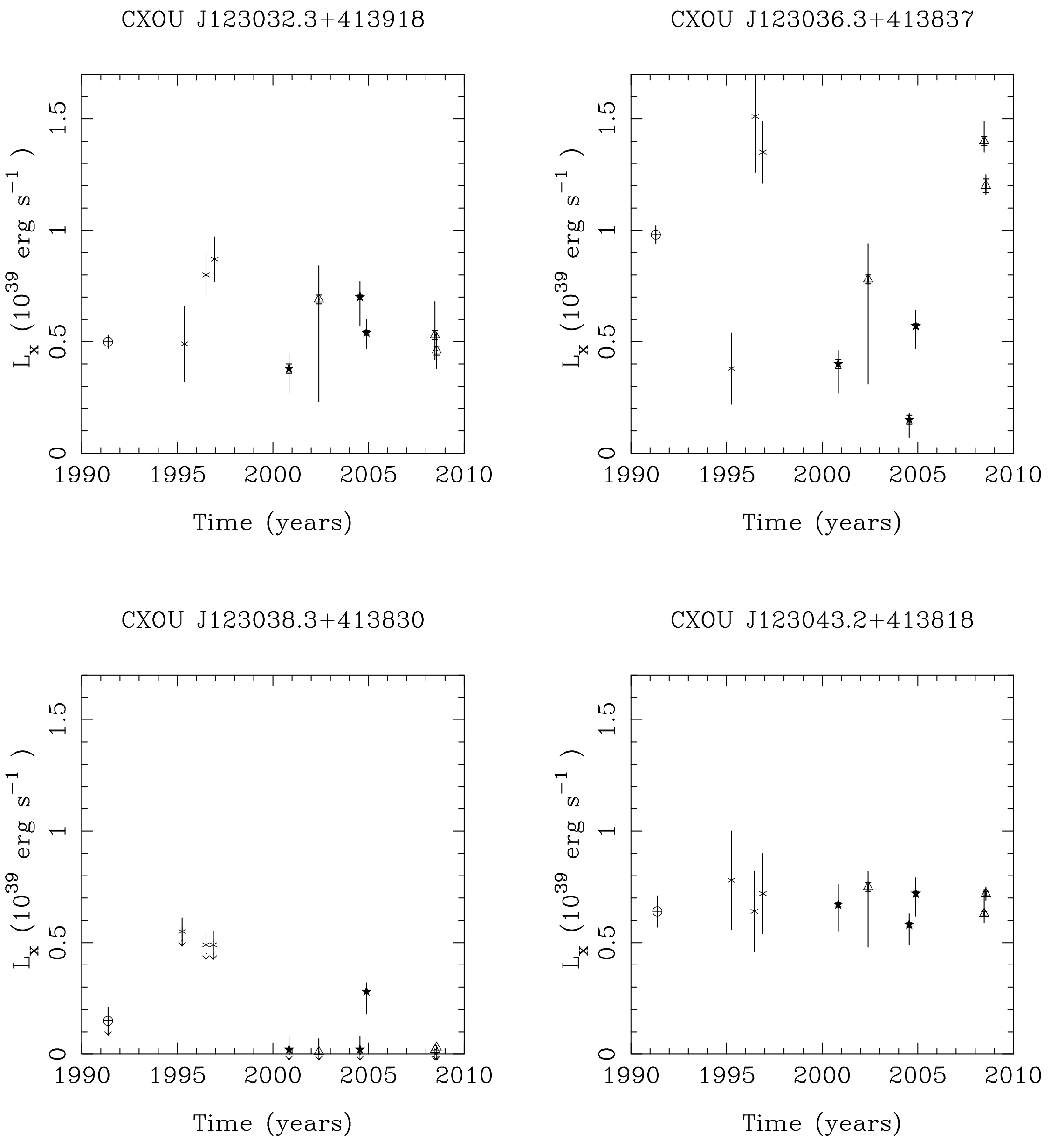

Figure 4.10: *continued.*

4.6.4 Implications for temporal variability studies

Initially we look for signs of intra-observational temporal variability using light curves extracted from observation X2, applying the techniques and analysis discussed in Section 4.3.3. We find that the combination of χ^2 fitting and excess variance calculations are still yet to reveal any statistical signs of variability for any ULX in these galaxies on short time-scales.

On longer, inter-observational time-scales, a range of variations are still observed. Here we extend the long-term light curves presented in Section 4.3.4 to include the two most recent *XMM-Newton* observations of this galaxy pair. These can be seen in Figure 4.10. Once again we note that these are constructed using the luminosity from the 0.5 – 2.0 keV band pass, so as to utilise data from all instruments, which results in luminosities that are generally lower than those indicated elsewhere. The long-term light curves for all but the potential SNR, CXOU J123029.5+413927, are shown in Figure 4.10. This source is shown in Figure 4.11 and is discussed in the next section.

A cursory look at these light curves reveals a range of variability across the sample. We can see that both CXOU J123043.2+413818 and CXOU J123030.8+413911 (since it turned on) continue to remain reasonably stable in their emission and when we apply the significance parameter, taken from Fridriksson et al. (2008), we find that they still continue to lie below the significance threshold ($S_{flux} > 3$). As noted in Section 4.6.3, the recently discovered transient (CXOU J123038.3+413830) has once again decreased its emission to an undetectable level, which is clearly evident Figure 4.10 where we see that the limits taken from this observation (using the best fitting model from our only detected observation) are well below that detected previously. We also find an increase in variability in a number of the ULXs in our sample, including CXOU J123030.6+414142 ($S_{flux} = 6.3$) and CXOU J123036.3+413837, which now reaches an S_{flux} of 14.8.

4.6.5 CXOU J123029.5+413927 - a possible SNR?

Our previous work discussed the nature of the possible supernova remnant, CXOU J123029.5 +413927, indicating that the long-term light curve of this source did reveal a decay in the emission of this source. The previous observations showed that this object must have

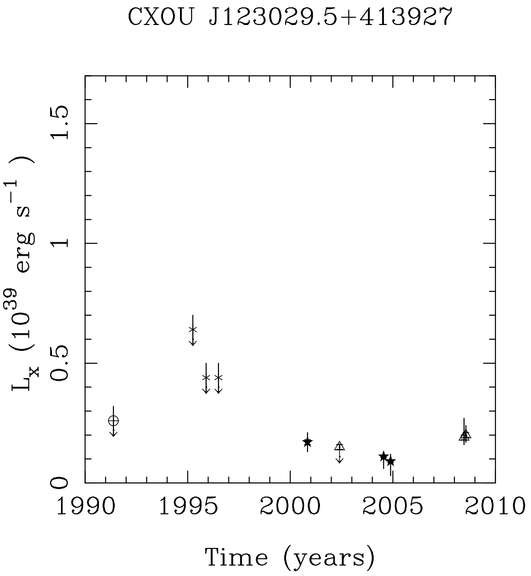

Figure 4.11: Extended long-term light curve for possible supernova remnant, CXOU J123029.5+413927. Symbols are as per Figure 4.10.

brightened (detonated?) some time after 1991, which would indicate that we may be looking at a young SNR, but that this rate of decay was too shallow for such a source. This lead to the suggestion that an additional component could be diluting the emission of the SNR and affecting the observed decay rate. An alternate idea was proposed by Fridriksson et al. (2008), stating that we may after all simply be observing an X-ray binary system.

Upon examination of the extended long term light curve of this source (shown in Figure 4.11) we find a spike in the emission of this source during X2 & X3. Such a spike would be very unlikely if we were observing a pure and undiluted SNR. We find that during this spike the source shows preference towards a MCDBB-like spectrum (for observation X2) if we use the lowest value of χ^2/DoF, with the possibility of a power-law fit discounted via the null hypothesis criteria. A MCDBB-like spectrum would indicate the presence of an accretion disc and therefore an X-ray binary system. We can therefore rule out the presence of an isolated young SNR. So the question remaining is whether we are observing emission that is purely from an X-ray binary system, or if the shallow decay witnessed in earlier in the long-term light curve of this source was the result of a young SNR in combination with an X-ray binary system.

4.6.6 Summary

Two recent observations made by the *XMM-Newton* telescope have provided us with the opportunity to revisit the pair of interacting galaxies, NGC 4485 & NGC 4490, and their large sample of ultraluminous X-ray sources, to test our previous conclusions and explore the nature of these systems in more detail. Whilst all sources continue to show no statistical signs of variability on short time-scales, the long term spectral and temporal trends observed previously in the majority of our sample appear to continue. We find that their spectra continue to exhibit a PL-like spectra at lower luminosities transiting to spectrum more easily described by a MCDBB at higher luminosities. The are two exceptions to this, the first is CXOU J123030.8+413911, which continues to display PL-like spectral shape up to a new high of $\sim 3.2 \times 10^{39}$ erg s^{-1}. This could indicated that we are looking at a slightly more massive BH than previously considered (but still possible as the end point of one star i.e. $M_{\rm BH} \lesssim 100 M_{\odot}$) . The other is CXOU J123030.6+414142, which in observation X2 displays a PL-like spectrum at 2.6×10^{39} erg s^{-1}. This result may challenge our previous ideas or may be the result of hysteresis.

Considering some of the other sources we have observed, we find that the near-nuclear source in NGC 4490, CXOU J123936.3+413837, exhibits a large amount of variability over longer time-scales, indicating that we may be observing a range of spectral states from sub to super-Eddington accretion rates. We also find that the transient source, identified in the previous sections as CXOU J123038.3+413820, has dropped below detection limits once again during X2 & X3, indicating that our previous detection may have been during a short outburst.

Finally we note that the spectrum of the possible young SNR, identified initially in RWWM02, is best modelled by a MCDBB in X2. This spectral shape discounts the possibility that we are observing a pure SNR, although we cannot at present rule out that the emission of such a source is present in conjunction with that of an X-ray binary system.

These new data highlight the need for more observations of high signal-to-noise in order to properly characterise the spectrum of these sources and to gain a greater understanding of their spectral variability.

Chapter 5

The Ultraluminous State

5.1 Introduction

Multi-wavelength approaches have started to open many doors within ULX research, but the true nature of these systems is still an enigma. Here we revisit the question of what the X-ray spectra of ULXs can tell us about the nature of their accretion flows, and how this constrains the nature of the accreting object. One method is to analyse the X-ray spectra of these sources, applying simple models of accretion systems, e.g. disc plus power-law. Results from such studies have revealed ~ 0.2 keV disc temperatures with a hard ($\Gamma < 2$) tail, implying black hole masses of $\sim 10^3\ M_{\odot}$ (e.g. Miller et al. 2003), which supports the IMBH interpretation. However, analysis of high quality data demonstrates the presence for curvature of the tail at the highest energies, with a photon deficit above 5 keV (Roberts et al. 2005; Stobbart, Roberts & Wilms 2006, SRW06 hereafter within this chapter; Miyawaki et al. 2009). Such curvature is never seen in the low/hard state at these low energies. Only the very high state shows similar curvature, but these generally have spectra which are steep. Thus the accretion flows in ULXs may not simply be scaled up versions of those seen in black hole binaries, as would be the case for the IMBH model. Instead, observation of ULXs may allow us to probe a new regime of accretion physics, a new 'ultraluminous state' (Roberts 2007; Soria 2007).

In this chapter we choose to use the best data available in the *XMM-Newton* public archives, as previous studies have shown the limitations of more moderate signal-to-noise data in samples of ULXs (e.g. Berghea et al. 2008). By using only the highest quality data from the widest band pass, highest sensitivity instruments available we can hope to avoid the ambiguity of previous analyses, and make definitive statements on the accretion processes in ULXs.

5.2 Source Selection

Following the example of SRW06, we aim to use only the highest quality data publicly available from the *XMM-Newton* Science Archive (XSA[1]) in order to provide the best characterisation of the structure of ULX spectra. We therefore choose only the best data sets, i.e. ULX observations with $\gtrsim 10,000$ accumulated EPIC counts ($\gtrsim 500$ independent spectral bins available for fitting). This restriction is imposed based on the work of SRW06, whose analysis shows that this is a reasonable threshold for statistically distinguishing between physically motivated models, particularly above 2 keV. This constraint provides a sample of 12 sources, which are listed in Table 5.1. We note that this may not be an exhaustive list, but that the number of sources in our sample is probably sufficient to allow global trends to become apparent. Some of this sample of ULXs have been observed on more than one occasion, in which case we select the longest individual exposure to provide the clearest view of their spectrum. The selected ULXs all reside within nearby galaxies ($\lesssim 10$ Mpc) due to restrictions enforced by data quality, and vary in foreground Galactic absorption in the range $1.39 - 31.1 \times 10^{20}$ cm^{-2}. Their X-ray luminosities are representative of the full ULX range, $\sim 10^{39}$ – a few 10^{40} erg s^{-1}.

5.3 Observations and Data Reduction

Data from the longest individual observation of each source in our sample were downloaded from the XSA. The data sets were reduced using standard tools in *XMM-Newton* - SAS software (version 7.0.0)[2]. We found that background flaring was severe enough in three cases that periods of data were lost, resulting in multiple exposure data sets within the same observation. Such flaring events took place during the observations of Holmberg II X-1 and M81 X-6 and caused multiple exposures in the MOS detectors only. In each case we find that one of the MOS exposures was heavily contaminated, so for these objects we

---

[1] See `http://xmm.esac.esa.int/xsa/`

[2] Details on the Science Analysis Software can be found at `http://xmm.esac.esa.int/sas/`

only use the other MOS data set, together with the pn data. The third observation to be affected in this way is that of M33 X-8. In this case we find that the pn data is split into 2 exposures whilst data from the MOS detectors is split into 3 exposures. The first exposure from each detector contained no usable information. On further examination we find that the second MOS exposure was also heavily contaminated by flaring. We therefore only use the second pn and third MOS exposures for the observation of this object. To remove any remaining flaring events from our observations we constructed good time interval (GTI) files from pn data using a full-field 10 – 15 keV background light curve and count rate criteria. The exact value of the count rate criteria used to construct the source GTI files vary according to field (typically excluding count rates higher than $\sim 1-1.5$ ct s^{-1}) to provide the longest exposure whilst minimising contamination. Details of these observations are included in Table 5.2, with listed exposure times incorporating the GTI corrections used during the reduction of the data.

The source spectra were extracted from circular apertures centred on the individual ULXs in each detector. This was straightforward for the majority of data, but we found that NGC 1313 X-2 was unfortunately positioned on the chip gap of the MOS1 detector so a polygonal source region was applied to optimise our data extraction. Background spectra were obtained from larger circular regions placed near to the source. Where possible, these were positioned on the same chip and at a similar distance from the read out node as the source. The only exception was NGC 4559 X-1, where the MOS detectors were operating in small window mode, therefore alternative background regions were selected on a separate chip in a position as close as possible to that used in the pn detector, whilst in the case of M81 X-6 no data was contained in the MOS1 observation. The size of the individual source and background extraction regions are recorded in Table 5.3 (in the case of NGC 1313 X-2 we only list the size of the circular apertures used in pn and MOS2).

Table 5.1: The ULX sample.

Source	Alternative names	RA (J2000)	Dec. (J2000)	$N_{\rm H}$ [a] (10^{20} cm^{-2})	d [b] (Mpc)	$L_{\rm X}$ [c] (10^{39} erg s^{-1})
NGC 55 ULX(1)	XMMU J001528.9-391319(2) NGC 55 6(3) Source 7(4)	00 15 28.9	-39 13 19.1	1.71	1.78(*i*)	1.1
M33 X-8(1)	CXOU J013351.0+303937(5) NGC 598 ULX1(6) Source 3(7)	01 33 50.8	+30 39 37.1	5.58	0.70(*i*)	1.0
NGC 1313 X-1(1)	IXO 7(8) Source 4(7)	03 18 20.0	-66 29 11.0	3.90	3.70(*i*)	3.7
NGC 1313 X-2(1)	IXO 8(8) NGC 1313 ULX3(9) Source 5(7)	03 18 22.3	-66 36 03.8	3.90	3.70(*i*)	4.7
IC 342 X-1(10)	CXOU J034555.7+680455(11) IXO 22(8) PGC 13826 ULX3(9)	03 45 55.5	+68 04 54.2	31.1	3.3(*ii*)	2.8
NGC 2403 X-1(1)	CXOU J073625.5+653540(12) Source 21(13) NGC 2403 X2(9)	07 36 25.6	+65 35 40.0	4.17	4.20(*i*)	2.4
Ho II X-1(1)	IXO 31(8) PGC 23324 ULX1(9) CXOU J081928.99+704219.4(12)	08 19 29.0	+70 42 19.3	3.42	4.50(*i*)	14.4
M81 X-6(1)	NGC 3031 ULX1(6) CXOU J095532.98+690033.4(12)	09 55 32.9	+69 00 33.3	4.16	3.63(*iii*)	2.2

Source	Alternative names	RA (J2000)	Dec. (J2000)	$N_{\rm H}$ [a] (10^{20} cm^{-2})	d [b] (Mpc)	$L_{\rm X}$ [c] (10^{39} erg s^{-1})
Ho IX X-1(1)	M81 X-9(1) NGC 3031 10(14) IXO 34(8) H 44(15) Source 17(7)	09 57 53.2	+69 03 48.3	4.06	3.55(*i*)	7.5
NGC 4559 X-1(1)	IXO 65(8) CXOU J123551.71+275604.1(12) X-7(16)	12 35 51.7	+27 56 04.1	1.49	9.70(*i*)	8.0
NGC 5204 X-1(1)	IXO 77(8) CXOU J132938.61+582505.6(12) Source 23(7)	13 29 38.6	+58 25 05.7	1.39	4.80(*i*)	5.3
NGC 5408 X-1(17)	J140319.606-412259.572(17) Source 25(7)	14 03 19.6	-41 22 59.6	5.67	4.80(*iv*)	3.7

Notes: [a]Absorption column values taken from Dickey & Lockman (1990) using WEBPIMMS. [b]Figures shown in brackets relate to following references, from which the assumed distance was taken: (*i*) SRW06, (*ii*) Saha et al. (2002), (*iii*) Liu & Di Stefano (2008), (*iv*) Karachentsev et al. (2002).[c]Observed X-ray luminosity (0.3 – 10.0 keV) based on the DKBBFTH model (see later). Numbers shown in superscript relate to the following references for source names: (1)SRW06, (2)Stobbart et al. (2004), (3)Read, Ponman & Strickland (1997), (4)Schlegel, Barrett & Singh (1997), (5)Grimm et al. (2005), (6)Liu & Mirabel (2005), (7)Feng & Kaaret (2005), (8)Colbert & Ptak (2002), (9)Liu & Bregman (2005), (10)Roberts & Warwick (2000), (11)Roberts et al. (2004), (12)Swartz et al. (2004), (13)Schlegel & Pannuti (2003), (14)Radecke (1997), (15)Immler & Wang (2001), (16)Vogler, Pietsch & Bertoldi (1997), (17)Kaaret et al. (2003).

Table 5.2: Observation details.

Source	Obs ID	Date	Off axis angle[a] (arcmins)	Exp[b] (s)
NGC 55 ULX	0028740201	2001-11-14	4.2	30410
M33 X-8	0102640101	2000-08-04	0.4	8650
NGC 1313 X-1	0405090101	2006-10-15	0.8	90200
NGC 1313 X-2	0405090101	2006-10-15	6.2	90200
IC 342 X-1	0206890201	2004-08-17	3.6	19750
NGC 2403 X-1	0164560901	2004-09-12	5.4	58470
Ho II X-1	0200470101	2004-04-15	0.3	40800
M81 X-6	0111800101	2001-04-22	3.2	88300
Ho IX X-1	0200980101	2004-09-26	0.3	80400
NGC 4559 X-1	0152170501	2003-05-27	0.3	38300
NGC 5204 X-1	0405690201	2006-11-19	0.2	33700
NGC 5408 X-1	0302900101	2006-01-13	0.2	99300

Notes: [a]Off axis angle of source in the *XMM-Newton* EPIC field of view, [b]Sum of good time intervals for each observation (taken from pn data), calculated as per in the text.

The best quality data (FLAG = 0) were extracted in each case with PATTERN $\leq$ 4 for pn and PATTERN $\leq$ 12 for MOS. The response and ancillary response files were created automatically by the standard SAS tasks and spectral files were grouped to a minimum of 20 counts per bin, to improve statistics. The number of independent spectral bins after this process was completed are listed in Table 5.3, along with the combined EPIC source count rates.

5.4 ULX Spectral Properties

Our aims in this work are twofold. Firstly we aim to investigate the basic shape of the ULX X-ray spectra, and in doing so evaluate the evidence for the presence of a soft excess and a power-law break (at energies of a few keV) in ULX spectra. As these have been suggested as the two distinguishing spectral features of a new, ultraluminous accretion state (Roberts 2007) it is important to examine the evidence for their presence in the highest quality ULX spectra offered by *XMM-Newton*, and so determine the validity of claims of a new accretion state. Secondly, we will investigate the physical insights that a range of models can afford us on the nature of the accretion flows in this putative

Table 5.3: Extraction regions and details of the resultant spectra.

Source	Extraction radius (arcseconds) Source	Extraction radius (arcseconds) Background	Spectral bins[a]	Rate[b] (ct s^{-1})
NGC 55 ULX	34	51	884	2.13
M33 X-8	50	75	1252	9.56
NGC 1313 X-1	40	60	1616	1.19
NGC 1313 X-2	40*	60	1600	1.04
IC 342 X-1	36	54	516	0.68
NGC 2403 X-1	35	52.5	843	0.48
Ho II X-1	52	78	1358	4.93
M81 X-6	22	33	989	0.69
Ho IX X-1	42	63	2139	2.49
NGC 4559 X-1	34	51	593	0.50
NGC 5204 X-1	40	60	873	1.55
NGC 5408 X-1	40	60	990	1.42

Notes: [a]Number of spectral bins available for fitting from combined EPIC detectors; [b]combined EPIC count rate of source during observation in the 0.3 – 10 kev band. *Alternative extraction region used in MOS1 because source positioned on edge of chip gap.

state. The models we use vary from the simplest empirical models (power-law continua), through accretion disc models, to models in which we consider both an accretion disc and a Comptonising corona surrounding its inner regions, and the interplay between the two.

All spectra are fit in XSPEC version 11.3.2 over the 0.3 – 10.0 keV energy range (unless otherwise stated). To maximise data quality, pn and MOS data were fit simultaneously, with the addition of a constant multiplicative factor to compensate for calibration difference between the cameras. The pn constant is fixed at unity, whilst those for each MOS camera remain free, with the fitted values generally agreeing to within ∼10 % (larger discrepancies only occurred with disparate extraction regions; see Section 5.3 above for more details). In each case, the spectra are fit with two absorption components; one fixed at the column observed along the line of sight within our own Galaxy as listed in Table 5.1 (from Dickey & Lockman 1990), and a second component that is allowed to vary to represent any absorption within the host galaxy and/or intrinsic to the ULX. The absorption columns are modelled using the TBABS model (Wilms, Allen & McCray 2000). All quoted errors

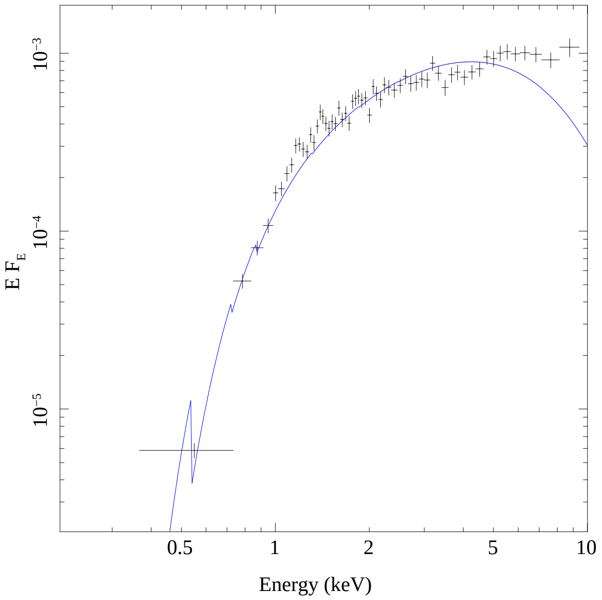

Figure 5.1: *XMM-Newton* EPIC pn data from IC 342 X-1, fit with an absorbed multi-colour disc model (DISKBB, in blue). We plot only the pn data, shown in black, which we rebin to a minimum of 10σ statistical significance, or 10 channels per data point for clarity. Although this is statistically one of the better fits to a MCD model within our sample, a visual inspection quickly reveals the residuals (particularly evident at high energies) that explain why it is still rejected at high significance.

are the 90 per cent confidence interval for one interesting parameter.

5.4.1 Single component phenomenological models

Simple, single component models have been used rather successfully to describe the featureless spectra of ULXs in the low-to-moderate quality data regime for some years (e.g. Humphrey et al. 2003; Swartz et al. 2004; Feng & Kaaret 2005; Winter, Mushotzky & Reynolds 2006). Here we use only the highest quality data to perform our analysis, yet we still find the the X-ray spectra of these objects to appear relatively smooth and featureless. Therefore, the application of these simple, single continuum models is a good starting point in their analysis. We start by applying an absorbed power-law continuum (PO in XSPEC syntax) and an absorbed multi-coloured disc blackbody (hereafter MCD) compo-

Table 5.4: Simple power-law continuum spectral fits.

Source	TBABS*TBABS*PO		χ^2/DoF†
	$N_{\rm H}$[a]	Γ[b]	
NGC 55 ULX	0.455±0.008	3.30±0.03	1288.8/879
M33 X-8	0.249*	2.218*	2527.3/1247
NGC 1313 X-1	0.188±0.005	1.85±0.02	2138.5/1611
NGC 1313 X-2	0.341±0.008	1.81±0.02	1982.4/1595
IC 342 X-1	0.57±0.04	1.83±0.05	534.3/511
NGC 2403 X-1	0.51±0.02	2.38±0.03	1247.3/838
Ho II X-1	0.158±0.003	2.63±0.01	1602.6/1363
M81 X-6	0.39±0.01	2.09±0.02	1825.9/985
Ho IX X-1	0.105±0.003	$1.606^{+0.01}_{-0.009}$	2863.4/2112
NGC 4559 X-1	0.120±0.009	2.29±0.04	586.5/588
NGC 5204 X-1	0.153 ±0.006	2.52±0.03	986.3/868
NGC 5408 X-1	$0.091^{+0.004}_{-0.003}$	3.12±0.02	1801.9/985

Notes: Model is abbreviated to XSPEC syntax: TBABS - absorption components for both Galactic and external absorption; PO - power-law; [a]External absorption column ($\times 10^{22}$ cm^{-2}) left free during fitting, Galactic columns listed in Table 5.1; [b] power-law photon index;.*Best fitting models to this data give a reduced χ^2 greater than 2, hence we do not place constraints due to the paucity of the fit. †Here and elsewhere we use 'DoF' to abbreviate the number of degrees of freedom available when fitting a model.

nent (DISKBB in XSPEC ; Mitsuda et al. 1984) separately to the data. The resultant fits can be seen in Tables 5.4 and 5.5.

Table 5.4 shows that a single power-law is not a particularly good fit to ULX data of this high quality. Although a rough representation of the observed spectra (reduced χ^2, $\chi^2_\nu < 2$) is found for 11/12 objects, only two objects provide statistically acceptable fits (null hypothesis probability > 5 per cent). Notably, these two objects - IC 342 X-1 and NGC 4559 X-1 - also have the worst quality data in the sample. The vast majority of the other ULX data reject this model at very high significance. The situation is even worse when fitting the MCD model (Table 5.5), where the quality of the fits are so bad they can only roughly represent five of the twelve spectra, and only one data set (NGC 2403 X-1) does not reject this model at high significance.

Nonetheless, it is instructive to compare the parameters derived from these fits, since lower quality data would not be able to show the inadequacy of these models. For the

Table 5.5: Simple MCD continuum spectral fits.

Source	TBABS*TBABS*DISKBB		χ^2/DoF
	$N_{\rm H}{}^a$	$kT_{\rm in}{}^b$	
NGC 55 ULX	0.123*	0.573*	2067.2/879
M33 X-8	0.007 ± 0.003	1.11 ± 0.01	1470.7/1247
NGC 1313 X-1	0.008*	1.420*	5531.5/1611
NGC 1313 X-2	0.115 ± 0.004	1.53 ± 0.02	2091.5/1595
IC 342 X-1	0.19 ± 0.02	$1.75^{+0.07}_{-0.06}$	775.1/511
NGC 2403 X-1	$0.168^{+0.01}_{-0.009}$	1.06 ± 0.02	891.0/838
Ho II X-1	0.0*	0.580*	8242.0/1363
M81 X-6	0.111 ± 0.006	1.31 ± 0.02	1210.1/985
Ho IX X-1	0.0*	1.624*	9164.3/2112
NGC 4559 X-1	0.0*	0.708*	1545.6/588
NGC 5204 X-1	0.0 *	0.618*	2533.2/868
NGC 5408 X-1	0.0*	0.314*	8294.8/985

Notes: Model is abbreviated to XSPEC syntax: TBABS - absorption components for both Galactic and external absorption; DISKBB - MCD. Specific notes: ^{a}External absorption column ($\times$ 10^{22} cm^{-2}) left free during fitting, Galactic columns listed in Table 5.1; ^{b} inner-disc temperature (keV). *Best fitting models to this data give a reduced χ^2 greater than 2, hence we do not place constraints due to the paucity of the fit.

spectra that are best represented by an absorbed MCD (again using the $\chi^2_\nu < 2$ criterion) we find that $kT_{\rm in} \sim 1.06 - 1.7$ keV. These are close to those seen in high mass accretion rate Galactic sources in the high/soft (thermal dominated) state (e.g. McClintock & Remillard 2006), which if taken at face value would indicate that the ULXs contain standard stellar mass black holes accreting at fairly high mass accretion rates. Conversely, with a power-law model, Table 5.4 shows that the photon index measured when these objects are represented by an absorbed power-law range from $1.6 < \Gamma < 3.3$. While the steepest spectra would correspond to the very high (steep power-law) state, those with with $\Gamma < 2.1$ correspond instead to the low/hard state (McClintock & Remillard 2006). The low/hard state is only seen at very sub-Eddington mass accretion rates ($< 0.1L/L_{\rm Edd}$), so a naïve interpretation of this spectral decomposition suggests that we are observing at least some IMBHs.

Clearly the fits from these models contradict one another as individual ULXs cannot be both stellar and IMBH – we note that the ULX data that is best represented by MCD fits generally also fits with power-law continua with $\Gamma < 2.3$. It is therefore evident that problems can arise when we attempt to draw physical meaning from simple phenomenological models applied to ULX data. Our sample data are of sufficient quality to demonstrate that the underlying spectrum is more complex than either standard disc or power-law models. As we have no reason to think our ULX sample is atypical of the class, then by extension this should apply to all ULXs, if sufficient data were available for them. This calls into question any physical conclusions drawn from simple model fits to low-to-moderate quality ULX data.

Single component phenomenological models do not provide enough flexibility in fitting to accurately constrain the majority of the data, nor do they consistently provide a physically realistic basis on which to interpret the data. As our next step, we therefore turn to more complex phenomenological models that have been used to characterise the spectra of black hole binaries and ULXs.

5.4.2 Combined phenomenological models

Here we combine the two simplest continuum models to further characterise the spectral shape and features of these sources. This combination of a disc component plus a power-law has been used extremely effectively in black hole binaries (McClintock & Remillard 2006 and references therein), since although these models are physically simplistic, they provide a good approximation to an optically thick geometrically thin accretion disc with an optically thin Comptonising corona over the 3 – 20 keV range. It has also, of course, been used as the basis for claims of IMBHs underlying ULXs (see Chapter 1 and Section 5.1 for further discussions). Each source spectrum is initially fit by an absorbed power-law component, then a multi-coloured disc component is added to this to look for any improvement of fit. The results of these fits can be seen in Table 5.6.

Figure 5.2(a) illustrates the need for a second spectral component in ULX spectra. Here we see the spectrum of NGC 5408 X-1 deconvolved with the best fitting absorbed MCD plus power-law model. It is clear from this data that a soft component is present in the spectrum, as an excess above a harder continuum. In fact, we find that all our sources show a significant improvement in χ^2 with the addition of a disc component (Table 5.6). This implies that some form of soft excess is ubiquitous in ULX spectra at this level of data quality.

Table 5.6: Combined power-law plus MCD spectral fits.

Source	TBABS*TBABS*(PO+DISKBB)				$\Delta\chi^{2\ d}$
	$N_{\rm H}{}^{a}$	Γ^{b}	$kT_{\rm in}{}^{c}$	χ^2/DoF	
NGC 55 ULX	0.46 ± 0.02	3.7 ± 0.1	$0.77^{+0.03}_{-0.04}$	1042.7/877	246.06
M33 X-8	0.09 ± 0.02	2.0 ± 0.1	$1.05^{+0.03}_{-0.04}$	1216.0/1245	1311.30
NGC 1313 X-1	$0.26^{+0.02}_{-0.01}$	$1.70^{+0.03}_{-0.02}$	0.23 ± 0.01	1796.5/1609	341.88
NGC 1313 X-2	$0.29^{+0.03}_{-0.02}$	$2.0^{+0.2}_{-0.1}$	1.7 ± 0.1	1599.7/1593	382.77
IC 342 X-1	$0.7^{+0.2}_{-0.1}$	1.7 ± 0.1	$0.32^{+0.1}_{-0.09}$	518.0/509	16.29
NGC 2403 X-1	$0.38^{+0.08}_{-0.07}$	$2.9^{+0.3}_{-0.4}$	$1.12^{+0.04}_{-0.05}$	853.7/836	393.69
Ho II X-1	0.116 ± 0.007	2.42 ± 0.04	0.37 ± 0.02	1503.9/1361	98.71
M81 X6	$0.30^{+0.05}_{-0.04}$	$2.6^{+0.4}_{-0.3}$	$1.42^{+0.04}_{-0.05}$	1093.9/983	732.01
Ho IX X-1	0.135 ± 0.007	1.46 ± 0.02	$0.27^{+0.02}_{-0.01}$	2440.0/2110	423.44
NGC 4559 X-1	$0.16^{+0.03}_{-0.02}$	$2.14^{+0.07}_{-0.05}$	0.17 ± 0.02	528.1/586	58.36
NGC 5204 X-1	0.09 ± 0.01	$2.18^{+0.08}_{-0.09}$	0.39 ± 0.02	925.1/866	61.16
NGC 5408 X-1	$0.068^{+0.005}_{-0.006}$	2.68 ± 0.04	$0.186^{+0.007}_{-0.003}$	1320.5/983	481.41

Notes: models are abbreviated XSPEC syntax, as per Table 5.4 & 5.5. Specific notes: [a]External absorption column in units of 10^{22} atoms cm^{-2}; [b]power-law photon index; [c]inner disc temperature (keV); [d]χ^2 improvement over the absorbed power-law fit (see Table 5.4), for two extra degrees of freedom.

Interestingly, in only 7/12 cases is the resulting disc 'cool' i.e. with $kT_{\rm in} < 0.5$ keV as in Miller et al. (2004). Instead we find that the temperature from the disc component appears to vary over a much wider range, from $0.17 < kT_{\rm in} < 1.7$ keV, covering both the cool and standard disc temperature range. However, where the disc is hot – and so forms the predominant component at higher energies – we find that the power-law component contributes the soft excess, agreeing with previous work (e.g. Stobbart, Roberts & Warwick 2004; Foschini et al. 2004; Roberts et al. 2005). As with these analyses, we note that the power-law extends to lower energies than its putative seed photons. This is not physically realistic and so requires more plausible physical modelling.

Inspection of the residuals from these fits also reveals a possible break or turn over above ∼ 2 keV. In some cases this is also clearly visible in their spectra. We can see in Figure 5.2 that the power-law cannot model such a feature and so is plotted in an average position whilst the data curves around it. Such a feature is not present in standard black hole binary states and so deserves further investigation, which is carried out in the next section.

Another point worthy of note is that the object with the highest inner-disc temperature is NGC 1313 X-2, a ULX that has exhibited much cooler disc temperatures in previous observations (e.g. 0.16 keV, Miller et al. 2003) leading to the suggestion it harbours an IMBH. We note that a local minimum in χ^2 was observed at ~ 0.16 keV in our data, but that the global minimum in our best fit occurs at much higher temperatures ($kT_{\rm in} = 1.7$ keV). It is clear that these results are contradictory – NGC 1313 X-2 cannot change from an IMBH to a stellar mass black hole binary between observations – demonstrating yet again that drawing physical conclusions from this soft component can be hazardous and should therefore be approached with care.

5.4.3 A high energy break

We investigate the prevalence of a high energy downturn following the analysis of SRW06, i.e. by comparing a power-law and a broken power-law description of the data above 2 keV. We do not include absorption in these fits as it is not easily constrained by data above 2 keV, and besides the wider band fits infer columns that have little effect above 2 keV. The resulting fits are shown in Table 5.7.

This break is clearly evident in the spectrum of NGC 1313 X-2, as seen in Figure 5.2(b). In fact we find that the broken power-law is statistically preferred ($>$ 98 per cent significance improvement in fit according to the F-test) in eleven out of the twelve ULXs in our sample, with break energies in the $\sim 3.5 - 7.0$ keV range, and a typical steepening of the power-law slope by $\Delta\Gamma \sim 1-2$. This near ubiquity is made all the more remarkable when it is considered that the one ULX without evidence for a break here – NGC 5204 X-1 – has displayed evidence for such a feature in previous observations (Roberts et al. 2005, SRW06). While this break is clearly expected from the 'hot disc' fits, where the MCD component dominates at high energies, the break is also seen at high significance in the 'cool disc' objects. These are the sources where the IMBH model is apparently favoured, implying that these ULX are analogous to the low/hard state observed in Galactic black hole binaries. Yet the high energy data show a break at ~ 5 keV, which is not seen in this accretion state. The ubiquity of the high energy break shows that the ULX spectra are *not* well described by a cool disc plus power-law as expected from the IMBH model.

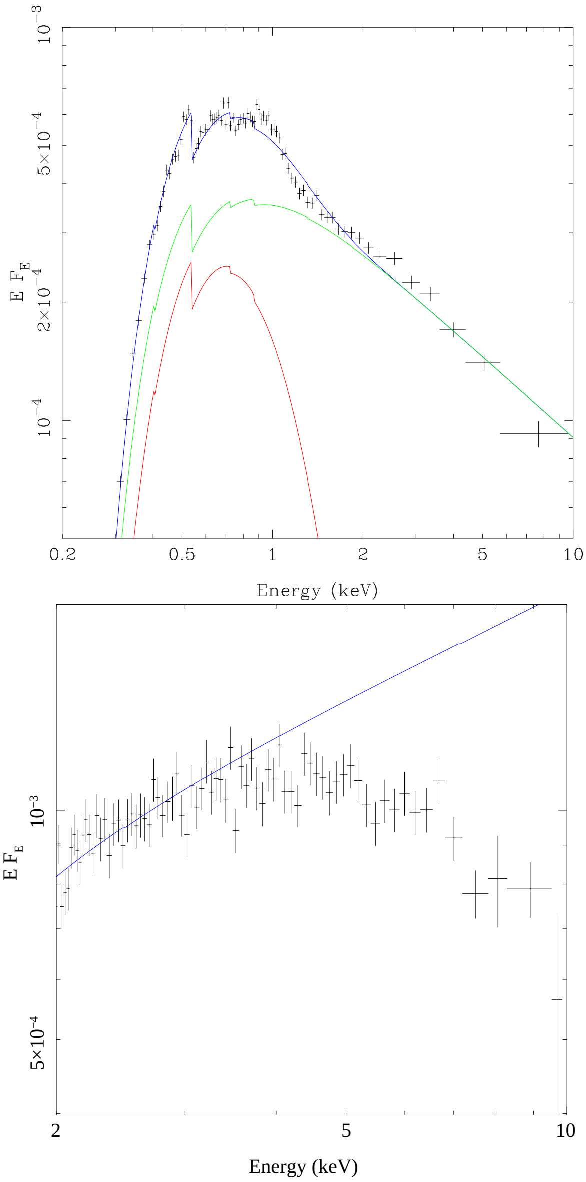

Figure 5.2: *XMM-Newton* EPIC pn data from (a) NGC 5408 X-1 and (b) NGC 1313 X-2. NGC 5408 X-1 data is rebinned to a minimum of 30 σ significance or 30 channels, shown with the best fitting multi-colour disc plus power-law model (blue line). The contributions of the separate model components to the overall fit are shown in green (power-law continuum) and red (MCD). This clearly shows the motivation for an additional soft component in the spectrum, though the excess at $\sim$ 1 keV also shows evidence for contributions from hot gas. NGC 1313 X-2 is rebinned to a minimum of 15 σ, or 15 channels. We show the data fit by a power-law component (blue) based on the slope and normalisation of the low energy (pre-break) component of the broken power-law fit to this data. It is very clear from this data that some form of break or curvature is present above 2 keV.

Table 5.7: A comparison of power-law to broken power-law spectral fits in the 2–10 keV band.

Source	PO		BKNPOWER				$\Delta\chi^{2\ e}$	1-P(F-test)^f
	Γ^a	χ^2/DoF	$\Gamma_1{}^b$	$E_{\rm break}{}^c$	$\Gamma_2{}^d$	χ^2/DoF		
NGC 55 ULX	3.57 ± 0.06	429.8/314	3.1 ± 0.1	3.9 ± 0.3	$4.9^{+0.5}_{-0.4}$	323.1/311	106.7	>99
M33 X-8	2.60 ± 0.03	855.6/679	$2.17^{+0.08}_{-0.1}$	$4.0^{+0.2}_{-0.3}$	3.4 ± 0.2	641.6/677	214.0	>99
NGC 1313 X-1	1.06 ± 0.02	1054.2/1043	$1.60^{+0.03}_{-0.05}$	$6.3^{+0.3}_{-0.9}$	$2.6^{+0.3}_{-0.5}$	992.9/1041	61.3	>99
NGC 1313 X-2	1.91 ± 0.02	1195.8/1034	$1.53^{+0.1}_{-0.07}$	$3.7^{+0.7}_{-0.2}$	$2.3^{+0.2}_{-0.1}$	1011.0/1032	184.8	>99
IC 342 X-1	$1.58^{+0.06}_{-0.05}$	281.3/269	1.53 ± 0.07	$6.7^{+0.7}_{-1.0}$	$2.7^{+1}_{-0.8}$	273.7/267	7.6	>99
NGC 2403 X-1	$2.67^{+0.05}_{-0.06}$	478.1/335	2.1 ± 0.1	4.0 ± 0.2	4.0 ± 0.3	335.0/333	147.1	>99
Ho II X-1	$2.58^{+0.02}_{-0.03}$	772.7/795	2.51 ± 0.04	$5.4^{+0.5}_{-0.6}$	$3.1^{+0.3}_{-0.2}$	750.5/793	22.2	>99
M81 X-6	2.31 ± 0.03	903.9/538	$1.72^{+0.07}_{-0.1}$	4.1 ± 0.2	3.4 ± 0.2	554.9/536	349.0	100
Ho IX X-1	1.46 ± 0.02	1672.6/1544	1.38 ± 0.02	$6.2^{+0.3}_{-0.4}$	2.2 ± 0.2	1561.1/1542	111.5	>99
NGC 4559 X-1	$2.22^{+0.07}_{-0.09}$	141.1/153	2.1 ± 0.1	$4.8^{+1}_{-0.9}$	$2.8^{+0.8}_{-0.4}$	133.8/151	7.3	98.1
NGC 5204 X-1	2.40 ± 0.06	319.5/307	$2.36^{+0.09}_{-0.2}$	5^{+3}_{-2}	$2.7^{+2}_{-0.5}$	316.7/305	2.8	73.9
NGC 5408 X-1	$2.84^{+0.04}_{-0.06}$	442.0/417	2.80 ± 0.06	$7.1^{+1}_{-0.9}$	7^{+7}_{-2}	432.4/415	9.6	98.9

Notes: models are abbreviated to XSPEC syntax: PO - as before; BKNPOWER - broken power-law model. Specific notes: ^{a}Photon index from PO model, ^{b}photon index before the break in BKNPOWER model, ^{c}break energy (keV), ^{d}photon index after the break energy, $^e\chi^2$ improvement over a single power-law fit, ^{f} statistical probability (in per cent) that the broken power-law model provides an improvement to the fit over a single PO model, from the F-test.

Instead, these high quality data show that the disc is either hot, implying a stellar mass black hole (which must be accreting at or above Eddington in order to produce the observed luminosity) but with a previously unseen soft excess (an alternative would be that the power-law is simply broadening the disc spectrum, which would be consistent with a modified high state; see Section 5.5 for more detailed discussions), or the disc is cool but with a high energy tail which is quite unlike that seen in the standard spectral states of black hole binaries (e.g. McClintock & Remillard 2006). **This new combination of observational characteristics - a cool disc and a broken harder component - suggests that these ULXs are operating in an accretion state not commonly seen in the Galactic black hole binaries**. We term this new combination of observational characteristics the **'ultraluminous state'**, and it seems most straightforward to assume that this state accompanies extremely high accretion rates onto stellar remnant black holes. As we also have no reason to think our ULX sample atypical of the class as a whole, we can only presume that this spectrum may be endemic to the majority of ULXs.

5.4.4 More physical models: slim disc

The investigations and results described above have focused on the application of simple phenomenological models used to characterise the shape of the observed spectra of these sources. This work has revealed the presence of both a soft excess and a break above ~ 2 keV. These studies have also shown the limitations of these models at this level of data quality, especially the MCD fits. Disc spectra should be more complex than this simple sum-of-blackbodies approach. Firstly, relativistic effects broaden the spectrum, so it is less strongly peaked than an MCD (Cunningham 1975; Ebisawa et al. 2001; Li et al. 2005). Secondly, the intrinsic spectrum from material at a given radius is not a true blackbody as there is not enough absorption opacity to thermalise the emission at all energies (Davis et al 2005). This can be approximated by a colour temperature correction (Shimura & Takahara 1995), but this is only an approximation and the best current models of disc spectra show weak atomic features in the continuum emission. Hence, even relativistic, colour corrected blackbody discs are not an accurate description of the best theoretical disc spectra over the 0.3 – 10.0 keV bandpass, though they are normally an excellent fit to the 3 – 20 keV energy range (Done & Davis 2008). This can be seen in real data from

Table 5.8: Spectral fits for the p-free disc model.

Source	TBABS*TBABS*DISKPBB			
	$\mathrm{N}_H{}^a$	$\mathrm{T}_{in}{}^b$	p^c	χ^2/DoF
NGC 55 ULX	0.38 ± 0.01	$1.12^{+0.06}_{-0.05}$	0.408 ± 0.005	1019.9/878
M33 X-8	$0.090^{+0.009}_{-0.01}$	$1.36^{+0.03}_{-0.04}$	$0.599^{+0.01}_{-0.009}$	1242.0/1246
NGC 1313 X-1	$0.188^{+0.003}_{-0.005}$	7.9 ± 0.8	0.521 ± 0.002	2113.2/1610
NGC 1313 X-2	$0.251^{+0.009}_{-0.01}$	$2.31^{+0.09}_{-0.1}$	$0.583^{+0.009}_{-0.006}$	1601.2/1594
IC 342 X-1	0.57 ± 0.04	13^{+7}_{-4}	0.523 ± 0.007	532.1/510
NGC 2403 X-1	0.27 ± 0.03	1.24 ± 0.06	$0.60^{+0.03}_{-0.02}$	850.5/837
Ho II X-1	0.149 ± 0.003	$2.80^{+0.1}_{-0.10}$	0.436 ± 0.001	1557.0/1362
M81 X-6	$0.23^{+0.01}_{-0.02}$	$1.60^{+0.05}_{-0.06}$	$0.61^{+0.02}_{-0.01}$	1091.7/984
Ho IX X-1	0.103 ± 0.003	$8.9^{+2}_{-0.4}$	$0.557^{+0.001}_{-0.002}$	2853.2/2111
NGC 4559 X-1	$0.121^{+0.01}_{-0.009}$	$6.2^{+0.6}_{-0.8}$	$0.466^{+0.004}_{-0.002}$	574.7/587
NGC 5204 X-1	$0.147^{+0.007}_{-0.004}$	3.0 ± 0.2	$0.446^{+0.002}_{-0.003}$	977.5/867
NGC 5408 X-1	0.085 ± 0.004	$1.97^{+0.1}_{-0.05}$	0.392 ± 0.002	1855.5/984

Notes: Model is abbreviated to XSPEC syntax: TBABS - absorption components for both Galactic and external absorption; DISKPBB - p-free disc. Specific notes: ^{a}External absorption column ($\times\ 10^{22}$ cm^{-2}) left free during fitting, Galactic columns listed in Table 5.1; ^{b} inner-disc temperature (keV); $^c p$ value, where disc temperature scales as r^{-p} and r is the radius.

disc dominated black hole binary systems e.g. the 0.3 – 10.0 keV spectrum from LMC X-3 is better fit by full disc models than by DISKBB (Davis, Done & Blaes 2006). However, only a few ULX fit well even to these full disc models (Hui & Krolik 2008).

These models also assume that advection of radiation is not important, yet in ULXs we may be observing a super-Eddington accretion flow. The disc becomes so optically thick at these extreme mass accretion rates that the energy released in the mid-plane of the disc does not have time to diffuse to the photosphere. Instead, the photons are advected radially resulting in additional cooling to the inner regions of the accretion disc. This so called 'slim disc' predicts that spectra are less sharply curved than that of a standard disc (Abramowicz et al. 1988; see Section 1.6.4 for more details).

To take these physical differences into account we replace the standard MCD model with a modified version, the 'p-free' disc model. This allows the disc temperature to scale as r^{-p}, where r is the radius and p is a free parameter. Standard (MCD) discs have p fixed at 0.75, but increasing amounts of advection can be modelled by decreasing p, with fully

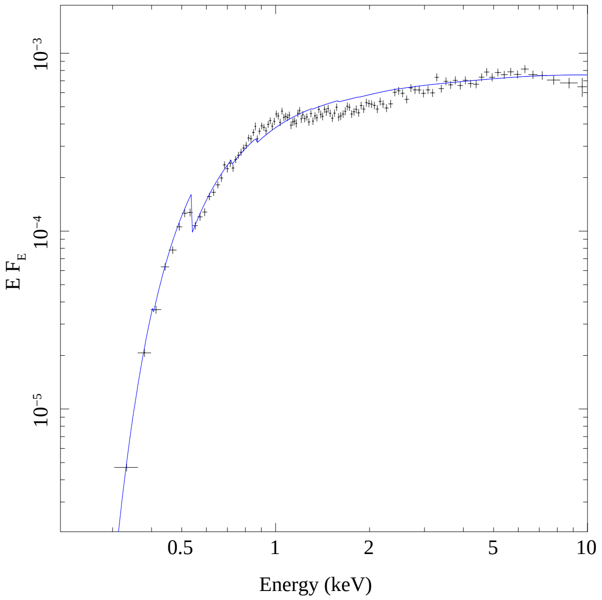

Figure 5.3: *XMM-Newton* data of NGC 1313 X-1, deconvolved with the 'p-free' model (shown in blue). The data is plotted as per the previous figure, and binned to a minimum of 20σ or 20 channels for clarity. This model is used as a simplified description of the theoretically predicted 'slim disc' model. Although the p value ($p \sim 0.5$) for this data could be considered in support of a slim disc, the best fit provides an unrealistic disc temperature ($kT_{\rm in} \sim 7.9$ keV).

advective discs having $p \simeq 0.5$ (e.g Watarai et al. 2001, Vierdayanti et al. 2006, Miyawaki et al. 2006). Hence a p-free disc fitting with $p \sim 0.5$ would be indicative of the slim disc model, and also gives a broader spectrum which can approximate both relativistic effects and the colour temperature correction.

The p-free model gives a slightly better overall fit to the data than a single power-law, with all ULXs being at least roughly represented with this gentle spectral curvature. Indeed, five out of twelve ULXs have statistically acceptable fits to this model. If we consider the values derived from best fits to the data we find, at first glance, that our results appear to be in good agreement with the slim disc model, with $p \sim 0.4 - 0.6$ (see Table 5.8), but on closer inspection problems begin to emerge. Table 5.8 shows that while some of the derived inner disc temperatures are in the $1 - 3$ keV range expected for such super-Eddington flows onto stellar mass black holes, some are extremely high, with four of the twelve sources providing fits above 6 keV (including two of the acceptable fits). Such temperatures are high even for maximally spinning black holes (Ebisawa et al. 2003), making these fits physically unrealistic. These high quality data sets also clearly show that the spectral curvature is more complex in many cases, even for this modified disc model. One clear example of this is NGC 1313 X-1 (one of the unphysically high temperature spectra) where there is a marked inflection present in the spectral data at $\sim$ 2 keV which cannot be matched in the p-free models (Figure 5.3; this is also obvious in the spectra of several other ULXs, see Figure 5.7). So, although a p-free model with slim disc characteristics (or indeed a full standard disc model: Hui & Krolik 2008) cannot be ruled out in the minority of cases, it does not seem to be a good explanation for ULXs as a class. The two component phenomenological model (MCD plus power-law) is clearly a better statistical description of the majority of ULX spectra, though the presence of a high energy break clearly also shows it limitations. As a next step we replace the power-law with a Comptonisation model, to explore the nature of the high energy break.

5.4.5 Comptonisation Models

We have demonstrated that the highest quality ULX data indicates many of these objects are in a new, ultraluminous accretion state. The next, obvious question is: what are the physics of the accretion flow producing this shape of spectrum? In order to further explore the nature of these systems, we now replace the power-law continuum with more physically realistic Comptonisation models. We use an alternative disc model, DISKPN (Gierliński et al. 1999), which incorporates an approximate stress-free inner boundary condition as opposed to the continuous stress assumed in DISKBB. The resulting spectra differ by less than 5 per cent for the same temperature, but we use DISKPN so as to be able to directly compare our results with those of SRW06.

(*i*) DISKPN+COMPTT

We initially use COMPTT (Titarchuk 1994) to model the coronal emission. This is an analytic approximation to non-relativistic thermal Comptonisation which assumes that the seed photons for Comptonisation have a Wien spectrum. We tie the temperature of these seed photons to the temperature of the accretion disc ($T_{\rm max}$). In each case the

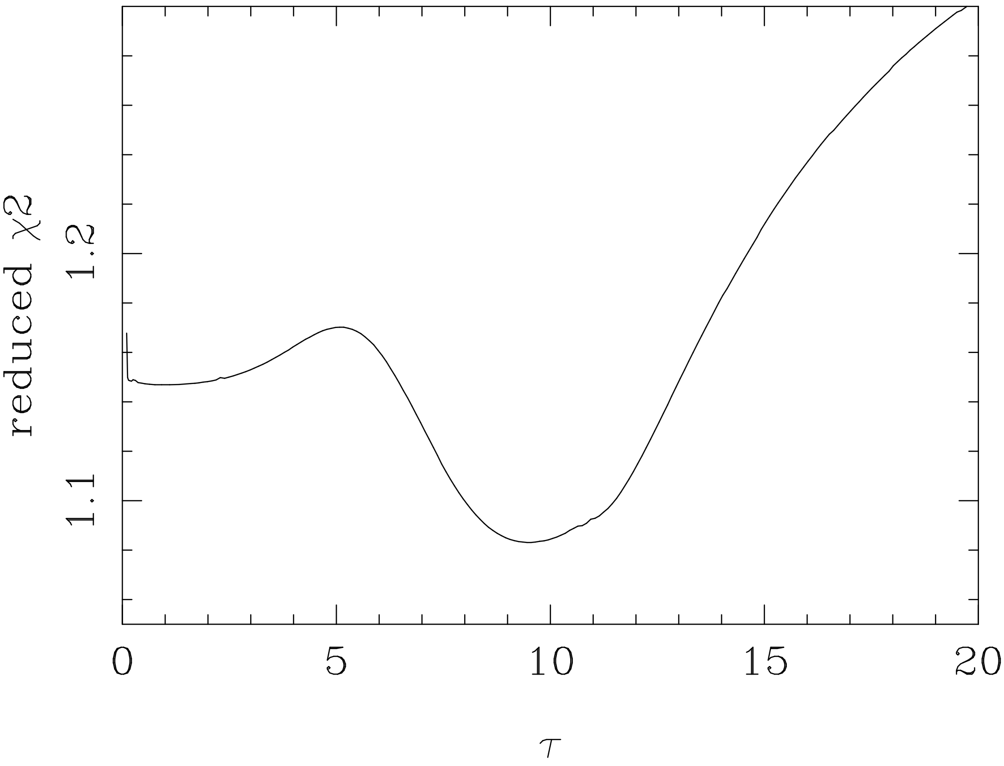

Figure 5.4: Variation in χ^2 over a range of optical depths derived from the fitting of an absorbed DISKPN plus COMPTT to the data from Ho IX X-1. A local minimum is observed at lower optical depths but this clearly shows that the global minimum occurs at $\tau \sim 9.5$, an optically thick solution.

redshift is fixed at zero due to the proximity of these systems, whilst the optical depth and plasma temperature are free to vary. We show the results of our spectral fitting in Table 5.9.

We find in each case that there is a local minimum in χ^2 space which corresponds to a hot, optically thin Comptonising corona ($kT_{\rm e} \sim 50$ keV, $\tau \lesssim 1$), similar in nature to that seen in Galactic black hole binaries in classic accretion states. However, the global minimum in χ^2 occurs for a fit that describes a cool, optically thick corona ($kT_{\rm e} \sim 1-3$ keV and $\tau \sim 6-80$). This is a very different scenario to those of the standard black hole accretion states. We illustrate this in Figure 5.4, which shows χ^2 versus τ for Ho IX X-1. Here we find that a local minimum is observed at low optical depths, but a clear global minimum occurs at $\tau \sim 9.5$, an optically thick solution.

Table 5.9: Application of Comptonisation models: DISKPN+COMPTT spectral fits

Source	TBABS*TBABS*(DISKPN+COMPTT)				χ^2/DoF	$\Delta\chi^{2\ e}$	1-P(F-test)^f
	$N_{\mathrm{H}}{}^a$	$T_{\mathrm{max}}{}^b$	$kT_e{}^c$	τ^d			
NGC 55 ULX	0.235 ± 0.004	$0.221^{+0.010}_{-0.006}$	$0.83^{+0.05}_{-0.04}$	9.9 ± 0.4	986.3/876	252.6	> 99
M33 X-8	0.041 ± 0.003	$0.87^{+0.04}_{-0.2}$	$1.39^{+0.08}_{-0.03}$	80^{+100}_{-30}	1204.4/1244	42.2	> 99
NGC 1313 X-1	0.21 ± 0.01	0.23 ± 0.01	2.1 ± 0.1	$8.5^{+0.6}_{-0.5}$	1705.7/1608	192.0	> 99
NGC 1313 X-2	$0.195^{+0.004}_{-0.005}$	$0.7^{+0.2}_{-0.1}$	1.51 ± 0.02	$15.3^{+0.4}_{-1}$	1613.2/1592	281.6	> 99
IC 342 X-1	$0.58^{+0.10}_{-0.1}$	$0.30^{+0.2}_{-0.08}$	$2.78^{+8}_{-0.6}$	7^{+3}_{-7}	515.5/508	4.4	87.5
NGC 2403 X-1	$0.18^{+0.06}_{-0.01}$	$0.27^{+0.1}_{-0.05}$	0.98 ± 0.04	12.5 ± 0.7	844.7/835	131.4	> 99
Ho II X-1	0.033 ± 0.002	$0.23^{+0.02}_{-0.01}$	$2.12^{+0.1}_{-0.10}$	5.5 ± 0.2	1375.4/1360	44.2	> 99
M81 X-6	0.181 ± 0.006	$0.7^{+0.1}_{-0.2}$	$1.15^{+0.02}_{-0.01}$	31^{+4}_{-3}	1082.7/982	56.8	> 99
Ho IX X-1	0.099 ± 0.006	0.26 ± 0.02	$2.27^{+0.1}_{-0.09}$	9.5 ± 0.5	2284.2/2109	126.4	> 99
NGC 4559 X-1	$0.13^{+0.03}_{-0.02}$	0.16 ± 0.02	$1.8^{+0.6}_{-0.3}$	$7.4^{+0.7}_{-1}$	513.1/585	32.4	> 99
NGC 5204 X-1	$0.035^{+0.007}_{-0.009}$	0.26 ± 0.03	$2.2^{+2}_{-0.4}$	6^{+2}_{-3}	886.2/865	3.9	87.5
NGC 5408 X-1	0.029 ± 0.005	$0.170^{+0.006}_{-0.007}$	$1.5^{+0.3}_{-0.2}$	$6.5^{+0.8}_{-0.9}$	1240.9/982	41.1	> 99

Notes: models are abbreviated to XSPEC syntax: DISKPN - accretion disc model, COMPTT - Comptonisation model. Specific notes: [a]External absorption column in units of 10^{22} atoms cm^{-2}, [b]maximum temperature in the accretion disc (keV), [c]plasma temperature in the Comptonising corona, [d]optical depth of corona, [e,f]χ^2 improvement , and statistical probability (in per cent) of the fit improvement over a hot optically thin corona with $kT_e = 50$ keV fixed.

To quantify this improvement, we have compared the fits achieved in each scenario and find that in ten of the twelve spectra the improvement in χ^2 is highly significant ($\Delta\chi^2 > 30$) (see Table 5.9), while the other two still show $\Delta\chi^2 > 3.9$ i.e. the break is detected at 90 per cent significance. To test this further we fix the temperature of the corona at 50 keV (all hot corona local minima fits lie at approximately this temperature within errors). We compare the resultant fits to those given in Table 5.9 using the F-test, finding that in ten out of twelve cases in our sample shows a $>$ 99 per cent statistical probability of improvement when applying a cool optically thick corona over a hot optically thin one. The possible presence of such an extraordinary corona is therefore the first major clue as to the origin in the physical differences between sub-Eddington accretion states, and the ultraluminous state.

A second characteristic found in fitting this model to our ULX data is that the disc temperatures are generally cool. In fact, Table 5.9 shows that 9/12 disc temperatures reside (on face value) in the IMBH range ($T_{\rm max} < 0.5$ keV), while the remaining three objects have hotter discs that might imply stellar mass objects. Similar results – a combination of a cool disc, and an optically thick cool Comptonising corona – have been found in previous studies of individual sources (e.g. Ho IX X-1 by Dewangan et al. 2006; Ho II X-1 in Goad et al. 2006; also SRW06). However, in interpreting the cool disc component we must consider the implications of the presence of an optically thick corona. It is likely that such a medium would mask the inner-most radii of the disc. It is also likely that material and power may be drawn from the disc to feed the corona. A combination of these factors could greatly impact the observed temperature of the accretion disc, invalidating any conclusions drawn on this basis. We return to this point later.

(*ii*)**DISKPN+EQPAIR**

We now apply an alternative, more physically self-consistent Comptonisation model to test our provisional result from the DISKPN + COMPTT model further. Here we use EQPAIR (Coppi 1999), a model which allows both thermal and non-thermal electrons, and calculates the resulting spectrum without assuming that the electrons are non relativistic, and where the seed photons can have a disc or blackbody spectrum. We choose to use only thermal electrons plus disc emission to allow for comparison to COMPTT, and again

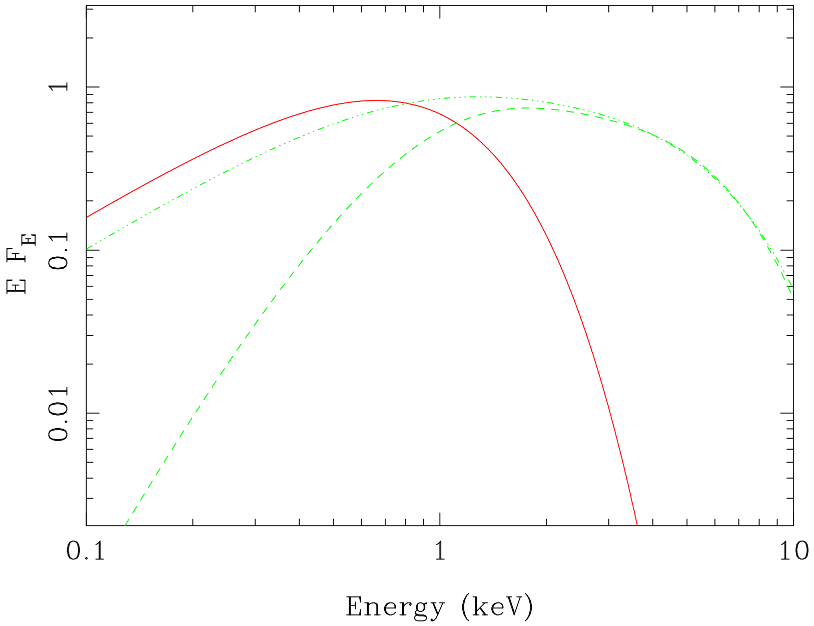

Figure 5.5: Comparison of disc plus Comptonisation models used within our analysis. An average cool disc is plotted in red with coronal components representative of those found in our fits shown in green (dashed line – COMPTT; dashed & dotted line – EQPAIR). Although the Comptonisation components have different spectral structure at lower energies, it is clear that the same cool optically thick corona is dominant at higher energies in the *XMM-Newton* band pass. The differences in the Comptonised spectrum in the lower part of our energy range are accounted for by differences in the fit parameters of the disc and absorption components.

tie the temperature of the seed photons to that of the inner accretion disc.

Comparing the fits to the data for DISKPN + COMPTT (Table 5.9) with DISKPN + EQPAIR (Table 5.10), we find that similar χ^2 values are achieved in all cases. Results once again indicate that the global fitting minima are achieved by a relatively cool accretion disc ($0.18 < T_{\rm max} < 0.63$ keV) with a cool optically thick corona ($\tau \sim 7.0 - 27.6$), thick enough to potentially hide the inner disc.

Figure 5.5 illustrates the similarity in results between the two Comptonisation models. Here we plot typical values from our fits for both Comptonisation components in green (COMPTT – dashed line; EQPAIR – dashed & dotted line) along with an average disc shown in red. We can clearly see that each of these models exhibits similar curvature at

Table 5.10: Application of Comptonisation models: DISKPN+EQPAIR spectral fits

Source	TBABS*TBABS*(DISKPN+EQPAIR)				χ^2/DoF
	$N_{\rm H}{}^a$	$T_{\rm max}{}^b$	$l_{\rm h}/l_{\rm s}{}^c$	τ^d	
NGC 55 ULX	$0.250^{+0.01}_{-0.004}$	$0.253^{+0.01}_{-0.005}$	1.24 ± 0.03	$26.9^{+0.7}_{-2}$	990.2/876
M33 X-8	$0.036^{+0.004}_{-0.005}$	0.63 ± 0.02	$0.70^{+0.03}_{-0.02}$	$13.2^{+0.5}_{-0.8}$	1204.0/1244
NGC 1313 X-1	$0.210^{+0.005}_{-0.01}$	$0.271^{+0.004}_{-0.010}$	4.02 ± 0.07	$17.9^{+0.5}_{-0.6}$	1711.6/1608
NGC 1313 X-2	0.204 ± 0.01	$0.37^{+0.02}_{-0.04}$	$2.28^{+0.05}_{-0.06}$	$17.7^{+0.6}_{-0.8}$	1601.8/1592
IC 342 X-1	$0.64^{+0.08}_{-0.07}$	$0.32^{+0.02}_{-0.05}$	$3.2^{+0.5}_{-0.1}$	$11^{+3}_{-0.3}$	516.1/508
NGC 2403 X-1	$0.24^{+0.04}_{-0.02}$	$0.32^{+0.04}_{-0.05}$	$1.87^{+0.05}_{-0.07}$	27.6 ± 2	849.3/835
Ho II X-1	$0.050^{+0.002}_{-0.001}$	$0.267^{+0.007}_{-0.003}$	$1.011^{+0.009}_{-0.01}$	7.00 ± 0.02	1391.2/1360
M81 X-6	$0.20^{+0.02}_{-0.03}$	$0.30^{+0.1}_{-0.02}$	$2.6^{+0.1}_{-0.6}$	25^{+3}_{-1}	1085.2/982
Ho IX X-1	$0.109^{+0.005}_{-0.004}$	$0.312^{+0.01}_{-0.006}$	4.99 ± 0.08	$18.5^{+0.4}_{-0.3}$	2293.1/2109
NGC 4559 X-1	$0.14^{+0.01}_{-0.02}$	0.177 ± 0.009	2.2 ± 0.1	14 ± 2	513.8/585
NGC 5204 X-1	0.047 ± 0.003	0.314 ± 0.01	$1.35^{+0.07}_{-0.05}$	10^{+1}_{-2}	894.3/865
NGC 5408 X-1	$0.033^{+0.002}_{-0.001}$	$0.184^{+0.003}_{-0.002}$	$1.140^{+0.02}_{-0.009}$	$12.9^{+0.4}_{-0.6}$	1244.2/982

Notes: models are abbreviated to XSPEC syntax: DISKPN - accretion disc model, EQPAIR - Comptonisation model. Specific notes: ^{a}External absorption column in units of 10^{22} atoms cm^2, ^{b}maximum temperature in the accretion disc (keV), ^{c}ratio between the compactness of electron and the compactness of seed photon distribution, ^{d}optical depth.

higher energies, while the difference at lower energies arises form the differing assumptions about the spectrum of the seed photons. The difference in the spectrum of these coronal components lies at lower energies where subtle variations in the disc and absorption components can compensate for this. Each of these models can therefore explain the curvature observed at both higher and lower energies within our band-pass. The soft excess at low energies is modelled well by a cool accretion disc, whilst the optically thick corona causes the downturn at high energies (irrespective of model choice).

When these results are compared to the findings of SRW06, we find that we achieve similar fits to the data[3]. Their results also indicate the presence of a cool accretion disc ($0.08 < kT_{\rm max} < 0.29$ keV) in all cases, whilst an optically thick corona is observed in almost all sources (τ ranges from 0.2 – 33). It is therefore clear that these appear to be the physical characteristics of ULXs, and hence the ultraluminous state. This clearly demonstrates that we appear to be observing a radically different accretion flow to the classic accretion states viewed in Galactic black hole binaries.

---

[3] We have five data sets in common with SRW06, and a further four sources with improved data.

We should note, however, that there are at least two Galactic black hole candidates that occasionally exhibit similar (albeit less extreme) spectral traits when modelled similarly – an unusually cool accretion disc, and a cool optically thick corona – to the ULXs observed within our sample (when band pass is considered). These objects are GRS 1915+105 and XTE J1550-564, and in each case these objects are thought to be accreting at, or above, the Eddington limit when displaying such traits (Kubota & Done 2004; Middleton et al. 2006; Ueda et al. 2009). This is further evidence to support the assertion that the ultraluminous state represents a super-Eddington accretion flow.

5.4.6 Energetic disc-corona coupling

We now move on to the final stage in our analysis to further explore the results provided by Comptonisation models. The models above implicitly assume that we can still observe the disc down to its innermost stable orbit. This assumption requires that the optically thick corona does not intercept our line of sight to the inner disc and that the underlying disc spectrum is independent of that of the corona (see Kubota & Done 2004). Yet both assumptions are probably flawed. An optically thick corona could easily mask the innermost regions (depending on its geometry: Kubota & Done 2004). Secondly, we must consider the energetics of both components. Both the disc and the corona must be ultimately powered by gravitational energy release. If we are observing a powerful corona, this implies less energy is available for heating the disc (Svensson & Zdziarski 1994). The only code currently available that enables us to explore the effect of relaxing these assumptions is DKBBFTH (Done & Kubota 2006). This was designed to model the extreme very high state spectra seen in black hole binaries such as XTE J1550-564 and GRS 1915+105. It incorporates the energetic disc-corona coupling model of Svensson & Zdziarski (1994), which assumes that the corona extends over the inner disc from $R_{\rm in}$ to $R_{\rm T}$, taking a fraction f of the gravitational energy available at these radii. Only the remaining fraction $(1-f)$ is available to power the inner disc emission, so the inner disc is cooler, but more importantly, less luminous than it would be if the corona were not present. This distorted inner disc spectrum is the source of seed photons for the Comptonisation (Done & Kubota 2006).

Table 5.11: The ultraluminous model: DKBBFTH

Source	TBABS*TBABS*(DKBBFTH)							χ^2/DoF
	$N_{\mathrm{H}}{}^{a}$	$kT_{\mathrm{disc}}{}^{b}$	$R_{\mathrm{c}}/R_{\mathrm{in}}{}^{c}$	$R_{\mathrm{in}}{}^{d}$	Γ^{e}	$kT_{\mathrm{e}}{}^{f}$	τ^{g}	
NGC 55 ULX	$0.239^{+0.02}_{-0.006}$	$0.38^{+0.02}_{-0.01}$	$1.5^{+0.1}_{-0.2}$	700^{+300}_{-100}	$2.0^{+0.3}_{-0.5}$	$0.79^{+0.1}_{-0.08}$	$10.6^{+0.3}_{-0.5}$	989.1/876
M33 X-8	$0.036^{+0.004}_{-0.006}$	1.03 ± 0.04	$2.7^{+1}_{-0.7}$	65^{+10}_{-6}	$3.6^{+0.1}_{-1}$	6^{+30}_{-4}	$1.5^{+0.2}_{-1}$	1201.9/1244
NGC 1313 X-1	$0.211^{+0.004}_{-0.005}$	$0.60^{+0.03}_{-0.04}$	$2.82^{+0.10}_{-0.07}$	460^{+40}_{-30}	$1.66^{+0.03}_{-0.02}$	$2.19^{+0.2}_{-0.09}$	$7.79^{+0.03}_{-0.02}$	1708.5/1608
NGC 1313 X-2	$0.21^{+0.01}_{-0.02}$	$1.18^{+0.05}_{-0.1}$	$4.3^{+1}_{-0.5}$	130^{+80}_{-30}	$2.5^{+0.1}_{-0.2}$	3^{+6}_{-1}	$3.5^{+0.1}_{-0.2}$	1594.8/1592
IC 342 X-1	$0.55^{+0.08}_{-0.03}$	1.0 ± 0.2	$2.8^{+3}_{-0.8}$	160^{+400}_{-80}	$1.6^{+0.2}_{-0.5}$	$2.4^{+7}_{-0.7}$	$7.9^{+0.2}_{-0.5}$	515.7/508
NGC 2403 X-1	$0.234^{+0.009}_{-0.03}$	$0.85^{+0.08}_{-0.1}$	$2.4^{+0.4}_{-0.6}$	170^{+40}_{-30}	$1.9^{+0.2}_{-0.4}$	$1.003^{+10}_{-0.003}$	$9.7^{+0.2}_{-0.4}$	846.9/835
Ho II X-1	$0.079^{+0.008}_{-0.007}$	$0.30^{+0.02}_{-0.01}$	$5.6^{+1.0}_{-0.1}$	3900 ± 100	$2.53^{+0.02}_{-0.01}$	$13.2^{+1}_{-0.6}$	$1.43^{+0.02}_{-0.01}$	1399.4/1360
M81 X-6	0.19 ± 0.02	$0.98^{+0.08}_{-0.05}$	3.3 ± 0.2	140 ± 40	$2.15^{+0.2}_{-0.07}$	$1.39^{+0.07}_{-0.2}$	$6.87^{+0.2}_{-0.07}$	1080.7/982
Ho IX X-1	$0.121^{+0.008}_{-0.005}$	$1.01^{+0.03}_{-0.04}$	$4.0^{+0.2}_{-0.1}$	220^{+50}_{-30}	1.58 ± 0.03	2.5 ± 0.2	$7.92^{+0.03}_{-0.03}$	2286.9/2109
NGC 4559 X-1	$0.138^{+0.008}_{-0.01}$	$0.31^{+0.06}_{-0.04}$	$2.0^{+0.2}_{-0.1}$	3000^{+3000}_{-2000}	$1.95^{+0.09}_{-0.10}$	$1.9^{+0.6}_{-0.3}$	$6.73^{+0.09}_{-0.10}$	513.8/585
NGC 5204 X-1	0.036 ± 0.007	0.54 ± 0.02	$1.8^{+0.2}_{-0.1}$	610^{+100}_{-90}	2.0 ± 0.2	1.9 ± 0.4	$6.5^{+0.2}_{-0.2}$	889.1/865
NGC 5408 X-1	$0.029^{+0.007}_{-0.004}$	$0.255^{+0.006}_{-0.005}$	$1.47^{+0.01}_{-0.05}$	3000^{+200}_{-40}	$2.31^{+0.04}_{-0.03}$	$1.6^{+0.2}_{-0.1}$	$5.80^{+0.04}_{-0.03}$	1246.5/982

Notes: models are abbreviated to XSPEC syntax: DKBBFTH - energetically coupled disc - Comptonised corona model. Specific notes: ^{a}External absorption column in units of 10^{22} atoms cm^{2}, ^{b}un-Comptonised disc temperature (keV), ^{c}external radius of corona, ^{d}inner radius of the accretion disc (in km), ^{e}photon index, ^{f}temperature of the Comptonising corona, ^{g}optical depth, τ, is not a fit parameter of the model, but is derived from Γ and kT_e.

This model has five free parameters (only one more than in the purely phenomenological MCD plus power-law model and the same as for all the disc plus Comptonisation models). The first two are the temperature of the Comptonising plasma, kT_e, and its optical depth (parameterised by the asymptotic spectral index, Γ). The disc is assumed to extend from some inner radius, R_{in}, which is given by the overall normalisation of the model, and with a temperature distribution *in the limit of no corona being present* of $T(R)_0 = T_{in}(R/R_{in})^{-3/4}$ i.e. as in the DISKBB model. However, the model assumes that the corona extends homogeneously (constant temperature and optical depth) in a slab over the disc, from its inner radius to R_{T} (in units of the Schwartzschild radius, $R_{\mathrm{s}} = 2GM/c^2$). For all radii between this and R_{in}, the calculated disc temperature is $T(R) = T(R)_0(1-f)^{1/4}$ where f is the fraction of power dissipated in the corona (assumed constant with radius) which is self consistently calculated via iteration from the coronal spectral parameters (Done & Kubota 2006). The resulting disc luminosity underneath the corona is reduced by a factor $(1-f)$, but only a fraction $e^{-\tau}$ of this is seen directly, with the remainder being Compton scattered by the corona (Done & Kubota 2006).

Despite being more physically constrained, the model gives an equivalently good fit to the data as the disc plus Comptonisation models discussed above. Figure 5.6 shows this fit for Ho IX X-1, with the outer (un-Comptonised) disc emission (red solid line) dominating at soft energies. The inner disc emission (red dotted line) is much lower than in standard disc models as much of the energy is powering the corona. These form the seed photons for the Compton scattering, but since this scattering is in an optically thick corona, these photons are *not* seen as almost all of them are upscattered to form the Comptonised spectrum (solid green line).

Figure 5.7 shows the model fit to all our sources, with the pn data corrected for absorption to show the intrinsic spectral shape. This clearly shows the difficulties in interpreting the parameters from simple, phenomenological spectral fits. Again, using Ho IX X-1 as an example, the data have an inflection at soft energies that characterises the soft excess. The characteristic energy of this feature is interpreted as the peak of the disc emission in the MCD plus power-law model (giving a very low temperature: hence IMBHs), while the high energy break forms the peak of the disc temperature in single component

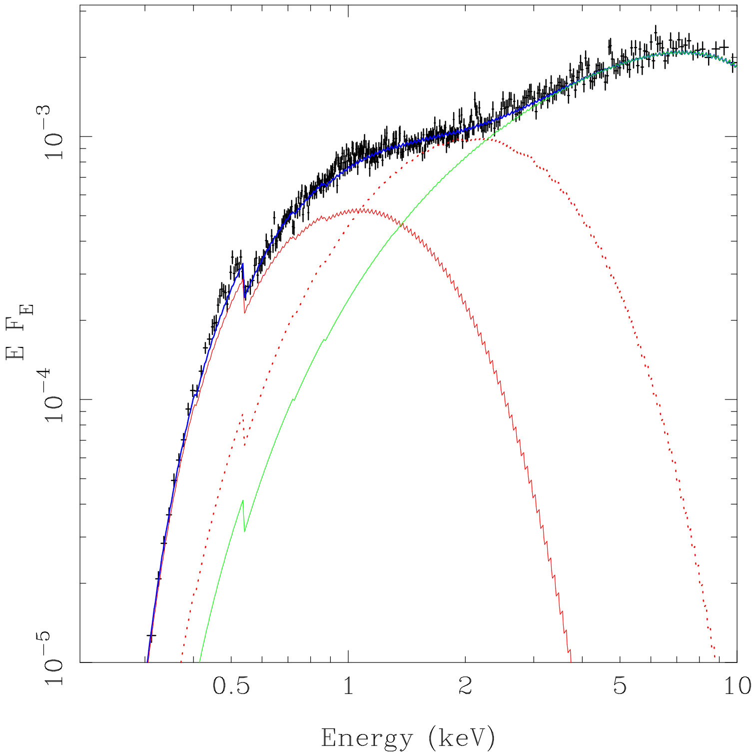

Figure 5.6: *XMM-Newton* EPIC pn data from Ho IX X-1, fit with an absorbed ultraluminous model (DKBBFTH, in blue). We plot only the pn data, shown in black, which we rebin to a minimum of 15 σ significance or 15 channels for clarity. We also plot the various components of the accretion system described by the model, once again disc components are plotted in red whilst the corona is in green. The visible regions of the outer disc and the optically thick corona are plotted with a solid line, whilst the masked emission from the cooled, energetically-coupled inner disc is represented by a dotted line. This shows that the curvature at lower energies is due to emission from the outer accretion disc (we are not able to directly observe emission from the innermost regions), and the break or turnover at higher energies is caused by the emission from the optically thick corona.

disc models (giving a very high temperature: too extreme even for stellar mass black holes). In these coupled disc-corona models, the 'true' disc temperature is not given by either of these observed features! The high energy break is from the very low plasma temperature of the Comptonising region, while the low energy inflection occurs when the outer, un-Comptonised disc emission starts to dominate the spectrum. The inferred intrinsic inner disc temperatures, recovered from the assumption of disc-corona energy partition, range from $0.3 < kT_{\rm disc} < 1.2$ keV with 8/12 giving fits where $kT_{\rm disc} > 0.5$ keV, which lies in the stellar mass black hole regime. This can be seen explicitly by converting the inferred inner radius into black hole mass assuming that the disc extends down to the last stable orbit around a Schwarzschild black hole at $R_{in} = 6GM/c^2 = 8.9M$. All these 'hot' ULXs ($kT_{\rm disc} > 0.5$ keV) have inferred black hole masses $< 100\ M_\odot$, consistent with stellar mass black holes, and consequent derived $L_X/L_{Edd} \gtrsim 1$.

However, a third of these source spectra are best fit by $kT_{\rm disc} < 0.5$ keV, hence giving black hole masses in the range $80 - 430\ M_\odot$ and *sub*-Eddington accretion rates assuming that the disc extends down to the last stable orbit. We propose instead that this very cool temperature and hence large radius is *not* associated with the direct disc emission but instead arises as the accretion rate increases beyond that of standard super-Eddington accretion. In a super-critical accretion regime, the inner regions of the disc and corona may be blown off in the form of a wind, forming an optically thick photosphere out to large radii (e.g. Poutanen et al. 2007). We return to this point in the next section.

5.5 Discussion: ultraluminous X-ray sources, super-Eddington accretion and the ultraluminous state

We have examined twelve of the highest quality ULX data sets currently available in the public archives of the *XMM-Newton* telescope. Initial characterisation of the spectrum of these sources reveals the presence of both a soft excess and a break at higher energies (within the *XMM-Newton* band pass). The existence of curvature at lower energies is apparent in many of the standard black hole binary accretion states, and is regularly fit by an accretion disc (Done, Gierliński & Kubota 2007). It is this standard practice which led to the suggestion that these objects were intermediate mass black holes, due to the low temperature of the apparent disc emission.

However, the detection of a break or curvature at higher energies (~ 5 keV) brings new insights. Such a feature has been observed in ULXs previously (e.g. Foschini et al. 2004; Feng & Kaaret 2005; SRW06; Miyawaki et al 2009), but here we show that it is nearly ubiquitous in the highest quality spectral data, with $\gtrsim$ 10,000 counts. No such break at these low energies is observed in the high energy tail of any of the standard accretion states observed in black hole binaries (Remillard & McClintock 2006; Done, Gierlinski & Kubota 2007)[4] so this challenges the basic assumption of the IMBH model, which is that we are observing standard accretion states that are scaled with the mass of the compact object. Thus we must consider the alternative, that we are observing a different accretion state than those generally seen in black hole binaries. A new accretion state would require us to be observing a different mass accretion rate with respect to Eddington than those seen in the standard states. Since these span ($\sim 10^{-7} - 1$) $L_{\rm Edd}$ (McClintock & Remillard 2006) then this is most likely a super-Eddington state, so requires a stellar mass rather than IMBH accretor.

We therefore suggest that a new observational state should be defined based on the characteristic signatures of ULXs. The **ultraluminous state** is one in which we observe a new combination of observational signatures; both a cool disc and a break or roll over at high energies in the band pass of the *XMM-Newton* telescope. We caution that high quality data is required for a clear identification; the high energy break in particular is difficult to identify with less than $\sim 10,000$ counts in the X-ray spectrum.

In order to explore the physical origins of this state we applied more physically motivated models to the data. One theory that has been presented to explain such an accretion state is the 'slim disc' model, where advection of radiation suppresses the emitted disc luminosity of the innermost regions (Abramowicz et al. 1988). We apply a simplifed model often used for such spectra, where the temperature profile in the disc is assumed to be $T \propto r^{-p}$, with p a free parameter rather than fixed at 0.75 as for standard discs (Watarai et al. 2001). Our data give $0.4 \leq p \leq 0.6$, similar to the $p = 0.5$ expected for advection dominated discs, but the derived inner disc temperatures are unrealistically high ($T_{\rm in} \geq$

---

[4] Whilst there is a break in the high energy tail of the low/hard and very high states, it is at energies $\gtrsim$ 100 keV and 20-30 keV, respectively cf. McClintock & Remillard (2006).

6 keV) for one third of our sample. Figure 5.3 illustrates this for NGC 1313 X-1, where $T \sim 8$ keV. Plainly, the disc temperature is set by the presence of the high energy break, but such high inner disc temperatures are not expected even for stellar mass black holes (Ebisawa et al 2003). However, we caution against interpreting these parameters physically as the model fails to account for the inflection that occurs at ~ 2 keV. These slim disc models cannot simultaneously produce *both* the soft excess at low energies *and* the high energy break seen in the high quality data used here, though this deficiency may be hidden in lower signal-to-noise data.

In order to explore the nature of these sources in more detail, we consider a combination of a disc plus Comptonisation due to its successes in describing the emission of other accretion-powered black hole binary systems. Two different Comptonisation models are applied to the data, COMPTT and EQPAIR, giving two slightly different approximations to thermal Compton up-scattering of accretion disc photons (see Figure 5.5). Irrespective of which model is used, we find evidence for a cool, optically thick corona, where the high energy break is set by the electron temperature of this Comptonising plasma. The parameters of this corona are rather different than anything observed in any of the standard accretion states of black hole binaries. It has lower temperature and higher optical depth than even the most extreme optically thick corona seen in the very high state (Done & Kubota 2006). Such material must block our view of the inner disc (Kubota & Done 2004), and most likely also change the energy dissipated in the disc (Done & Kubota 2006).

We attempt to recover the intrinsic disc spectrum by modelling a corona over the inner disc that both Comptonises the inner regions of the disc and is energetically coupled to it. Both corona and disc are ultimately powered by gravity, so increasing the power dissipated in the corona at a given radius must mean that the disc is less luminous than expected at that radius (Done & Kubota 2006; Svensson & Zdziarski 1994). Again the parameters indicate a more extreme version of the very high state, but unlike the phenomenological disc plus Comptonisation models, these coupled disc-corona models allow us to infer what the source would have looked like without any corona.

The spectral energy distributions derived on the basis of this model can be put into a potential sequence of ULX spectra, as shown in Figure 5.7. The first class are those which have spectra which increase monotonically in νf_ν, with maximum power output at the

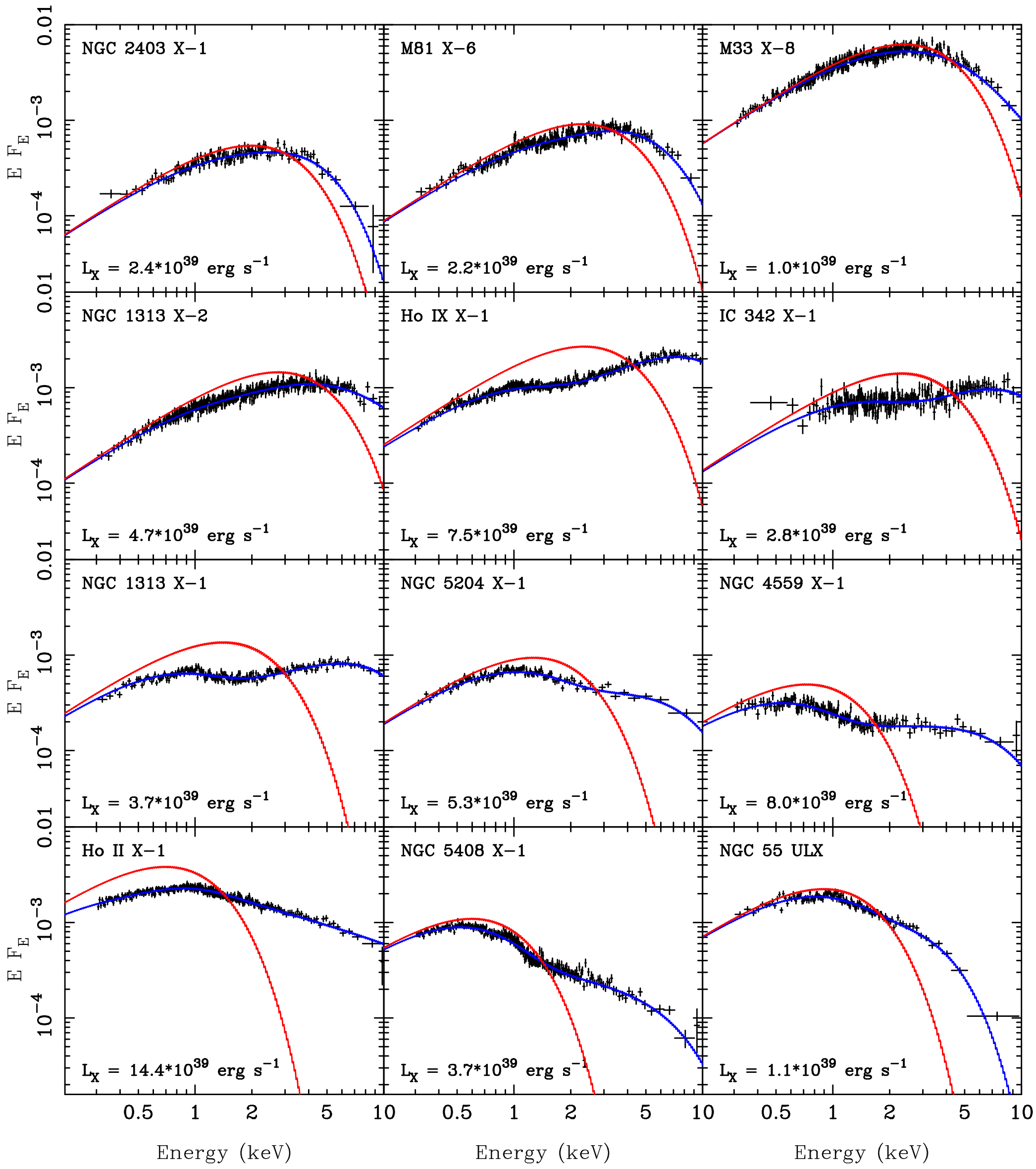

Figure 5.7: *XMM-Newton* EPIC pn data (black) for all sources in our sample, absorption-corrected and deconvolved with DKBBFTH (shown in blue). The 'true' disc spectrum is over-plotted in red, this is the disc spectrum that would be observed in each case if the corona was removed. It is evident from these spectral plots that we are observing a variety of spectral shapes. The first four objects (NGC 2403 X-1 , M81 X-6, M33 X-8 and NGC 1313 X-2) appear very disc-like in structure and could be representative of the high or very high state. As we move further down the plots an inflection begins to emerge at ∼ 2 keV, signifying a break from the standard sub-Eddington accretion states, which we suggest represents a transition to a new super-Eddington accretion state. As the apparent disc temperature cools, the spectrum tips, indicating the possible presence of strong winds enveloping the inner regions of the accretion disc, leading to the most extreme cases (Ho II X-1, NGC 5408 X-1 & NGC 55 ULX).

energy given by the high energy break. All these sources give a 'hot disc' ($kT_{\rm in} > 1$ keV) in the canonical MCD plus power-law fits, with the 'power-law' producing the additional flux at the softest energies. This is probably due to the MCD model providing a poor description of the broader spectra expected from more realistic disc models (Done & Davis 2008; Hui & Krolik 2008). However, these spectra still look fairly similar to the standard disc spectra seen in the disc-dominated state (NGC 2403 X-1; M81 X-6 and M33 X-8). Small amounts of emission from a hot corona can also contribute to the spectrum at the highest energies (see e.g. the spectral decompositions for the most luminous states on XTE J1817-330 in Figure 4 of Gierliński, Done & Page 2009). We note that all of these ULXs have luminosities $\lesssim 3 \times 10^{39}$ erg s^{-1}, so can be close to Eddington for moderately massive ($30 - 50M_{\odot}$) stellar remnant black holes, similar to that found in IC 10 X-1 (see Introduction). The next source in the sequence, NGC 1313 X-2, has a spectrum where the high energy emission seems stronger than expected from a disc dominated state, so this could instead be a type of very high state, again with a moderately massive stellar remnant black hole. Hence, it appears as though the low luminosity end of the ULX population could potentially overlap with sub-Eddington processes seen in the black hole binary population, albeit for larger black holes.

The next category are those where there is clearly a soft inflection as well as a high energy break, but where the total power still peaks at the high energy break (Ho IX X-1; IC 342 X-1; NGC 1313 X-1). These are the ones where the simple disc plus (broken) power-law fits give a cool disc together with a high energy rollover, which we identify with a new *ultraluminous* state. For these data the coupled disc-corona models give an intrinsic disc temperature that is not given by either of these observed characteristic energies, and where the effect of Comptonisation in an optically thick, low temperature corona, is most marked. These spectra do not correspond to any of the known states, but can form from a more extreme (higher optical depth, lower temperature) version of the very high state corona. These are typically brighter than those in the previous class (though there is also substantial overlap in luminosity) so are most likely super-Eddington accretion flows.

There is then a clear observational sequence of spectral shapes, through the sources where the ratio of power between Comptonisation (the high energy peak) and the outer disc (low energy peak) steadily decreases, from NGC 5204 X-1 and NGC 4559 X-1, to the most extreme systems, namely Ho II X-1, NGC 5408 X-1 and NGC 55 ULX. These are the ones where the inferred intrinsic disc temperature from the coupled disc-corona model is $\lesssim 0.4$ keV, far lower than expected from stellar remnant accretion.

To understand these, we look first at what happens physically to the flow as it approaches and then exceeds the Eddington limit. It has long been known that the Eddington limit for a disc is somewhat different than that for spherical accretion (Shakura & Sunyaev 1973). A thin disc, which radiates at the Eddington limit at all radii, has an integrated luminosity $L \sim (1 + ln(\dot{m}))L_{\rm Edd}$ where $\dot{m} = \dot{M}/\dot{M}_{\rm Edd}$ is the mass accretion rate scaled to that which gives the Eddington luminosity for spherical accretion. However, this can only be achieved if excess energy over and above that expected from a constant mass inflow rate, radiating with constant efficiency, is somehow lost from the system. There are two ways to do this, either by changing the mass accretion rate as a function of radius through expelling the excess mass via winds (Shakura & Sunyaev 1973; Begelman et al. 2006) or by changing the radiative efficiency by advecting the photons along with the flow (slim discs, as above). Importantly, both can operate simultaneously (Poutanen et al 2007), as indeed is shown in the most recent 2D radiation hydrodynamic simulations of super-Eddington accretion flows (Ohsuga 2006; 2007; 2009; Kawashima et al. 2009; Takeuchi, Mineshige, & Ohsuga 2009).

This then gives a possible framework to interpret our results. It is clear that the objects with ~ 1 keV disc emission are probably just more extreme versions of the brightest high and very high spectral states known from black hole binaries. The super-Eddington, ultraluminous state sources are then distinguished by their cool, optically thick coronae and apparently cooler discs. One obvious source of higher optical depth in the corona is the increasing importance of winds as the source starts to accrete past the Eddington limit, and this mass loading of the coronal particle acceleration mechanism leads to lower temperatures of the Comptonising electrons.

These winds will become increasingly important as the flows become increasingly super-Eddington, completely enveloping the inner regions of the disc-corona out to an increasing photospheric radius (as in SS 433, Poutanen et al. 2007). Hence the observed temperature decreases in line with the Stefan-Boltzmann law (Shakura & Sunyaev 1973; Begelman et al. 2006; Poutanen et al. 2007). The outflow is inherently (at least) two dimensional, so viewing angle will change the apparent system luminosity (Ohsuga 2006; 2007). We suggest the most extreme objects seen in our current sample, namely NGC 4559 X-1, Ho II X-1, NGC 5408 X-1 and NGC 55 ULX[5], are dominated by reprocessing in a wind, and that much of their luminosity output is channelled into kinetic energy.

Thus it seems most likely that we are seeing the ULX transit between the brightest high and very high states, through to a super-Eddington *ultraluminous* state which is similar to the very high state but with lower temperature and higher optical depth in the corona, to a completely new (hyper-accreting) state where the wind dominates the spectrum. In none of these states do we require the presence of IMBHs to explain the X-ray spectrum; all can be explained by stellar mass black holes at high accretion rates, albeit perhaps black holes up to a few times larger than those known in our own Galaxy.

5.6 Summary

The highest quality data has been collated and utilised to both characterise the spectra of ultraluminous X-ray sources and to constrain their nature. These show that while some ULX (typically the lowest luminosity ones) have spectra which are probably similar to the high and (especially) the very high state in Galactic black hole binaries, the majority show more complex curvature which can be modelled by a cool disc component together with a power-law which breaks/rolls-over above $\sim$ 3 keV. This combination of spectral features is not commonly present in any of the known (sub-Eddington) Galactic black hole binary states, and we therefore propose these features as observational criteria for a new *ultraluminous state* and identify it with super-Eddington accretion flows.

More physical models for these spectra show they are not well fit by (approximate, 'p-free') slim disc models as these cannot simultaneously produce both the soft excess and high energy break. Instead, disc plus Comptonisation models give a much better description of this complex curvature, indicating that the break above $\sim$ 3 keV comes from a cool, optically thick corona. This suggests a more extreme version of the coronae seen in

---

[5] The relatively low luminosity of NGC 55 ULX may be an effect of its disc being close to edge-on to our line-of-sight, evidence for which comes from the dipping behaviour seen in its X-ray light curve (Stobbart et al. 2004).

the very high state of black hole binaries, as might be expected for super-Eddington flows. However, such coronae obscure the inner disc and alter its energetics (Done & Kubota 2006), so we model these effects to recover the intrinsic disc temperatures. Many of these are in the range expected for stellar remnant black holes, showing that the apparent cool disc temperature derived from simple disc models does not require an IMBH. However, there are some objects where the recovered disc temperature (corrected for the corona) is cooler than expected for a stellar remnant black hole. We suggest these are most likely to represent the most extreme super-Eddington accretion flows, where the wind from the accretion disc becomes so powerful that it envelops the inner disc out to a large photospheric radius, producing the cool spectral component.

There are occasional spectra from black hole binaries at the highest luminosities which are indeed better described by optically-thick Comptonisation (GRO J1655-40 and GRS 1915+105: Makishima et al. 2000; Middleton et al. 2006; Ueda et al. 2009). Similarly, the highest Eddington fraction AGN such as RE J1034+396 (Middleton et al. 2009) and RX J0136-35 (Jin et al. 2009) also show such spectra. We suggest that all these sources are in this new super-Eddington *ultraluminous* accretion state. It now appears that ULXs, rather than revealing a new population of IMBHs, are providing us with a template for accretion at super-Eddington rates.

Chapter 6

Conclusions

6.1 Introduction

Throughout this thesis we have sought to explore the nature of ultraluminous X-ray sources via optical and X-ray studies. This chapter seeks to conclude this thesis by returning to the questions laid out in Section 1.9. We will now approach each of these questions in turn and summarise the answers that have arisen during the course of this work. Following on from this we will describe future multi-wavelength work that could be performed in order to increase our knowledge of these systems, and further explore their nature.

6.2 What are the stellar counterparts to ULXs?

In Chapter 2 we collated a catalogue of nearby ($\lesssim 5$ Mpc) ULXs from the literature,with the aim of searching for optical counterparts to these sources. Of the 45 ULXs residing nearby, 31 have both *Chandra* and *Hubble Legacy Archive*. We find that 23 of these ULXs have a total of 38 identifiable counterparts (multiple counterparts were often visible within the error circle). Photometric analysis of these counterparts included the application of stellar templates. From this we find that the optical counterparts of nearby ULXs can be explained by a wide variety of stellar templates. We note, however that most of these are consistent with OB type stars (ranging from main sequence to supergiants) as seen in previous studies. This is perhaps unsurprising, given the apparent association many ULXs have with areas of recent star formation (see Section 1.8), however, a small number of sources are best described as later stars, particularly by a red K – M giants/supergiants. In these cases, we speculate that we may be looking at systems similar to that of GRS 1915+105. This is an X-ray binary containing a K – M giant, where accretion is fed via Roche lobe overflow (Greiner et al. 2001). However our initial optical spectroscopic studies, shows that the continuum of our ULX sample may be non-stellar in origin (see Chapter 3). This highlights the need for more high quality spectroscopic data, in order to unlock the nature of these ULX counterparts.

6.3 How do these sources vary over time?

Throughout this work we have investigated a range of variability from these sources in the X-rays (Chapter 4), and possible variations in the optical emission (see Chapter 2).

During our study of the ULX population contained within NGC 4485 & 4490, we find a lack of intra-observational variability in the X-ray light curves of these sources. However, inter-observational variability reveals a heterogeneous behaviour in our sample. A multi-mission X-ray survey was performed using moderate quality data. The results of this show that some of our sample remained remarkably stable in their emission over a $\sim$ 18 year period, showing no statistical signs of temporal variability. It also revealed that sources exhibiting large scale temporal variations (of up to an order of magnitude) appear to change their spectral shape from a power-law like structure to a more curvilinear shape (well fit by a multi-coloured disc model) with increasing luminosity. Such a change in spectral shape suggests a possible change in spectral state, from the very high state to a possible ultraluminous state. As such a transition would occur at around the Eddington limit for that source, this change of shape could also be used to give us a mass estimate for these source.

During our photometric study of the optical counterparts of these systems (Chapter 2), we found in some cases we needed to use multiple observations to expand our wavelength coverage of the systems. By doing this, we needed to look for possible temporal variation that could affect the fitting of stellar templates. We found that, as with X-ray emission, some sources remain reasonably stable over periods of time, whilst others can show larger scale variations in their emission. As so few of our sample were considered in this way, further study would be required to look into this in more detail.

6.4 What is the accretion geometry of these systems?

Photometric studies of the optical counterparts of ULXs reveals that we are probably observing HMXBs (Chapter 2), while X-ray spectral fitting of some of the highest quality data currently publicly available, indicates that the presence of a cool optically thick accretion disc with an optically thick Comptonising corona (Chapter 5). Such an accretion disc, and corona, would require a large amount of matter to be transferred from the companion. This combination of results supports the theoretical suggestions that we are observing systems that contain a compact object accreting from a high mass companion via Roche lobe overflow.

The presence of a cool accretion disc could indicate that we may be observing an intermediate mass black hole, or it could be that we are looking at an extreme accretor, where the inner regions of the disc are buried under an optically thick corona and/or photosphere. X-ray spectral fits reveal a set of parameters that are more extreme than those of the very high state. We therefore apply a physically motivated model designed to describe the more extreme very high state sources observed within our Galaxy. The resulting fits indicated that both mass and energy would be removed from the inner disc to feed the corona, as the accretion rate increases. In the most extreme cases, this material (and some energy) would be lost in the form of a wind that could become powerful enough to envelope the inner disc out to a large photospheric radius.

6.5 Do these systems contain intermediate mass black holes and are there multiple classes of ULX?

One feature of the ultraluminous source population that stands out is the heterogeneous behaviour of these sources. If we consider initially the optical emission of these sources, we find that the optical counterparts are either consistent with OB stars or red K − M type stars and range from main sequence to supergiants (Chapter 2). In our optical spectroscopic survey we find that high excitation lines can be emitted from either the nebula or the source. A large amount of energy would need to be released in the extreme ultraviolet and X-rays to power excitation of these scales (Chapter 3).

When we consider the X-ray emission from these sources, we find no short-term variability in our sample (Chapter 4), but other ULXs have shown the presence of measurable short-term variability, with some even containing QPOs (Section 1.8). On longer time scales, large scale variations have been observed in the light curves of some sources, while others remain remarkably stable (Chapter 4). Transients are also contained within the sample of ULXs, along with the possible identification of a black hole Be binary system (further research is required to confirm its nature).

Optical Spectroscopic analysis of the environments of these systems indicate that there could be interactions between the inter-stellar medium, the nebula and the ULX, which cause variations in extinction across the field. This could also explain 'bright patchy' emission present in some studies (see Chapter 3 for further information). This could be as a results of outflows. X-ray spectroscopic analysis reveals that a ~ 5 keV break in the spectrum is almost ubiquitous in high quality data, a break that is not observed in any of the standard accretion states (Chapter 5). This combination of results, when combined with those outlined above, would indicate that we are not looking at intermediate mass black holes. It would instead suggest that we are looking at an extreme form of accretion onto a stellar mass black hole.

In fact, we were able to gain mass estimates for the compact objects contained within these systems in Chapters 4 & 5. The possible state transition highlighted above and discussed in Chapter 4 provides estimates of $10 - 15\ M_{\odot}$, whilst the energetically coupled disc and corona models used in Chapter 5 argued that the majority of ULXs contained within the sample indicated the presence of stellar mass ($\lesssim 100\ M_{\odot}$) black holes. In those cases where the model showed a cool underlying disc, we argue that the systems appeared even more extreme, with possible evidence for strong winds and the presence of a photosphere. In these cases the model would no longer be able to provide a clear estimate for the mass. However, given the heterogeneity of these sources, it is possible that a small minority of ULXs may still contain IMBHs.

6.6 Future work

In the short-term, there are many ways to explore the nature of ultraluminous X-ray sources, building on the work of this thesis. As with all observational work, the first suggestion is to obtain more high quality data of these sources. In the X-rays, an application should be made for a 'large project' ($\gtrsim$ 300 ks) to undertake a series of high quality ($\gtrsim$ 10,000 accumulates EPIC counts) observations of an individual ULX. This would allow us to test our theories on the changing spectral shape, its relation to the Eddington limit and the physical meaning that we derived from this change.

Another option is to return to the public archives of X-ray telescopes (expanding our search to include *Swift*) to explore the possible change in state identified in Chapter 4. The proposal would be to carry out a systematic survey of ULXs, using the data to identify the model preference, or state, and transitions between them. By collating data from a wider sample, we would gain more opportunity to observe the overall trends in these sources. This transitional luminosity can then be used to test our ideas and gain further $M_{\rm BH}$ estimates.

However, optical radial velocity curves still represent the most reliable means available to measure masses of black holes in binary systems. Using data awarded by to us by the Gemini Observatory, we will use identified He II 4686 Å to potentially gain radial velocity measurements. The results from these programmes could then be used to calculate the mass functions of these systems. We will also visit the archives of other large facilities to collate the spectra of other ULXs to perform similar emission/absorption line surveys as those outlined in Chapter 3, giving multiple constraints on the processes occurring within these systems. Alternative steps can also be taken to gain more information from the optical spectra of these, for example we could work with packages such as the STSDAS tool *NEBULAR*[1] or the package *CLOUDY*[2].These tools will allow us to gain a greater understanding of the nature of ULX environments.

Our optical photometric survey provides us with a large sample of counterparts that can be exploited in various ways. One option is to return to this sample with X-ray

---

[1] Further details of *NEBULAR* can be found at `http://iraf.noao.edu/irafnews/dec94/dec94-S-13.html`.

[2] Information of *CLOUDY* can be found at `http://www.nublado.org/`.

irradiation models which describe the optical emission that would be observed from an irradiated accretion disc (and star). This would allow us to explore the nature of potential counterparts in more detail, and possibly help us to better constrain the nature of these systems.

The colours of nearby bright stars can also be used to construct colour-magnitude diagrams in each field, to estimate the reddening and, with the addition of isochrones for stellar populations, we will be able to place constraints on the maximum age of these systems. By returning to the *Hubble Legacy Archive*, we will also be able look further into optical variations of these sources. This can be done basically by performing the same analysis as is described in Chapter 2. A far cleaner approach, however, would be to collate multiple observations of the same band for an individual source. A similar technique was recently applied by Liu, Bregman & McClintock (2009), in which the authors were able to find a 6.1 day periodic oscillation in the light curve of NGC 1313 X-2. Although it is unlikely that we could receive such a result from archival observations, it shows the potential of such a technique.

On longer time-scales we will be able to take advantage of the next generation in optical and X-ray telescopes to explore ULXs in more detail. Projects such as the E-ELT[3] will allow us to look at fainter counterparts, providing us with the opportunity to perform optical spectroscopic studies on a much larger proportion of ULX counterparts. While in X-rays, missions such as ASTRO-H[4] and IXO[5] will provide us with unprecedented spectral and timing resolution, hopefully allowing us to answer the remaining questions surrounding these sources, whilst inspiring new questions.

---

[3] For more information of the ELT, see `http://www.eso.org/public/astronomy/teles-instr/e-elt.html`.

[4] Details on the ASTRO-H mission can be found at `http://astro-h.isas.jaxa.jp/si/index_e.html`.

[5] Information on IXO can be found at `http://ixo.gsfc.nasa.gov/science/goals.html`.

Bibliography

[1] Abolmasov P., Fabrika S., Sholukhova O., Afanasiev V., 2007, AstBu, 62, 36

[2] Abolmasov P., Fabrika S., Sholukhova O., Kotani T., 2008, arXiv, arXiv:0809.0409

[3] Abramowicz M. A., Czerny B., Lasota J. P., Szuszkiewicz E., 1988, ApJ, 332, 646

[4] Aretxaga I., Benetti S., Terlevich R. J., Fabian A. C., Cappellaro E., Turatto M., della Valle M., 1999, MNRAS, 309, 343

[5] Balbus S. A., Hawley J. F., 1991, ApJ, 376, 214

[6] Balbus S. A., 2005, ASPC, 330, 185

[7] Baldwin J. A., Phillips M. M., Terlevich R., 1981, PASP, 93, 5

[8] Bauer F. E., Brandt W. N., Sambruna R. M., Chartas G., Garmire G. P., Kaspi S., Netzer H., 2001, AJ, 122, 182

[9] Begelman M. C., 2002, ApJ, 568, L97

[10] Begelman M. C., King A. R., Pringle J. E., 2006, MNRAS, 370, 399

[11] Berghea C.T., Weaver K. A., Colbert E. J. M., Roberts T. P., 2008, ApJ, 687, 471

[12] Belczynski K., Sadowski A., Rasio F. A., 2004, ApJ, 611, 1068

[13] Belczynski K., Sadowski A., Rasio F. A., Bulik T., 2006, ApJ, 650, 303

[14] Belczynski K., Bulik T., Fryer C. L., Ruiter A., Vink J. S., Hurley J. R., 2009, arXiv, arXiv:0904.2784

[15] Belczynski K., Ziolkowski J., 2009, arXiv, arXiv:0907.4990

[16] Beloborodov A. M., 1998, MNRAS, 297, 739

[17] Belloni T., Psaltis D., van der Klis M., 2002, ApJ, 572, 392

[18] Bisiacchi G. F., Dultzin D., Firmani C., Hacyan S., 1974, ApJ, 190, L59

[19] Böhm-Vitense E., 1989, “Introduction to Stellar Astrophysics”, Cambridge University Press, Cambridge

[20] Bolton C. T., 1972, Natur, 240, 124

[21] Bohlin R. C., Savage B. D., Drake J. F., 1978, ApJ, 224, 132

[22] Boroson T. A., 2002, ApJ, 565, 78

[23] Bouchet P., Lequeux J., Maurice E., Prevot L., Prevot-Burnichon M. L., 1985, A&A, 149, 330

[24] Boumis P., et al., 2007, MNRAS, 381, 308

[25] Braes L. L. E., Miley G. K., 1971, Natur, 232, 246

[26] Bragg W.L., 1913, Proc. Camb. Phil. Soc, 17

[27] Britton J., Walker C., 1996, "Astronomy before the Telescope", ed Walker C., British Museum Press, London, p. 42

[28] Cardelli J. A., Clayton G. C., Mathis J. S., 1989, ApJ, 345, 245

[29] Charles P. A., Coe M. J., 2006. in: "Compact Stellar X-ray Sources", eds. Lewin W.H.G. and va der Klis M., Cambridge University Press, Cambridge, p. 215

[30] Chevalier R. A., Fransson C., 1994, ApJ, 420, 268

[31] Clemens M. S., Alexander P., Green D. A., 2000, MNRAS, 312, 236

[32] Colbert E. J. M., Mushotzky R. F., 1999, ApJ, 519, 89

[33] Colbert E. J. M., Ptak A. F., 2002, ApJS, 143, 25

[34] Colbert E. J. M., Heckman T. M., Ptak A. F., Strickland D. K., Weaver K. A., 2004, ApJ, 602, 231

[35] Copernicus N., 1543, De revolutionibus orbium coelestium, Norimbergae

[36] Copperwheat C., Cropper M., Soria R., Wu K., 2005, MNRAS, 362, 79

[37] Copperwheat C., Cropper M., Soria R., Wu K., 2007, MNRAS, 376, 1407

[38] Coppi P. S., 1999, ASPC, 161, 375

[39] Cropper M., Soria R., Mushotzky R. F., Wu K., Markwardt C. B., Pakull M., 2004, MNRAS, 349, 39

[40] Cropper M., Soria R., Mushotzky R. F., Wu K., Markwardt C. B., Pakull M., 2004a, MNRAS, 353, 1024

[41] Culhane J. L., Sanford P. W., 1981, Faber and Faber Limited, London

[42] Cunningham C. T., 1975, ApJ, 202, 788

[43] Dam H. J. W., 1896, Marie Curie Magazine, Vol. 6, No. 5.

[44] Davis S. W., Blaes O. M., Hubeny I., Turner N. J., 2005, ApJ, 621, 372

[45] Davis S. W., Done C., Blaes O. M., 2006, ApJ, 647, 525

[46] Dewangan, G. C., Miyaji, T., Griffiths, R. E., & Lehmann, I. 2004, ApJ, 608, L57

[47] Dewangan G. C., Griffiths R. E., Rao A. R., 2006, ApJ, 641, L125

[48] Dickey J. M., Lockman F. J., 1990, ARA&A, 28, 215

[49] Dolan J. F., 1970, SSRv, 10, 830

[50] Dolan J. F., 1971, Natur, 233, 109

[51] Done C., 2002, RSPTA, 360, 1967

[52] Done C., Kubota A., 2006, MNRAS, 371, 1216

[53] Done C., Gierliński M., Kubota A., 2007, A&ARv, 15, 1

[54] Done C., Davis S. W., 2008, ApJ, 683, 389

[55] Ducci L., Sidoli L., Mereghetti S., Paizis A., Romano P., 2009, MNRAS, 1090

[56] Dubner G. M., Holdaway M., Goss W. M., Mirabel I. F., 1998, AJ, 116, 1842

[57] Dubus G., Charles P. A., Long K. S., 2004, A&A, 425, 95

[58] Ebisuzaki, T., et al. 2001, ApJ, 562, L19

[59] Ebisawa K., Kubota A., Mizuno T., Życki P., 2001, ApSSS, 276, 11

[60] Ebisawa K., Życki P., Kubota A., Mizuno T., Watarai K.-y., 2003, ApJ, 597, 780

[61] Elmegreen D. M., Chromey F. R., Knowles B. D., Wittenmyer R. A., 1998, AJ, 115, 1433

[62] Eracleous M., Shields J. C., Chartas G., Moran E. C., 2002, ApJ, 565, 108

[63] Esin A. A., McClintock J. E., Narayan R., 1997, ApJ, 489, 865

[64] Fabbiano G., Trinchieri G., 1987, ApJ, 315, 46

[65] Fabbiano, G., 1989, ARA&A, 27, 87

[66] Fabbiano, G., 1995, in "X-ray Binaries", eds. Lewin W. H. G., van Paradijs J. and van den Heuvel E. P. J., Cambridge University Press, Cambridge, p. 390

[67] Fabbiano G., Zezas A., Murray S. S., 2001, ApJ, 554, 1035

[68] Fabbiano G., Zezas A., King A. R., Ponman T. J., Rots A., Schweizer F., 2003, ApJ, 584, L5

[69] Fabbiano G., et al., 2003a, AAS, 35, 1409

[70] Fabbiano G., 2004, RMxAC, 20, 46

[71] Falcke H., Körding E., Markoff S., 2004, A&A, 414, 895

[72] Fender R., 2006. in: "Compact Stellar X-ray Sources", eds. Lewin W.H.G. and va der Klis M., Cambridge University Press, Cambridge, p. 381

[73] Feng H., Kaaret P., 2005, ApJ, 633, 1052

[74] Feng H., Kaaret P., 2008, ApJ, 675, 1067

[75] Feroci M., 1999, MmSAI, 70, 905

[76] Forman W., Jones C., Cominsky L., Julien P., Murray S., Peters G., Tananbaum H., Giacconi R., 1978, ApJS, 38, 357

[77] Forman W., Schwarz J., Jones C., Liller W., Fabian A. C., 1979, ApJ, 234, L27

[78] Foschini L., et al., 2002, A&A, 392, 817

[79] Foschini L., Rodriguez J., Fuchs Y., Ho L. C., Dadina M., Di Cocco G., Courvoisier T. J.-L., Malaguti G., 2004, A&A, 416, 529

[80] Frank J., King A., Raine D. J., 2002, " Accretion Power in Astrophysics: Third Edition", Cambridge University Press, Cambridge

[81] Freedman W. L., et al., 1994, ApJ, 427, 628

[82] Fridriksson J. K., Homan J., Lewin W. H. G., Kong A. K. H., Pooley D., 2008, ApJS, 177, 465

[83] Fryer C. L., Kalogera V., 2001, ApJ, 554, 548

[84] Fukazawa Y., et al., 1994, PASJ, 46, L141

[85] Gao Y., Wang Q. D., Appleton P. N., Lucas R. A., 2003, ApJ, 596, L171

[86] Ghosh K. K., Finger M. H., Swartz D. A., Tennant A. F., Wu K., 2006, ApJ, 640, 459

[87] Gonçalves A. C., Soria R., 2006, MNRAS, 371, 673

[88] Giacconi R., Gursky H., Paolini F. R., Rossi B. B., 1962, PhRvL, 9, 439

[89] Giacconi R., Gorenstein P., Gursky H., Waters J. R., 1967, ApJ, 148, L119

[90] Giacconi R., Gorenstein P., Gursky H., Usher P. D., Waters J. R., Sandage A., Osmer P., Peach J. V., 1967a, ApJ, 148, L129

[91] Giacconi R., Kellogg E., Gorenstein P., Gursky H., Tananbaum H., 1971, ApJ, 165, L27

[92] Giacconi R., et al., 1979, ApJ, 230, 540

[93] Gierliński M., Zdziarski A. A., Poutanen J., Coppi P. S., Ebisawa K., Johnson W. N., 1999, MNRAS, 309, 496

[94] Gierliński M., Done C., Page K., 2009, MNRAS, 392, 1106

[95] Goad M. R., Roberts T. P., Knigge C., Lira P., 2002, MNRAS, 335, L67

[96] Goad M. R., Roberts T. P., Reeves J. N., Uttley P., 2006, MNRAS, 365, 191

[97] Greenhill J. G., Giles A. B., Coutures C., 2006, MNRAS, 370, 1303

[98] Greiner J., Cuby J. G., McCaughrean M. J., Castro-Tirado A. J., Mennickent R. E., 2001, A&A, 373, L37

[99] Griffiths R. E., Ptak A., Feigelson E. D., Garmire G., Townsley L., Brandt W. N., Sambruna R., Bregman J. N., 2000, Sci, 290, 1325

[100] Grimm H.-J., Gilfanov M., Sunyaev R., 2003, MNRAS, 339, 793

[101] Grimm H.-J., McDowell J. C., Zezas A., Kim D.-W., Fabbiano G., 2005, AAS, 37, 1281

[102] Greiner J., Cuby J. G., McCaughrean M. J., Castro-Tirado A. J., Mennickent R. E., 2001, A&A, 373, L37

[103] Grisé F., Pakull M., Motch C., 2005, in:Semaine de l'Astrophysique Francaise, eds Casoli F., Contini T.,, Hameury J. M., Pagani L., EdP-Sciences, 2005, p. 54

[104] Grisé F., Pakull M. W., Soria R., Motch C., 2009, AIPC, 1126, 201

[105] Gursky, H., Giacconi, R., Paolini, F. R., & Rossi, B. B. 1963, Physical Review Letters, 11, 530

[106] Hasinger G., Burg R., Giacconi R., Schmidt M., Trumper J., Zamorani G., 1998, A&A, 329, 482

[107] Heger A., Fryer C. L., Woosley S. E., Langer N., Hartmann D. H., 2003, ApJ, 591, 288

[108] Heil L. M., Vaughan S., Roberts T. P., 2009, MNRAS, 397, 1061

[109] Holt S. S., 1993, A&AS, 97, 367

[110] Holt S. S., Gotthelf E. V., Tsunemi H., Negoro H., 1994, PASJ, 46, L151

[111] Hoskin M., Gingerich O., 1997, "The illustrated history of astronomy", eds Hoskin M., Cambridge University Press, Cambridge, p. 50

[112] Hu C., Wang J.-M., Ho L. C., Chen Y.-M., Zhang H.-T., Bian W.-H., Xue S.-J., 2008, ApJ, 687, 78

[113] Hui Y., Krolik J. H., 2008, ApJ, 679, 1405

[114] Humphrey P. J., Fabbiano G., Elvis M., Church M. J., Bałucińska-Church M., 2003, MNRAS, 344, 134

[115] Hutchings J. B., Crampton D., Glaspey J., Walker G. A. H., 1973, ApJ, 182, 549

[116] Immler S., Wang Q. D., 2001, ApJ, 554, 202

[117] Immler S., Lewin W. H. G., 2003, LNP, 598, 91

[118] Immler S., Kuntz K. D., 2005, ApJ, 632, L99

[119] Isobe N., et al., 2009, PASJ, 61, 279

[120] Jeffreys H., 1961, "Theory of Probability", Oxford University Press, Oxford

[121] Jin C., Done C., Ward M., Gierliński M., 2009, arXiv, arXiv:0903.4698 (submitted to MNRAS)

[122] Johnson H. L., Morgan W. W., 1953, ApJ, 117, 313

[123] Kaaret, P., Corbel, S., Prestwich, A. H., & Zezas, A. 2003, Science, 299, 365

[124] Kaaret P., Ward M. J., Zezas A., 2004, MNRAS, 351, L83

[125] Kaaret P., 2005, ChJAS, 5, 139

[126] Kaaret P., Simet M. G., Lang C. C., 2006, ApJ, 646, 174

[127] Kaaret P., Corbel S., 2009, ApJ, 697, 950

[128] Kalberla P. M. W., Burton W. B., Hartmann D., Arnal E. M., Bajaja E., Morras R., Poeppel W. G. L., 2005, yCat, 8076, 0

[129] Karachentsev I. D., et al., 2002, A&A, 385, 21

[130] Kass R.E., Raftery A.E., 1995, Journal of American Statistical Association, 90, 773

[131] Kawashima T., Ohsuga K., Mineshige S., Heinzeller D., Takabe H., Matsumoto R., 2009, arXiv, arXiv:0904.4123

[132] Kepler J., 1609, Astronomia nova, Pragae

[133] Kepler J., Ptolemaeus C., Fludd R., 1619, Harmonices mvndi, Austriae

[134] Kewley L. J., Dopita M. A., 2002, ApJS, 142, 35

[135] King A. R., Davies M. B., Ward M. J., Fabbiano G., Elvis M., 2001, ApJ, 552, L109

[136] King A. R., 2004, MNRAS, 347, L18

[137] King A. R., 2008, MNRAS, 385, L113

[138] King A. R., 2009, MNRAS, 393, L41

[139] King D. A., 1996, "Astronomy before the Telescope", ed Walker C., British Museum Press, London, p. 143

[140] Kong A. K. H., 2003, MNRAS, 346, 265

[141] Kong A. K. H., Yang Y. J., Hsieh P.-Y., Mak D. S. Y., Pun C. S. J., 2007, ApJ, 671, 349

[142] Körding E., Falcke H., Markoff S., 2002, A&A, 382, L13

[143] Körding E., Colbert E., Falcke H., 2005, A&A, 436, 427

[144] Kraft R. P., Kregenow J. M., Forman W. R., Jones C., Murray S. S., 2001, ApJ, 560, 675

[145] Kubota A., Mizuno T., Makishima K., Fukazawa Y., Kotoku J., Ohnishi T., Tashiro M., 2001, ApJ, 547, L119

[146] Kubota A., Done C., 2004, MNRAS, 353, 980

[147] Kubota A., Mizuno T., Makishima K., Fukazawa Y., Kotoku J., Ohnishi T., Tashiro M., 2001, ApJ, 547, L119

[148] Kuncic Z., Soria R., Hung C. K., Freeland M. C., Bicknell G. V., 2006, in:"Black Holes: from Stars to Galaxies - across the Range of Masses" (Proceedings of the 238th Symposium of the IAU, 2006), eds Karas, V., Matt, G., Cambridge University Press, Cambridge, 2007., pp.247-250

[149] Kuntz K. D., Gruendl R. A., Chu Y. H., Chen C.-H. R., Still M., Mukai K., Mushotzky R. F., 2005, ApJ, 620, L31

[150] La Parola V., Peres G., Fabbiano G., Kim D. W., Bocchino F., 2001, ApJ, 556, 47

[151] Lang C. C., Kaaret P., Corbel S., Mercer A., 2007, ApJ, 666, 79

[152] Laue M., 1913, AnP, 347, 397

[153] Lee H., Skillman E. D., Cannon J. M., Jackson D. C., Gehrz R. D., Polomski E. F., Woodward C. E., 2006, ApJ, 647, 970

[154] Lehmann I., et al., 2005, A&A, 431, 847

[155] Lewin W. H. G., et al., 1976, ApJ, 207, L95

[156] Li L. X., Zimmerman E. R., Narayan R., McClintock J. E., 2005, ApJS, 157, 335

[157] Lira P., Ward M., Zezas A., Alonso-Herrero A., Ueno S., 2002, MNRAS, 330, 259

[158] Liu J. F., Bregman J. N., Seitzer P., 2002, ApJ, 580, L31

[159] Liu J. F., Bregman J. N., Irwin J., Seitzer P., 2002, ApJ, 581, L93

[160] Liu, J. F., Bregman, J. N., & Seitzer, P. 2004, ApJ, 602, 249

[161] Liu J. F., Bregman J. N., 2005, ApJS, 157, 59

[162] Liu J. F., Bregman J. N., Irwin J., 2006, ApJ, 642, 171

[163] Liu J. F., Bregman J., Miller J., Kaaret P., 2007, ApJ, 661, 165

[164] Liu J., Di Stefano R., 2008, ApJ, 674, L73

[165] Liu J., Bregman J. N., McClintock J. E., 2009, ApJ, 690, L39

[166] Liu Q. Z., Mirabel I. F., 2005, A&A, 429, 1125

[167] Long K. S., Helfand D. J., Grabelsky D. A., 1981, ApJ, 248, 925

[168] Madau, P., Rees, M. J. 2001, ApJ, 551, L27

[169] Madhusudhan N., Justham S., Nelson L., Paxton B., Pfahl E., Podsiadlowski P., Rappaport S., 2006, ApJ, 640, 918

[170] Madhusudhan N., Rappaport S., Podsiadlowski P., Nelson L., 2008, ApJ, 688, 1235

[171] Makishima K., et al., 2000, ApJ, 535, 632

[172] Mapelli M., Colpi M., Zampieri L., 2009, MNRAS, 395, L71

[173] Marshall F. J., Clark G. W., 1984, ApJ, 287, 633

[174] Mason K. O., Bignami G., Brinkman A. C., Peacock A., 1995, AdSpR, 16, 41

[175] Matsumoto H., Tsuru T. G., Koyama K., Awaki H., Canizares C. R., Kawai N., Matsushita S., Kawabe R., 2001, ApJ, 547, L25

[176] Maxfield L., Spinrad H., Stern D., Dey A., Dickinson M., 2002, AJ, 123, 2321

[177] Mayer W. F., 1975, JHATD, 14, 14

[178] Mayer M., Pringle J. E., 2007, MNRAS, 376, 435

[179] McHardy I. M., Lawrence A., Pye J. P., Pounds K. A., 1981, MNRAS, 197, 893

[180] McHardy I. M., Koerding E., Knigge C., Uttley P., Fender R. P., 2006, Natur, 444, 730

[181] McClintock J.E., Remillard R.A., 2006. in:"Compact Stellar X-ray Sources", eds. Lewin W.H.G. and va der Klis M., Cambridge University Press, Cambridge, p. 157

[182] McHardy I. M., Koerding E., Knigge C., Uttley P., Fender R. P., 2006, Natur, 444, 730

[183] Meinel A., Aveni A., Stockton M. W., 1981,'Catalogue of Emission lines in astrophysical objects', University of Arizona, Arizona

[184] Mendez M., van der Klis M., 1997, ApJ, 479, 926

[185] Meyer F., Meyer-Hofmeister E., 1994, A&A, 288, 175

[186] Middleton M., Done C., Gierliński M., Davis S. W., 2006, MNRAS, 373, 1004

[187] Middleton M., Done C., Ward M., Gierliński M., Schurch N., 2009, MNRAS, 394, 250

[188] Miller, J. M., Fabbiano, G., Miller, M. C., & Fabian, A. C., 2003, ApJ, 585, L37

[189] Miller, J. M., Fabian, A. C., & Miller, M. C., 2004a, ApJ, 607, 931

[190] Miller M. C., Colbert E. J. M., 2004, IJMPD, 13, 1

[191] Miller N. A., Mushotzky R. F., Neff S. G., 2005, ApJ, 623, L109

[192] Mirabel I. F., Rodríguez L. F., 1999, ARA&A, 37, 409

[193] Mitsuda K., et al., 1984, PASJ, 36, 741

[194] Miyaji T., Lehmann I., Hasinger G., 2001, AJ, 121, 3041

[195] Miyawaki R., Sugiho M., Kubota A., Makishima K., Namiki M., Tanaka T., Tsunoda N., 2006, in: Proceedings of The X-ray Universe 2005, eds. Wilson, A., ESA Publications Division, ESTEC, Noordwijk, p.433

[196] Miyawaki R., Makishima K., Yamada S., Gandhi P., Mizuno T., Kubota A., Tsuru T. G., Matsumoto H., 2009, PASJ, 61, 263

[197] Mizuno T., Kubota A., Makishima K., 2001, ApJ, 554, 1282

[198] Mizuno T., et al., 2007, PThPS, 169, 229

[199] Morgan W. W., Kellman E., Hoffleit D., 1943, Sci, 97, 536

[200] Morris P. W., Stolovy S., Wachter S., Noriega-Crespo A., Pannuti T. G., Hoard D. W., 2006, ApJ, 640, L179

[201] Mucciarelli P., Zampieri L., Falomo R., Turolla R., Treves A., 2005, ApJ, 633, L101

[202] Murdin P., Webster B. L., 1971, Natur, 233, 110

[203] Narayan R., Yi I., 1995, ApJ, 452, 710

[204] Negueruela I., 2009, arXiv, arXiv:0907.2883

[205] Newton I., 1687, Philosophiae naturalis principia mathematica, Streater, London

[206] Ohsuga K., 2006, ApJ, 640, 923

[207] Ohsuga K., 2007, ApJ, 659, 205

[208] Ohsuga K., Mineshige S., Mori M., Kato Y., 2009, arXiv, arXiv:0903.5364

[209] Okajima T., Ebisawa K., Kawaguchi T., 2006, ApJ, 652, L105

[210] Osterbrock D. E., 1989, ‘Astrophysics of gaseous nebulae and active galactic nuclei’, University Science Books, USA

[211] Osterbrock D. E., Ferland G. J., 2006, ‘Astrophysics of gaseous nebulae and active galactic nuclei’, 2nd Edition, University Science Books, USA

[212] Paczynski B., 1974, A&A, 34, 161

[213] Pagel B. E. J., Edmunds M. G., Blackwell D. E., Chun M. S., Smith G., 1979, MNRAS, 189, 95

[214] Pakull M. W., Mirioni L., 2002, astro, arXiv:astro-ph/0202488

[215] Pakull M. W., Mirioni L., 2003, RMxAC, 15, 197

[216] Pakull M. W., Grisé F., Motch C., 2006, IAUS, 230, 293

[217] Pannuti T. G., Schlegel E. M., Lacey C. K., 2007, AJ, 133, 1361

[218] Patruno A., Zampieri L., 2008, MNRAS, 386, 543

[219] Ptak A., Colbert E., van der Marel R. P., Roye E., Heckman T., Towne B., 2006, ApJS, 166, 154

[220] Portegies-Zwart S. F., Dewi J., Maccarone T., 2004, MNRAS, 355, 413

[221] Portegies-Zwart S. F., McMillan S.L.W., 2002, ApJ, 576, 899

[222] Pounds K. A., Nandra K., Stewart G. C., Leighly K., 1989, MNRAS, 240, 769

[223] Poutanen J., Krolik J. H., Ryde F., 1997, MNRAS, 292, L21

[224] Poutanen J., Lipunova G., Fabrika S., Butkevich A. G., Abolmasov P., 2007, MNRAS, 377, 1187

[225] Prendergast K. H., Burbidge G. R., 1968, ApJ, 151, L83

[226] Prestwich A. H., et al., 2007, ApJ, 669, L21

[227] Radecke, H.-D. 1997, A&A, 319, 18

[228] Ramsey C. J., Williams R. M., Gruendl R. A., Chen C.-H. R., Chu Y.-H., Wang Q. D., 2006, ApJ, 641, 241

[229] Rappaport S. A., Podsiadlowski P., Pfahl E., 2005, MNRAS, 356, 401

[230] Rausch G., Frankenbach K., Trogus W., Bachor E., 1982, aans.symp,

[231] Read A. M., Ponman T. J., Strickland D. K., 1997, MNRAS, 286, 626

[232] Remillard R. A., McClintock J. E., 2006, ARA&A, 44, 49

[233] Reynolds C. S., Ward M. J., Fabian A. C., Celotti A., 1997, MNRAS, 291, 403

[234] Roberts T. P., Warwick R. S., 2000, MNRAS, 315, 98

[235] Roberts T. P., Goad M. R., Ward M. J., Warwick R. S., O'Brien P. T., Lira P., Hands A. D. P., 2001, MNRAS, 325, L7

[236] Roberts T. P., Warwick R. S., Ward M. J., Murray S. S., 2002, MNRAS, 337, 677

[237] Roberts T. P., Goad M. R., Ward M. J., Warwick R. S., Lira P., 2002a, in: Proceedings of New Visions of the X-ray Universe in the XMM-Newton and Chandra Era, ESTEC, The Netherlands

[238] Roberts T. P., Warwick R. S., Ward M. J., Goad M. R., 2004, MNRAS, 349, 1193

[239] Roberts T. P., Warwick R. S., Ward M. J., Goad M. R., Jenkins L. P., 2005, MNRAS, 357, 1363

[240] Roberts T. P., Kilgard R. E., Warwick R. S., Goad M. R., Ward M. J., 2006, MNRAS, 371, 1877

[241] Roberts T. P., 2007, Ap&SS, 311, 203

[242] Roberts T. P., Levan A. J., Goad M. R., 2008, MNRAS, 387, 73

[243] Ruggles C., Hoskin M., 1997, "The illustrated history of astronomy", eds Hoskin M., Cambridge University Press, Cambridge, p. 2

[244] Hoskin M., Gingerich O., 1997, "The illustrated history of astronomy", eds Hoskin M., Cambridge University Press, Cambridge, p. 50

[245] Saha A., Claver J., Hoessel J. G., 2002, AJ, 124, 839

[246] Sandage A., et al., 1966, ApJ, 146, 316

[247] Schwarz G., 1978, Annals of Statistics, 6, 461

[248] Schlegel E. M., 1995, RPPh, 58, 1375

[249] Schlegel E. M., Barrett P., Singh K. P., 1997, AJ, 113, 1296

[250] Schlegel D. J., Finkbeiner D. P., Davis M., 1998, ApJ, 500, 525

[251] Schlegel E. M., Pannuti T. G., 2003, AJ, 125, 3025

[252] Serway R. A., 1996, "Physics for Scientist and Engineers with Modern Physics", Fourth Edition, Saunders College Publishing, USA

[253] Shakura N. I., Sunyaev R. A., 1973, A&A, 24, 337

[254] Shapiro S. L., Lightman A. P., Eardley D. M., 1976, ApJ, 204, 187

[255] Shimura T., Takahara F., 1995, ApJ, 445, 780

[256] Silverman J. M., Filippenko A. V., 2008, ApJ, 678, L17

[257] Sirianni M., et al., 2005, PASP, 117, 1049

[258] Smith J. F., Courtier G. M., 1976, RSPSA, 350, 421

[259] Smith D. A., Wilson A. S., 2001, ApJ, 557, 180

[260] Snowden S. L., et al., 1995, ApJ, 454, 643

[261] Soria R., Wickramasinghe D. T., Hunstead R. W., Wu K., 1998, ApJ, 495, L95

[262] Soria R., Motch C., Read A. M., Stevens I. R., 2004, A&A, 423, 955

[263] Soria R., Cropper M., Pakull M., Mushotzky R., Wu K., 2005, MNRAS, 356, 12

[264] Soria R., 2007, Ap&SS, 311, 213

[265] Soria R., Kuncic Z., 2008, AdSpR, 42, 517

[266] Stanton A., 1896, Natur, 53, 274

[267] Stobbart A.-M., Roberts T. P., Warwick R. S., 2004, MNRAS, 351, 1063

[268] Stobbart A. M., Roberts T. P., Wilms J., 2006, MNRAS, 368, 397

[269] Stocke J. T., Wang Q. D., Perlman E. S., Donahue M. E., Schachter J. F., 1995, AJ, 109, 1199

[270] Strohmayer T. E., Mushotzky R. F., 2003, ApJ, 586, L61

[271] Strohmayer T. E., Mushotzky R. F., Winter L., Soria R., Uttley P., Cropper M., 2007, ApJ, 660, 580

[272] Strickland D. K., Colbert E. J. M., Heckman T. M., Weaver K. A., Dahlem M., Stevens I. R., 2001, ApJ, 560, 707

[273] Svensson R., Zdziarski A. A., 1994, ApJ, 436, 599

[274] Swartz D. A., Ghosh K. K., Tennant A. F., Wu K., 2004, ApJS, 154, 519

[275] Swartz D. A., Soria R., Tennant A. F., 2008, ApJ, 684, 282

[276] Swartz D. A., Tennant A. F., Soria R., 2009, arXiv, arXiv:0907.4718

[277] Takano M., Mitsuda K., Fukazawa Y., Nagase F., 1994, ApJ, 436, L47

[278] Takeuchi S., Mineshige S., Ohsuga K., 2009, arXiv, arXiv:0904.4598

[279] Tanaka Y., et al., 1984, PASJ, 36, 641

[280] Tanaka Y., Inoue H., Holt S. S., 1994, PASJ, 46, L37

[281] Tauris T. M., van den Heuvel E. P. J., 2006. in: “Compact Stellar X-ray Sources”, eds. Lewin W.H.G. and va der Klis M., Cambridge University Press, Cambridge, p. 623

[282] Temple R. F., Raychaudhury S., Stevens I. R., 2005, MNRAS, 362, 581

[283] Terashima Y., Wilson A. S., 2003, ApJ, 583, 145

[284] Terashima Y., Inoue H., Wilson A. S., 2006, ApJ, 645, 264

[285] Tipler P. A., 1999, ”Physics for Scientist and Engineers”, Fourth Edition, W.H. Freeman and Company, New York

[286] Titarchuk L., 1994, ApJ, 434, 570

[287] Thronson H. A., Jr., Hunter D. A., Casey S., Latter W. B., Harper D. A., 1989, ApJ, 339, 803

[288] Toomer G. J., 1996, "Astronomy before the Telescope", ed Walker C., British Museum Press, London, p. 68

[289] Trinchieri G., Fabbiano G., Peres G., 1988, ApJ, 325, 531

[290] Trudolyubov S. P., 2008, MNRAS, 387, L36

[291] Truemper J., 1982, AdSpR, 2, 241

[292] Tsunemi H., Kitamoto S., Okamura S., Roussel-Dupre D., 1989, ApJ, 337, L81

[293] Tsunoda N., Kubota A., Namiki M., Sugiho M., Kawabata K., Makishima K., 2006, PASJ, 58, 1081

[294] Turner M. J. L., et al., 1989, PASJ, 41, 345

[295] Ueda Y., et al., 1998, Natur, 391, 866

[296] Ueda, Y., Yamaoka, K., Remillard, R., 2009, arXiv, arXiv:0901.1982

[297] van der Klis M., 2006. in:"Compact Stellar X-ray Sources", eds. Lewin W.H.G. and va der Klis M., Cambridge University Press, Cambridge, p. 39

[298] van Paradijs J., McClintock J. E., 1995, in "X-ray Binaries", eds. Lewin W. H. G., van Paradijs J. and van den Heuvel E. P. J., Cambridge University Press, Cambridge, p. 58

[299] Vázquez G. A., Hornschemeier A. E., Colbert E., Roberts T. P., Ward M. J., Malhotra S., 2007, ApJ, 658, L21

[300] Vierdayanti K., Mineshige S., Ebisawa K., Kawaguchi T., 2006, PASJ, 58, 915

[301] Vierdayanti K., Watarai K.-Y., Mineshige S., 2008, PASJ, 60, 653

[302] Vogler A., Pietsch W., Bertoldi F., 1997, A&A, 318, 768

[303] Vogler, A., & Pietsch, W. 1999, A&A, 342, 101

[304] Ward M. J., Geballe T., Smith M., Wade R., Williams P., 1987, ApJ, 316, 138

[305] Warwick R. S., et al., 1981, MNRAS, 197, 865

[306] Watarai K. Y., Fukue J., Takeuchi M., Mineshige S., 2000, PASJ, 52, 133

[307] Watarai K., Mizuno T., Mineshige S., 2001, ApJ, 549, L77

[308] Watson J. D., Crick H. C., 1953, Natur, 171, 737

[309] Webster B. L., Murdin P., 1972, Natur, 235, 37

[310] Wegner W., 2006, MNRAS, 371, 185

[311] Weisskopf M. C., 1999, AAS, 31, 1514

[312] Weisskopf M. C., Wu K., Tennant A. F., Swartz D. A., Ghosh K. K., 2004, ApJ, 605, 360

[313] Wells R. A., 1996, "Astronomy before the Telescope", ed Walker C., British Museum Press, London, p. 28

[314] White N. E., Peacock A., 1988, MmSAI, 59, 7

[315] White N. E., Nagase F., Parmer A. N., 1995, in "X-ray Binaries", eds. Lewin W. H. G., van Paradijs J. and van den Heuvel E. P. J., Cambridge University Press, Cambridge, p. 1

[316] Williams R. M., Chu Y.-H., Gruendl R., 2006, AJ, 132, 1877

[317] Wilms J., Allen A., McCray R., 2000, ApJ, 542, 914

[318] Winter L. M., Mushotzky R. F., Reynolds C. S., 2006, ApJ, 649, 730

[319] Wood K. S., et al., 1984, ApJS, 56, 507

[320] Yukita M., Swartz D. A., Soria R., Tennant A. F., 2007, ApJ, 664, 277

[321] Zampieri L., Mucciarelli P., Falomo R., Kaaret P., di Stefano R., Turolla R., Chieregato M., Treves A., 2004, NuPhS, 132, 387

[322] Zampieri L., Mucciarelli P., Falomo R., Kaaret P., Di Stefano R., Turolla R., Chieregato M., Treves A., 2004, ApJ, 603, 523

[323] Zezas A., Fabbiano G., Rots A. H., Murray S. S., 2002, ApJS, 142, 239

[324] Zezas A., Fabbiano G., Baldi A., Schweizer F., King A. R., Rots A. H., Ponman T. J., 2007, ApJ, 661, 135

[325] Zombeck M. V., 1990, "Handbook of space astronomy and astrophysics", Cambridge University Press, Cambridge